On the Application of Highly Nonlinear Solitary Waves for Nondestructive Evaluation

by

Amir Nasrollahi

Master's degree, Earthquake Engineering, BHRC Institute, 2010

Submitted to the Graduate Faculty of

the Swanson School of Engineering in partial fulfillment

of the requirements for the degree of

Doctor of Philosophy

University of Pittsburgh

2018

UNIVERSITY OF PITTSBURGH

SWANSON SCHOOL OF ENGINEERING

This thesis/dissertation was presented

by

Amir Nasrollahi

It was defended on

October 19, 2018

and approved by

Piervincenzo Rizzo, Ph.D., Professor
Department of Civil and Environmental Engineering, University of Pittsburgh

Jinkyu Yang, Ph.D., Associate Professor
Aeronautics & Astronautics College of Engineering, University of Washington

Lev Khazanovich, Ph.D., Professor
Department of Civil and Environmental Engineering, University of Pittsburgh

Luis Vallejo, Ph.D., Professor
Department of Civil and Environmental Engineering, University of Pittsburgh

On the Application of Highly Nonlinear Solitary Waves for Nondestructive Evaluation

Amir Nasrollahi, PhD

University of Pittsburgh, 2018

Highly nonlinear solitary waves (HNSWs) are compact nondispersive waves that can form and propagate in slightly compacted 1D chains of identical particles. Such a 1D chain is a heterogeneous lattice, which holds nonlinearity due to geometry and periodicity. Depending on the dynamic excitation, the particles support linear, weakly nonlinear, or highly nonlinear waves. The latter are triggered when the excitation generates a dynamic force much higher than the initial precompression.

Over the last decade, there has been a great effort to use HNSWs in engineering applications such as shock absorbers, energy harvesting, and nondestructive evaluation (NDE). For NDE application, many examples available in the literature show that the stiffness of the material/structure in contact with a chain of particles, where HNSWs are generated, affects the number, amplitude, and arrival time of the solitary waves.

In this dissertation, the dynamic interaction between HNSW and structure is investigated for three NDE applications: (1) determination of the elastic modulus and ultimate strength of concrete material, (2) measurement of the internal pressure and bouncing characteristics of tennis balls, and (3) estimation of axial stress in beams and continuous welded rails (CWRs). In the concrete application, the aim is to study the effect of water-to-cement ratio on the entire mix and on the surface of fresh concrete (simulating the undesirable water added to the fresh concrete by rain) on the solitary wave features. An experimental setup including seven solitary wave transducers and a

numerical analysis simulating concrete samples as semi-infinite material is conducted to prove the feasibility and accuracy of the proposed HNSW method.

Table of Contents

List of Tables

List of Figures

Preface

These words are dedicated to those…

who have been supportive, encouraging, and inspiring…

who have a passion for learning, discovering, and teaching…

and who think, design, and create.

1.0 Introduction

Metamaterials are assemblies of multiple unit cells fashioned from conventional materials and constructed into repeating patterns. Metamaterials derive their properties not from the compositional properties of the cell, but from their exactingly-designed structure [1, 2]. They are increasingly proposed in many applications [1-11] including acoustics (see the excellent review [2]), nondestructive testing (NDT) [12-22], energy harvesting [23-27], and lensing [28-31], just to name a few.

One example of metamaterial is a closely packed 1-D chain of elastically interacting particles [32-37] which supports the formation and propagation of highly nonlinear solitary waves (HNSWs), which are compact waves fundamentally different from those waves typically encountered in acoustics and ultrasound. Those waves are linear and characterized by having a return force linearly dependent on the displacement. HNSWs are instead nonlinear; for instance, in chains of spherical particles the return force F is nonlinearly proportional to the displacement from equilibrium according to the Hertz's law [34, 38] $F=A\delta^{3/2}$. Here, δ is the indentation also known as closest approach between two adjacent identical beads, and A is the contact stiffness. HNSWs exhibit a power-law dependence of the phase velocity V_s on the force F as $V_s \propto F^{1/6}$, i.e. the wave speed is proportional to the wave amplitude. In practice, a strong pulse propagates faster than a weak pulse. This property is not seen in linear waves.

Many researchers investigated the interaction between HNSWs and structural and biological materials to exploit new noninvasive ways to characterize materials that are in dry point contact with the chain or to discover new dynamical phenomena. Yang et al. [39] demonstrated that the formation and propagation of reflected HNSWs depend on the modulus of elasticity and geometry

of the adjacent medium. Schiffer et al. studied the effect of subsurface voids on the propagation of HNSWs [40] and demonstrated in [41] that the formation and propagation of reflected HNSWs depend on the modulus of elasticity and geometry of the adjacent medium. Job et al. evaluated the collision of a single solitary wave with elastic walls with various stiffness [42] and studied in another paper [43] the wave scattering at the interface between two particles of different masses. Manciu and Sen [44] investigated the wave reflections from rigid wall boundaries. Falcon et al. [45] studied the collision of a column of N beads with a fixed wall. Rizzo and co-authors [14, 15, 18, 46-50] investigated the interaction of HNSWs with cement, plates and slender beams. Vergara [51] studied the propagation of solitary waves in a chain with two segments of different beads and found that a train of solitary waves with smaller energy emerge at the interface between the two segments. Ni et al. [52] monitored the curing of fresh cement using a HNSW-based transducer. Recently, our group has investigated the interaction of HNSWs with slender beams [15, 53-55].

A graphical representation about the use of HNSW for nondestructive evaluation (NDE) applications is shown **Figure 1-1**: a 1-D chain of spherical particles is in contact with the material to be assessed; the impact of a striker, i.e. a particle of equal size and mass of the other particles composing the chain or a mechanical striker, generates a single incident solitary wave (ISW) propagating in the chain. When the ISW reaches the interface with the material to be tested, the pulse is partially reflected giving rise to the primary reflected solitary wave (PSW). When the incident pulse interacts with a medium that is much softer than the particles carrying the acoustic energy, one or more secondary reflected solitary waves (SSWs) [39, 45, 52, 56] forms and travels within the chain. Many studies, including some from the University of Pittsburgh, determined that the characteristics of the reflected pulses such as amplitude and time of flight (TOF) are correlated to the modulus of the underlying material. Here, the TOF denotes the transit time at a given bead

in the granular crystal between the incident and the reflected waves. The TOF of the PSW and SSW are typically estimated by measuring the arrival time of the peak amplitude of the ISW and the PSW or the SSW at a given particle. The HNSW features include the TOF, PSW-to-ISW ratio (PSW/ISW), and SSW-to-ISW ratio (SSW/ISW) is functions of the structure or the bulk material in contact with the chain of particles.

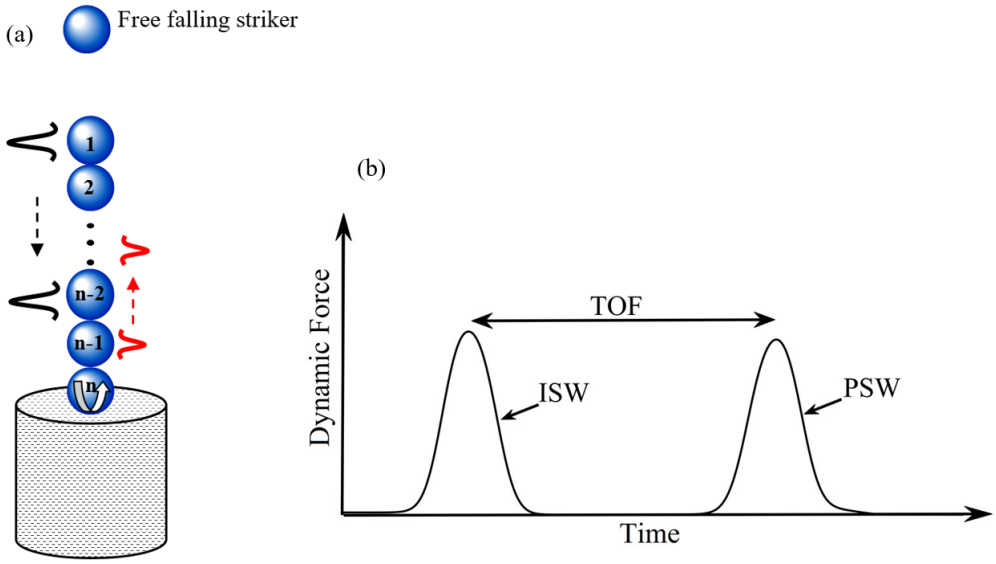

Figure 1-1 (a) The general idea of HNSWs propagating in a chain of particles in contact with a test material. (b) Example of a single incident pulse (ISW) reflected from a rigid wall in the form of a primary reflected solitary wave (PSW) in contact with one end of the chain

This dissertation focuses on the application of HNSWs in NDE using particles discussed in **Figure 1-1**. The research hypothesis is that the detection and analysis of the traveling solitary pulses can lead to a noninvasive determination of various mechanical properties of the contact material.

For the generation and detection of the waves, a few general devises, hereinafter referred to as HNSW transducer, was assembled. The transducer and the nondestructive testing system consist of five main parts: 1. one actuating mechanism, 2. one chain of spherical particles (or beads), 3. one sensing system for detecting the waves propagating within the chain, 4. one frame or tube holding the chain , and 5. one data acquisition (DAQ) system with a function generator to drive the transducer and a digitizer to collect and store the time-waveforms.

In this study, the actuating system is either an electromagnet which lifts and releases the first particle of the chain, and the HNSW is generated by the impact of the first particle to the second one, or a shaker connected to a half-bead, which represents the striker. The particles are made of stainless-steel spheres of 19.05 mm diameter. Depending upon the application, the sensing system based on magnetosctriction, referred to as magnetostrictive sensor (MsS) hereinafter, and indicated as the M-transducer (**Figure 1-2**) or based on an embedded piezoelectric (PZT) disc and indicated as the P-transducers (**Figure 1-2**).

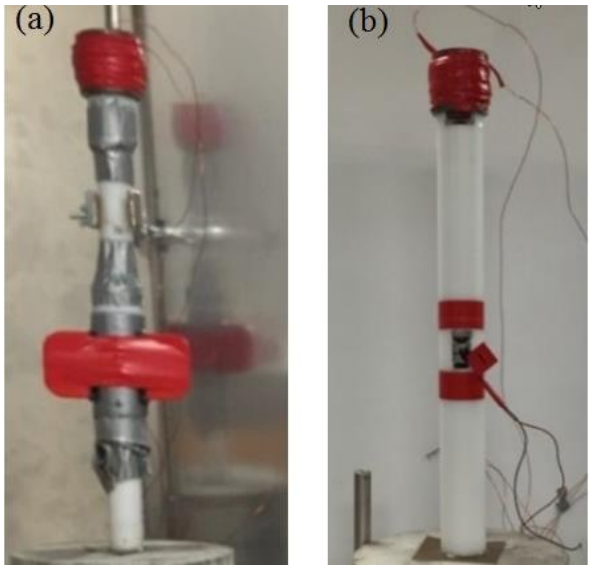

Figure 1-2 Example of the (a) M-transducers and (b) of one P-transducer designed and assembled

1.1 Motivation

1.1.1 Elastic Modulus of Hardened Concrete

Many NDE techniques have been proposed to determine the elastic modulus or to estimate the ultimate strength of existing concrete. Most of these techniques are based on the measurement of the velocity of linear bulk ultrasonic waves propagating through a concrete sample. Traditionally, commercial transducers are used to generate longitudinal waves or both longitudinal and shear waves. Parameters, such as wave speed and attenuation are measured and empirically correlated to the material properties. This approach is usually referred to as the ultrasonic pulse velocity (UPV) method. To obtain an acceptable signal-to-noise ratio (SNR), longitudinal wave transducers cannot be used to generate transverse waves and vice-versa. Thus, to use both shear and longitudinal waves, four transducers at least are required. If the access to the back wall of the sample is impractical, the wave reflection method can be adopted. In this approach, the amplitude of the shear waves or the longitudinal waves, or both at an interface between a buffer material, typically a steel plate, and the concrete is monitored over time. The amount of wave reflection depends on the reflection coefficient, which in turn is a function of the acoustical properties of the materials that form the interface.

In the work presented in this dissertation, the capability of the novel sensing device based on the propagation of HNSWs was studied for the determination of the elastic modulus of concrete and for the prediction of the compressive strength of existing concrete in bridge decks. To validate the reliability of the proposed approach, the method was compared to conventional ultrasonic method based on pitch-catch mode. To test the research hypothesis, several cured concrete slabs, cylinders with various *w/c* ratios, and short beams with excessive water at the bottom or top

surfaces during concreting were inspected. One of the hypotheses is that the HNSW-based technique or the ultrasonic technique or both can determine the modulus of concrete, which might have been compromised by environmental factors or accidental damage. By knowing the modulus of concrete, the ultimate strength of the concrete can be inferred using empirical relations such as the one according to ACI 318.

1.1.2 Internal Pressure of Tennis Balls

The properties of tennis balls are specified by the rules of tennis. Even so, a variety of balls with different physical properties is manufactured. In Europe, tennis balls tend to be more expensive and durable, as the average customer expects them to last for several months. In the United States, balls tend to be less expensive and less durable since players generally prefer to use new balls after a few sets. Over time, tennis balls "age" suffering from internal pressure loss and reduced coefficient of restitution (CoR). Predicting the dynamics of tennis balls on court surfaces during impacts can be extremely complicated; still, this response plays a major role in tennis and can influence the style of professional and amateur players.

One of the standard methodologies to measure the CoR is the dropping test, where the ball is released from a height of 2.54 m onto a concrete slab. An approved ball must bounce to a height between 1.35 m and 1.47 m. This test can be staged by manufacturers and testing authorities but cannot be implemented at home or at sports facilities.

The capability of HNSW transducers was tested in detecting the changes in the internal pressure of sport balls, and as a result, on their mechanical performance such as CoR. If the results show that the HNSW transducers can estimate the internal pressure of the sport balls, the methodology can be applied to more complex structures. To the author's best knowledge, none of the existing

works have led to the development of a hand-held device able to estimate anytime anywhere the pressure and serviceability of tennis balls.

Based on the thickness-to-radius of the ball, the ball performs as a thin-walled shell or a membrane. The internal pressure stretches the ball bladder, and this stretch causes geometric stiffness, which is added to the material stiffness of the ball. In the study presented in this dissertation, the research hypothesis was that the characteristics of the PSE and SSW detect the changes in the stiffness of the balls due to the change in internal pressure.

1.1.3 Thermal Buckling of Rails

CWRs are track segments welded together. With respect to joint rails, CWRs are stronger and smoother, require less maintenance, and can be traveled at higher speeds. When anchored, a CWR is pre-tensioned to counteract the thermal expansion occurring in warm days. Typical pre-tension is such that the rail neutral temperature (RNT), i.e. the temperature at which the longitudinal force is zero, is between 90°F and 110°F. The pre-tension force cannot be higher because material contraction in winter may break the rail. Over the years, the RNT decreases to an unknown value comprised between 50°F and 70 °F, increasing the risk of extreme thermal compression in summer when the temperature of the rail exceeds the ambient temperature by 30°F or more. The compression can be over 250 kip [57] raising the possibility of thermal buckling (**Figure 1-3**), a structural problem that caused hundreds of derailments and millions of dollars in damage in the U.S. alone during the last decade.

Figure 1-3 Buckling of CWRs [58]

The “physiological” reduction of the RNT combined with climate change and the increase in passenger and freight tonnage, escalates the risk of thermal buckling in CWRs. As such, the first and foremost impact for practice of this project is the prevention of derailments with obvious benefits for safety, economy, and environment. This project addresses the long-standing challenge [58-60] of nondestructively and reliably measuring stress and RNT. The consequence is that the railroad industry is still searching for NDE methods able to provide the necessary level of accuracy with minimum traffic disruption.

To address this interest, the study presented in this dissertation investigates the feasibility of a HNSW-based NDE method to quantify the stress or the RNT of CWRs without disturbing the track structure, without prior knowledge of the RNT, with a few measurements that do not require day-long observations under favorable weather, and without permanent wayside installations. Recently, Rizzo and co-authors proposed a new NDE method to estimate the axial stress in thin

beams [13-15, 61] based on the propagation of HNSWs. In this dissertation, the same methodology will be generalized applied on thick beams and rail segments.

1.2 Novelty

Based on the above, the novelty of this Ph.D. work is: 1. Design and reliability assessment of HNSW transducers, 2. estimating the elastic modulus of hardened concrete with HNSW transducers, 3. estimating the internal pressure of tennis balls and/or their serviceability using HNSW transducer, and 4. proposing a "*plug-and-play*" device to determine the neutral temperature and the axial stress of CWRs using HNSW transducers. We call this device *ANTEUSW*: **A**dvanced **N**eutral **T**emperature **E**stimation **U**sing **S**olitary **W**aves. The straight transducers will be used for evaluating the elastic modulus of hardened concrete, the axial stress in CWRs, and internal pressure of sport balls, whereas the L-shaped transducers will be used to evaluate the thermal buckling of CWRs.

1.3 Outline

This dissertation is oriented as follows: Chapter 2 presents the background of HNSWs, Chapter 3 focuses on the application of HNSWs for the NDE of the elastic modulus of hardened concrete, and illustrates three studies : in the first study, four HNSW transducers were build and were tested against some materials to assess their repeatability and reliability in determining the elastic modulus of the material in dry contact with the transducer; in the second study, the HNSW-based method applied to the samples and compared to the conventional ultrasonic method and destructive method for determining the elastic modulus of concrete with various water-to-cement

ratio; and the last part proposes the application of the method on the concrete samples experienced excessive surface water at the time of concreting. In Chapter 4, HNSW transducers are applied in the assessment of the internal pressure, rubber degradation, and the bouncing characteristics of tennis balls. This chapter describes also a generalized procedure for modeling HNSW transducers with more complex structures. Chapter 5 is devoted to the application of HNSWs in the axial stress measurement in thick beams and CWRs. Finally, chapter Six provides the main conclusions of the dissertation and suggest several potential applications of HNSW method for future studies.

2.0 Background

This chapter describes the underlying basis of HNSWs and follows the analytical formulation adopted in [52, 62]. **Figure 2-1** illustrates the general principles of the proposed method: a 1-D chain of spherical particles is in contact with the material to be assessed; the impact of a striker, i.e. a particle of equal size and mass of the other particles composing the chain or a mechanical striker, generates a single incident solitary wave (ISW) propagating in the chain. When the ISW reaches the interface with the material to be tested, the pulse is partially reflected giving rise to the primary reflected solitary wave (PSW). When the incident pulse interacts with a medium that is much softer than the particles carrying the acoustic energy, one or more secondary reflected solitary waves (SSWs) [39, 45, 52, 56] forms and travels within the chain. Many studies, including some from our group, determined that the characteristics of the reflected pulses such as amplitude and time of flight (TOF) are correlated to the modulus of the underlying material. Here, the TOF denotes the transit time at a given bead in the granular crystal between the incident and the reflected waves.

The interaction between two adjacent beads is governed by the Hertz's law [63, 64]:

$$\boldsymbol{F = A\delta^{3/2}} \tag{2.1}$$

and it establishes a relationship between the compression force F of the granules and the closest approach of the particle centers. In Eq. (2.1) the coefficient A is given by:

$$\boldsymbol{A = \begin{cases} A_c = E\sqrt{2a/3}\left(1-\nu^2\right) \\ A_w = \dfrac{4\sqrt{a}}{3}\left(\dfrac{1-\nu^2}{E}+\dfrac{1-\nu_w^2}{E_w}\right)^{-1} \end{cases}} \tag{2.2}$$

where A_c refers to the case of particle-to-particle contact, and A_w refers to the case of particle-to-wall (semi-infinite material) contact case. In Eq. (2.2), E, a, and ν are modulus of

elasticity, radius, and Poisson's ratio of the spherical beads, respectively, whereas E_w and ν_w are the modulus of elasticity and Poisson's ratio of the wall, respectively.

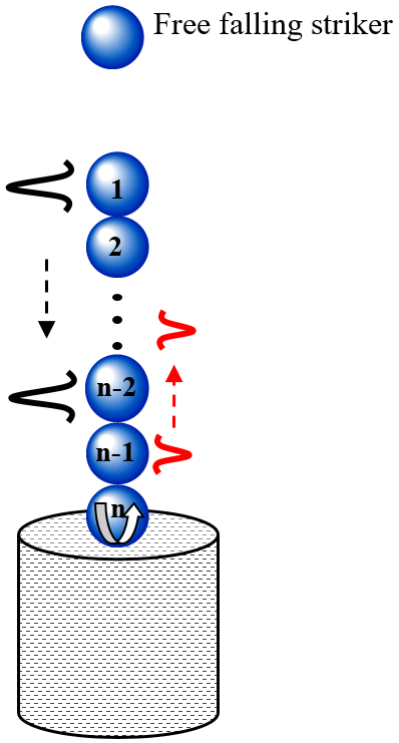

Figure 2-1 General scheme of the nondestructive evaluation method based on the propagation of highly nonlinear solitary waves.

The combination of the nonlinear interaction (Eq. 2.1) and a zero tensile strength in the chain of spheres leads to the formation and propagation of compact solitary waves [64]. When the wavelength is much larger than the particles' diameter, the speed V_S of the waves depends on the maximum dynamic strain ξ_m [64] which, in turn, is related to the maximum force F_m between the particles in the discrete chain [65]. When the chain of beads is under a static pre-compression force F_0 ($F_0 << F_m$), the initial strain of the system is referred to as ξ_0. It should be noted that in

configurations like the one shown in **Figure 2-1**, the pre-compression is provided by the self-weight of the chain. The speed V_s has a nonlinear dependence on the normalized maximum strain $\xi_r=\xi_m/\xi_0$, or on the normalized force $f_r=F_m/F_0$, expressed by the following equation [65]:

$$\begin{aligned} V_s &= c_0 \frac{1}{(\xi_r - 1)} \times \left[\frac{4}{15}\left(3 + 2\xi_r^{\frac{5}{2}} - 5\xi_r\right)\right]^{\frac{1}{2}} \\ &= 0.9314\left(\frac{4E^2F_0}{a^2\rho^2(1-\nu^2)^2}\right)^{\frac{1}{6}} \frac{1}{\left(f_r^{\frac{2}{3}} - 1\right)}\left[\frac{4}{15}\left(3 + 2f_r^{\frac{5}{3}} - 5f_r^{\frac{2}{3}}\right)\right]^{\frac{1}{2}} \end{aligned} \tag{2.3}$$

where c_0 is the wave speed in the chain initially compressed with a force F_0 in the limit f_r=1, and ρ is the density of the material.

When f_r (or ξ_r) is very large, Eq. (2.3) becomes:

$$V_s = 0.6802\left(\frac{2E}{a\rho^{\frac{3}{2}}(1-\nu^2)}\right)^{\frac{1}{3}} F_m^{\frac{1}{6}} \tag{2.4}$$

and the shape of a solitary wave can be closely approximated as [64]:

$$\xi = \left(\frac{5V_s^2}{4c^2}\right)\cos^4\left(\frac{\sqrt{10}}{5a}x\right) \tag{2.5}$$

where

$$c = \sqrt{\frac{2E}{\pi\rho(1-\nu^2)}} \tag{2.6}$$

and x is the coordinate along the wave propagation direction.

The equations above predict that the mechanical properties of the specimen in contact with the chain of particles influences the contact stiffness of the chain-material interface.

If the precompression between the beads is zero, the speed of sound in the periodic arrays of discrete beads is zero. This condition is called “sonic vacuum” which was first introduced by Nesterenko [38, 66, 67]. A slightly compressed array of periodic beads also exhibits a behavior

close to a sonic vacuum, supporting strongly nonlinear solitary waves with a finite wavelength [38]. HNSWs also exhibit a power-law dependence of their phase velocity V_s on the force amplitude F_m as $V_s \sim F_m^{1/6}$, i.e. stronger pulses propagate faster [66]. Moreover, the stiffness of the material in contact with the medium affects the properties of the solitary pulses reflected at the interface between the grain and the solid. These specific properties of the waves may be used to explore new NDE applications, which are not possible by using traditional acoustics. Highly nonlinear solitary waves are also tunable, i.e. a solitary pulse can be engineered by tuning the mechanical and/or the geometric properties of the nonlinear medium to attain the desired wavelength, speed, and amplitude.

3.0 Determination of Concrete Elastic Modulus

This chapter was written based on the content of papers published in *Sensors* [68], *Nondestructive Testing and Evaluation* [48], and *Applied Sciences* [49], which are on the application of HNSWs in NDE of concrete elastic modulus.

3.1 Introduction

In concrete and cement-based structures, the early stage of hydration and the conditions, at which curing occurs, influence the quality and the durability of the final products. For instance, as a result of the chemical reactions between water and the cement during hydration, the mixture progressively develops mechanical properties. Final set for the mixture is defined as the time that the fresh concrete transforms from plastic into a rigid state. At final set, measurable mechanical properties start to develop in concrete and continue to grow progressively. The durability and the strength of concrete may deviate from design conditions as a result of accidental factors. Some of these factors are *w/c* ratio not controlled well and rainfall that permeates the fresh concrete or dampens the forms prior to casting. As such, the development of nondestructive NDE methods able to determine anomalous concrete conditions is very much needed and has been a long-standing challenge in the area of material characterization. To date, many NDE methods for concrete have been proposed, and some of them resulted in commercial products. The interested reader is referred to the excellent monograph [69] to gain a holistic knowledge of such methods. The most common technique is probably the one based on propagation of bulk ultrasonic waves

through concrete which measures the speed of the waves propagating through the thickness of the test object to determine the elastic modulus of the concrete with an empirical formula [69-78]. If the access to the back wall of the sample is impractical, the ultrasonic testing is conducted in the pulse-echo mode.

Despite decades of research and developments, much research is still ongoing [79-93] and many interesting works covering a wide spectrum of NDE techniques are being investigated.

Many NDE methods for concrete have been proposed, tested, and commercialized in the last three decades. The most common method is perhaps the one based on the measurement of the velocity of linear bulk ultrasonic waves propagating through concrete. Traditionally, commercial transducers generate longitudinal [**94-102**] or both longitudinal and shear waves [**103**]. Parameters, such as wave speed and attenuation are measured and empirically correlated to the properties of the material. This approach is usually referred to as the UPV method. To obtain an acceptable signal-to-noise ratio (SNR), longitudinal wave transducers cannot be used to generate transverse waves and vice versa. Thus, in order to use both shear and longitudinal waves, at least four transducers are required. If the access to the back wall of the sample is impractical, the wave reflection method can be adopted. In this approach, the amplitude of the shear waves [**103-110**], the longitudinal waves [**111**, **112**], or both [**113**] at an interface between a buffer material, typically a steel plate, and the concrete is monitored over time. The amount of wave reflection depends on the reflection coefficient, which in turn is a function of the acoustical properties of the materials that form the interface [**103**].

With respect to ultrasonic-based NDE, the proposed HNSW-based approach: 1) exploits the propagation of HNSWs confined within the grains; 2) employs a cost-effective transducer; 3) measures different parameters (time of flight, speed, and amplitude of one or two solitary pulses)

that can be eventually used to correlate few concrete variables; 4) does not require any knowledge of the sample thickness; 5) does not require an access to the sample's back-wall.

In the study presented in this Chapter 3, four HNSW transducers were assembled. Each transducer consisted of a chain of sixteen spherical particles surmounted by an electromagnet to lift and release the top particle of the chain to excite a solitary pulse. A magnetic wire was wrapped around the nine-th particle of the chain to sense the propagating wave using the magnetostriction principles. The reliability of these transducers was quantified at inferring the modulus of a few materials placed in contact with the transducers.

Four sets of experiments were conducted. In the first one, the four HNSW transducers were tested against samples made of soft polyurethane, hard polyurethane, and steel. The cases of free transducers and transducers partially immersed in water were also considered to set a baseline data. The results were then compared to the numerical predictions obtained with a discrete particle model (DPM) to verify the accuracy of our instruments.

In the second investigation (Ch. 3.3), the same approach was used to find the modulus of elasticity of hardened concrete. The findings were then compared to the results obtained from the conventional UPV method, and the destructive tests standardized in the ASTM C469, ASTM C39, and the ACI 318 [**114-116**]. With this second investigation, we propose to develop an NDE method to estimate the strength of concrete in existing structures.

In the third study (Ch. 3.4), three of those four M-transducers, were used to infer the modulus of concrete samples with three different water-to-cement (*w/c*) ratios. The purpose was to nondestructively evaluate the characteristics of these samples and to evaluate the ability of the HNSW-based NDE at discriminating concrete of different characteristics. Three P-transducers were also assembled. As said in Ch. 1, they consisted of a lead zirconate titanate (PZT) disk

embedded in between two thick disks inserted in the chain. This assembly was investigated to overcome some of the limitations identified in [**117**] relative to the M-transducers. The findings from both transducers were then compared to the results of a conventional UPV test and to the elastic modulus measured in accordance with ASTM C469 method [**116**].

The fourth study expands (Ch. 3.5) expands the work presented in Ch. 3.4 to predict water in excess in short concrete beams made with *w/c*=0.42 but corrupted with water. Two conditions were simulated. The first one consisted of standing water in formworks prior to pouring concrete, whereas the second condition consisted of sprinkling water above the fresh concrete during casting and surface finishing. These two conditions may reflect adverse weather in the field. The objective of the study was the development of a system that, unlike the UPV method, can predict localized deterioration conditions associated with poor quality *w/c* ratio.

Three HNSW transducers were used to quantify the elastic modulus of the beams. The findings were then compared to the results of a conventional UPV test in order to evaluate and prove advantages and eventually limitations of the proposed approach. **Table 3-1** shows a summary of accomplished studies and published papers

Table 3-1 A summary of the tests and outcomes of concrete assessment using HNSW

Study	Outcome	Publication
Transducer design and repeatability test	Four M-transducers were designed and tested against some materials for repeatability	Paper published in Sensors [117]
Concrete cylinder test	Concrete cylinders with various *w/c* ratio were tested for elastic modulus	Paper published in Nondestructive Testing and Evaluation [48]
Short beam test	Short concrete beams with excessive water at top or bottom surfaces were tested for elastic modulus	Paper published in Applied Sciences [49]

3.2 Transducer Reliability at Determining the Modulus of Materials

3.2.1 Material Characterization: Experimental Setup

Figure 3-1 shows the scheme of a HNSW transducer with a magnetostrictive sensor (MsS) used in this part of this study. The chain consisted of 16 particles with $2a$=19.05 mm. The second bead from the top was made of nonferromagnetic steel (McMaster-Carr, AISI 304) whereas the other particles were made of ferromagnetic low-carbon steel (McMaster-Carr, AISI 1020). The properties of these two steels are listed in **Table 3-2** [118]. The chain was held by a Delrin Acetal Resin tube (McMaster-Carr 8627K219) with outer diameter D_0=22.30 mm and inner diameter slightly larger than $2a$ in order to minimize the friction between the striker and the inner wall of the tube and to minimize acoustic leakage from the chain to the tube. The striker was a ferromagnetic bead, and it was driven by an electromagnet. A constant axial magnetic field was created along the chain and centered at the 9th particle using two identical permanent bridge magnets (McMaster-Carr 5841K55). A coil was wrapped around the tube and around the magnetic field in order to attain an MsS utilized to measure the propagation of the solitary waves within the chain. Finally, a 0.254 mm thick aluminum sheet was glued to the tube's end to prevent the free fall of the particles.

Table 3-2 Mechanical properties of the materials used as the beads and interface.

Material	ρ (kg/m^3)	E (GPa)	υ
Stainless steel (AISI 304)	8000	200	0.29
Stainless steel (AISI 1020)	7860	200	0.29
Soft polyurethane (SAWBONES, #1522-03)	320	0.210	0.30
Hard polyurethane (SAWBONES, #1522-05)	640	0.759	0.30

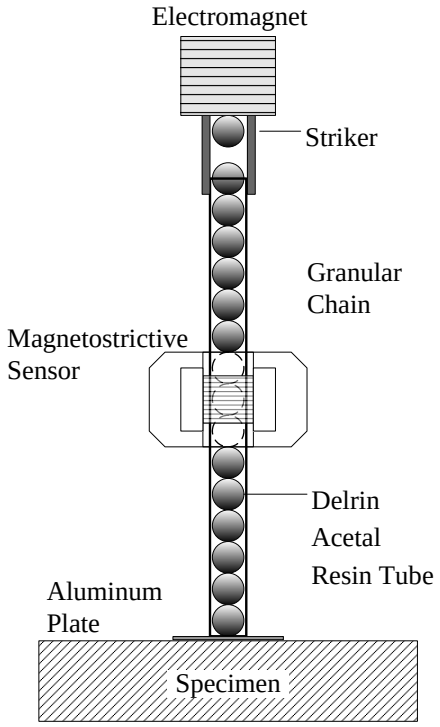

Figure 3-1 Schematic of the HNSWs transducer with a magnetostrictive sensor [118]

As reported in [119-121], magnetostriction can be used to excite and detect stress waves using the Fraraday's law and the Villari's effect, respectively. In this study, we used the Villari's effect, which states that a pulse propagating through a ferromagnetic material modulates an existing magnetic field and generates voltage in the coils. In our experiments, the AISI 1020 particles were magnetostrictive material and they were subjected to the magnetic field induced by the magnets. One of the authors used MsS to excite and detected guided ultrasonic waves [122-124].

Four transducers were built and driven simultaneously by a National Instrument-PXI (1042Q) unit running in LabVIEW and a DC power supply (BK PRECISION 1672). We used a Matrix Terminal Block (NI TB-2643) to branch the PXI output into four switch circuits. **Figure 3-2** shows the diagram of the switch circuit. A Metal–Oxide–Semiconductor Field-Effect Transistor

(MOSFET) was used for switching the electronic signals. In **Figure 3-2**, the symbols G, D, and S represent the Gate, Drain, and Source terminals of the MOSFET, respectively. Because the B (body) terminal of the MOSFET was connected to the source terminal, it is omitted in the diagram. EM1 to EM4 represents the four electromagnets mounted on the transducers 1 to 4, respectively. Switches 1 to 4 represent the digital switches. When one of them was set to 1, the switch was turned on. Figure 3-2(b) shows the NI-PXI utilized in the experiment; Figure 3-2(c) illustrates the DC Power used to provide the electromagnet with a direct voltage, and Figure 3-2(d) is the switch circuit with a MOSFET and two terminal blocks.

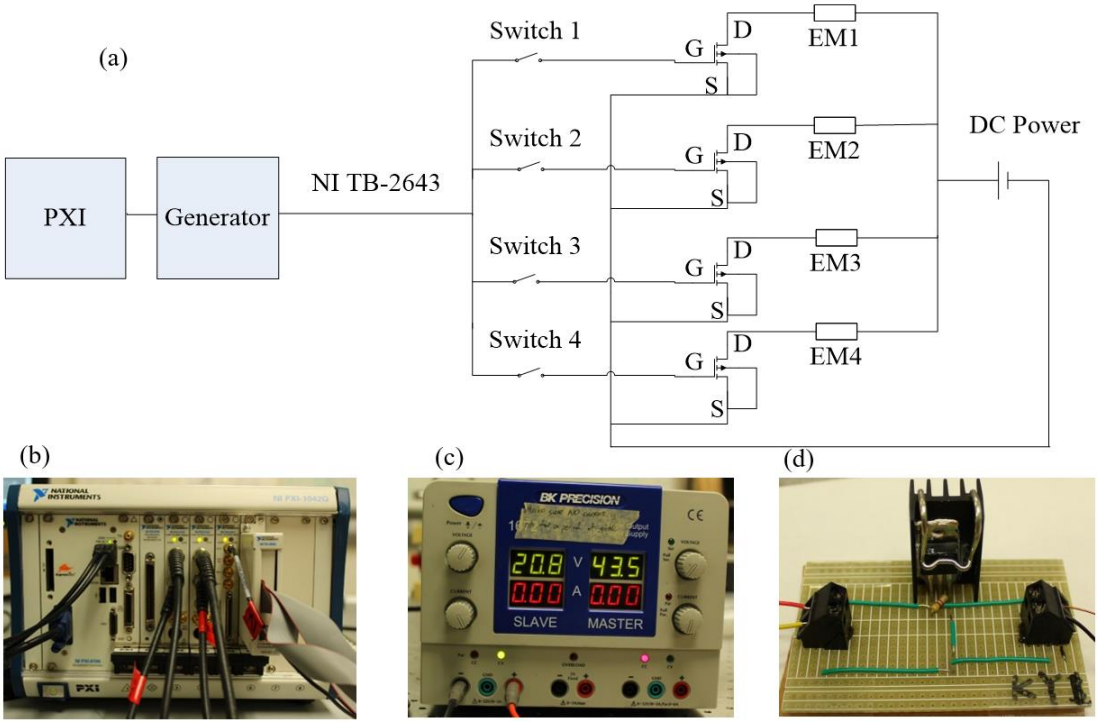

Figure 3-2 Experimental Setup. (a) The switch circuit; (b) The NI-PXI used to drive the transducers, and digitalize, and store the time waveforms; (c) The DC Power supply used to activate the electromagnets; (d) The switch circuit with a MOSFET and two terminal blocks

3.2.2 Material Characterization: Numerical Simulation

The differential equation of motion of 1-D chain of beads can be determined using the Lagrangian description of particle dynamics:

$$\boldsymbol{m\partial_{tt}^{2}u_{n}=A_{n}[u_{n-1}-u_{n}]_{+}^{\frac{3}{2}}-A_{n}[u_{n}-u_{n+1}]_{+}^{\frac{3}{2}}} \tag{3.1}$$

where u_i is the i^{th} particle displacement, $[x]_+$ denotes $max(x,0)$, and A_n is what was defined in Eq. (2.2). It was assumed that the displacement of wall in contact with the grains was zero.

By solving Eq. (3.1), the time-history of the particles' oscillation was obtained. To enable the comparison between the numerical results and the experimental findings, the model mirrored the experimental setup. Moreover, the material of the walls contacting the last particle of the chain was the same as the experiments. The mechanical properties of AISI 304 steel [125], hard polyurethane [126], and soft polyurethane [126] are listed in **Table 3-2**. The effect of the aluminum sheet at the bottom of the tubes was added to the numerical simulation based on the theory of membranes [127, 128]. For the case of the free transducers, the interface was the aluminum sheet in contact with the last particle. For the case of the transducers partially immersed in water, the contact effect was the sum of the sheet's stiffness and the pressure provided by a 5 *mm* water column, which was the same as the experiments.

Because in the experiments, the MsS recorded the oscillation of the 9th particle, all the results of the numerical simulation presented here are based on the wave features measured at the center of this particle. **Figure 3-3** shows the numerical force profiles when the five different interfaces were considered. To ease the readability of the graph, the profiles were offset by 150 N. The top two plots represent the baseline profiles; two peaks are visible in the shape of the PSW. This phenomenon occurs when the interface material or element is too weak to prevent the separation

of the last few particles from the rest of the chain. When they bounce back to the original rest position, they collide with the chain at slightly different times giving rise to the two humps. Overall, **Figure 3-3** demonstrates that the amplitude and the speed of both reflected waves are dependent on the material which is in contact with the chain: as the material's stiffness increases, the amplitude of the SSW decreases while the amplitude of the PSW increases, and their TOF_{PSW} and TOF_{SSW} diminish.

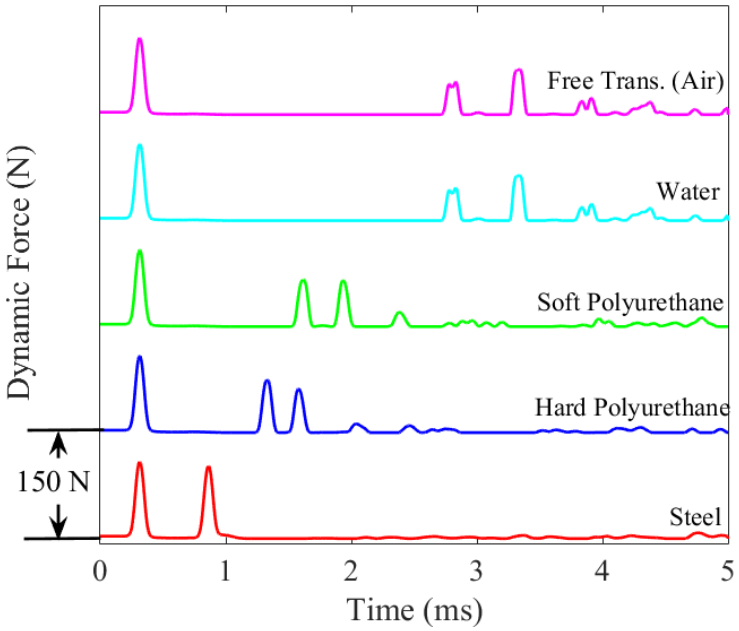

Figure 3-3 Numerical Results. Force profile measured at the center of the 9th bead

To generalize the findings of Figure 3-3, **Figure 3-4(a)** displays the TOF_{PSW} as a function of the modulus of elasticity and the Poisson ratio of the contact material. It is observed that the Poisson ratio has a small effect on the travel time whereas the modulus of elasticity has a significant impact on the TOF of the PSW when $E_w < 100\ GPa$. **Figure 3-4(b)** shows the ratio of the amplitude of the PSW to the amplitude of the ISW as a function of the modulus of elasticity

and the Poisson's ratio. Similar to the parameter of the TOF_{PSW}, the Poisson's ratio does not have a significant impact on the ratio. Moreover, PSW/ISW steadily increases with respect to the modulus of elasticity until the modulus is about 50 GPa, and then it remains constant. Similar to **Figure 3-4(b)**, **Figure 3-4(c)** shows the SSW/ISW as a function of the materials' mechanical properties. The surface is complementary to the surface seen in **Figure 3-4(b)**. This implies that when the stiffness of the contact material is low, a part of the energy carried by the incident pulse spent to generate the SSW. Interestingly, above 50 GPa, the secondary solitary wave is not triggered, and based on the plot of **Figure 3-4(b)**, more than 90% of the incident acoustic energy is reflected to the chain in the form of PSW.

Figure 3-5 shows the effect of the Poisson ratio on the TOF at three given values of the modulus of elasticity. The figure demonstrates that the effect of the Poisson ratio on the TOF is negligible. For example, at any given *E*, the variation of the TOF when the Poisson ratio varies from 0.1 to 0.3 is about 0.14%. As such, it can be concluded that the variation of the Poisson ratio at any given elastic modulus has a negligible effect on the features of the solitary waves propagating in a solid volume.

3.2.3 Material Characterization: Experimental Results

Figure 3-6 shows one of the four transducers suspended in air, i.e. the free transducer, partially immersed, and in contact with the soft polyurethane, hard polyurethane, and stainless-steel block. To assess the repeatability of the method and to verify that all four transducers were identical, one hundred measurements were taken for each medium for every transducer; hence, a total of 2,000 waveforms were analyzed. **Figure 3-7** shows the average of the 100 measurements for the five different media.

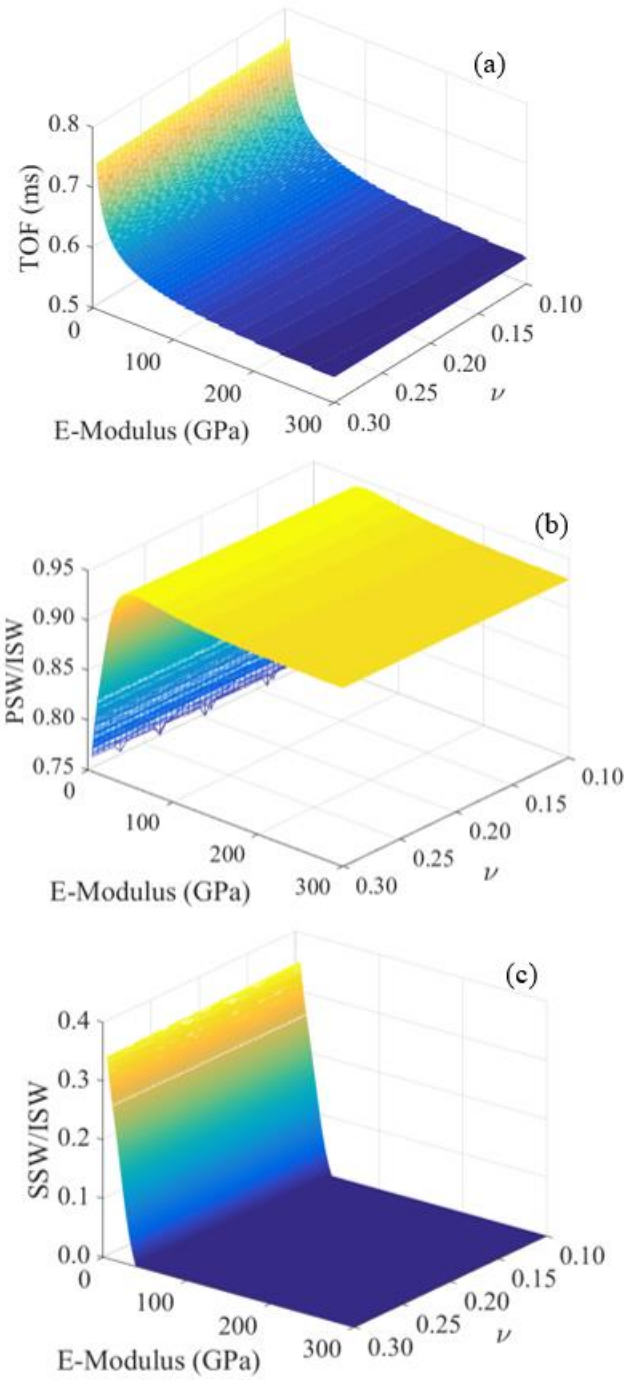

Figure 3-4 Numerical Results. (a) Time of flight of the primary solitary wave, (b) PSW-to-ISW ratio, (c) SSW-to-ISW ratio vs. the modulus of elasticity and Poisson ratio of the contact material

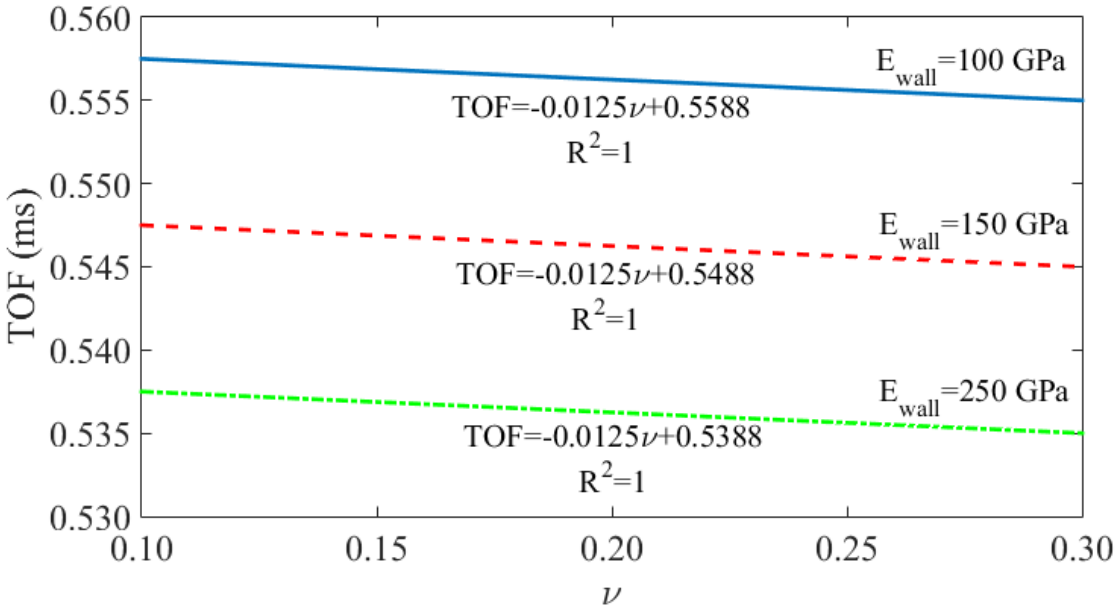

Figure 3-5 TOF as a function of the Poisson's ratio for some values of E_{wall}

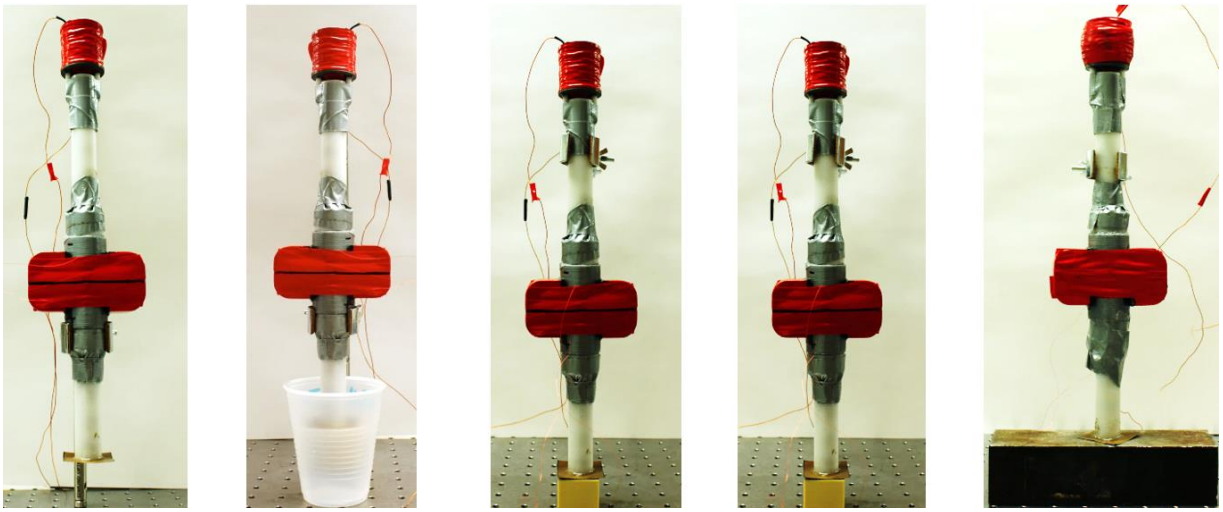

Figure 3-6 Photos of one HNSW transducer. From left to right: free transducer; partially immersed transducer; in contact with a soft polyurethane cube, hard polyurethane cube; stainless steel

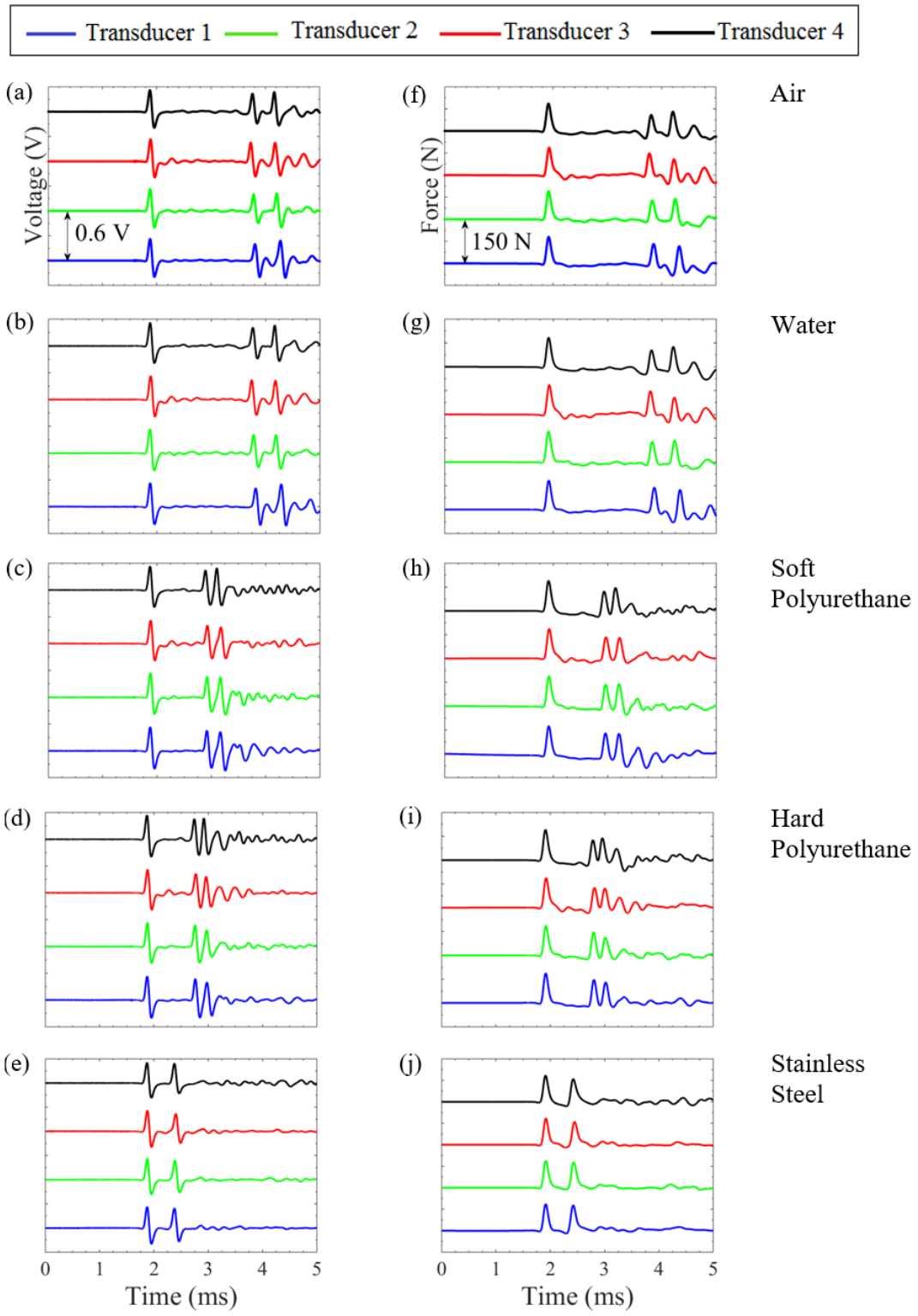

Figure 3-7 Experimental results. Average time waveforms (left column) and corresponding force profile (right column) measured by the four transducers under the five test scenarios

The time waveforms show both positive and negative voltage. When the solitary wave travels through the constant magnetic field induced by the permanent magnets, it increases the compression between two adjacent particles, and it creates a positive gradient of the magnetic flux, which in turn induces the positive voltage. When the pulse moves away, the dynamic compression disappears, a negative gradient of the magnetic flux is induced, and therefore, the output voltage has a negative gradient. In the figures, the first, second, and third pulses correspond to the ISW, PSW, and SSW, respectively.

The integral of the voltage $V(t)$, measured at the center of the 9th particle, is proportional to the dynamic contact force F i.e. [121]:

$$\boldsymbol{F(t) = K_c \int_0^t V(\tau) d\tau} \tag{3.2}$$

where K_c is a conversion factor expressed in N/V·μs.

Under the assumption that the numerical model presented in 3.2.2 mirrored the experimental setup, we calculated K_c by computing the ratio of the numerical dynamic force to the experimental time integral both associated with the ISW, which is the only pulse not affected by the presence of any underlying material. For each transducer, the 500 experimental pulses were considered. The results are listed in **Table 3-3**, and they reveal that the values of K_c are very similar. In fact, the difference between the smallest (6.42 N/V·μs) and the largest (6.67 N/V·μs) value is below 4% which proves the consistency of the assembled transducers. Moreover, within each transducer, the corresponding coefficients of variation, i.e. the ratio of the standard deviation σ to the mean value, are all below 5%, which is a good indicator of the repeatability of the incident pulse.

The values of K_c were then used in Eq. (3.2) to infer the dynamic force profile from the experimental time waveforms. **Figure 3-7(f)** to **(j)** represent the experimental force for each transducer in contact with the five different media. The ISW, PSW, and the SSW are visible. The

latter is absent when steel was tested. The graphs confirm the repeatability of the transducers and the excellent agreement with the numerical predictions presented in **Figure 3-3**.

Table 3-3 Conversion factors to compute the dynamic contact force

Transducer Number	Conversion Factor (N/V·µs)	Standard Deviation (N/V·µs)	Coefficient of Variation (%)
1	6.58	0.1664	2.53
2	6.42	0.1689	4.10
3	6.67	0.0947	1.42
4	6.67	0.1334	2.00

To quantify the experimental data, **Figure 3-8** shows, respectively, the values related to the TOF_{PSW} and TOF_{SSW} measured by the four transducers for the five interfaces. The dots represent the average of the 100 measurements whereas the vertical bars represent the 2σ. As expected from the analytical prediction, the TOF_{PSW} and TOF_{SSW} decrease with the increase of the stiffness of the interfaces. The four transducers provide almost identical results; the largest difference was below 6.0% when the steel was tested, and the smallest difference was equal to 0.0011% occurred for the free transducers. Moreover, the small standard deviations confirm the high repeatability of the measurements.

Table 3-4 compares the experimental and the numerical TOF_{PSW}. The differences between the numerical simulation and the experiments range between 0.43% and 18.6%. The first and second largest differences are relative to the soft, and the hard polyurethane, respectively. These differences stem mainly from viscoelastic behavior [39] of the polyurethane in the chain which was not modeled in the numerical simulation.

Table 3-4 Numerical and experimental time of flight relative to the primary reflected wave when the chain is in contact with the five media

Medium	Numerical TOF_{PSW} (ms)	Experimental TOF_{PSW} (ms)	Num. and Exp. difference (%)
Air	2.1350	1.9791	7.88
Water	2.1350	1.9837	7.62
Soft Polyurethane	1.3275	1.0802	18.63
Hard Polyurethane	1.0250	0.9237	9.88
Steel	0.5525	0.5549	0.43

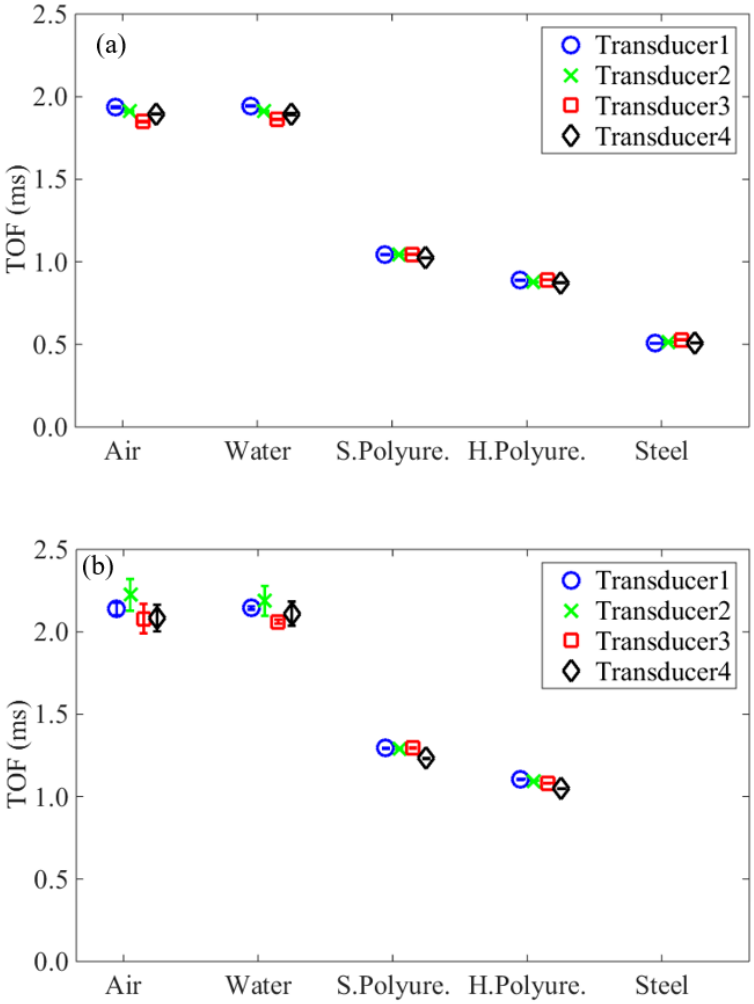

Figure 3-8 Time of flight of both (a) PSW and (b) SSW and the corresponding standard deviation as a function of the five different media

3.2.4 Testing Concrete Slabs

After proving the reliability of the transducers in terms of repeatability, we tested eight 300×300×50 mm^3 concrete slabs in order to study the capability of the novel technology to determine the modulus of elasticity of six-month-old hardened concrete. The concrete mix was designed with *w/c* = 0.42, and fine and coarse river gravel aggregates. The average mass of the slabs was 10.93±0.21 kg. Three cylinders made of the same batch were cast, cured for 28 days, and tested according to standard test methods to estimate the static modulus of elasticity and the Poisson's ratio of concrete. These values, namely $E_s^{ASTM\ C469}$ and *v*, are listed in **Table 3-5**.

Section 8.5.1 of ACI 318 provides an empirical relationship between the modulus of elasticity E_s^{ACI} and the ultimate compressive strength f'_c. Typical values for concrete span from f'_c =13.8 MPa (2 ksi) to 48.3 *MPa* (7 ksi) [116]. Since we obtained the compressive strength of the concrete mix according to ASTM C39, we can estimate the modulus of elasticity E_s^{ACI} as:

$$E_s^{ACI} = 33\left(\rho^{\frac{3}{2}}\right)\sqrt{f_c'} \tag{3.3a}$$

$$E_s^{ACI} = 0.0427\left(\rho^{\frac{3}{2}}\right)\sqrt{f_c'} \quad \text{(SI units)} \tag{3.3b}$$

In Eq. (3.3b) ρ is the density of concrete in kg/m^3, and f'_c is the compressive strength in MPa. The density of concrete is measured, and the compressive strength f'_c was obtained from the ASTM C39 at 28 days. The result is included in **Table 3-5**.

Table 3-5 Values of the compressive strength, the modulus of elasticity, and the Poisson ratio obtained from the ASTM C39, ASTM C469 Tests, and ACI 318 correlation

Samples	$E_s^{ASTM\ C469}$ (GPa)	*v*	f'_c (MPa)	E_s^{ACI} (GPa)
1	28.9	0.158	43.3	33.7
2	25.5	0.164	41.0	32.8
3	26.5	0.155	41.5	33.0

3.2.5 HNSW-based Method: Setup and Results

Figure 3-9 shows the experimental setup. The four HNSW-based transducers were placed above each specimen, and each specimen was tested at four different locations simultaneously, in order to average local surface heterogeneities. For each transducer, 100 measurements were taken using the same hardware/software system described in section 3. It is noted again that the tests were carried 6 months after casting the samples.

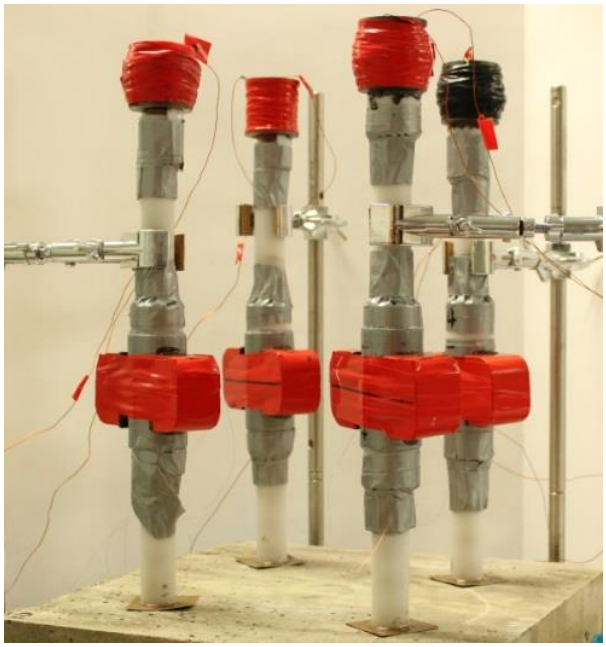

Figure 3-9 Concrete test setup. Photo of the four transducers placed above one of the eight samples

Figure 3-10 shows the force profile obtained after averaging the 100 measurements on slab 4. The presence of the ISW and PSW is clearly visible. The small hump tracing the PSW is the SSW. Despite the inhomogeneous nature of concrete and the use of different transducers, the waveforms are almost identical.

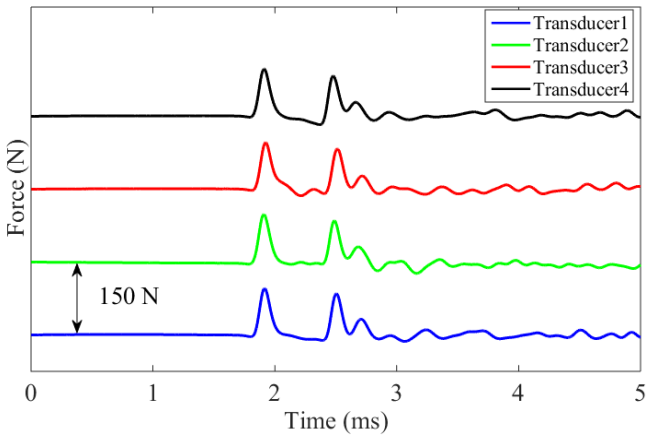

Figure 3-10 Experimental waveform measured by the four transducers when testing one of the eight slabs

Figure 3-11 displays the average TOF_{PSW} and TOF_{SSW}, and the corresponding standard deviation. The scatter of the features' values is below 5%, and it is likely due to the intrinsic slight differences among the transducers and the heterogeneity of the samples' surface. The empirical values of the TOF_{PSW} and the average Poisson ratio obtained with the ASTM C469 (ν=0.16) were used to derive the empirical dynamic modulus of elasticity (E_d^{HNSW}) from **Figure 3-11(a)**. It is remarked here that the selection of the Poisson's ratio could have been done using typical concrete values without affecting the results significantly. **Table 3-6** reports the E_d^{HNSW} computed from all four transducers for all eight samples. By looking at the eight readings from the same transducer, it is evident that the scatter of the data is much higher than the variability of the individual transducer. This suggests that the heterogeneous surface of the samples might have scattered the data. To support this hypothesis, **Figure 3-12** displays a close-up view of the surface of slab 1, slab 3, and slab 4. Many voids are visible on slabs 1 and 3. These voids (bugholes) typically result from the migration of entrapped air and to a less extent water, to the fresh concrete interfaces. These voids and the roughness of the surfaces may weaken the local stiffness of the concrete or may influence the dynamic interaction at the material/transducer interface.

Table 3-6 Concrete test. The TOFPSW, the predicted dynamic modulus of elasticity (E_d), and the corresponding static modulus of elasticity (E_s) of the slabs measured by the HNSW transducers

Slab Number	Sensor Number	TOF_{PSW} (ms)	Modulus of Elasticity (GPa)		
			E_d^{HNSW}	Average E_d^{HNSW}	Average E_s^{HNSW}
1	1	0.6250	22.9	**17.4***	14.4
	2	0.6477	16.8		
	3	0.6475	16.8		
	4	0.6650	13.1		
2	1	0.6225	26.1	28.5	23.7
	2	0.6193	28.8		
	3	0.6350	20.3		
	4	0.6001	39.0		
3	1	0.6400	18.8	**16.3***	13.5
	2	0.6442	18.7		
	3	0.6786	11.1		
	4	0.6486	16.8		
4	1	0.6075	35.0	37.8	31.4
	2	0.5827	59.8		
	3	0.6211	26.2		
	4	0.6125	30.2		
5	1	0.6050	35.0	26.5	22.0
	2	0.6000	39.0		
	3	0.6386	19.5		
	4	0.6685	12.6		
6	1	0.5975	41.1	38.4	31.9
	2	0.5800	64.0		
	3	0.6336	21.2		
	4	0.6186	27.5		
7	1	0.6125	30.1	28.7	23.8
	2	0.6175	27.5		
	3	0.6250	23.9		
	4	0.6075	33.3		
8	1	0.6275	23.9	24.9	20.7
	2	0.6175	27.4		
	3	0.6375	19.5		
	4	0.6150	28.8		
Average		**0.6250**	**27.3**	**30.8***	**25.6***

* The results of Slabs 1 and 3 were not used in the average.

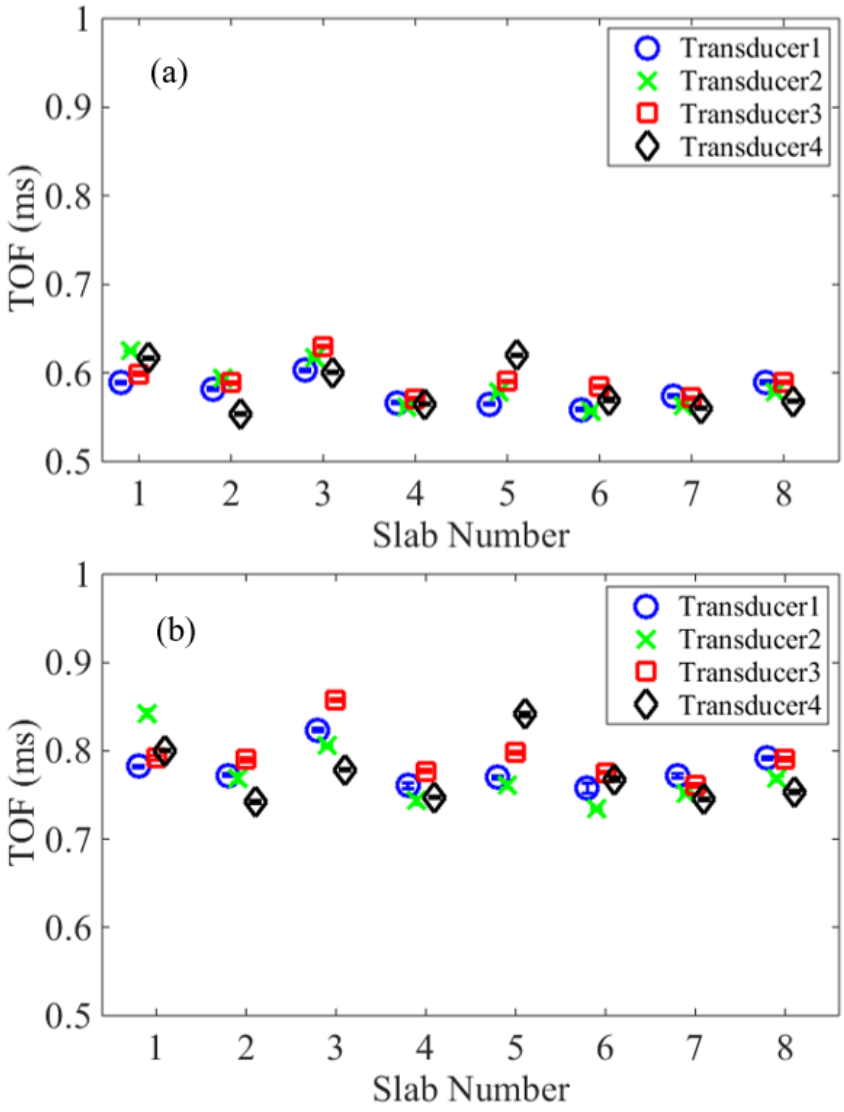

Figure 3-11 Average time of flight and the relative standard deviations of both (a) PSW and (b) SSW obtained from the four transducers for the eight concrete slabs

The dynamic modulus E_d^{HNSW} was converted into the static modulus of elasticity (E_s^{HNSW}) using the empirical formula proposed by Lydon and Balendran [129, 130]:

$$\boldsymbol{E_s = 0.83 E_d} \tag{3.4}$$

The results are also presented in **Table 3-6**. The superscript emphasizes the fact that these values were obtained with the novel NDE method. Apart from the outliers measured from slabs 1 and 3, the average E_d^{HNSW} is equal to 30.8 GPa and its corresponding static modulus is equal to 25.6 GPa.

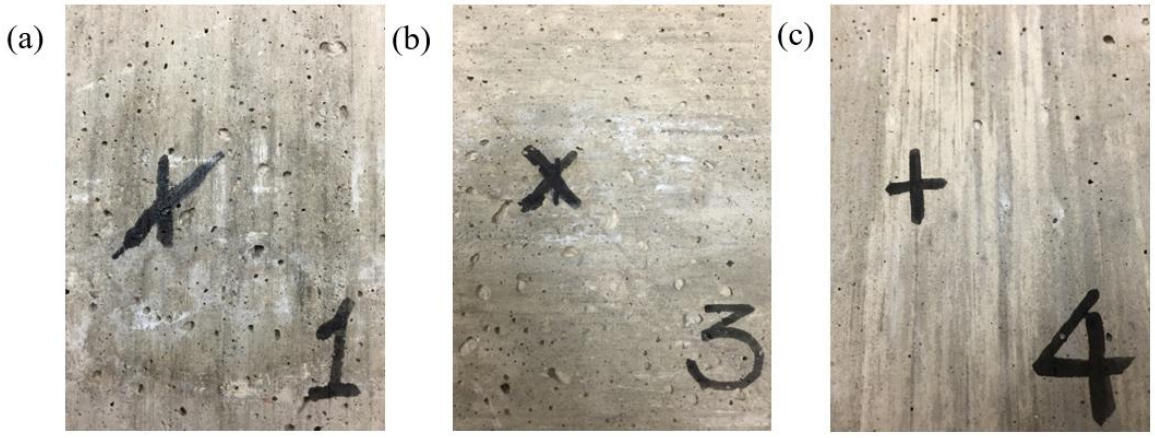

Figure 3-12 Close-up view of the surface of (a) slab 1, (b) slab 3, and (c) slab 4

3.2.6 Ultrasonic Pulse Velocity (UPV) Method: Setup and Results

For comparative purposes, we applied the UPV method using the setup presented in **Figure 3-13**. A function generator was used to excite a 5-cycle, 2 V peak-to-peak, 500 kHz sine wave. Two Olympus V103-RM transducers were used to transmit and receive the waves, respectively. Two Olympus 5660C amplifiers were used to amplify the signals. To mimic the setup with the solitary waves, we probed five different locations as shown in **Figure 3-13(b)**. The received

signals were digitized with an oscilloscope. **Figure 3-13(c)** shows an example of the transmitted and the detected waveforms. The longitudinal wave velocity is given by:

$$\boldsymbol{V = \sqrt{\frac{KE_d}{\rho}}} \quad \rightarrow \quad \boldsymbol{E_d^{UPV} = \frac{V^2 \rho}{K}} \tag{3.5}$$

where $K=(1-v)/[(1+v)(1-2v)]$, and ρ is density of the medium. The static value of Poisson ratio obtained from destructive test can be utilized in the absence of the dynamic Poisson ratio [131]. To adhere to the results associated with the solitary wave testing, we considered $v=0.16$. The ultrasonic wave velocity was calculated by considering the arrival time difference between the first peaks of the transmitted and the received signals. The pulse velocity, the dynamic modulus of elasticity computed from Eq. (3.5), and the static modulus derived from Eq. (3.5) are listed in **Table 3-7**. Each value is the average of the five measurements taken from each slab. The results show that the variation among the moduli is very small, and the slabs 1 and 3 are not outliers. The UPV test measures the pulse velocity of the waves traveling through the specimen; therefore, it is less susceptible to surface conditions.

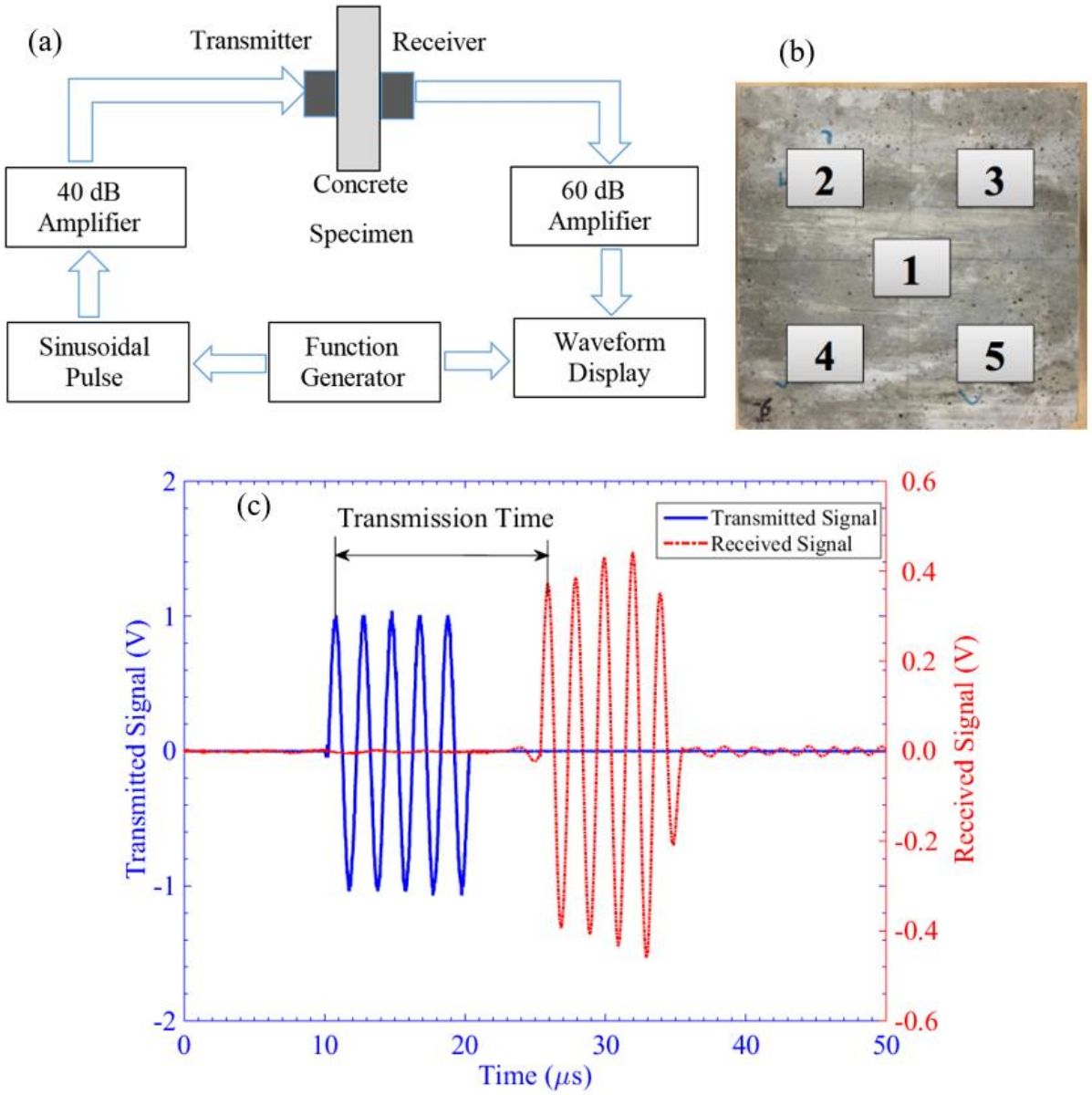

Figure 3-13 Experimental setup of the UPV test. (a) Overall schematic. (b) The tested areas on a concrete slab. (c) Typical time waveform of the transmitted (blue line) and the received (red dash line) signals

Table 3-7 UPV test. Velocity of the longitudinal wave and predicted dynamic and static modulus of elasticity

Slab Number	Average Bulk Wave Velocity (m/s)	E_d^{UPV} (GPa)	E_s^{UPV} (GPa)
1	3386	24.9	20.7
2	3646	29.1	24.2
3	3531	26.9	22.3
4	3387	24	19.9
5	3530	26.4	21.9
6	3436	25.3	21
7	3524	26.4	21.9
8	3637	27.7	23
Average	**3510**	**26.3**	**21.8**

3.2.7 Discussion and Conclusions

This article shows the working principles and the reliability of a transducer able to generate and detect HNSWs and the capability of a novel NDE method based on the properties of these waves at assessing the mechanical properties of the materials to be inspected.

The moduli obtained from the different testing methods are presented in **Table 3-8** and displayed in **Figure 3-14**. The HNSWs-based prediction ranges from 13.5 GPa to 31.9 GPa, the value for modulus from the UPV test range from 19.9 GPa to 24.2 GPa, and the modulus calculated from the empirical equation range from 32.8 GPa to 33.7 GPa. In the figure, the average values and the corresponding standard deviations are presented. There are small differences in the modulus of elasticity of the slabs measured by the UPV test. The differences among the eight slabs are mainly caused by the following three reasons: first, the rough surface of the specimen changes the thicknesses or the path lengths in different testing areas, and this problem results in inaccurate path length ΔL when calculated the pulse velocity; second, the aggregates are important factor for

the pulse velocity. Their sizes, types, and content can affect the test results; third, the rough surface results in insufficient contact with the commercial transducers, and a weaker pulse velocity will be received by the transducer; consequently, the onset of received signals may be difficult to be figured out. Based on the UPV measurements, the average dynamic modulus of elasticity of the 8 concrete slabs is 26.3 GPa, and its corresponding static modulus is equal to 21.8 GPa.

The results relative to the ASTM C469 conducted after 28 days from casting, the modulus of elasticity of the batch ranges from 25.5 to 28.9 GPa. **Figure 3-14** shows that the standard deviation of the empirical equation is the smallest among the four methods. Furthermore, the modulus of elasticity estimated via the UPV is smaller than the other methods, while HNSW-based transducers provide the static modulus of elasticity very close to the ASTM C469. The difference between HNSW-based method and the ASTM is about 5%, while the difference between ASTM and the UPV method and the empirical equation of the ACI 318 are 20% and 23%, respectively.

Table 3-8 Concrete tests. Estimated static modulus of elasticity of the test samples using two destructive and two nondestructive methods

Slab Number	Nondestructive methods		Destructive methods		
	E_s^{HNSW} (GPa)	E_s^{UPV} (GPa)			
1	**14.4***	20.7	**Sample**	$E_s^{ASTM\ C469}$ (*GPa*)	E_s^{ACI} (*GPa*)
2	23.7	24.2			
3	**13.5***	22.3	1	28.9	33.7
4	31.4	19.9			
5	22.0	21.9	2	25.5	32.8
6	31.9	21.0			
7	23.8	21.9	3	26.5	33.0
8	20.7	23.0			
Average	**25.6**	**21.8**	**Average**	**26.9**	**33.1**

* The results of Slabs 1 and 3 were not used in the average.

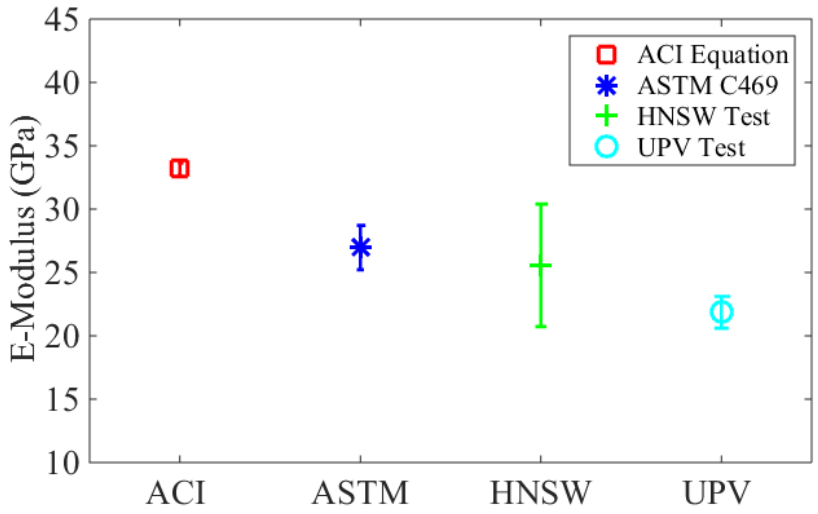

Figure 3-14 The average estimated static modulus of elasticity and the corresponding standard deviations of the four different methods

The main advantages of operating HNSW-based test are that its implementation is fast and easy; hence, it is possible to carry out many tests and take the average of the value of modulus of elasticity estimated from each observation. Another advantage of the HNSW-based method for evaluating the modulus of elasticity of the specimens is that the value obtained by this method is less susceptible to any damage and/or the presence of reinforcing steels existing inside the element. For example, cracks and dense reinforcing steel may cause refraction and dispersion of the ultrasonic waves while this problem does not affect the results of the HNSW-based transducers.

Future studies shall include more testing to verify the effect of concrete mix design on the properties of the solitary waves. An effort shall also be made to mitigate the effect of the concrete surface at the contact point with the chain.

3.3 Testing Concrete with Different Water-to-Cement Ratios

In the study presented here, three M-transducers and three P-transducers were used to quantify their reliability at inferring the modulus of concrete cylinders designed with three different *w/c* ratios. The objective and therefore the intrinsic novelty of the study is three-fold: (1) compare the two kinds of transducer to determine the best solution between the two designs; (2) evaluate nondestructively the characteristics of the samples that were different from these evaluated in [68] and [132]; and (3) evaluate the ability of the novel NDE method at discriminating concrete of different characteristics. To achieve these objectives, we compared the findings from both transducers to the results of a conventional UPV test and to the elastic modulus measured in accordance with the ASTM C469 [133].

3.3.1 Experimental Setup

Eighteen 152.4 mm (6 in) diameter by 304.8 mm (12 in) high concrete cylinders were cast and clustered in three groups of different *w/c* ratios, namely 0.42, 0.45, and 0.5. Nine cylinders were evaluated nondestructively and the remaining nine were tested according to the ASTM C469. **Table 3-9** lists the raw materials, the mixture designs (**Table 3-10**), and the samples label (**Table 3-11**). Each label consists of 3 digits: the first two digits represent the *w/c* ratio while the third digit, a letter A through F, identifies the individual specimen. The system was fully automated using a NI-PXI running in LabVIEW.

Three M-transducers and three P-transducers were assembled and are shown in **Figure 3-15**. Each transducer contained sixteen AISI 302 stainless steel particles. The second particle from the top was nonferromagnetic, whereas the others were ferromagnetic. The properties of the particles

were: diameter $2a$=19.05 mm, density ρ=7850 kg/m^3, mass m=27.8 g, modulus of elasticity E=193 GPa, and Poisson's ratio v=0.25. Each chain was held by a Delrin tube with outer diameter D_0=22.30 mm and inner diameter slightly larger than $2a$ in order to minimize the friction between the striker and the inner wall of the tube and to minimize acoustic leakage from the chain to the tube. The striker was driven by an electromagnet powered by a DC power supply. To achieve magnetostriction, a constant axial magnetic field was created along the chain and centered at the 9th particle using two identical permanent bridge magnets. A coil was wrapped around the tube and the magnetic field to measure the propagation of the solitary waves traveling through the 9th particle. It is known that magnetostriction can be used to excite and detect stress waves using the Faraday law and the Villari effect, respectively [134-136]. For example, one of the authors used MsS to excite and detect the guided ultrasonic waves [122-124]. In this study, the Villari effect is used. The falling height of the striker was 3.2 mm.

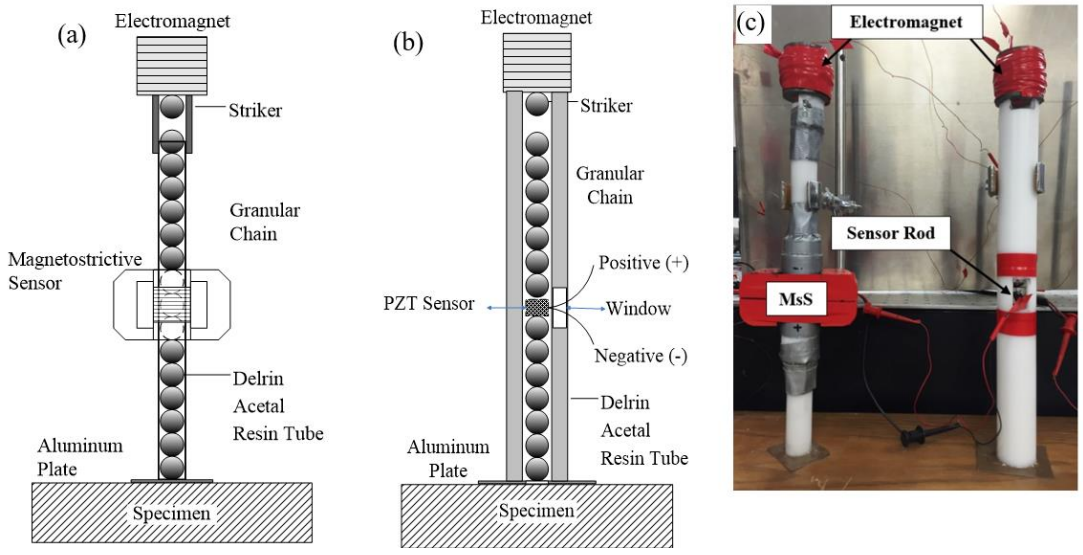

Figure 3-15 Scheme of the: (a) M-transducer and (b) P-transducer. (c) Photo of two of the six transducers used in this study

Table 3-9 The material used in the concrete mixtures

Material	Specific gravity	Water absorption capacity (%)
Cement	3.15	n/a
Coarse aggregate	2.71	0.50
Fine aggregate	2.67	1.24
GGBFS[1]	2.83	n/a

[1] ground-granulated blast-furnace slag

Table 3-10 The ingredients of each concrete batch

Batch	1	2	3
w/c ratio	0.42	0.45	0.50
Paste vol./concrete vol.	0.30	0.30	0.30
Air content (%)	6.50	5.00	6.25
Coarse agg. (kg/m^3)	1054	1054	1054
Fine agg. (kg/m^3)	666	666	666
Cement (kg/m^3)	303	291	274
GGBFS (kg/m^3)	101	97	91
Water (kg/m^3)	170	175	183
Slump (mm)	133	95	203

Table 3-11 The detailed information of the concrete cylinders

w/c ratio	Number of cylinders	NDE sample labels	ASTM C469 sample labels
0.42	6	42A, 42B, 42C	42D, 42E, 42F
0.45	6	45A, 45B, 45C	45D, 45E, 45F
0.50	6	50A, 50B, 50C	50D, 50E, 50F

For the P-transducers, the sensing element consisted of a sensor-rod located in lieu of the 9th particle. The sensor-rod was a piezo-ceramic embedded between two half rods. The disc was 19 mm diameter and 0.3 mm thick and insulated with Kapton tape. The two half-rods were made from the same material as the beads and had mass m_r = 27.8 g, height h_r=13.3 mm, and diameter D_r=19.05 mm. This sensing system had approximately the same mass of the individual particles

in order to minimize any impurity in the chain that may generate spurious HNSWs. Finally, the falling height of the striker was 4.5 mm.

At the bottom of the six transducers a 0.254 mm (0.1 in) thick aluminum sheet was glued to the plastic tube in order to prevent the free fall of the particles. For the P-transducers, a through-thickness hole was devised in order to establish a direct contact between the last particle of the chain and the concrete material, and to verify if this contact improves the sensitivity of the setup. Hereinafter M1, M2, and M3 denote the M-transducers 1, 2, and 3, respectively while P1, P2, and P3 label the P-transducers.

Figure 3-16(a) shows the TOF as a function of both the elastic modulus and the Poisson ratio of the wall material. The graph demonstrates that the elastic modulus affects significantly the wave feature and demonstrates that when the modulus of the specimen is higher than 25 GPa, small differences in the measurement of the TOF, let say 3%, yields about 60% change in the estimated modulus. This implies that high accuracy is required when the parameters of the solitary wave are to be determined. The Poisson ratio instead has much less effect in the interval considered here, which is typical for concrete. This implies that in field applications, when the value of the Poisson ratio of the concrete is unknown, a value between 0.15 and 0.20 can be assumed without affecting the accuracy of the estimate of the modulus of elasticity. For illustrative purposes **Figure 3-16(b)** shows the TOF as a function of the dynamic modulus of elasticity at ν=0.20, which is the value adopted in this study.

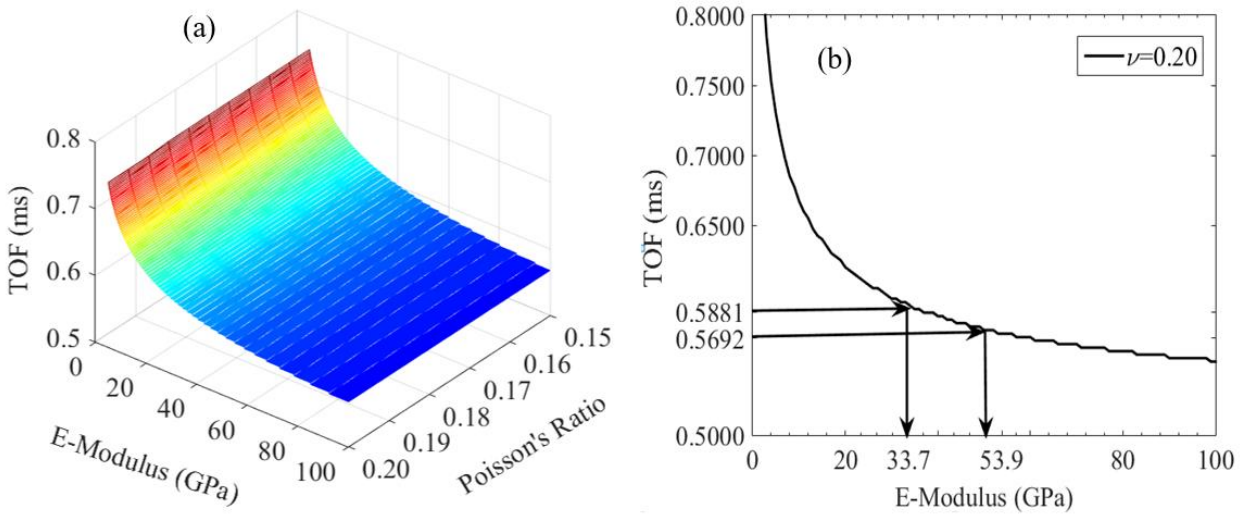

Figure 3-16 (a) TOF as a function of the dynamic modulus of elasticity and Poisson's ratio of the M- and the P-transducer; (b) TOF as a funct ion of the modulus of elasticity when ν=0.20

3.3.2 Test Protocol

All six HNSW-transducers were used to test nine specimens, i.e. the experiments were conducted in a round-robin fashion in order to prevent any skew of the data that may have stemmed from differences in the assembly of the transducers. For each test, 50 measurements were taken. The experiment started immediately after curing the samples at 95% relative humidity for 28 days, and it was completed in a day. **Figure 3-17(a)** shows the M-transducers placed above three specimens with same *w/c* ratio. Posts and clamps were used to hold the transducers. Similar to **Figure 3-17(a)**, **Figure 3-17(b)** shows one P-transducer. The same samples were then tested the next day using the UPV method. Finally, the remaining nine cylinders were tested in compression using the ASTM C469 [133] after 28 days and they were in saturated condition.

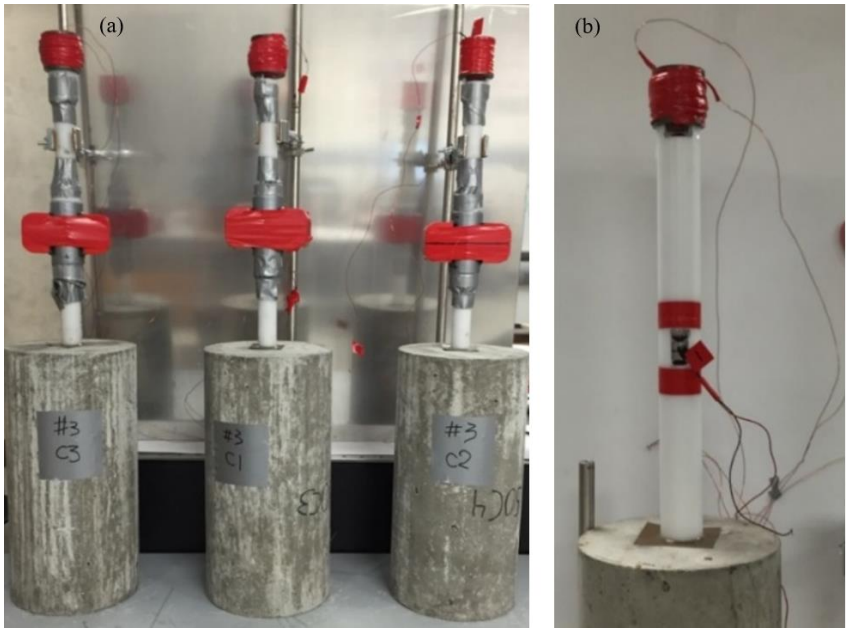

Figure 3-17 Photos (a) of the M-transducers and (b) of one P-transducer during the execution of the experiments

3.3.3 Elastic Modulus of Hardened Concrete

Figure 3-18(a) shows the time waveforms associated with one of the 50 measurements taken with the M1 transducer placed above specimens 42A, 45A, and 50A. The graph identifies the TOF which was taken by measuring the arrival time of the maximum amplitude of the incident and the reflected solitary wave.

To verify the repeatability of the M-transducers, **Figure 3-18(b)** displays the average value of the amplitude of the ISW for all the transducers and all nine concrete samples. The vertical bars represent the 2σ confidence interval. To ease the visualization, the experimental values were shifted horizontally. The amplitude of the incident wave depends exclusively on the velocity of the striker at the moment of the impact, the pre-compression of the chain, and the sensitivity of the coil; this, in turn, is associated with the axial magnetic bias provided by the permanent magnets.

The figure demonstrates that the average amplitude of the incident wave is essentially constant; the difference between the largest and the smallest values is about 3% whereas the mean of the twenty-seven averages is 0.285±0.003 V. The small relative standard deviation (RSD=1.053%), which is the ratio of the standard deviation to the mean, indicates the excellent reproducibility of the design of the M-transducers.

To evaluate the effect of the w/c ratio on the propagation of the HNSWs, **Figure 3-18(c)** presents the TOF as a function of the *w/c* ratio. The values of 2σ are represented by the vertical error bars and demonstrate that the standard deviations are smaller than the changes in the TOFs due to the *w/c* ratio. Although a neat discrimination among the three groups is not readily evident, a trend is visible. The data presented in **Figure 3-18(c)** are listed in **Table 3-12** which is completed by the corresponding RSD. The data confirms that the TOF increases with an increase in *w/c* ratio, and the variations relative to the cylinders with the same ratio vary much less than the values across the different ratios. Moreover, the small RSD, all comprised between 0.10% and 0.33% demonstrate the excellent repeatability of the experiments for each sample.

Table 3-12 Average TOF and corresponding relative standard deviation (RSD) associated with the measurements with the M-transducers

w/c ratio	Cylinder	M1		M2		M3	
		TOF (ms)	RSD	TOF (ms)	RSD	TOF (ms)	RSD
0.42	42A	0.5722	0.23%	0.576	0.26%	0.5807	0.19%
	42B	0.5646	0.19%	0.5704	0.33%	0.5706	0.12%
	42C	0.5774	0.21%	0.5815	0.19%	0.5816	0.21%
0.45	45A	0.5723	0.21%	0.5777	0.21%	0.5788	0.17%
	45B	0.5701	0.21%	0.5776	0.26%	0.5766	0.21%
	45C	0.5735	0.23%	0.5837	0.19%	0.5795	0.22%
0.50	50A	0.5749	0.26%	0.5798	0.24%	0.5782	0.16%
	50B	0.5767	0.17%	0.5843	0.10%	0.5827	0.19%
	50C	0.5804	0.24%	0.5833	0.21%	0.5822	0.21%

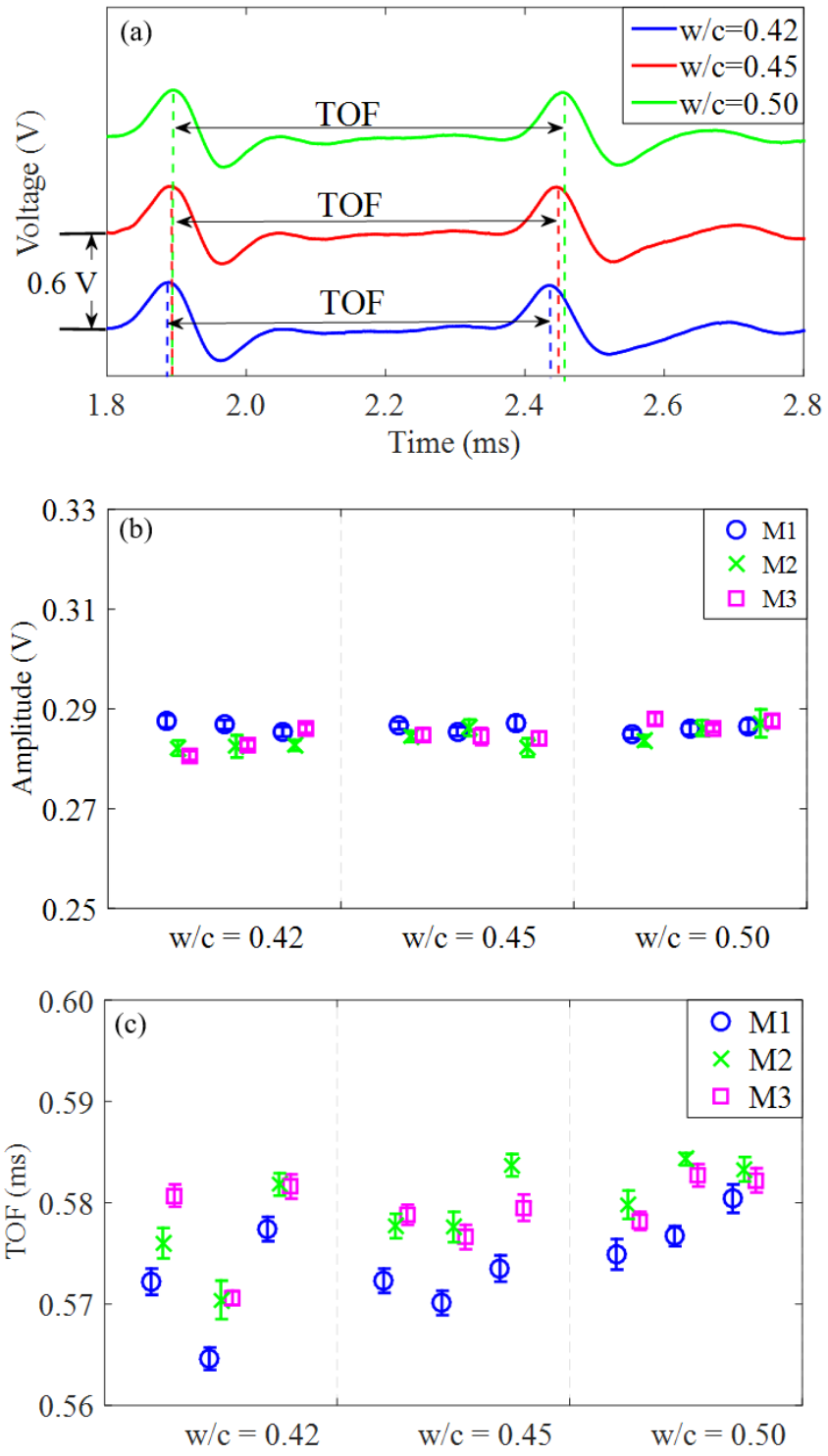

Figure 3-18 Experimental results of the M-transducers. (a) Time waveforms recorded by the M1 transducer at three cylinders with different w/c ratio. (a) Average amplitude of the incident solitary wave relative to the nine concrete samples. (c) Average TOFs relative to the nine concrete samples

Similar to **Figure 3-18**, **Figure 3-19** illustrates the results associated with the use of the P-transducers. **Figure 3-19(a)** shows one of the fifty waveforms recorded by the transducer P1 when it was placed above the samples 42A, 45A, and 50A. To ease the readability of the time waveforms, the amplitudes were offset. The figure shows that the TOF of the reflected wave increases with the increase of the *w/c* ratio.

To verify the repeatability of the P-transducers, **Figure 3-19(b)** displays the average value of the amplitude of the ISW for all the transducers and all nine concrete samples. The values of 2σ associated with the 50 measurements are represented by the vertical error bars. Similar to the M-transducers, the figure demonstrates that the average amplitude of the incident waves is constant. The difference between the largest and the smallest amplitude is about 8.5%, and the mean of the nine averages is 4.331±0.112 V. The RSD is therefore equal to 2.585% and it indicates the reproducibility of the design of the P-transducers. Interestingly, while the P-transducers denote better sensitivity to the change in concrete stiffness, they did not perform as well as the M-transducers in terms of repeatability. We note here that a visual comparison between **Figure 3-18(b)** and **Figure 3-19(b)** cannot be made because the range of the vertical axis is not the same.

To evaluate the effect of the *w/c* ratio on the propagation of the HNSWs, **Figure 3-19(c)** presents the TOF as a function of the *w/c* ratio. The values of 2σ demonstrate that the standard deviations are smaller than the changes in the TOFs due to the *w/c* ratio. The graph shows clearly the influence of the *w/c* ratio on the value of the TOF. The better sensitivity of the P-transducers to the stiffness change at the concrete surface, with respect to the M-transducer is mainly due to the sensing system embedded in the P-transducers and the direct contact between the last particle of the metamaterial and the samples. As a matter of fact, the coil wrapping the chain and the magnetic bias created by the permanent magnets provide an average value of the signal strength

traveling through the chain. The PZT disk provides instead a local measurement of the solitary wave. We argue that the direct contact of the bottom bead with the material improves the sensitivity to the stiffness of the specimen at the expense of the repeatability. Finally, the data presented in **Figure 3-19(c)** are listed in **Table 3-13**. The table demonstrates that the TOF measured with the P-transducers is close to the one measured with the M-transducers. The RSD ranges from 0.2% to 0.9% and proves the good repeatability of the P-transducers as well.

We used this figure to estimate the modulus of the samples by intersecting the experimental TOF listed in **Table 3-12** and **Table 3-13** to the numerical curve. The dynamic modulus E_d was then converted into the static modulus E_s using the empirical formula proposed by Lydon and Balendran [129, 137] using Eq. (3.4), and the results are summarized in **Table 3-14** and displayed in **Figure 3-20**. **Table 3-14** lists the values of E_s estimated by using the M-transducers and based on the values of the TOFs listed in **Table 3-12**. The column shows that an increase in the *w/c* ratio decreases the static modulus. Similar to **Table 3-14**, **Table 3-15** presents the modulus obtained from the measurements of the P-transducers. The findings from the two transducers are similar.

Table 3-13 Average TOF and corresponding relative standard deviation (RSD) associated with the measurements with the P-transducers.

w/c ratio	Cylinder	P1		P2		P3	
		TOF (ms)	RSD	TOF (ms)	RSD	TOF (ms)	RSD
0.42	42A	0.5722	0.31%	0.5721	0.31%	0.5699	0.61%
	42B	0.5712	0.30%	0.5762	0.56%	0.5692	0.93%
	42C	0.5719	0.30%	0.5765	0.62%	0.5738	0.63%
0.45	45A	0.5748	0.23%	0.5734	0.61%	0.5708	0.32%
	45B	0.5744	0.26%	0.5789	0.28%	0.5785	0.59%
	45C	0.5765	0.26%	0.5772	0.28%	0.5787	0.67%
0.50	50A	0.5878	0.37%	0.5803	0.31%	0.5814	0.69%
	50B	0.5881	0.39%	0.5815	0.28%	0.5881	0.97%
	50C	0.5775	0.33%	0.5801	0.31%	0.5805	0.47%

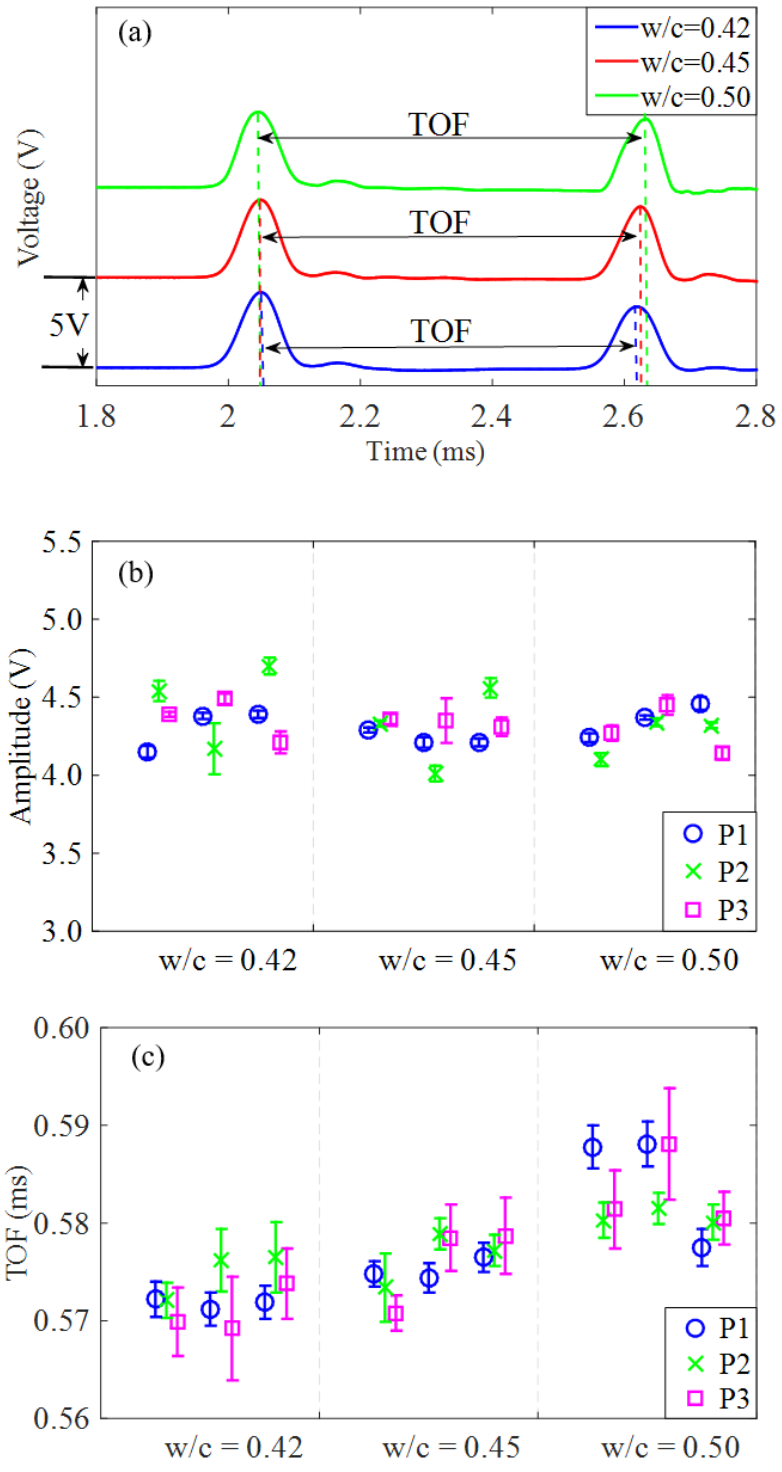

Figure 3-19 Experimental results of the P-transducers. (a) Time waveforms recorded by the M1 transducer at three cylinders with different w/c ratio. (a) Average amplitude of the incident solitary wave relative to the nine concrete samples. (c) Average TOFs relative to the nine concrete samples

Table 3-14 Estimated modulus of elasticity of each cylinder using the M-transducers data

w/c ratio	Cylinder	E (GPa) based on TOF of Primary Waves				
		M1	M2	M3	Average M-transducers	Samples' average ± RSD
0.42	42A	41.9	37.0	33.0	37.3	**38.9 ± 11.6%**
	42B	51.2	41.9	41.9	45.0	
	42C	37.0	33.0	33.0	34.3	
0.45	45A	41.9	34.9	34.9	37.2	**36.8 ± 3.24%**
	45B	41.9	34.9	37.0	37.9	
	45C	39.3	31.2	34.9	35.1	
0.50	50A	39.3	34.9	34.9	36.4	**34.0 ± 5.14%**
	50B	37.0	31.2	31.2	33.1	
	50C	33.0	31.2	33.0	32.4	

Table 3-15 Estimated modulus of elasticity of each cylinder using the P-transducers data

w/c ratio	Cylinder	E (GPa) based on TOF of Primary Waves				
		P1	P2	P3	Average P-transducers	Samples average ± RSD
0.42	42A	41.9	41.9	44.7	42.8	**41.1 ± 3.38%**
	42B	41.9	37.0	44.7	41.2	
	42C	41.9	37.0	39.3	39.4	
0.45	45A	39.3	39.3	41.9	40.2	**37.6 ± 4.82%**
	45B	39.3	34.9	34.9	36.4	
	45C	37.0	37.0	34.9	36.3	
0.50	50A	28.0	33.0	33.0	31.3	**31.8 ± 6.00%**
	50B	28.0	33.0	28.0	29.7	
	50C	37.0	33.0	33.0	34.3	

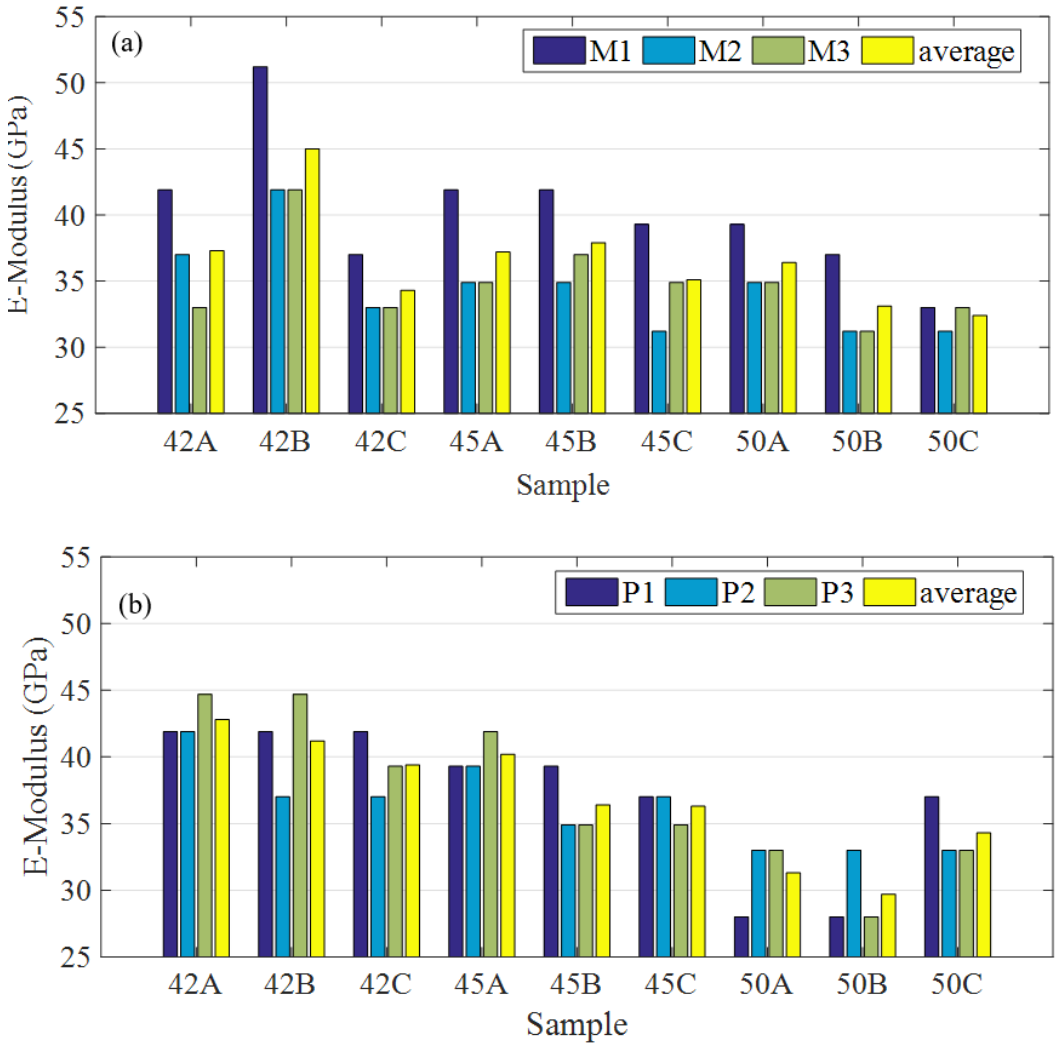

Figure 3-20 Estimation of the static elastic modulus using the solitary wave based NDE. (a) Results associated with the M-transducers. (b) Results associated with the P-transducers

3.3.4 Ultrasonic Pulse Velocity Tests

A UPV test using 250 kHz, 5 cycle sine tone burst signal was performed in the axial and transverse directions. The elastic modulus of concrete were determined from the ultrasonic signals using Eq. (3.5). **Figure 3-21** shows a typical transmitted and received ultrasonic pulse. The wave speed was determined by considering the arrival time of the first crest. The dynamic modulus of elasticity of the concrete was estimated and converted into the static modulus using Eq. (3.4). The Poisson ratio was set to 0.20, in order to be consistent with the analysis of the HNSW data. The results are presented in **Table 3-16**. The increase in w/c ratio reduced the speed of the wave and therefore the estimated E_s. The data do not show any significant difference between the two directions of propagation of the bulk waves. Moreover, the elastic moduli are smaller than the corresponding values determined with the HNSW-based transducers. This is perhaps due to the conversion factor used in Eq. (3.4). Finally, the RSD is smaller than those associated with the M- and the P-transducers.

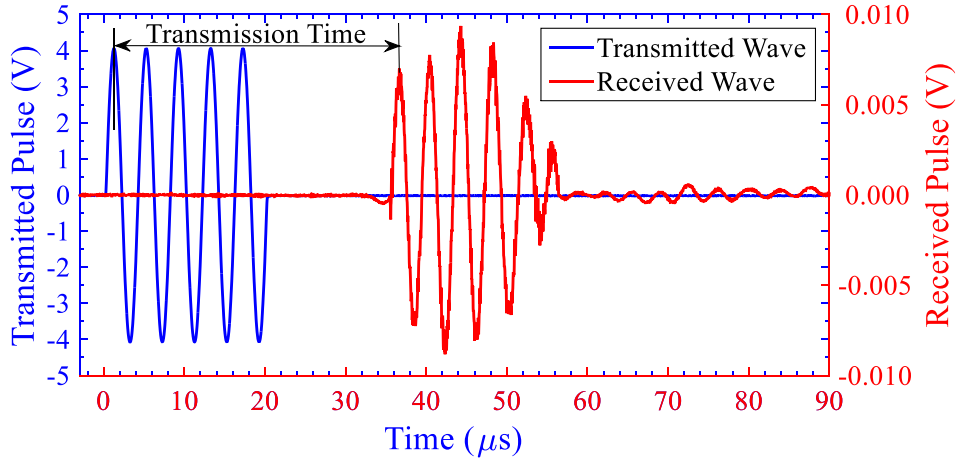

Figure 3-21 Typical waveform recorded from the UPV test

Table 3-16 The modulus of elasticity of each cylinder obtained by the UPV test

w/c ratio	Cylinder	Pulse Velocity (m/s)		Modulus of elasticity (GPa)		Average modulus of elasticity (GPa) ± RSD	
		Axial	Trans.	Axial	Trans.	Axial	Trans.
0.42	42A	4692	4664	34.4	34.8	**34.9 ± 1.43%**	**35.1 ± 0.59%**
	42B	4730	4710	34.8	35.1		
	42C	4740	4759	35.6	35.3		
0.45	45A	4340	4450	31.8	31.8	**31.8 ± 0.90%**	**31.4 ± 0.94%**
	45B	4456	4451	32.1	31.1		
	45C	4407	4415	31.4	31.3		
0.50	50A	4367	4332	29.6	30.1	**29.5 ± 0.64%**	**29.8 ± 1.11%**
	50B	4344	4330	29.6	29.8		
	50C	4330	4320	29.2	29.3		

3.3.5 ASTM C39 and ASTM C469 Results

Three specimens from each batch were tested according to the ASTM C39 and the ASTM C469. The samples were tested after curing them for 28 days at 21°C and a relative humidity of 95%, and they were saturated in accordance with ASTM specifications. These standards are the methods traditionally used to estimate the static modulus of elasticity and compressive strength of concrete. The results are presented in **Table 3-17**. As expected, the ultimate compressive strength and the modulus of elasticity decreased with an increase in the *w/c* ratio. The reduction of the compressive strength with respect to *w/c*=0.42 was 2.8% and 12.6% for *w/c*=0.45 and *w/c*=0.50, respectively. On average, the modulus of elasticity of the *w/c*=0.45 samples and the *w/c*=0.50 samples were, respectively, 7.5% and 9.2% smaller than the *w/c*=0.42 sample.

The graph of **Figure 3-22** shows the compressive strength (f'_c) and the corresponding static modulus of the samples tested according to the ASTM C39. Because most standards such as the ACI 318 report an empirical relationship like $E_s = k\sqrt{f_c'}$ we interpolated the experimental data

using a polynomial of the second order. Then, we used this polynomial to predict the compressive strength of the samples tested nondestructively, using the elastic modulus predicted using the M- and the P-transducers, as well as the UPV. The results are presented in **Table 3-18** for different methods and are compared with the compressive strength obtained with the ASTM C39. The table shows that largest error is below 8%. In field applications, the same approach can be adopted to reduce the number of sample cores; i.e. it is possible to take fewer cores to extrapolate the regression curve, and then test the rest of the structure nondestructively.

Table 3-17 Concrete compressive strength (ASTM C39) and static elastic modulus (ASTM C469)

***w/c* ratio**	**Sample**	**Compressive Strength (MPa)**	**Mean compressive Strength (MPa)**	**RSD**	**Elastic Modulus (GPa)**	**Samples average (*GPa*) ± RSD**
0.42	42D	41.9	43.2	1.06%	40.1	**38.6 ± 3.29**%
	42E	43.2			37.0	
	42F	44.5			38.8	
0.45	45D	42.8	42.0	1.41%	36.2	**35.7 ± 4.51**%
	45E	41.5			32.4	
	45F	41.6			35.2	
0.50	50D	34.6	36.7	4.05%	32.6	**32.4 ± 1.33**%
	50E	37.8			31.8	
	50F	37.7			32.8	

Table 3-18 The static modulus of elasticity estimated using various methods

***w/c* ratio**	**Modulus of elasticity (GPa)**			
	ASTM C469	**M-Transducers**	**P-transducers**	**UPV**
0.42	38.6	38.9	41.1	35.0
0.45	35.7	36.8	37.5	31.6
0.50	32.4	34.0	31.8	29.6

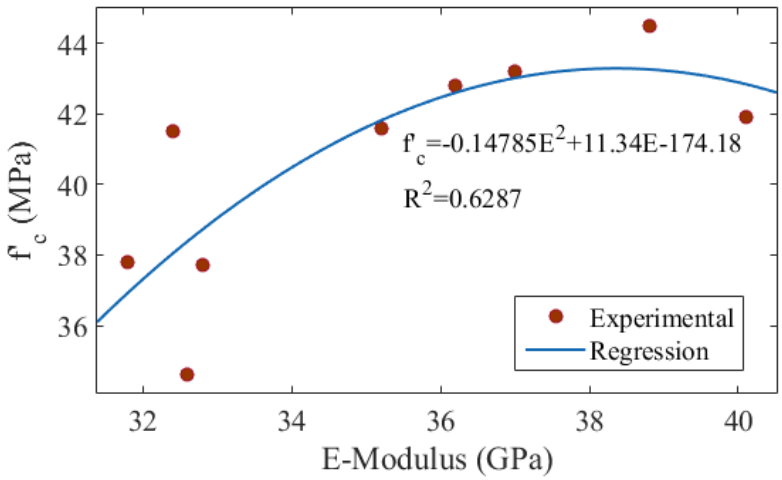

Figure 3-22 Results of the destructive testing. Compressive strength vs static elastic modulus. The polynomial of second order that fits the experimental data is overlapped

3.3.6 Discussion and Conclusions

In this section, the principles of a novel NDE method was presented for concrete based on the propagation of highly nonlinear solitary waves along a metamaterial in contact with the concrete to be evaluated. The method aims at determining the modulus of hardened concrete but, in principle, can be applied to any concrete or cement product of any age. Two kinds of transducer were used, and their results were compared to the results provided by the conventional ultrasonic pulse velocity method and the destructive tests set by the ASTM C39.

The results of the study are summarized in **Table 3-18** and **Figure 3-23** that show the estimated modulus of elasticity using the different testing methods adopted in this study. The results from the HNSW transducers are the average of the three M- and the three P-transducers, and for each transducer, we used the average value of fifty measurements. The results of the UPV test are the mean of the axial and transverse measurements. Considering ASTM C469 as the reference method,

the deviations of the M-transducers from the reference are 0.8%, 3.1%, and 4.9% for w/c ratio equal to 0.42, 0.45, and 0.50, respectively; the deviations of the P-transducers from the reference are 6.5%, 5.0%, and 1.9% for w/c ratio equal to 0.42, 0.45, and 0.50, respectively while these values for UPV method are 10.0%, 14.1%, and 12.9%, respectively. **Figure 3-23** shows the static modulus as a function of *w/c* ratio for each method. It is clearly visible that all the methods detect the decrease in stiffness of the concrete due to the increase in the water to cement ratio. Interestingly, the moduli estimated by the HNSW-based method are the closest to the data provided by the ASTM C469.

The results demonstrate that the P-transducers offer sufficient repeatability and better sensitivity with respect to the M-transducers to identify the differences of the modulus of concrete samples fabricated with different water-to-cement ratios. It is acknowledged here that the proposed method is not immune from the common concerns that affect some or most of the existing NDE methods. In particular, we acknowledge that: (1) further investigation is necessary in order to evaluate how the surface conditions of specimens would affect the measurements of the time of flight and other features of the solitary waves; (2) the positive correlation of modulus of elasticity and TOF, obtained using the transducers, should be validated by involving a larger amount of specimens.

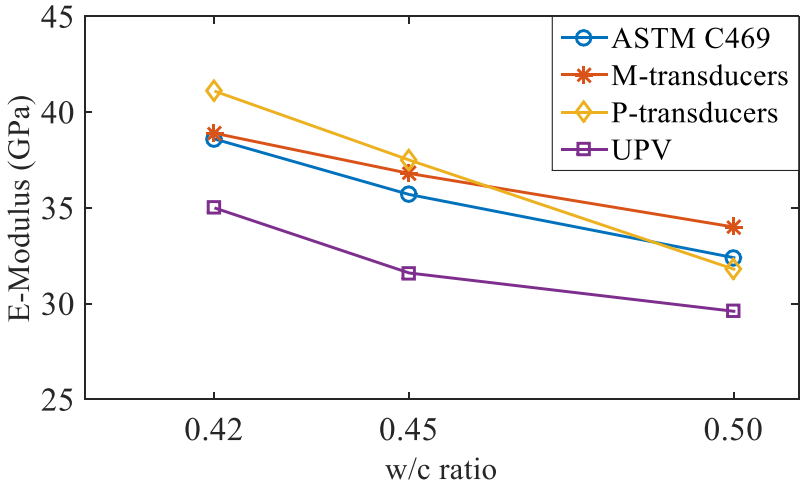

Figure 3-23 Average value of the static modulus of elasticity at the three w/c ratio determined using the solitary wave based method, the UPV test, and the ASTM C469

With respect to existing methods, the advantages of the proposed HNSW-based technique are the easy and fast implementation, the possibility to carry out a large number of tests simultaneously, and independence upon internal damage and/or the presence of reinforcing steels inside the concrete. Moreover, the technique does not detect any acoustic signal that propagates within or through the concrete sample thickness, but in fact is looking at the effect of the concrete surface on the solitary wave propagation in the chain of particles. Finally, being a local and contact method, the approach can be successfully applied to characterizing effects of finishing and curing conditions.

In the future, the proposed method could be improved by increasing the sampling rate of the signals, and by tuning the size and the material of the spherical particles. The increase of the sampling rate reduces the measurement error of the elastic modulus; the change of the particles characteristics should shift the curve of **Figure 3-16(b)** toward the right, i.e. in a region of interest

where the variation of the elastic modulus of concrete determines more significant variation of the time of flight of the HNSWs.

3.4 Testing Concrete Samples Affected by Water

The study presented in this section expands on the work presented in the previous section where HNSWs were used to determine the elastic modulus of concrete cylinders fabricated with three different *w/c* ratios, namely 0.42, 0.45, and 0.50 [138]. In the present work we use some of the findings from [138] in order to predict water in excess in short concrete beams made with *w/c*=0.42 but corrupted with water. Two conditions were simulated. The first one consisted of standing water in formworks prior to pouring concrete, whereas the second condition consisted of sprinkling water above the fresh concrete during casting and surface finishing. These two conditions may reflect adverse weather in the field. The objective of the study was the development of a system that, unlike the UPV method, can predict localized deterioration conditions associated with poor quality *w/c* ratio. We used three HNSW transducers, referred with the descriptor P1, P2, and P3, to quantify the elastic modulus of the beams. The findings were then compared to the results of a conventional UPV test in order to evaluate and prove advantages and eventually limitations of the proposed approach.

3.4.1 Experimental Setup

Eighteen cylinders which were tested and studied in Section 3.4 were used as the baseline data. The cylinders were 152.4 mm (6 in.) in diameter and 304.8 mm (12 in.) high. Three *w/c* ratios,

namely 0.42, 0.45, and 0.50, were considered. Moreover, sixteen 15.2 cm x 15.2cm x 30.4cm (6 in. × 6 in. × 12 in.) beams were fabricated using concrete mix design with *w/c*=0.42. The beams were subject to the four different scenarios sketched in **Figure 3-24**. Each scenario represented either two surface finishing or two standing water situations in the formworks. Conditions 1 and 2 reflected the field case where water accumulates on the formwork as a result of rainfall prior to the placement of the concrete. To create conditions 1 and 2, a predetermined volume of water based on the surface area of the beam mold was measured and poured on the sealed molds. Concrete was placed as evenly as possible into the molds and a shaft vibrator was then used to consolidate the concrete mixture before finishing the top surface. During the fabrication, the standing water was seen migrating to the top as shown in **Figure 3-25(a)**. After consolidation, the top surfaces of the beam molds were finished.

Conditions 3 and 4 simulated instead the occurrence of rainfall during placement and finishing of the concrete. To create these conditions, a specific procedure was developed in order to best simulate the finishing of rainfall would occur on a job site. The procedure began by placing the concrete into the dry beam mold without any consolidation or finishing performed. The predetermined volume of surface water, similarly based on the base area of the beam mold, was then divided into thirds. The first application of surface water (one-third of the total surface water) was completed immediately after the concrete was placed into the beam mold. After the first application of surface water, a shaft vibrator was used to consolidate the concrete in the mold. The top surface of the beam mold was then struck off and rodded with the rod only penetrating into the concrete approximately 25 mm (1 in). The second application of surface water was then completed. Following this second application of surface water, the top surface was again finished (**Figure 3-25(b)**) and rodded (**Figure 3-25(c)**). The third and final application of surface water was then

applied before the top surface was finished for the last time. This surface finishing process was found to be the best way in controlling the application of surface water and simulating what happens on a bridge project. This modified amount of surface water was applied in three separate stages (one-third volume per application), as described above.

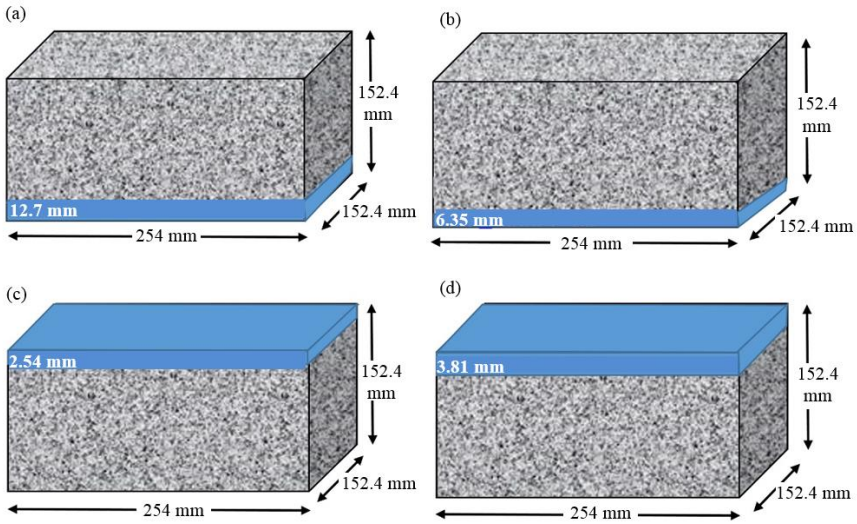

Figure 3-24 Schematics of the four conditions simulated on the 152.4 × 152.4 × 254 mm3 concrete beams. (a) Condition 1 in which 12.7 mm of water sits at the bottom of the form and (b) Condition 2 in which 6.35 mm of water sits at the bottom of the form mimicking standing water on the formwork before concreting. (c) Condition 3 in which 2.54 mm of water is sprinkled at the top of the beam and (d) Condition 4 in which 3.81 mm of water is sprinkled at the top of the beam mimicking rainfall during concreting

Two beams per condition per day were cast. We note here that the amount of water added in the four conditions raised the true *w/c* ratio to 0.627, 0.524, 0.462, and 0.483, respectively for Conditions 1 to 4. The calculations assumed that the water standing on the formworks or sprinkled above the fresh concrete, was uniformly distributed across the entire volume of the specimens.

The P-transducers described in Section 3.3 were used in this part of the study. A UPV test was also performed in the top-bottom direction.

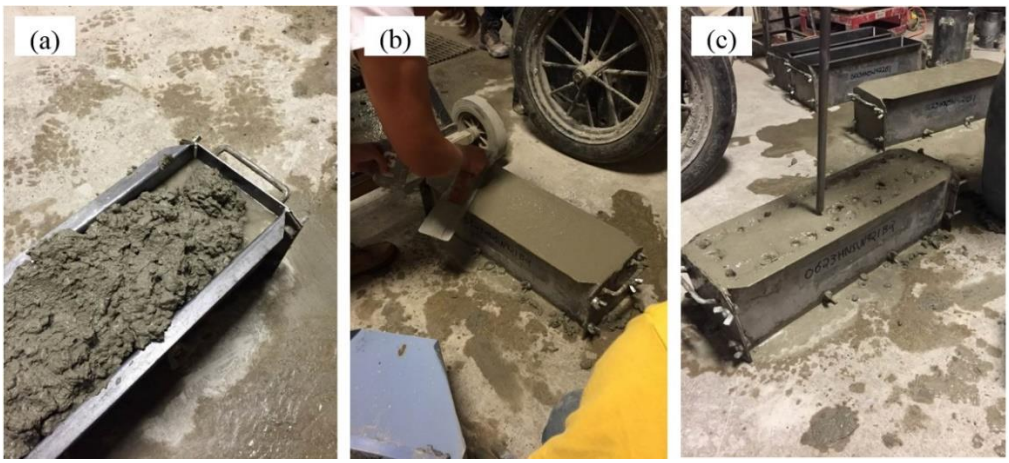

Figure 3-25 Photos of the preparation of the samples. (a) Close-up view of one of the samples under condition 2; standing water from bottom of beam mold migrates to the top. (b) Preparation of one of the samples under condition 3: finishing beam surface after second application of water. (b) Rodding the same sample shown in (b) during the third and final application of surface water

3.4.2 Test Protocol

All the HNSW-transducers were used to test the specimens, i.e. the experiments were conducted in a round-robin fashion, in order to prevent any bias in the results that may have stemmed from differences during the assembly. The cylinders were tested using the HNSWs immediately after curing the samples at 21 °C (70 °F) 95% relative humidity for 28 days, and completed in a day. The experiments were conducted in a single day. For each test, 50 measurements were taken.

The beams were tested at room conditions after 28 days of curing at 21 °C (70 °F) and at relative humidity of 95%. The UPV method was employed the day after testing with the solitary waves. Both top and bottom surfaces of the beams were tested. All the transducers were placed on the surface of the beam simultaneously, and fifty measurements were recorded by each transducer. **Figure 3-26** shows the setups relative to the solitary wave measurements. Each sample was tested simultaneously with three transducers and at three different locations. This translates in time and cost-savings. Posts and clamps were used to hold the transducers.

Figure 3-26 Photo of the three transducers during the experiment

3.4.3 Experimental Results

Figure 3-27(a) to (d) show one of the fifty waveforms recorded by the transducer P1 when it was placed above the beams with different eccessive water conditions. **Figure 3-27(e) to (h)** is a

close-up view of **Figure 3-27(a) to (d)** and it shows the differences between the measurements. These differences might be due to the excessive water and differences between surface conditions.

Table 3-19 summarizes the results associated with the beam subject to condition 1, i.e. with the presence of 12.7 mm (0.5 in.) of standing water at the bottom of the formwork. The average value of the fifty TOF measurements per transducer is listed along with the corresponding elastic modulus. The data refer to both the beam's top and bottom face. The latter was exposed to the presence of water. However, as is said earlier and displayed in **Figure 3-25(a)**, water migrated toward the top due to vibration and the weight of the concrete. The mean of the twelve moduli is presented in the shaded row along with the corresponding standard deviation and RSD. Surprisingly, the modulus estimated for the top surface is higher than the modulus at the bottom where the standing water was originally located. The results are, therefore, consistent with the empirical evidence that water migrated to the top and the experimental procedure that water was mixed with the concrete throughout the specimen. The RSD associated with the measurement at the top is almost double the corresponding value at the bottom. This is the result of point-by-point variations due to the presence of water at the top, whereas the conditions at the bottom were more uniform due to the self-weight of the concrete and smoothness of the mold. We will observe that this consideration about the RSD applies to all four conditions.

The last three rows of **Table 3-19** list the elastic modulus of the baseline cylinders predicted by the same transducers. They are presented here again to ease the prediction of the resulting *w/c* ratio at the two surfaces of the beams. By comparing the values relative to the beams and to the cylinders, the solitary wave-based technique estimates a ratio higher than 0.50 at the top and around 0.46-0.47 at the bottom.

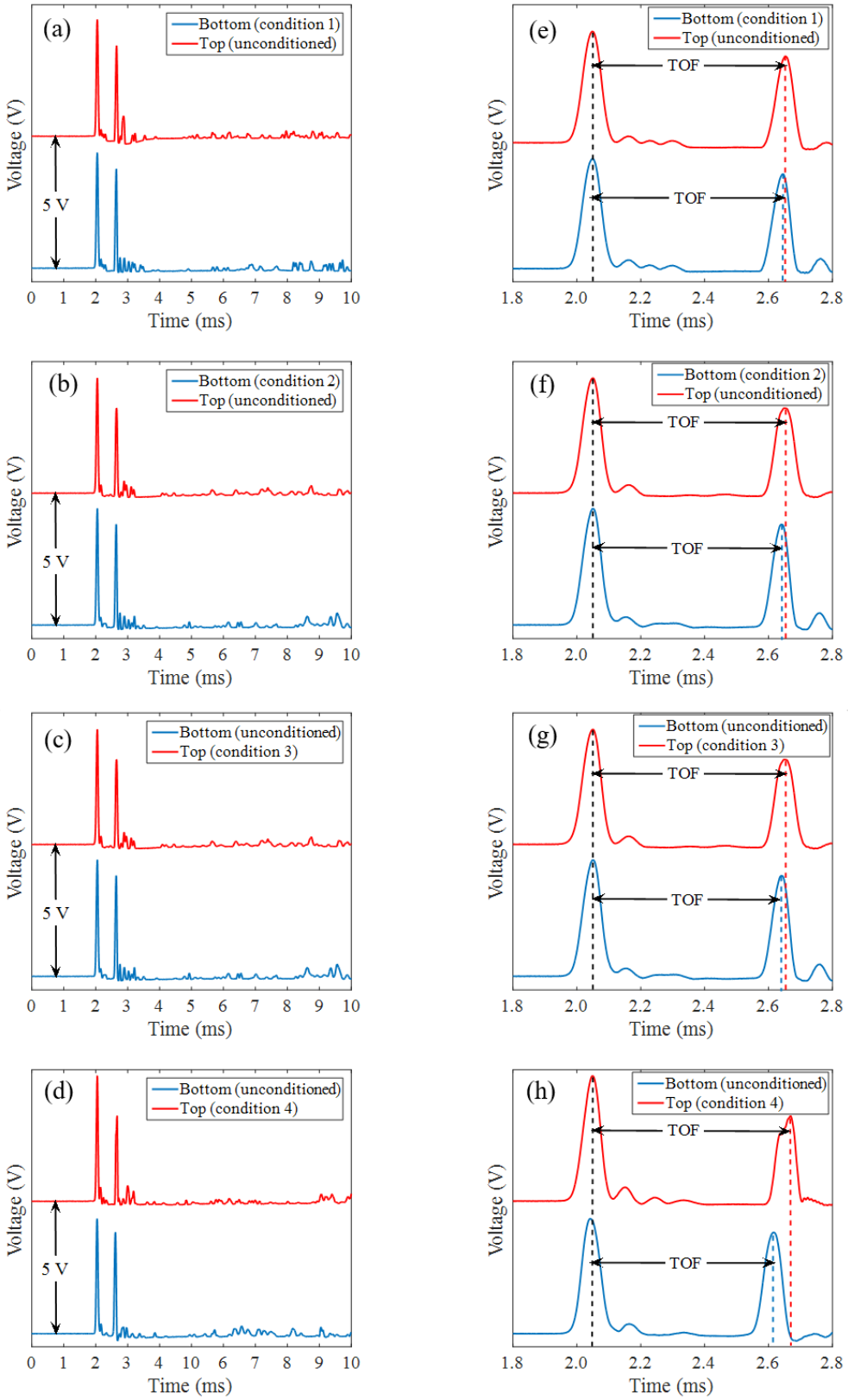

Figure 3-27 The time waveforms and their close-up views obtained from the short beams tests

Similar to **Table 3-19**, **Table 3-20** presents the results relative to condition 2 where the amount of standing water was half the amount in condition 1. By looking at the mean of the elastic modulus we observe that the value relative to the top surface is very close to the value reported in **Table 3-18**, whereas the *w/c* ratio estimated at the bottom is 0.45. The results suggest that the difference in the amount of standing water between condition 1 and 2 was not relevant to change the *w/c* ratio of the overall beam. By looking at the three bottommost rows of **Table 3-19**, we can reach the same conclusions for both conditions: the HNSW transducers were able to capture the circumstance that the short beams were corrupted by water in excess.

Table 3-19 The TOF and modulus of elasticity of the beams in which condition 1 was imposed

Cast day	**Sample**	**Top**		**Bottom**	
		TOF (ms)	E (GPa)	TOF (ms)	E (GPa)
Day 1	1	0.59224	27	0.57640	37
		0.60296	21	0.58092	33
		0.60428	21	0.57044	42
	2	0.59316	25	0.58244	33
		0.58156	33	0.58072	33
		0.59200	27	0.57508	37
Day 2	3	0.58536	30	0.58364	31
		0.57764	35	0.57880	35
		0.57624	37	0.57728	37
	4	0.57892	35	0.56896	45
		0.60128	22	0.58384	31
		0.56924	45	0.58648	30
Average *E* (GPa) Short beam *w/c*=0.42		**29.83 ± 7.08 (23.73%)**		**35.33 ± 4.37 (12.35%)**	
Cylinder *w/c*=0.42		**41.1 ± 1.389 (3.38%)**			
Cylinder *w/c*=0.45		**37.6 ± 1.815 (4.82%)**			
Cylinder *w/c*=0.50		**31.8 ± 1.907 (6.00%)**			

Table 3-20 The TOF and modulus of elasticity of the beams in which condition 2 was imposed

Cast day	Sample	Top		Bottom	
		TOF (ms)	E (GPa)	TOF (ms)	E (GPa)
Day 1	1	0.58332	31	0.57592	37
		0.60476	21	0.57420	39
		0.58260	31	0.56976	45
	2	0.60224	22	0.56684	48
		0.58900	28	0.58128	33
		0.60460	21	0.57644	37
Day 2	3	0.58320	31	0.59280	25
		0.59096	27	0.58152	33
		0.57112	42	0.57180	42
	4	0.57972	35	0.57800	35
		0.57908	35	0.58512	30
		0.58492	31	0.57236	42
Average *E* (GPa) Short beam *w/c*=0.42		**29.58 ± 6.02 (20.35%)**		**37.17 ± 6.24 (16.80%)**	
Cylinder *w/c*=0.42		**41.1 ± 1.389 (3.38%)**			
Cylinder *w/c*=0.45		**37.6 ± 1.815 (4.82%)**			
Cylinder *w/c*=0.50		**31.8 ± 1.907 (6.00%)**			

The TOF and the static modulus at the surfaces of the beams experiencing condition 3 are summarized in **Table 3-21**. Under this scenario, 2.54 mm (0.1 in.) of water was sprinkled above the samples, whereas the bottom surface was pristine with *w/c*=0.42. It is observed that the estimated static modulus for the top surface is 31.8 GPa and it matches the cylinders with *w/c*=0.50. When compared to the corresponding values presented in **Table 3-19** and **Table 3-20**, the modulus is slightly higher, and this is likely because the volume of water sprinkled on the samples was lower. Moreover, the value is much smaller than the modulus of elasticity estimated for the cylinders with *w/c*=0.42. The elastic modulus measured at the bottom surface was higher than the previous two scenarios; this is expected since the specimens with conditions 3 and 4 were not vibrated and therefore it is unlikely that the water sprinkled on the top reached the bottom of the specimen.

Table 3-21 The TOF and modulus of elasticity of the beams in which condition 3 was imposed

Cast day	Sample	Top		Bottom	
		TOF (ms)	E (GPa)	TOF (ms)	E (GPa)
Day 1	1	0.57672	37	0.57420	39
		0.58312	31	0.57420	39
		0.57660	37	0.57888	35
	2	0.57164	42	0.56576	48
		0.59256	25	0.57420	39
		0.57924	35	0.57292	39
Day 2	3	0.59048	27	0.57600	37
		0.57988	35	0.57200	42
		0.58828	28	0.57400	39
	4	0.58448	31	0.57872	35
		0.59096	27	0.57000	42
		0.59000	27	0.57600	37
Average *E* (GPa) Short beam *w/c*=0.42		**31.83 ± 5.07 (15.96%)**		**39.25 ± 3.394 (8.650%)**	
Cylinder *w/c*=0.42		**41.1 ± 1.389 (3.38%)**			
Cylinder *w/c*=0.45		**37.6 ± 1.815 (4.82%)**			
Cylinder *w/c*=0.50		**31.8 ± 1.907 (6.00%)**			

Finally, the TOF and the modulus of elasticity of the beams subjected to condition 4 are summarized in Table 3-22. Under this condition, more water was added onto the fresh concrete. Consistently with the larger volume of liquid, the predicted modulus at the top was lower than what estimated under scenario 3. The table demonstrates that the HNSW-based measurement estimated that the *w/c* of the unconditioned surface of the concrete beam was close to 0.42, as it is expected, and above 0.50 for the surface of the beam that was sprinkled with 3.8 mm (0.15 in) of water.

Table 3-22 The TOF and modulus of elasticity of the beams in which condition 4 was imposed

Cast day	Sample	Top		Bottom	
		TOF (ms)	E (GPa)	TOF (ms)	E (GPa)
Day 1	1	0.59608	24	0.57420	39
		0.58260	31	0.57420	39
		0.57944	35	0.57768	35
	2	0.59276	25	0.57644	37
		0.58484	31	0.57668	37
		0.59608	24	0.57420	39
Day 2	3	0.57892	35	0.57401	39
		0.57768	35	0.57200	42
		0.58492	31	0.57800	35
	4	0.58932	28	0.57600	37
		0.58512	30	0.56740	48
		0.57172	42	0.57600	37
Average *E* (GPa) Short beam *w/c*=0.42		**30.92 ± 5.107 (16.52%)**		**38.67 ± 3.37 (8.73%)**	
Cylinder *w/c*=0.42		**41.1 ± 1.389 (3.38%)**			
Cylinder *w/c*=0.45		**37.6 ± 1.815 (4.82%)**			
Cylinder *w/c*=0.50		**31.8 ± 1.907 (6.00%)**			

UPV was adopted to test the beams, as well. The results are summarized in **Table 3-23**. The means of the modulus are much closer to each other than what found with the HNSW method. This remarks the fact that the novel NDE method is capable of capturing surface conditions that may have been altered by the presence of water. Moreover, the RSD is smaller suggesting more homogeneous conditions throughout the four samples. Finally, if we compare the UPV data from **Table 3-23** with the results of HNSWs, we notice that the UPV method estimates an amount of *w/c* ratio above 50% for all samples, without any ability at discriminating poor from good surface conditions.

Table 3-23 Elastic modulus of the beams in which different conditions measured by UPV test

Condition	E (GPa) Mean ± standard deviation	RSD (%)
1	31.44 ± 0.966	3.07
2	31.13 ± 1.558	5.00
3	32.37 ± 1.354	4.18
4	29.42 ± 2.660	9.04

3.5 Discussion and Conclusion

In this section, we showed the principles of a novel NDE method for concrete based on the propagation of highly nonlinear solitary waves along a metamaterial in contact with the concrete to be evaluated. The method aimed at determining the modulus of hardened concrete and in particular to estimate the water-to-cement ratio in a concrete volume close to HNSW transducer. We demonstrated that the transducers designed and assembled to exploit the principles offer sufficient repeatability and reliability to identify the differences in the amount of water purposely added to the beams in order to mimic rainfall situations.

The advantages of the proposed HNSW-based method is the easy and fast implementation, the possibility to carry out a large number of tests simultaneously, and independence upon internal damge and/or the presence of reinforcing steels inside the concrete. Finally, being a local and contact method, the approach can be successfully applied to characterizing effects of finishing and curing conditions.

The proposed NDE method may resemble the Schmidt hammer, which can be used to estimate the hardness and strength of concrete [139] and rock [56]. The Schmidt hammer is a spring-driven steel hammer that hits the specimen with a defined energy. Part of the impact energy is absorbed

by the plastic deformation of the specimen and transmitted to the specimen, and the remaining impact energy is rebounded. The rebound distance depends on the hardness of the specimen and the conditions of the surface. The harder is the surface, the shorter is the penetration time or depth; as a result, the higher is the rebound. Based on the knowledge available in the literature, there are several differences between the Schmidt hammer and the solitary wave transducer that can be summarized as follows: the Schmidt hammer can be used to test hardened material but the HNSW approach can be applied also onto fresh concrete and cement as demonstrated in [16, 52]; only one parameter, the rebound value, is used in the Schmidt hammer test, while multiple HNSWs features can, in principle, be exploited to assess the condition of the underlying material. Some studies [56] suggest that the reliability and repeatability of the Schmidt hammer are not guaranteed when the elastic modulus of the sample is low. Moreover, the Schmidt hammer may induce plastic deformation or micro-cracks to the specimen, while the HNSW approach is purely nondestructive as there is not mechanical impact on the material under testing.

4.0 Dynamic Interaction Between Solitary Waves and Tennis balls

This chapter presents the study on tennis balls and has been reported in the *ASME Journal of Applied Mechanics* [140], *Experimental Mechanics* [141], and the *ASME Journal of Nondestructive Evaluation, Diagnostics and Prognostics of Engineering Systems* [142]. The content of Ch. 4 is largely taken from those publications.

4.1 Introduction

This chapter discusses the dynamic interaction between the solitary waves propagating along a chain of spherical particles and a thin-walled spherical pressure vessel in contact with the chain according to the scheme shown in **Figure 4-1**. The objective is to investigate the effect of the internal pressure on the characteristics (amplitude and arrival time) of the HNSWs. The long-term aim is the development of a new NDE method to infer the internal pressure of deformable systems for which conventional pressure gages cannot be used non-invasively. A finite element model was created in MATLAB® software using quadrilateral axisymmetric elements to investigate the dynamic interaction between the metamaterial and the vessel. The chain was treated as a discrete system of masses connected with nonlinear springs, whereas the vessel was discretized using axisymmetric finite elements. The model was then applied to the specific case of a monoatomic chain in contact with a tennis ball with the aim of developing a novel and portable NDT technique to estimate the serviceability of tennis balls anywhere, anytime. The numerical results were then

compared to the results of a series of experiments in which commercial tennis balls were tested using a HNSW transducer designed and built at the University of Pittsburgh.

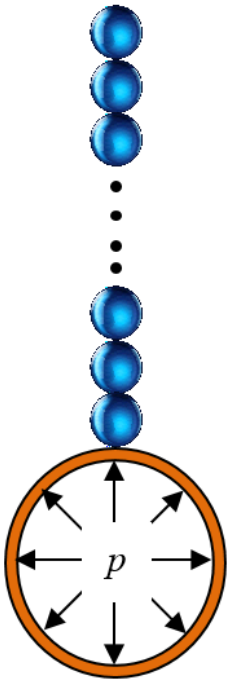

Figure 4-1 Thin-walled spherical pressure vessel in contact with a metamaterial

The study presented here improves the work published recently by Bagheri and Rizzo [143] in which the interaction of HNSWs and tennis ball was modeled numerically using ANSYS software and a discrete particle model. The novelty of this with respect to [143] is three-fold and quite significant. First, the present study introduces the general framework of a more accurate finite element analysis (FEA) carried out without using any commercial finite element code to model the interaction between monoatomic periodic chains and thin-walled pressure vessels. Second, the specific application to tennis balls does not consider the ball as part of the metamaterial as done in Bagheri and Rizzo [143] and does not consider the center of mass of the ball as a rigid element

moving under the influence of the solitary waves. As such, the present model better portrays the physical phenomenon to be investigated, and the true local deformation at the ball-chain interface. Third, while the work in [143] was only numerical, here many experiments were conducted to validate the numerical findings and to compare the values of the internal pressure obtained with the new NDT method with the values measured invasively with a pressure gage needle.

The study presented in this chapter embraces three parts: first, the finite element model and several experiments were used to infer the internal pressure of pristine and deflated tennis balls; second, the static and the dynamic characteristics of tennis balls were correlated to the features of HNSWs when they are inspected by HNSW transducers; and third, the impact of ball aging on its dynamic characteristics and HNSW features are discussed in the last part of this chapter.

4.2 Finite Element Model: Implementation, Setup, And Results

Shells and membranes are 3D structures that can be modeled with FEA using tetrahedral or hexahedral elements. The computational effort can be reduced whenever the problem being considered is axisymmetric, as the one shown in **Figure 4-1**. In this case, triangular or quadrilateral elements can be used to reduce significantly the number of degrees of freedom. In this study, the four-node quadrilateral isoparametric element (QIS) showed in **Figure 4-2** was used. Each node had one degree of freedom in the radial direction $r(u_1, u_2, u_3, u_4)$ and one degree of freedom in the axial direction $z(w_1, w_2, w_3, w_4)$.

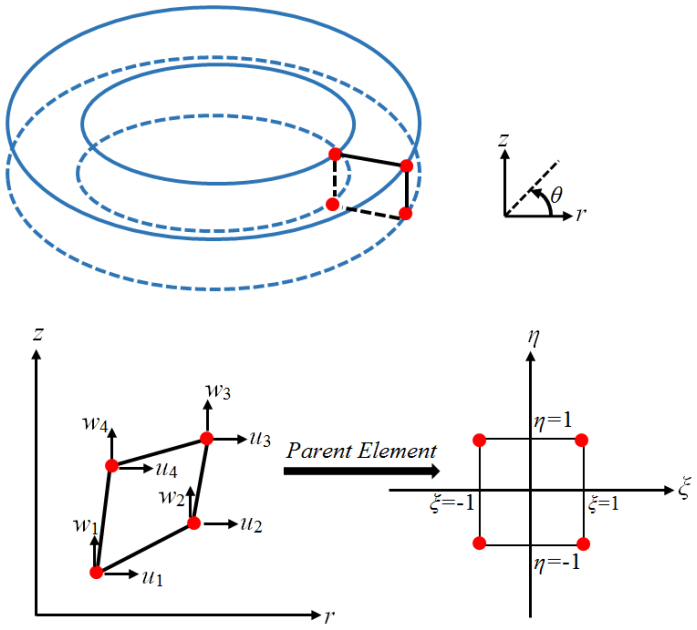

Figure 4-2 Scheme of four-node quadrilateral isoparametric element

The stress vector $\underline{\sigma}=[\sigma_r\ \sigma_z\ \sigma_\theta\ \tau_{rz}]^T$ and the strain vector $\underline{\varepsilon}=[\varepsilon_r\ \varepsilon_z\ \varepsilon_\theta\ \varepsilon_{rz}]^T$ were linked through the stress-strain relationship:

$$\boldsymbol{\sigma} = \boldsymbol{C}.\boldsymbol{\epsilon} \tag{4.1}$$

The stiffness matrix $\boldsymbol{K}$ of the element is given by [144]:

$$\begin{aligned}\boldsymbol{K} &= 2\pi \int_{-1}^{1}\int_{-1}^{1} \left(\boldsymbol{B^T}(\xi,\eta)\cdot\boldsymbol{C}\cdot\boldsymbol{B}(\xi,\eta)r(\xi,\eta)\det\boldsymbol{J}\,(\xi,\eta)\right)d\xi d\eta \\ &\cong 2\pi \sum_{i=1}^{m}\sum_{j=1}^{m} w_{ij}\boldsymbol{B^T}(\xi_i,\eta_j)\cdot\boldsymbol{C}\cdot\boldsymbol{B}(\xi_i,\eta_j)r(\xi_i,\eta_j)\det\boldsymbol{J}(\xi_i,\eta_j)\end{aligned} \tag{4.2}$$

where m is the number of Gaussian points used in the numerical integration, w_{ij} are weight coefficients, $\boldsymbol{J}$ is the Jacobian matrix, and $\boldsymbol{B}$ is the matrix connecting the strain to the nodal displacement vector $\boldsymbol{d}$ as:

$$\boldsymbol{\epsilon} = \boldsymbol{B}\cdot\boldsymbol{d} \tag{4.3}$$

Similarly, mass matrix and nodal force vector are calculated as:

$$\boldsymbol{M} = 2\pi\rho \int_{-1}^{1}\int_{-1}^{1} \left(\boldsymbol{N^T}(\xi,\eta) r(\xi,\eta) \det \boldsymbol{J}(\xi,\eta)\right) d\xi d\eta$$
$$\cong 2\pi\rho \sum_{i=1}^{m}\sum_{j=1}^{m} w_{ij} \boldsymbol{N^T}(\xi_i,\eta_j) r(\xi_i,\eta_j) \det \boldsymbol{J}(\xi_i,\eta_j) \tag{4.4}$$

$$\boldsymbol{F} = 2\pi \int_{-1}^{1}\int_{-1}^{1} \left(\boldsymbol{N^T}(\xi,\eta) \begin{Bmatrix} T_x \\ T_y \end{Bmatrix} r(\xi,\eta) \det \boldsymbol{J}(\xi,\eta)\right) d\xi d\eta$$
$$\cong 2\pi \sum_{i=1}^{m}\sum_{j=1}^{m} w_{ij} \boldsymbol{N^T}(\xi_i,\eta_j) \begin{Bmatrix} T_x \\ T_y \end{Bmatrix} r(\xi_i,\eta_j) \det \boldsymbol{J}(\xi_i,\eta_j) \tag{4.5}$$

where $\boldsymbol{N}$ is the shape functions vector, ρ is the density of the material, T_x and T_y are the tractions along x and y directions, respectively. In this study, T_x and T_y were the components of internal pressure in x and y directions respectively. To obtain the stiffness and mass matrices as well as the load vector of the whole shell, $\boldsymbol{K}$ and $\boldsymbol{M}$ and $\boldsymbol{F}$ were determined for each element in the mesh and they were then assembled using the connectivity matrix. The connectivity matrix was formulated by implementing the advancing front method [145].

To analyze the propagation of HNSWs along the chain of N particles, the equation of motion of each bead was written as:

$$\ddot{u}_1 = \frac{A_b}{m_b}[u_2(t) - u_1(t)]_+^{\frac{3}{2}} - g \tag{4.6a}$$

$$\ddot{u}_1 = \frac{A_b}{m_b}[u_{i+1}(t) - u_i(t)]_+^{\frac{3}{2}} - \frac{A_b}{m_b}[u_i(t) - u_{i-1}(t)]_+^{\frac{3}{2}} - g, \quad i = 2,3,\dots,N-1 \tag{4.6b}$$

$$\ddot{u}_1 = \frac{A_V}{m_b}\left[u_{M,V}(t) - u_N(t)\right]_+^{\frac{3}{2}} - \frac{A_b}{m_b}[u_N(t) - u_{N-1}(t)]_+^{\frac{3}{2}} - g \tag{4.6c}$$

In Eq. (4.6), $u_i(t)$ is the displacement of the i^{th} particle, m_b is the mass of the bead, g is the gravitational acceleration, $[x]_+$ means $\max(x,0)$, A_V is the contact stiffness of the vessel/bead

interface, $u_{M,V}$ the displacement of the degree of freedom of the vessel at the direction of the last particle's movement, and A_b is the Hertzian contact stiffness.

The equation of motion of the thin-walled pressure vessel was instead given by:

$$\ddot{\boldsymbol{u}}(t) = \boldsymbol{M_{rg}^{-1}} \cdot \boldsymbol{F_{rg}}(t) - \left(\boldsymbol{M_{rg}^{-1}} \cdot \boldsymbol{K_{rg}}\right) \cdot \ddot{\boldsymbol{u}}(t) \tag{4.7}$$

where $\boldsymbol{M_{rg}}$, $\boldsymbol{K_{rg}}$, and $\boldsymbol{F_{rg}}(t)$ are, respectively, the reduced global mass and the reduced global stiffness matrices and reduced global force vector, which are obtained after applying the boundary conditions. $\boldsymbol{F_{rg}}(t)$ includes static force due to the internal pressure and dynamic force of the HNSW. By solving simultaneously Eqs. (4.6) and (4.7), the displacement of the beads and the vessel was found. These displacements were then replaced in the Hertz's contact law:

$$F_1(t) = A_b[u_2(t) - u_1(t)]_+^{\frac{3}{2}} \tag{4.8a}$$

$$F_i(t) = \frac{1}{2}\left(A_b[u_{i+1}(t) - u_i(t)]_+^{\frac{3}{2}} + A_b[u_i(t) - u_{i-1}(t)]_+^{\frac{3}{2}}\right), \quad i = 2,3,\dots,N-1 \tag{4.8b}$$

$$F_N(t) = \frac{1}{2}\left(A\_V\left[u_{M,V}(t) - u_N(t)\right]_+ + A_b[u_N(t) - u_{N-1}(t)]_+^{\frac{3}{2}}\right) \tag{4.8c}$$

to determine the dynamic force at each bead of the metamaterial.

When the pressure inside the shell increases, the overall volume increases (**Figure 4-3**) as well as the material stiffness. The change in stiffness alters the interaction between the HNSWs and the shell and this effect can be formulated through the geometric nonlinear stiffness matrix $\boldsymbol{K^{geo}}$ [144]:

$$\begin{aligned} \boldsymbol{K^{geo}} &= 2\pi \int_{-1}^{1}\int_{-1}^{1} \left(\boldsymbol{\beta^T}(\xi,\eta) \cdot \boldsymbol{\sigma} \cdot \boldsymbol{\beta}(\xi,\eta) r(\xi,\eta) \det \boldsymbol{J}\right) d\xi d\eta \\ &\cong 2\pi \sum_{i=1}^{m}\sum_{j=1}^{m} w_{ij} \boldsymbol{\beta^T}\left(\xi_i,\eta_j\right) \cdot \boldsymbol{\sigma} \cdot \boldsymbol{\beta}\left(\xi_i,\eta_j\right) r\left(\xi_i,\eta_j\right) \det \boldsymbol{J}\left(\xi_i,\eta_j\right) \end{aligned} \tag{4.9}$$

where $\boldsymbol{\beta}$ is a matrix with the terms of the derivatives of the shape functions [144]. Given the above, the total stiffness of the pressure vessel is the sum of $\boldsymbol{K}$ and $\boldsymbol{K^{geo}}$.

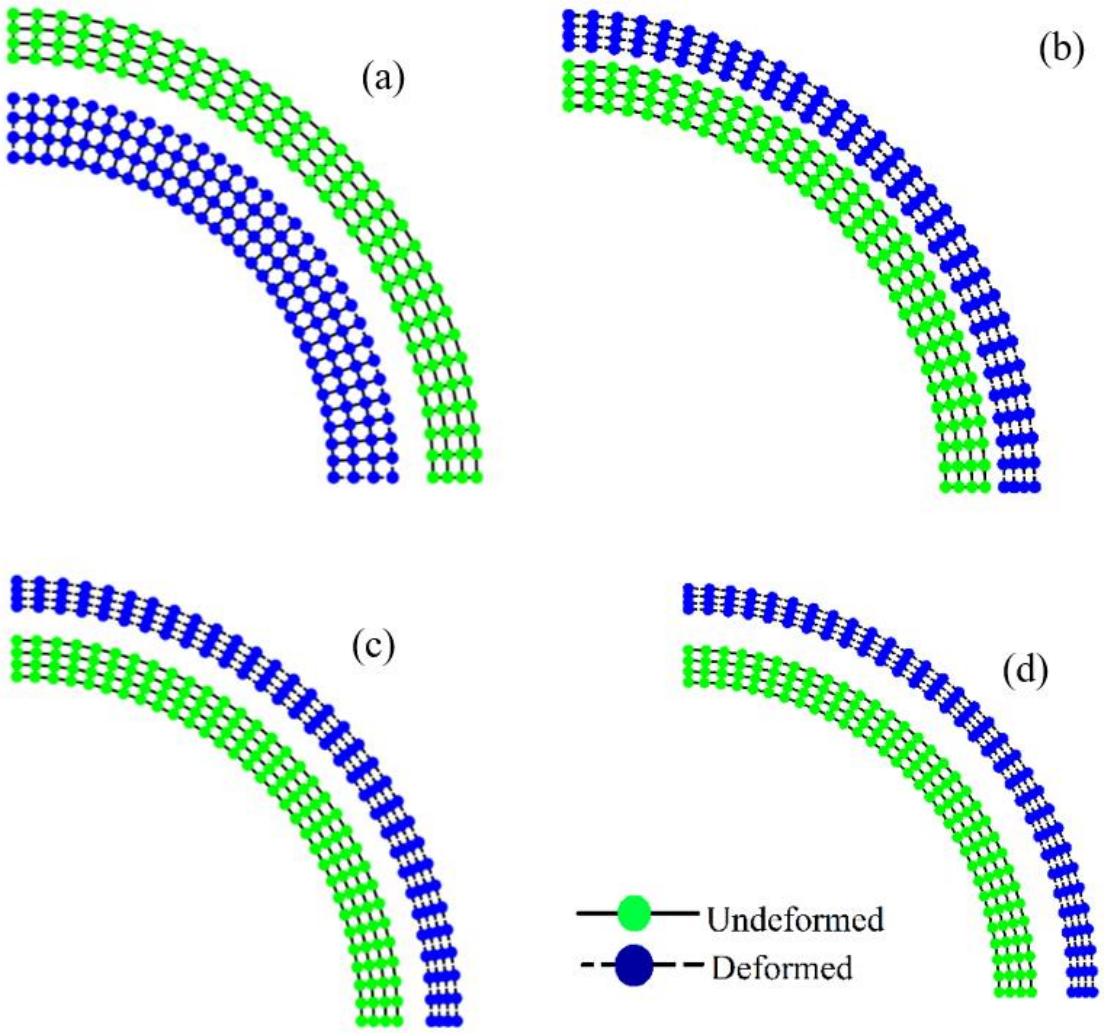

Figure 4-3 Stretched shell due to internal pressure equal to: (a) -80 MPa, (b) 40 MPa, (c) 60 MPa, and (d) 80 MPa. To ease visibility, the deformations have been magnified 5000 times

The general framework described in the previous section was applied to predict the interaction between HNSWs and tennis balls, which can be considered as thin-walled pressure vessels. The mesh and the boundary condition are shown in **Figure 4-4**. Only the rubber core was considered, whereas the thin layer of adhesive and the felt-like material were neglected. The ball radius and thickness were 30 mm and 3 mm, respectively. The elastic modulus and the Poisson ratio of the rubber were equal to 2.82 MPa and 0.49, respectively [143].

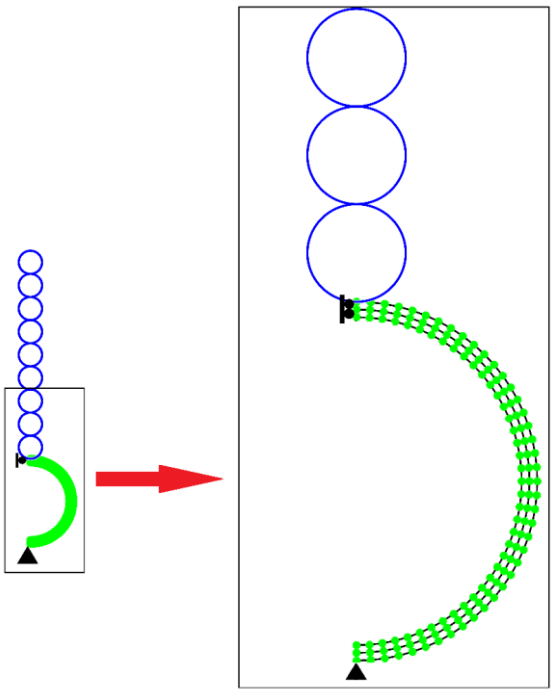

Figure 4-4 Schematic of the FEM of a tennis ball model in contact with a HNSW transducer

To describe the non-linear stress-strain behavior of the rubber and predict the deformation of the ball surface under the action of the HNSWs, the 3rd-order Ogden model was considered [143, 146]. In the Ogden model, the stress-strain relation is given by:

$$\sigma_i = \sum_{j=1}^{n} \frac{\mu_j}{J}\left[\epsilon_i^{*\alpha_i} - \sum_{k=1}^{3} \frac{\epsilon_k^{*\alpha_i}}{3}\right], \quad J = \epsilon_1\epsilon_2\epsilon_3, \quad \epsilon_i^* = \frac{\epsilon_i}{j^{\frac{1}{3}}} \tag{4.10}$$

where n is set to 3 to account for the order of the model, ε_i represents the strain along direction i, μ is the shear modulus, and α is a constant exponent dependent on the order of the Ogden model. **Table 4-1** summarizes the mechanical properties of the rubber and the constants used in Eq. (4.10). The Ogden model was used to calculate the bead-to-ball contact stiffness A_V, i.e. the contact stiffness between the last particle of the chain and the tennis ball. **Figure 4-5** shows that such stiffness is not constant but is linearly dependent on the internal pressure, which in this study ranged from 0 to 100 kPa at 20 kPa step.

Table 4-1 Mechanical properties of the ball rubber and the 3rd-order Ogden hyperelastic model

Rubber	ρ (kg/m^3)	E (MPa)	ν	μ_j (MPa)			α_j		
				μ_1	μ_2	μ_3	α_1	α_2	α_3
	1500	2.82	0.49	0.0018	1.970	2.109	15.43	1.648	1.648

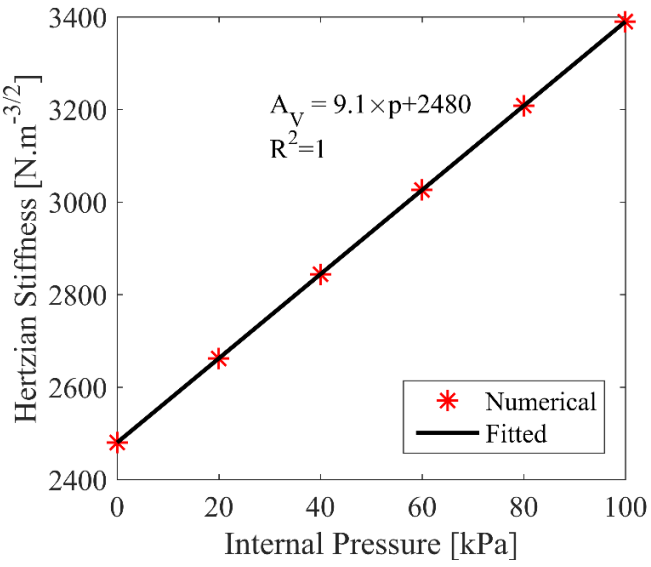

Figure 4-5 Ogden model used as Hertzian stiffness to describe the particle-to-ball interaction

The chain consisted of nine Φ=19.05 mm steel spheres with ρ=7850 kg/m^3. The elastic modulus and the Poisson ratio of the steel were 200 GPa and 0.3, respectively. The action of a striker falling from a height of 4 mm was simulated by setting the initial speed of the top particle of the chain equal to 0.2801 m/s. These 4 mm were chosen to emulate the experimental setup described in the next section.

Figure 4-6 shows the dynamic force (time waveform) of the HNSWs measured at the center of the 5th particle from the top and relative to three internal pressures, namely 0, 60, and 100 kPa. The vibration of the ball surface in contact with the metamaterial generates the pulses visible around and after 4 ms (**Figure 4-6(a)**) or after 3 ms (**Figure 4-6(b)** and **Figure 4-6(c)**). The response of these vibration-related pulses is ignored in this study and will not be discussed any further in this paper.

Figure 4-6 shows that the internal pressure influences the arrival time of the PSW and the SSW and the relative amplitude of the secondary wave with respect to the primary wave. In addition, the time delay between the two reflected waves is also pressure dependent. Finally, **Figure 4-6** reveals that the PSW and SSW carry two peaks each. The origin of these twin-peaks was originally explained in [67]. The dynamic force on each bead is the average of the dynamic force of the two adjacent beads. This is illustrated in **Figure 4-7** where the dynamic forces exerted by the two particles adjacent to the N^{th} sphere are presented along with their average value ($F_{average}$), which is the value measured at the center of the particle. When the body in contact with the chain is much softer than the particles forming the metamaterial, or the pre-compression is small, the time delay between the two dynamic forces is relatively large (**Figure 4-7(c)**) giving rise to the twin-peaks.

To quantify the effects of the internal pressure on the propagation of the HNSWs, a few features were extracted from the numerical time waveforms. They were the amplitude of the incident wave, the TOF of the primary and secondary solitary waves, the ratio of the amplitude of the PSW and SSW to the amplitude of the ISW. Here, the TOF denotes the transit time at the 5^{th} bead from the top of the metamaterial between the incident and the corresponding reflected wave. The results are presented in **Figure 4-8** where these features are plotted as a function of the internal pressure. Surprisingly, the amplitude of the ISW (**Figure 4-8(a)**) changes slightly with the internal pressure. Intuitively, the amplitude of the signal triggered by the collision of the striker should remain constant. The origin of this apparent contradiction will be discussed shortly. While there is no uniform trend associated with the amplitude (**Figure 4-8(b)** and **Figure 4-8(c)**) of the reflected waves, **Figure 4-8(d)** and **Figure 4-8(e)** reveal the monotonic trend of the PWS and SSW time-of-flight with the increase of the internal pressure. This trend suggests that a direct and univocal link can be established between the characteristics of the solitary waves and the pressure inside the tennis ball. Quantitatively, the TOF decreases by 12% across the 0-100 kPa range (**Figure 4-8(f)**). It is not excluded, though, that longer chains, smaller/larger particles, or different material particles may provide even higher sensitivities.

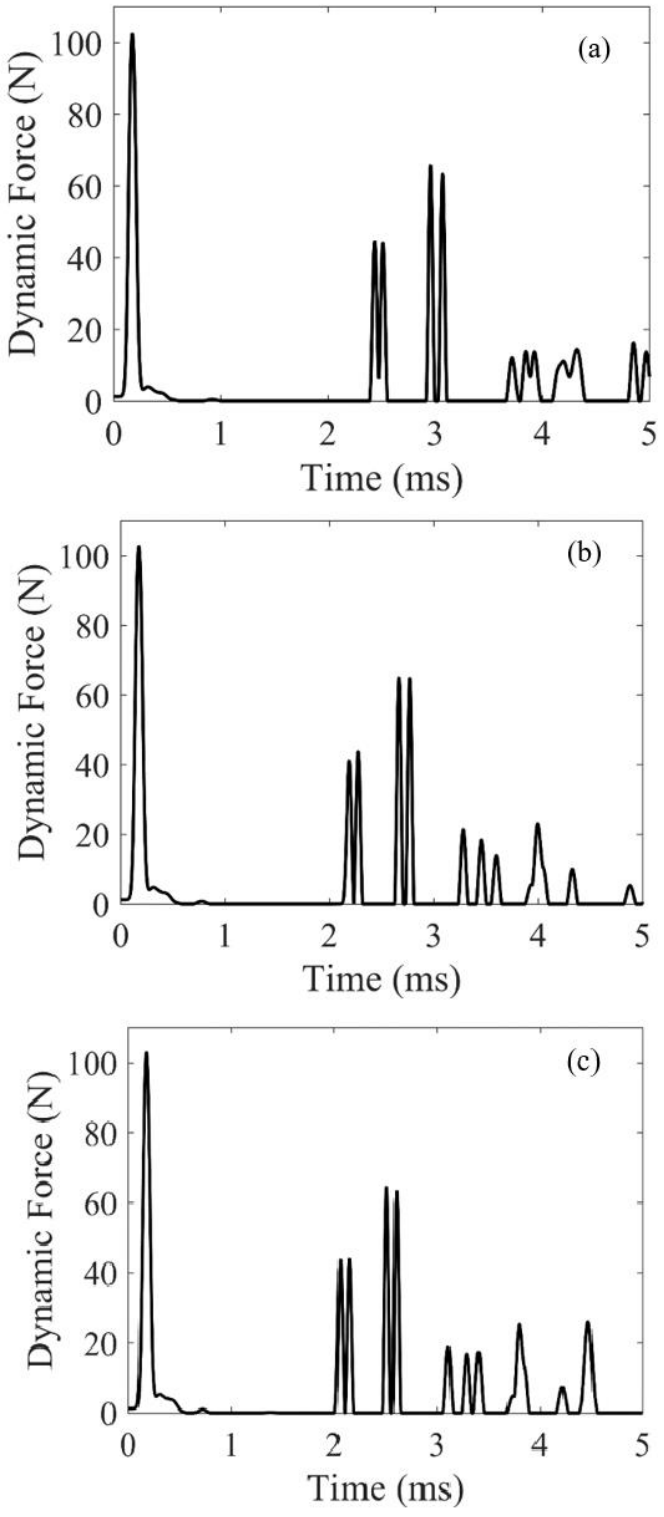

Figure 4-6 Numerical simulation: Time waveform of the HNSW chains in contact with the ball with internal pressure of (a) 0, (b) 60 kPa, and (f) 100 kPa

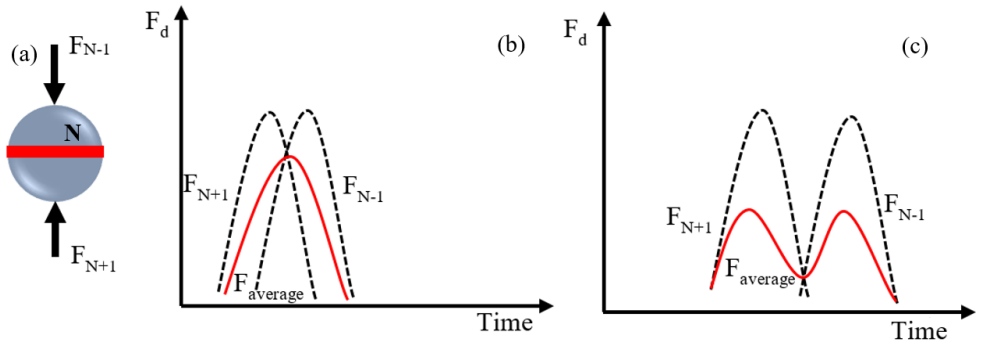

Figure 4-7 Dynamic forces exerted on the Nth particle of the chain in presence of: (a) strong pre-compression or hard interface material, (b) strong pre-compression or stiff material in contact with the metamaterial, (c) weak pre-compression or soft material in contact with the metamaterial

To find the origin of the slight increase of the amplitude of the ISW with the increase of the internal pressure (**Figure 4-8(a)**), a metamaterial made of 20 spheres was considered and the waves were measured at the center of the 5th sphere from the top. The results are presented in **Figure 4-9**. The time-waveform (**Figure 4-9(a)**) relative to the 100 kPa case shows some spurious bumps between the ISW and the PSW whereas the amplitude of the ISW (**Figure 4-9(b)**) remains constant. It is concluded that, irrespective of the length of the chain, when the striker impacts the chain it bounces up decreasing temporarily the overall weight of the metamaterial on the ball. The change of the weight causes a slight deformation of the ball, which in turn, triggers a small pulse propagating upward along the metamaterial. The deformation and the consequent upward pulse are dependent upon the internal pressure of the ball. The stiffer the ball (due to higher internal pressure) the stronger is the upward pulse.

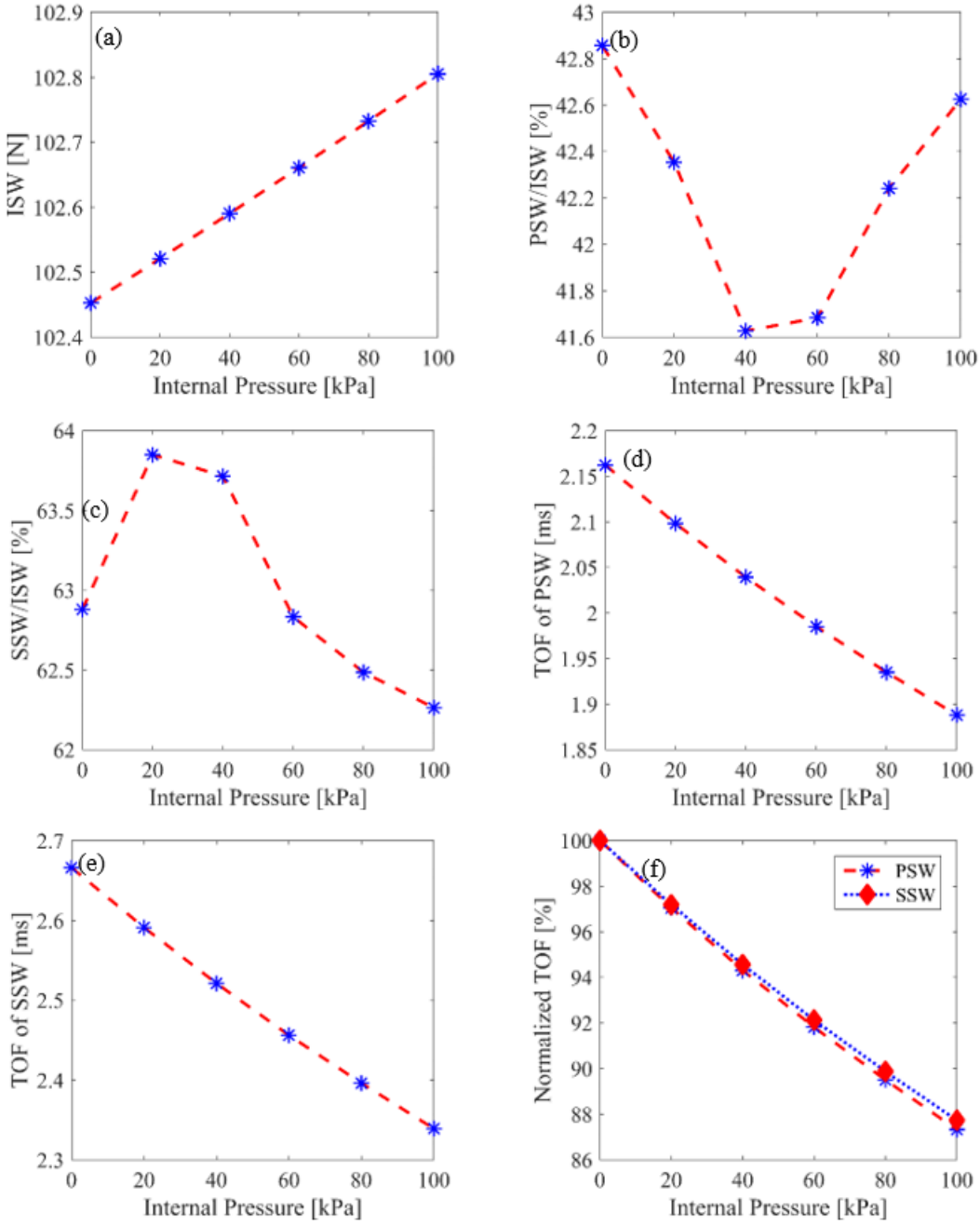

Figure 4-8 Numerical Simulation. Effect of the internal pressure on some selected features. (a) Amplitude of the incident wave; (b) Amplitude of the primary reflected wave to the amplitude of the incident wave; (c) Amplitude of the secondary reflected wave to the amplitude of the incident wave; (d) time-of-flight of the PSW; (e) time-of-flight of the SSW, (f) normalized time-of-flight

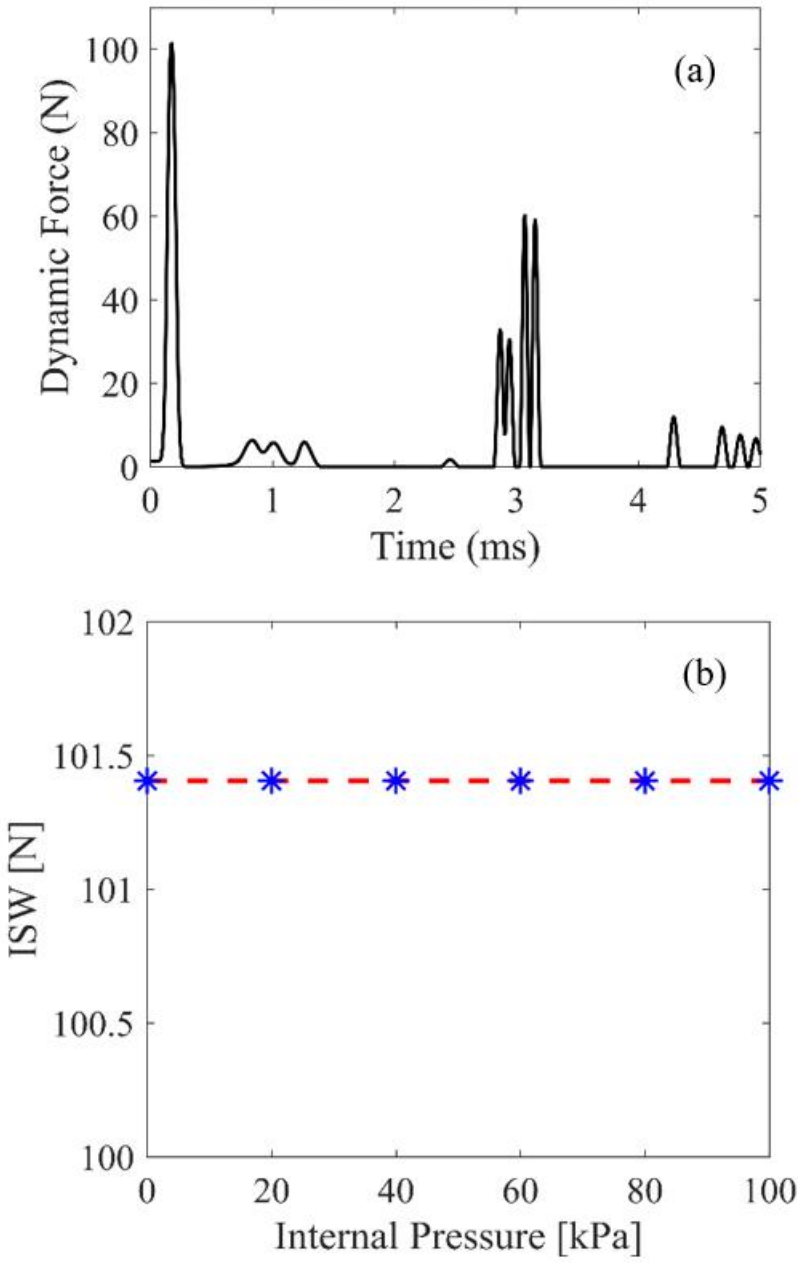

Figure 4-9 (a) The time waveform of the 5th particle of a 20-particle chain for internal pressure of 100 kPa. (b) the ISW vs the internal pressure of the 5th particle of the 20-particle chain for internal pressure of 100 kPa

4.3 Experimental Study

4.3.1 Experimental Setup

Four kinds of tennis balls were tested: Penn Championship Extra-Duty, Penn Championship Regular-Duty, Gamma Quick Kids 60, and Gamma Quick Kids 78. “Regular-duty” balls are designed for use on clay courts where they travel slower than hard or grass courts; they have a thinner felt covering so that the balls will pick up less clay. Extra-duty balls are instead manufactured to be used on hard and grass courts; they are covered with thicker felt to allow for longer usage on hard courts. Gamma Quick Kids 60 balls are low compression, medium bounce soft training tennis balls designed for beginners and are suited to be used in shorter (60 feet) courts. These balls allow more time to react and set up each shot for more consistency and control when learning. Finally, the Gamma Quick Kids 78 balls are 25% slower than a standard tennis ball and are designed to be used in regular (78 feet) courts.

The outer radius and the thickness of each ball are summarized in **Table 4-2**. The balls were tested pristine immediately after opening the cans and then after piercing them with a hollow needle connected to a pressure gauge to measure the internal pressure under pristine conditions. Three balls per kind were tested; hence twelve balls total were probed with one HNSW transducer.

Table 4-2 Nomenclature and physical properties of tennis balls used in the study

Ball Name	Number of Balls	Ball Type	Deflated Diameter (mm)	Deflated Thickness (mm)	Ave. Gauge Pressure* (kPa)
Penn Extra Duty (PED)	3	Pressurized	62	3.0	88.2
Penn Regular Duty (PRD)	3	Pressurized	62	3.0	69.6
Gamma Quick Kids 60 (G60)	3	Unpressurized	60	3.0	0.0
Gamma Quick Kids 78 (G78)	3	Unpressurized	60	3.7	0.0

The HNSW transducer was a straight chain made of eight steel spheres, 19.05 mm in diameter. The chain embedded one Φ=19.05 mm, 0.3 mm thin PZT glued between two Φ=19.05 mm, 6.5 mm thick steel disks. This assembly represented the sensor-disk used to measure the propagating pulses within the metamaterial. The total height of the assembly was 13.4 mm and its weight was purposely equal to the weight of the single particles to avoid the formation of any impurity at the sphere-disk interface. **Figure 4-10(a)** shows the scheme of the HNSW transducer while **Figure 4-10(b)** display the overall setup with one of the twelve specimens. The ISW was triggered by lifting and releasing the top particle (the striker) with an electromagnet connected to a DC power supply and driven by a National Instrument PXI running in LabView using a graphical user interface (GUI) designed in the lab. An aluminum foil was glued to the bottom of the transducer to avoid the free fall of the beads. The GUI controlled the repetition rate of the measurements, i.e. controlled the time interval between two consecutive lifts and releases. The transducer was assembled such that the lift-off distance of the striker was 4 mm. For each tennis ball, 50 measurements were taken to quantify the repeatability of the setup. The waveforms were sampled at 1 MHz. While the numerical trigger, i.e. the instant at which t=0, was set to the initial motion of the striker, the experimental trigger was coincident to the time of arrival of the maximum amplitude of the incident wave. A 10% pre-trigger was included in the digitized signal to avoid the truncation of relevant signals.

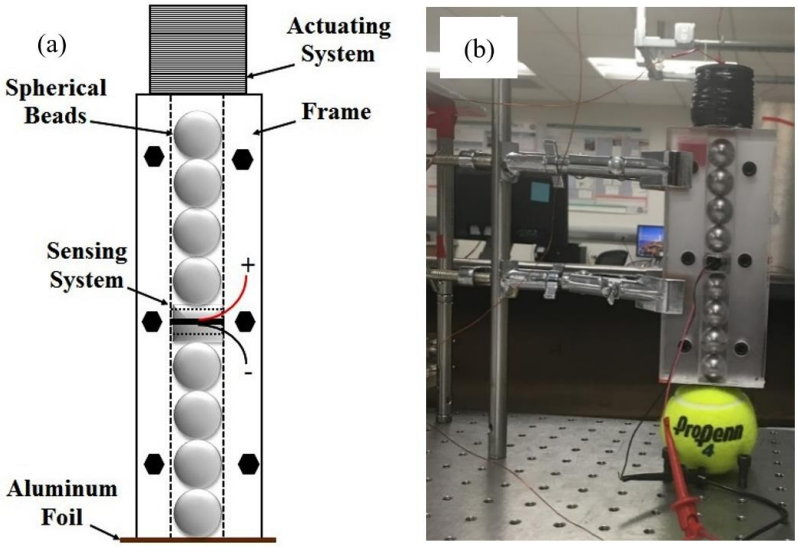

Figure 4-10 (a) Scheme of the HNSW transducer. (b) Photo of the transducer above one of the ball

4.3.2 Results

Figure 4-11 displays one of the fifty waveforms taken under pristine condition and one taken after piercing the extra-duty specimen #2. To ease the comparison between the experimental (**Figure 4-11**) and the numerical (**Figure 4-6**) waveforms, the time scale of **Figure 4-11** was offset to overlap the arrival time of the incident wave. The comparison between the two figures: (1) reveals that the arrival time of the reflected pulses with respect to the incident pulse are very similar; (2) confirms the slight influence of the internal pressure on the amplitude of the incident wave; (3) confirms the formation of twin-peaks; (4) suggests that the model may have overestimated the amplitude of the secondary waves when compared to the amplitude of the primary reflected wave. In the model, the damping in the rubber was neglected, and this may have overestimated the deformation of the ball core due to the arrival of the incident wave at the interface.

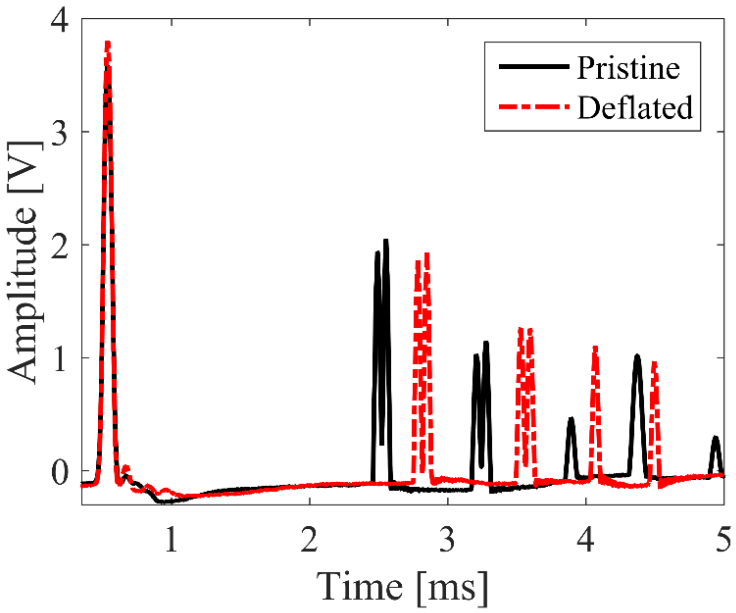

Figure 4-11 Time waveform relative to sample PED #2 under pristine and deflated conditions

Similar to what done in the numerical study, several features were extracted from the experimental time-waveforms and the results are displayed in **Figure 4-12**, where the average of the 50 measurements and the corresponding 95% confidence interval are presented for each ball under pristine and deflated conditions. **Figure 4-12(a)** shows that when the pressurized balls (specimens PED and PRD) are deflated the amplitude of the primary reflected waves decreases by 10%-15%. This result is expected as the absence of pressure allows larger deformation of the rubber, giving rise to a stronger secondary pulse. This evidence is confirmed by looking at the complementary response of the SSW displayed in **Figure 4-12(b)**. The unpressurized balls instead do not show any particular trend before and after piercing, demonstrating that the internal pressure is the main parameter attributable to the HNSW response.

Figure 4-12(c) and **Figure 4-12(d)** show instead the TOF of both reflected waves. The TOF relative to the primary reflected waves (**Figure 4-12(c)**) display strong repeatability and clear

difference between inflated and deflated balls. As such, this parameter may be an excellent indicator to measure noninvasively the internal pressure of tennis balls. The arrival time of the secondary waves (**Figure 4-12(d)**) instead does not show the same definite trend seen in **Figure 4-12(c)** and therefore a firm conclusion about its ability at inferring the internal pressure of the tennis ball cannot be made. Overall, it can be said that the TOFs of PSW and SSW of pressurized balls increase significantly when they are deflated. On the other hand, the arrival time of the solitary waves associated with the unpressurized balls are not univocally affected after piercing the ball. Hence, it can be concluded that the variation in the TOFs is due to the internal pressure which changes the stiffness of balls through geometric stiffness of the balls and hyperelastic behavior of rubber.

In the case of the unpressurized balls, the TOF of the PSW and the SSW associated with the G78 specimens is overall smaller than the G60 because the G78 ball has thicker rubber. Finally, it is noted that the arrival time associated with the primary reflected wave does not have much difference between the extra-duty and the regular-duty. This suggests that this wave feature is dependent on the rubber characteristics which are identical for both kinds of balls.

4.3.3 Estimation of the Internal Pressure

As the arrival time of the primary reflected waves seems the best candidate to infer the internal pressure of tennis balls, this parameter was further investigated. The results displayed in **Figure 4-12(c)** are summarized in **Figure 4-13** that displays the average and the corresponding confidence interval of the 150 total measurements taken for each kind of ball, and **Table 4-3**, which shows the standard deviation and the coefficient of variation (CoV) of the measurements. The fact that the CoV is about 1.0% or less proves the strong repeatability of the setup.

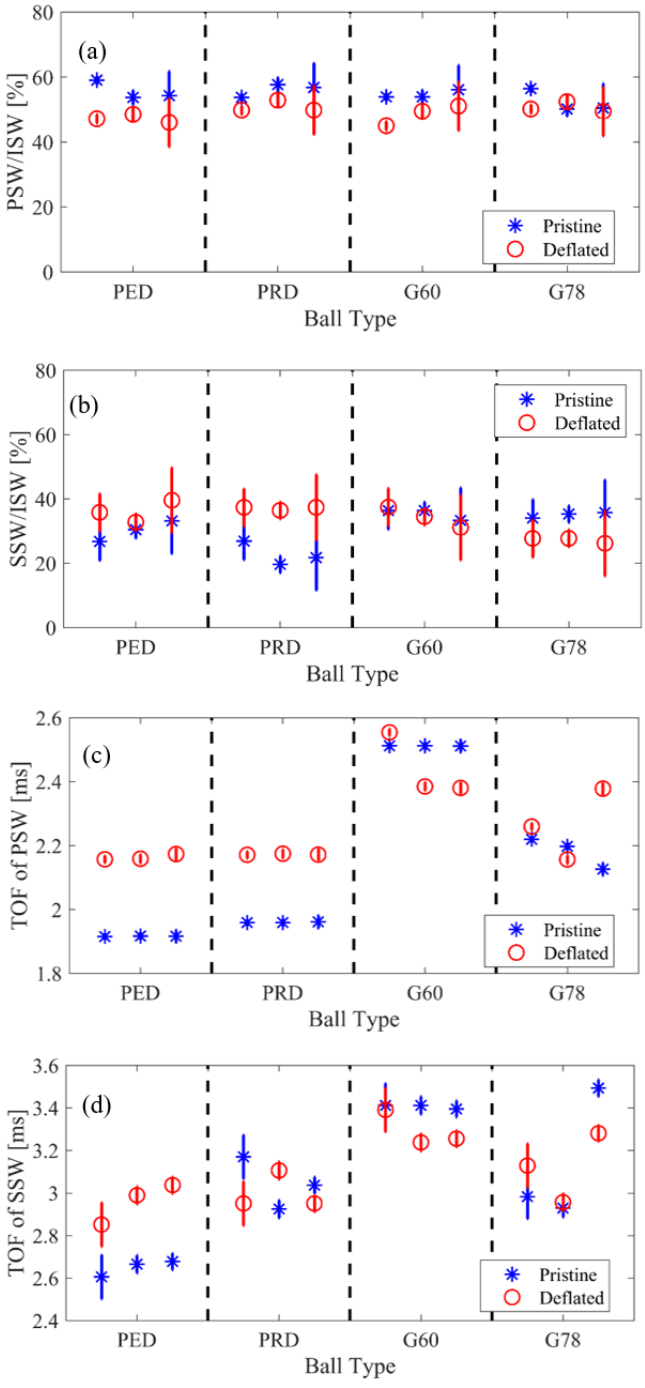

Figure 4-12 Experimental results. Amplitude ratio of the (a) primary reflected wave and (b) secondary reflected wave to the amplitude of the incident wave. Time of flight of the (c) primary reflected wave and (d) secondary reflected wave

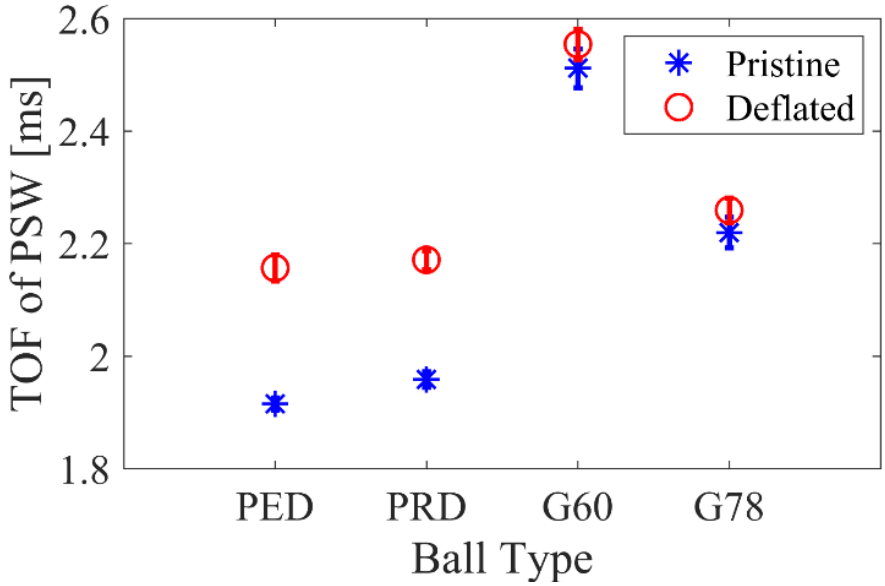

Figure 4-13 Error bars of TOF of PSW for different ball types in pristine and deflated states

Table 4-3 The statistical data of the TOF of the PSW of different balls

Ball Type	Ball #1			Ball #2			Ball #3		
	Mean (ms)	SD (ms)	CoV (%)	Mean (ms)	SD (ms)	CoV (%)	Mean (ms)	SD (ms)	CoV (%)
Pristine									
PED	1.915	0.011	0.6	1.917	0.013	0.7	1.916	0.029	1.4
PRD	1.959	0.013	0.6	1.959	0.016	0.8	1.961	0.017	0.9
G60	2.512	0.034	1.4	2.512	0.034	1.4	2.512	0.028	1.1
G78	2.220	0.027	1.2	2.197	0.029	1.3	2.226	0.026	1.0
Deflated									
PED	2.157	0.023	1.1	2.159	0.023	1.0	2.173	0.025	1.1
PRD	2.171	0.017	0.8	2.174	0.014	0.6	2.172	0.017	0.8
G60	2.554	0.027	1.0	2.485	0.014	0.6	2.680	0.032	1.4
G78	2.259	0.022	1.0	2.156	0.025	1.1	2.378	0.023	1.0

SD: standard deviation; CoV: coefficient of variation

Knowing that stiffer balls induce smaller TOF, the inflated PED and PRD are harder than the G60 and almost comparable than the G78 even though the latter is 23.3% ticker than the pressurized balls. This variation may be due to different material properties. To prove this

hypothesis, we cut one sample of each ball type (**Figure 3-14**) and found that the material used for unpressurized balls are different from the pressurized balls. Moreover, they are 20% thicker. This was confirmed by the information publicly available: the rubber used for the G60s and the G78s is a low-compression rubber and different than conventional tennis ball [147].

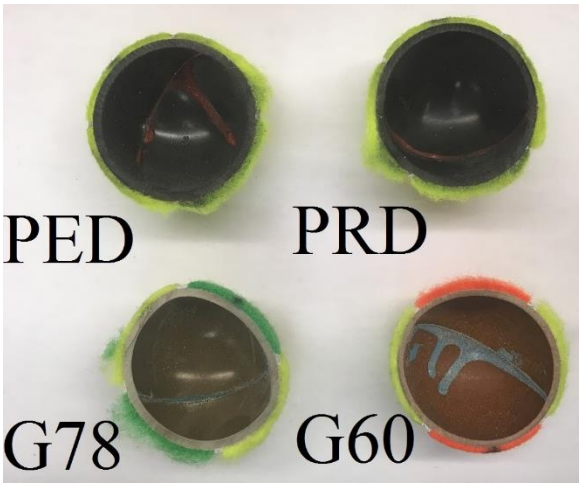

Figure 4-14 A cut of each ball type shows that they are made of different materials

To infer the internal pressure from the HNSW data, a general relationship was extracted from the numerical data. This relationship is shown in **Figure 3-15** and consists of a second-degree polynomial that links the internal pressure to the time of flight of the primary reflected waves propagating in the metamaterial assembled in the experimental study. It is noted here that the polynomial applies only to this type of metamaterial, i.e. to a specific number of particles in the chain made of steel and 19.05 mm in diameter. The empirical estimation of the pressure was conducted by plugging the experimental times of flight listed in **Table 4-4**, left column of each data set, into the above polynomial. The results are presented in **Table 4-4** and **Figure 4-16**. The noninvasive estimation of the pressure is compared with the measurement obtained destructively

using a pressure gage and the match between the noninvasive approach and the invasive approach is excellent. The discrepancy between the solitary wave-based method and the gauge values is well below 1%. Since the internal pressure of the deflated balls equalizes the atmospheric pressure, the differential pressure is obviously equal to zero.

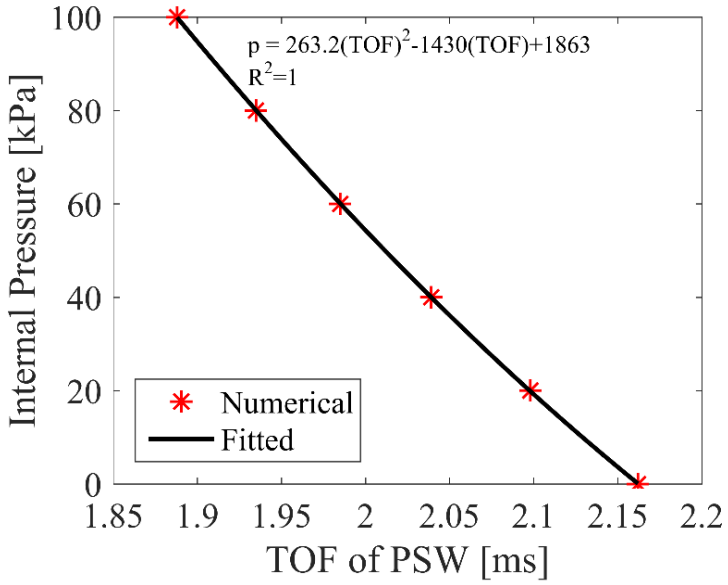

Figure 4-15 Internal pressure vs. TOF of PSW and the fitted curve

Table 4-4 Results of internal estimation of pressurized balls (values in kPa)

Ball Type	Mean Gauge	STD Gauge	Mean HNSW	STD HNSW
	Pristine			
PED	88.2	0.4	88.0	0.2
PRD	69.6	0.4	70.2	0.4
	Deflated			
PED	0.0	0.0	-0.2	2.1
PRD	0.0	0.0	-2.9	0.4

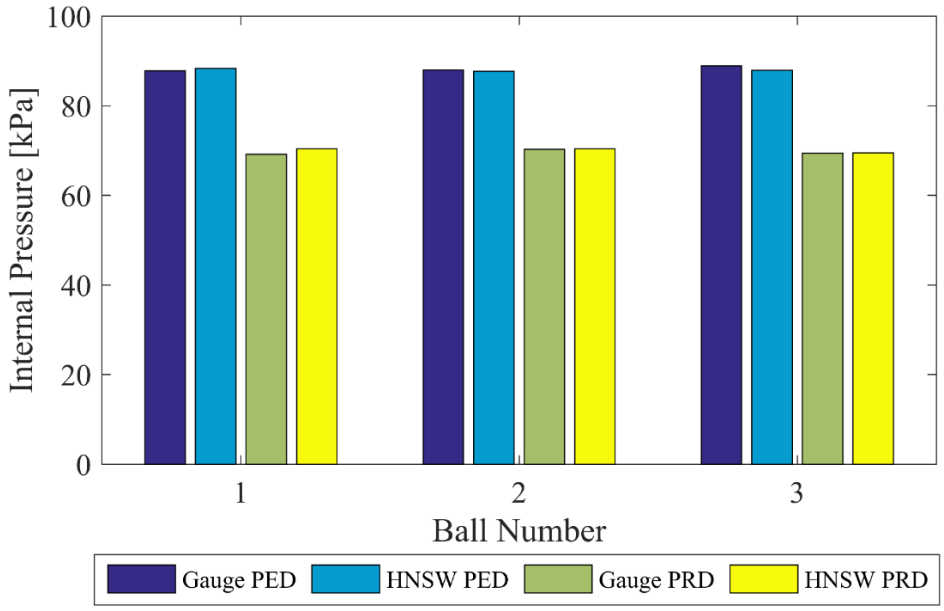

Figure 4-16 The results of internal pressure estimation of the pressurized balls

4.3.4 Conclusions

This paper investigated numerically and experimentally the dynamic interaction of highly nonlinear solitary waves propagating along 1-dimensional chains of spherical particles with tennis balls, in contact with the chain, of varying internal pressure. We found that the waves reflected at the interface and in particular their time of flight are affected by the internal pressure of the ball. We quantified these dependencies numerically by implementing a general finite element analysis that can be applied to any thin-walled pressure vessel and then we applied this model to the specific case of a tennis ball. The finite element model was then validated experimentally by testing four kinds of tennis balls. The experimental results demonstrated that the nondestructive evaluation method to infer the internal pressure of tennis balls using the highly nonlinear solitary waves matches very well the internal pressure measured destructively with a gauge pressure that pierces the balls making them useless afterward.

The findings of this paper demonstrate that the propagation of highly nonlinear solitary waves can detect pressure changes in a tennis ball, i.e. can be used to monitor the serviceability of used balls or to establish the conformity of new manufactured balls to the standards set by the international tennis federation. Future studies shall investigate different chains configurations in terms of particles size and particles material to provide the configuration that provides the highest sensitivity to small variations of internal pressure.

4.4 Solitary Waves to Assess Internal Pressure and Rubber Degradation

The study presented in Ch. 4.3 was expanded to account for tennis ball material degradation. One several balls of one type were focused and tested in pristine state and after being played, and after being pierced. The material degradation was considered in the numerical simulation by changing the elastic modulus of core rubber over a range. The internal pressure of tennis balls was measured using a pressure gauge before the last set of experiments using solitary waves.

4.4.1 Materials and Setup

Eighteen commercial Penn Championship Extra-Duty tennis balls from six cans (three balls per can) were tested. These balls belong to Class Type 2 that must satisfy the ITF standards listed in **Table 4-5**. The balls were purchased at the same moment from the same vendor and shall therefore be considered or at least expected identical. The full test protocol is schematized in **Table 4-6**, where the specimens are labelled to ease identification. One can was opened but never used

while the others were opened and played once or twice for about 90 minutes by amateur players on the concrete court of an indoor recreational facility. The balls in cans #2, 5, and 6 were played once, whereas the specimens #7 through #12 were played twice. The balls were tested four times using the solitary waves and a modified rebound test, described later. The last round of experiments was completed after piercing each ball with a needle connected to a pressure gage to measure the internal pressure.

Table 4-5 Properties of Type 2 tennis balls according to the ITF

Property	Type 2 (Medium)
Mass (gr)	56.0 – 59.4
Size (cm)	6.54 – 6.86
Rebound (cm)	135 – 147
Forward deformation (cm)	0.56 – 0.74
Return deformation (cm)	0.80 – 1.08
Color	white / yellow

Table 4-6 Specimens label and testing protocol

Can #	Ball #	Day opened	Day Played	Day Pierced	Day Tested
1	1-3	Dec. 4	Never	Dec. 17	Dec. 4, 8, 13, and 18
2	4-6	Dec. 4	Dec. 6	Dec. 17	Dec. 4, 8, 13, and 18
3	7-9	Dec. 4	Dec. 6 and 9	Dec. 17	Dec. 4, 8, 13, and 18
4	10-12	Dec. 4	Dec. 6 and 9	Dec. 17	Dec. 4, 8, 13, and 18
5	13-15	Dec. 4	Dec. 12	Dec. 17	Dec. 4, 8, 13, and 18
6 *	16-18	Dec. 4	Dec. 12	Dec. 17	Dec. 4, 13, and 18

***Note that specimens 16-18 (Can #6) accidentally were not tested on Dec. 8.**

The granular crystal, which used in the previous section and consisted of eight identical spheres (diameter d=19.05 mm) made of stainless steel (elastic modulus E=200 GPa, Poisson's ratio ν =0.3, and density ρ=7,850 kg/m^3), was placed at the top of a HNSW transducer as shown in **Figure 4-17** and were run to generate and detect the solitary waves of the chain in contact with the ball.

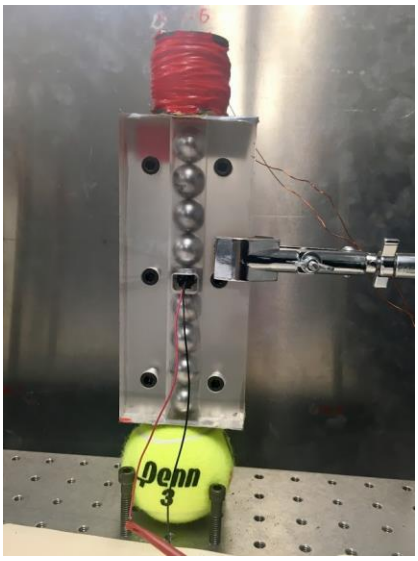

Figure 4-17 A HNSW transducer in contact with a tennis ball

After the HNSWs measurements, the specimens were subjected to a modified rebound test. It consisted of dropping vertically the ball from a height of h_0 = 2.14 m (84.25 in.) on a concrete floor covered with typical laboratory vinyl tiles. A microphone was placed a few cm from the point of impact to measure the time $2\Delta t$ between the sounds associated with the two consequent collisions of the ball to the surface. This time was used to determine the rebound height h_1 using the equation:

$$h_1 = \frac{g}{2}\Delta t^2 \tag{4.11}$$

where g is the gravitational acceleration. From h_1, expressed in meters, the CoR e was estimated as:

$$e = \frac{v_1}{v_0} = \frac{\sqrt{2gh_1}}{\sqrt{2gh_0}} = \sqrt{\frac{h_1}{2.14}} \tag{4.12}$$

Each ball was dropped 15 times to account for possible test-to-test variabilities.

4.4.2 Numerical Results

Figure 4-18(a) and **Figure 4-18(b)** shows the dynamic force (time waveform) of the HNSWs measured at the center of the 5th particle from the top of the chain and in contact with a 67 mm in diameter, 3 mm thick tennis ball with rubber modulus equal to 2.8 MPa and internal pressure equal to 0 and 100 kPa, respectively. To mimic a 4 mm falling of the striker, the initial speed of the first bead of the chain was set equal to 0.28 m/s. All plots show the presence of the incident, primary reflected, and secondary reflected waves, and the latter two carry two peaks each. The origin of these twin-peaks originally detailed in Section 4.3. After 3.2 ms, the vibration of the ball induced other spurious pulses that were ignored in the study and will not be discussed any further. The comparison of **Figure 4-18(a)** with **Figure 4-18(b)** suggests that the pressure influences the travel time of the reflected waves because it influences the geometric stiffness of the rubber.

Figure 4-18(c) and **Figure 4-18(d)** show instead the waveforms associated with rubber modulus equal to 2.0 MPa and pressure equal to 0 and 100 kPa, respectively. The comparison between insets (a) and (c) and between insets (b) and (d) does show some variation in the feature of the solitary waves due to the rubber modulus. The secondary wave is larger than the PSW because the rubber is much softer than the steel bead and the acoustic energy of the incident wave is significantly converted into the inelastic deformation of the rubber.

To quantify the effects of the internal pressure and rubber modulus on the propagation of the waves, the TOF of the primary and secondary solitary waves, and the ratio of the amplitude of the PSW and SSW to the amplitude of the ISW were extracted. The results are presented in **Figure 4-19** where the ratios of the amplitude of the PSW and of the amplitude of the SSW to the amplitude of the ISW are presented in **Figure 4-19(a)** and **Figure 4-19(b)**, respectively as a function of the internal pressure and for different moduli of the rubber. Note that the amplitude

considered in the graphs is the average of the twin peaks observed in **Figure 4-18**. At a given modulus, the amplitude of the PSW is proportional to the internal pressure; the inverse trend is visible for the SSW. A rapid analysis of the vertical axes of **Figure 4-18(a)** and **Figure 4-18(b)** reveal that the variation between the ball at 0 kPa and 100 kPa is about 2% at a given modulus, and less than 0.5% across the values of the elastic modulus at a given pressure. **Figure 4-18(c)** shows instead the TOF between the first peak of the PSW and the incident wave. This value is also presented as a function of the internal pressure for different elastic modulus. The feature is inversely proportional to both the pressure and the modulus, because the internal pressure changes the geometric stiffness of the balls and the hyperelastic behavior of the rubber.

To quantify the percentage variation of this solitary wave feature, **Figure 4-18(d)** presents the value of the TOF normalized with respect to the case of E_r=2.8 MPa and pressure equal to 80 kPa. These numbers represent with very good approximation the typical values of a pristine ball just manufactured. **Figure 4-18(d)** reveals that the effect of the internal pressure is larger than the effect of the rubber modulus. For example, halving the pressure from 80 kPa to 40 kPa, increases the TOF by 4% at a given rubber modulus. Conversely, decreasing the rubber modulus from 3.0 MPa to 1.6 MPa, at a given internal pressure, increases the TOF by 2%. The comparison between **Figure 4-18(d)** and **Figure 4-18(a)** and **Figure 4-18(b)** ultimately suggests that the time-based feature is more sensitive than the amplitude-based features. Similar conclusions can be drawn by considering the arrival time of the secondary wave.

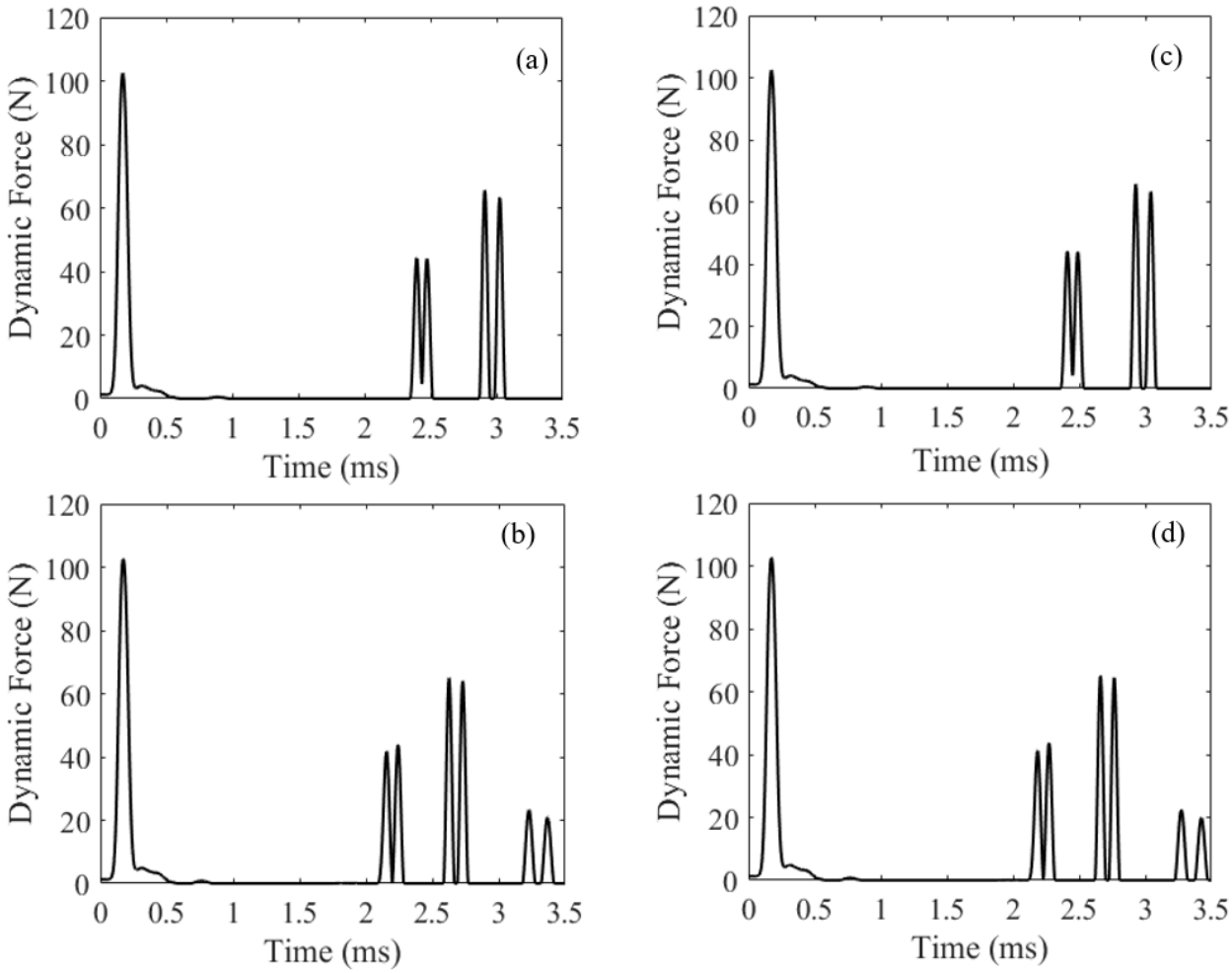

Figure 4-18 Numerical simulation: time waveforms of the HNSW of a tennis ball with varying rubber modulus (Er) and internal pressure (IP). (a) Er = 2.8 MPa and IP=0, (b) Er = 2.8 MPa and IP=100 kPa, (c) Er = 2.0 MPa and IP=0, (d) Er = 2.0 MPa and IP=100 kPa

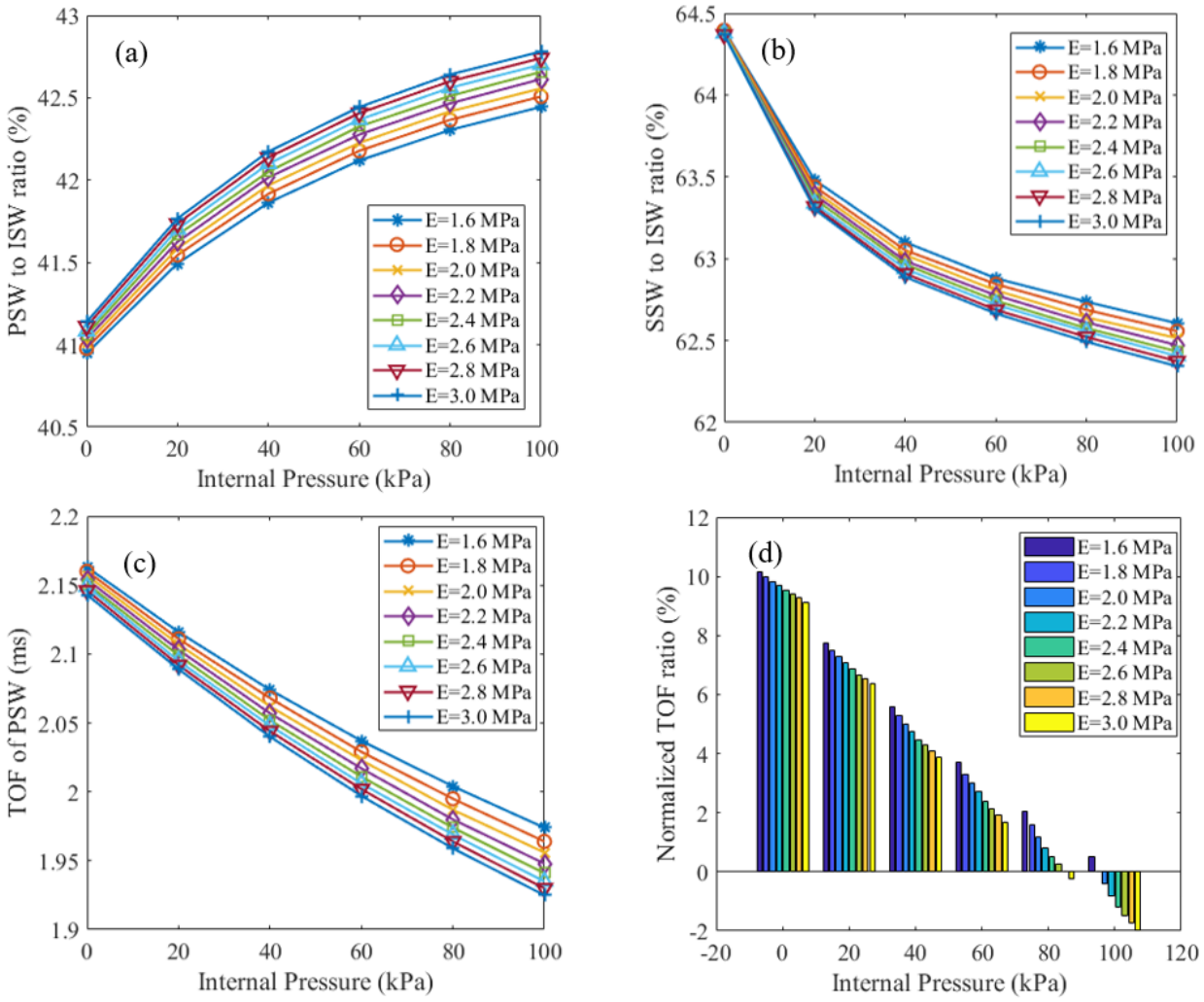

Figure 4-19 Numerical Simulation. Effect of the internal pressure and rubber elastic modulus on some selected features of the solitary waves. (a) Ratio of the amplitude of the primary reflected wave to the amplitude of the incident wave; (b) Ratio of the amplitude of the secondary reflected wave to the amplitude of the incident wave; (d) time-of-flight of the primary reflected wave; (d) value of the time-of-flight normalized with respect to the case of internal pressure equal to 80 kPa and elastic modulus equal to 2.8 MPa.

4.4.3 Experimental Results

Figure 4-20 shows one of the time waveforms measured from specimen #13, which was played on Dec. 12. As the ball aged, the arrival time of the primary and secondary waves changed significantly, and there is a visible difference between the waveforms before and after game day, and before and after it was pierced. Interestingly, the overall shape of the secondary wave changed. The comparison between the numerical (**Figure 4-18**) and the experimental (**Figure 4-20**) waveforms: (1) reveals that the arrival time of the reflected pulses with respect to the incident pulse is very similar; (2) confirms the formation of twin-peaks at the chain-specimen interface; (3) suggests that the model overestimates the amplitude of the secondary waves when compared to the amplitude of the primary reflected wave. In addition, when the specimen was pierced, the secondary wave seemed to be fragmented in multiple pulses. The absence of pressure allows larger deformation of the rubber, giving rise to stronger and fragmented secondary pulses. The latter two issues are worth further investigation and could be the subject of future studies as the model may have not predicted in full the complex dynamical phenomena associated with the formation of the secondary waves. For this reason, the effect of the ball characteristics on the SSW was not elaborated any further in this study.

It is noted here that a direct comparison between the abscissa in **Figure 4-18** and **Figure 4-20** cannot be made as the trigger used for the numerical simulation is different that the trigger used for the experiments.

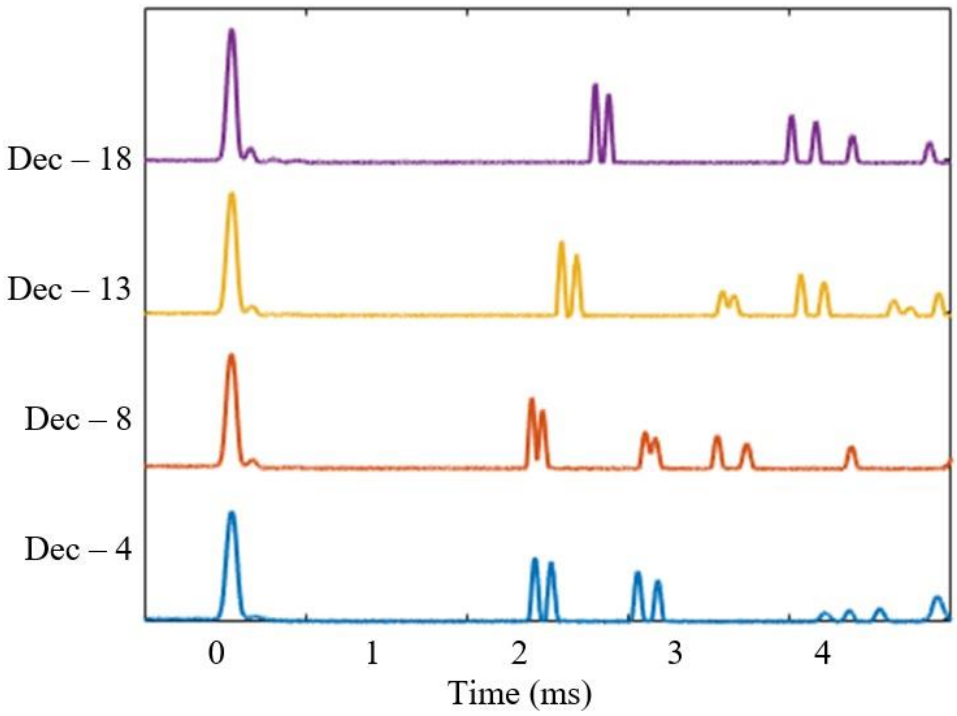

Figure 4-20 Experimental results. Waveforms relative to tennis ball #13 and measured at each day

Similar to what done for the numerical data, some features of the experimental waves were extracted. First, the amplitude of the ISW was analyzed to estimate any day-to-day operational variability of the HNSW transducer. In general, the ISW is not expected to change with respect to the property of the rubber or the internal pressure because this wave is generated by the impact of the striker and does not interact dynamically with the interface between the rubber and the chain. However, in [140, 142] we demonstrated that the amplitude of the ISW is directly proportional to the internal pressure due to a constructive interference between the ISW and a spurious wave generated at the chain/rubber interface at the moment of the impact. When the striker taps the chain, it bounces up decreasing temporarily the overall weight of the metamaterial on the ball. The change of the weight causes a slight deformation of the ball, which in turn, triggers the spurious pulse propagating upward. The stiffer the ball (due to higher internal pressure) the stronger is the

upward pulse. However, it was found in [140, 142] that this effect can be neglected; according to the model, the amplitude of the ISW increases by 0.4% when the internal pressure goes from 0 to 100 kPa. **Figure 4-21(a)** shows the amplitude for all six cans and for all four days of testing. Each bar is the average of the 150 measurements taken, fifty for each ball of the can. Some random fluctuation of the amplitude is visible and is quantified in **Figure 4-21(b)** where the amplitudes are normalized with respect to the largest ISW, which occurred on day 3 (Dec. 13) for can #6. These normalized values are comprised between 0.96 and 1 and demonstrate that the day-to-day variability associated with the HNSW device did not exceed 3.7%. This means that the day-to-day operation variability had a negligible impact on the speed of the incident pulse because the speed is proportional to $F^{1/6}$. The data presented in **Figure 4-21** are, therefore, a solid proof of the repeatability of the transduction mechanism used to probe the tennis balls with the solitary waves.

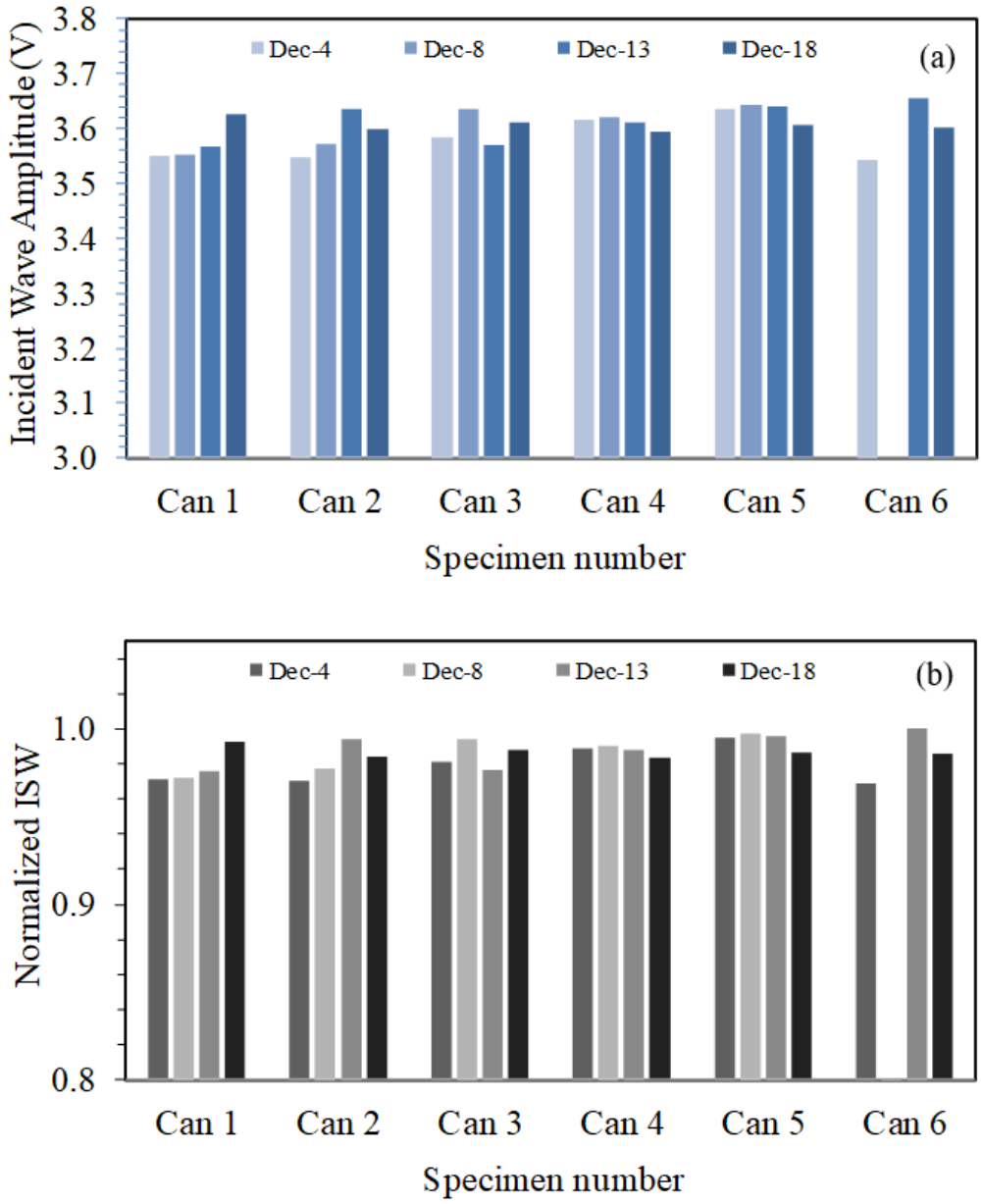

Figure 4-21 Experimental results. (a) Amplitude and (b) normalized amplitude of the incident solitary wave. Each bar represents the average value of the mean of the fifty measurements taken for each ball of the can.

Now that the repeatability was demonstrated, **Figure 4-22** shows the time of flight (**Figure 4-22(a)**) and the normalized time of flight (**Figure 4-22(b)**) of the primary solitary wave. The normalization was computed with respect to the lowest value, recorded for the can #3 during the first day of test. Each bar represents the average of the 150 measurements taken. The average value of the feature measured when the balls were new, and the cans just opened was equal to 1.923 ± 0.012 ms. The fact that the relative error, i.e. the ratio of the standard deviation 0.012 ms to the mean 1.923 ms, was equal to 0.61% shows that the balls could be truly considered identical. The empirical value of 1.923 ms matches remarkably well the numerical value of 1.960 ms predicted numerically for the case of E_r=2.8 MPa and internal pressure equal to 80 kPa. This 2% difference between the numerical and the experimental values is believed to be mainly due to differences in the impact velocity of the striker. Some other relevant remarks can be made from **Figure 4-22(a)**. First, there is a clear difference between the TOF of the pressurized and the pierced balls. With respect to pristine, never used, balls (Can #1) there was an increase of 14%-18%. Second, the game days can be retrieved. For example, the bars relative to can #2 show a clear difference between Dec. 4th and Dec. 8th. According to **Table 4-6**, specimens #4 - #6 were used Dec. 6th. The results relative to cans #3 and #4 demonstrate show that the tennis balls were used twice: once before the 8th and once before the 13th. Finally, there is a visible variation in the time of flight of balls 13-18, i.e. cans #5 and #6, before and after Dec. 13th. A look at **Table 4-6** reveals that these balls were used on Dec. 12th. Among the 18 tennis balls, the only incongruence is the decrease in the arrival time of the can #2 samples between Dec. 8th and 13th; the origin of this slight incongruence is unclear.

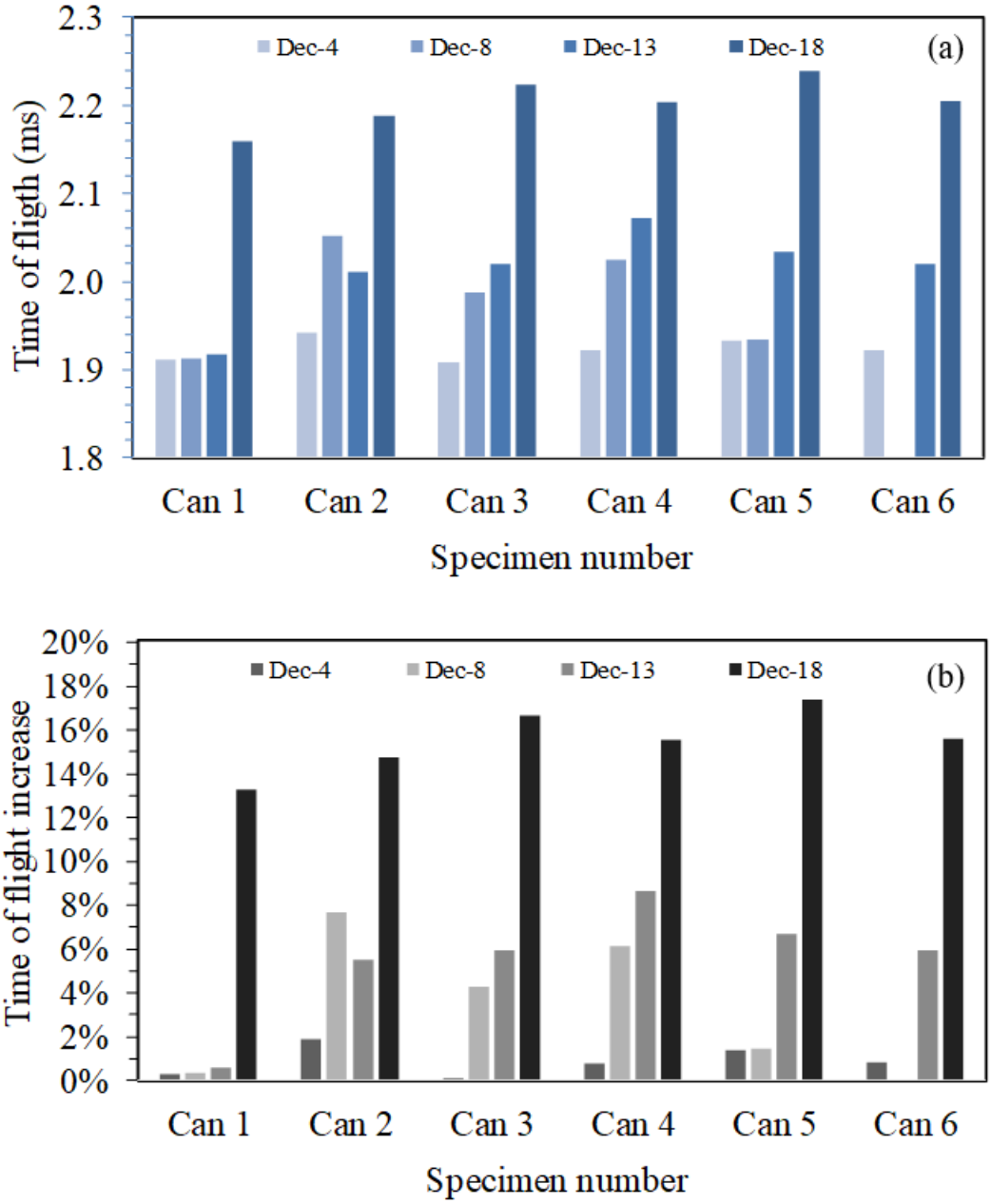

Figure 4-22 Experimental results. (a) Time of flight and (b) time of flight increase of the primary solitary wave. Each bar represents the average value of the mean of the fifty measurements taken for each ball of the can.

To quantify the increase in the travel time of the PSW with respect to the pristine new balls and to compare such increase to the day-to-day operability of the HNSW transducer, **Figure 4-23(b)** displays the increase in percentage with respect to the minimum value of the feature, which was recorded for can #3 measured on Dec. 4^{th}. Between the first and the third day of testing, the feature of the TOF relative to the tennis balls played increased by 2% - 6%. This is aligned with the numerical prediction and will be further elaborated later in this section.

To compare the proposed solitary wave method to the conventional rebound test, **Figure 4-23** shows the COR calculated from Eq. (4.13) and applied to the rebound test data. The absolute and the normalized values of the coefficient are presented in **Figure 4-23(a)** and **Figure 4-23(b)**, respectively. Neither graph helps to determine whether a ball was used to play tennis. The only noticeable variation is between inflated and deflated balls, but this difference is below 10%, which is lower than what observed with the solitary waves. Therefore, it can be concluded that the HNSW-based method is more effective at detecting subdue differences in the dynamical properties of the rubber and more sensitive at measuring differences in the internal pressure.

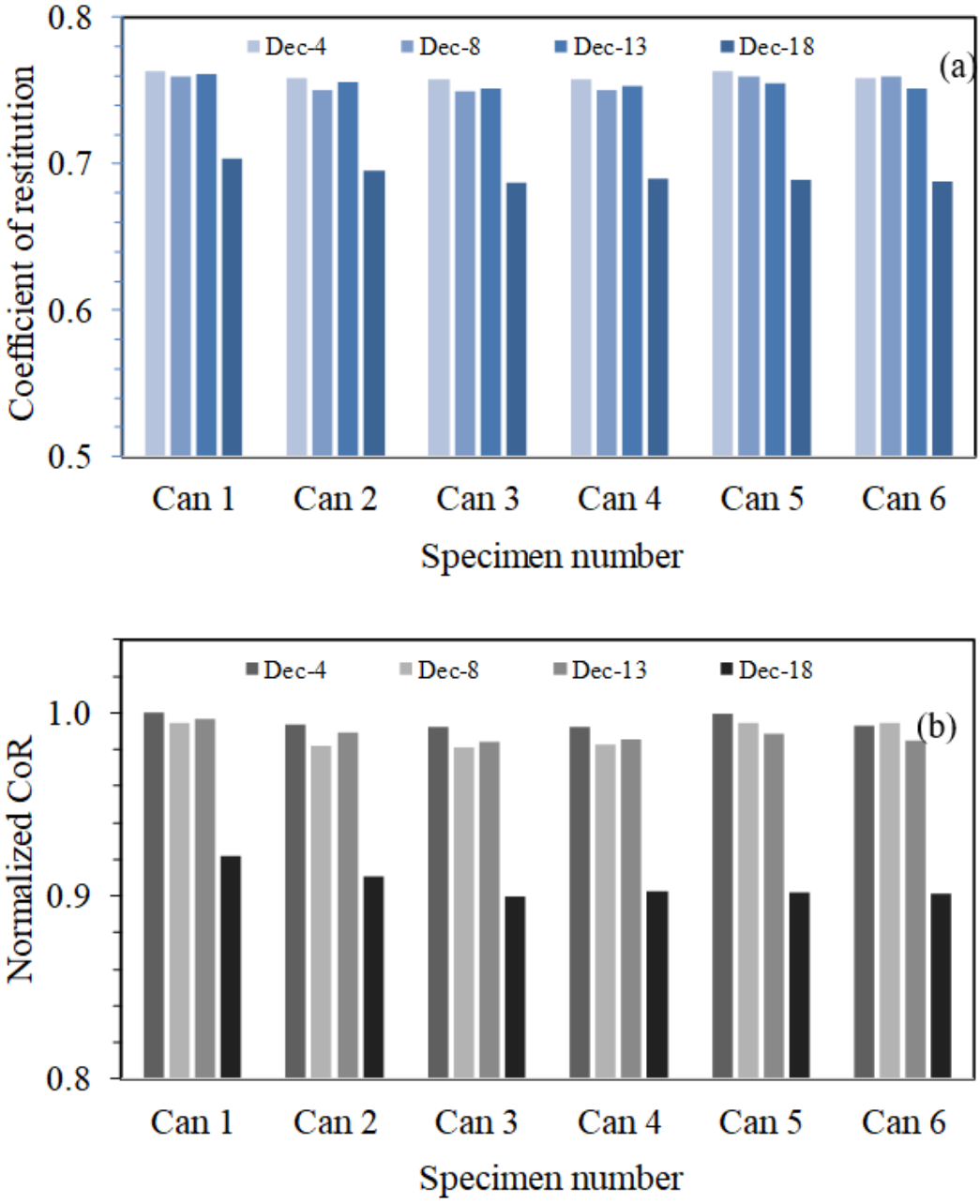

Figure 4-23 Experimental results. (a) Coefficient of restitution and (b) its normalized value measured with a modified rebound test. Each bar represents the average value of the mean of the fifty measurements taken for each ball of the can.

As was said earlier, the tennis balls were pierced with the needle of a pressure gage to measure the remaining pressure. **Figure 4-24(a)** shows the measured pressure for all 18 specimens whereas **Figure 4-24(b)** displays the average value of the three balls for each can. As expected, the balls from can #1 had the highest pressure, for they were never played. The average value of 81.1 kPa is very close to the typical pressure of new balls, namely 82.7 kPa. The specimens with the lowest pressure were #10 - #12, i.e. those belonging to can #4. According to **Table 4-6**, these balls were played twice and therefore this result is also expected. The balls from can #3 were also played twice, but their pressure was closer to the samples played once. Such discrepancy likely depends on the number and the quality of the games played by the players. To quantify the relative change in internal pressure, **Figure 4-24(c)** show the pressure normalized with respect to can #1. The worse balls had a 20% drop in internal pressure, while those played once (can #2, #5, and #6) experienced a pressure drop comprised between 5% and 15%.

To elaborate further on the link between the internal pressure and the HNSW data, **Figure 4-25(a)** presents the TOF recorded on the third day of testing, i.e. a few days before piercing the specimens. The plot demonstrates a direct link between wave features and the measured pressure. As a matter of fact, the highest TOF occurred for can #4, namely the worst balls; conversely, the lowest TOF corresponded to the newest specimens (can #1).

To compare the numerical prediction and the experimental results, **Figure 4-25(b)** shows the increase in TOF with respect to the new balls. The comparison of the two figures suggests that the numerical method underestimated the effects of rubber deterioration and internal pressure. As a matter of fact, the experimental increase of the wave features is larger than predicted numerically. This is likely due to the absence of dissipation in the model and to the fact that the model assumes point-wise contact between the steel bead and the rubber ball.

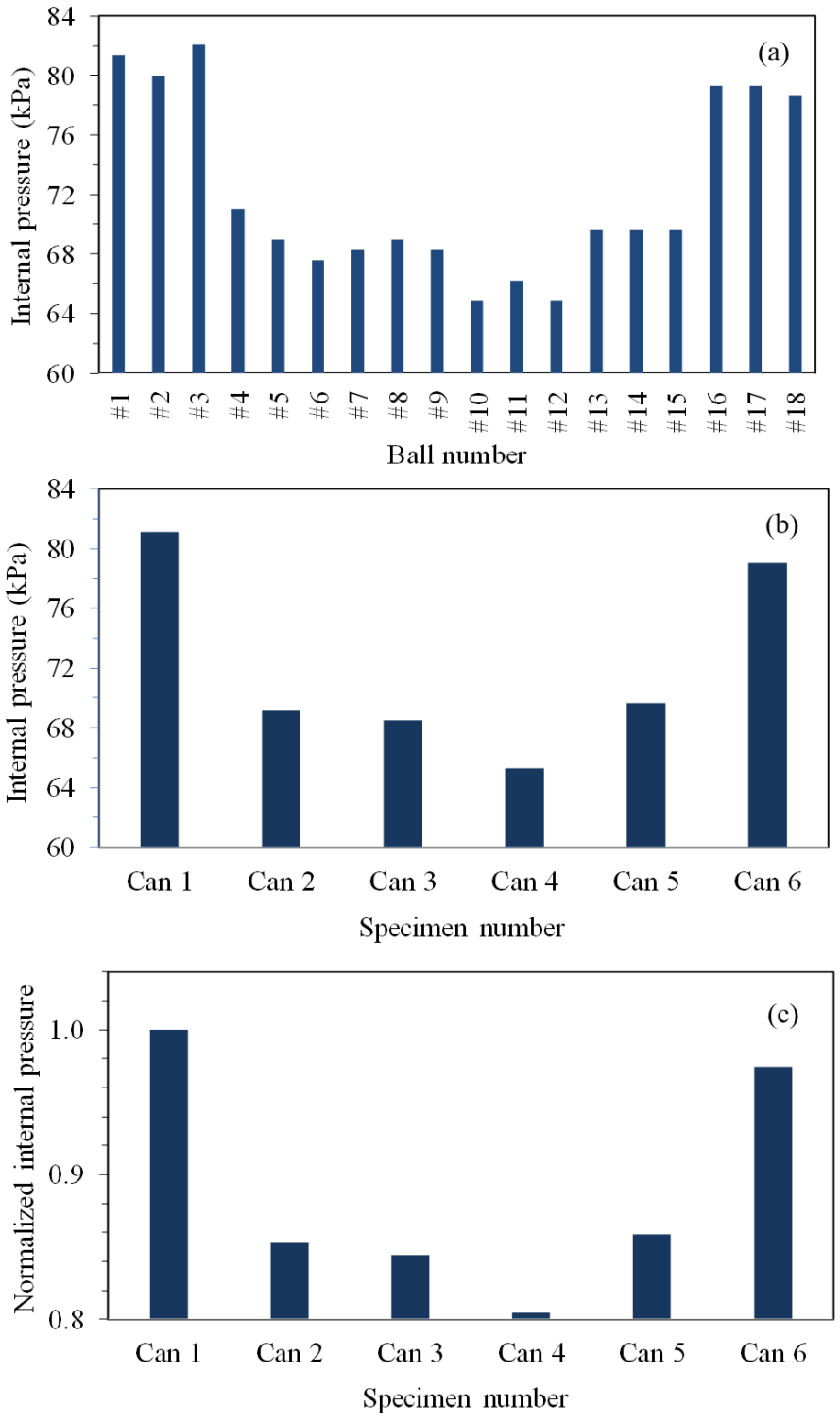

Figure 4-24 Experimental results. (a) Internal pressure of the 18 tennis balls, (b) internal pressure of the balls clustered according to their cans, (c) normalized internal pressure. The pressure was measured invasively with a pressure gauge by piercing the 18 specimens

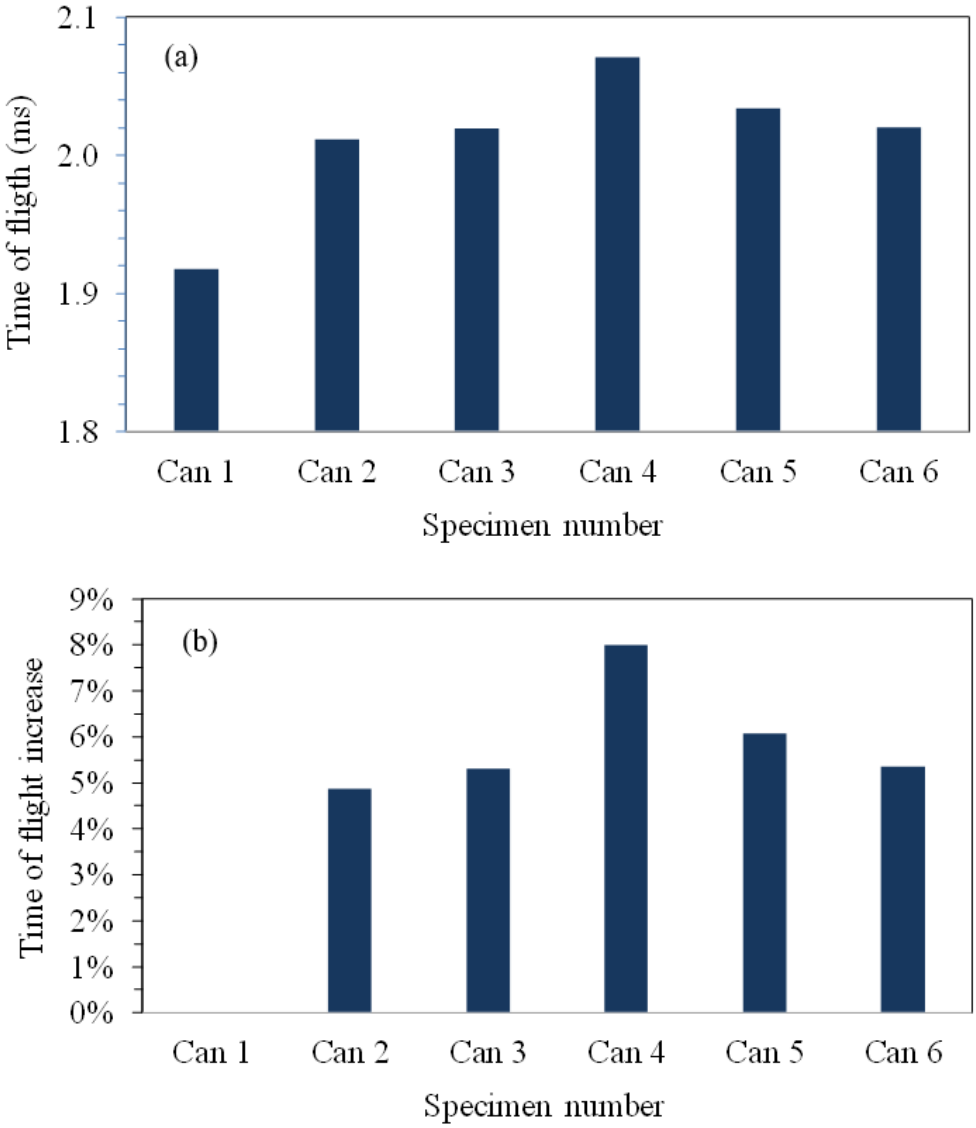

Figure 4-25 Experimental results. (a) Time of flight measured before piercing the ball and (b) increase of the same time of flight with respect to can #1, i.e. the balls that were never used.

4.4.4 Conclusions

This article investigated numerically and experimentally the effects of internal pressure and rubber degradation on the interaction of between highly nonlinear solitary waves propagating along 1-dimensional chains of spherical particles and tennis balls placed in contact with one end of the chain. The scope of the study was the formulation of a new nondestructive method to assess the serviceability and the conformity of tennis balls to the guidelines set by the International Tennis Federation. On a much broader perspective, the objective of the study was the exploration of a new method to assess the elastic properties of rubber material for any engineering application or commodity in which rubber is used. It was found that the travel time of the waves reflected at the interface between the last particle of the chain and the rubber is affected mainly by the internal pressure of the ball and partially by the modulus. These dependencies were quantified numerically by implementing a finite element model in which the internal pressure and the elastic modulus of the rubber are the variables. The model was validated by testing 18 tennis balls from the same brand and type and aging was induced by asking amateur players to use the balls on a concrete court. Overall, the experimental results demonstrated that the nondestructive evaluation method is capable of determining whether or not any given ball was used, observing changes in balls characteristics, and of inferring pressure loss. The results also demonstrated that the method based on the highly nonlinear solitary waves is better than a conventional rebound test typically used to determine the bouncing height of balls.

In this study, the effect of the felt was ignored in the numerical model as its stiffness is negligible compared to the rubber core. Moreover, it was found that the stiffness of the felt is a function of loading direction and loading rate [148, 149]. Therefore, any model and mechanical characteristics of the felt could be unrealistic in the numerical model. However, because the

purpose of felt is to reduce the speed of the ball on hard courts, the felt adds damping to the system in reality, which was also ignored in this study. This might be the reason that the amplitude of the solitary wave pulses are smaller in the experiments compared to the numerical simulation. Future studies may take into the account the damping characteristics of the felt.

4.5 Characterization

To have their tennis balls approved, manufacturers are required to send some samples to an ITF Technical Center. Here, the samples are subjected to the following sequence of tests: pre-testing, mass and size measurement, deformation, rebound, and durability. To begin with, the balls are acclimatized for 24 hours in a climate-controlled laboratory at a temperature of 20 ± 2 °C and relative humidity of 60 ± 5%. Each ball is then pre-compressed to remove any "set", which is a property that occurs in some materials when they are not subjected to varying forces. This pre-compression is performed with a machine that deforms each ball by 2.54 cm (1 in.) three times along three perpendicular directions using pneumatic actuators [150]. After these pre-testing, the mass and size of the balls are measured.

The compression test measures the deformation of the ball under a known load. The specimen is compressed between two plates: after a small initial load of 15.6 N (3.5 lbf), the forward deformation is measured when the applied compressive force is equal to 80.07 N (18 lbf); then, the ball is compressed further until its initial diameter decreases by 25.4 mm (1 in.); finally, the compression is reduced back to 80.07 N (18 lbf) at which the deformation is measured again and is usually referred to as the return deformation.

The next test is the rebound test in which the sample is dropped vertically from a height of 2.54 m (100 in.) onto a calibrated surface and the rebound is measured. According to [150], a vacuum pipe holds the specimen at the correct height before being released on a smooth granite block onto which the ball bounces. A video camera and a light source are used to measure the bouncing height from the shadow of the ball that is cast against a scale.

The last experiment evaluates the durability of the samples. Introduced in the 2009, the durability measures the changes in mass, size, deformation and rebound of six balls after standardized wearing regime in which laboratory equipment simulates the effects of nine games.

4.5.1 Experimental Setup

Three balls of four kinds, i.e. twelve specimens total, were subjected to the rebound test, the quasi-static loading, and the HNSWs measurements. The balls were Penn Championship Extra-Duty (PED), Penn Championship Regular-Duty (PRD), Gamma Quick Kids 60 (G60), and Gamma Quick Kids 78 (G78). The Penn Championships belong to the ITF Type 2 category [150]. The "regular-duty" are designed for clay courts as they have less felt cover in order to pick-up less clay. The "extra-duty" are manufactured with denser fabric to allow for longer usage on hard and grass courts. Gamma Quick Kids 60 are ITF Stage 2 [150] category balls. According to the information publicly available, these low compression balls are designed for use on 60-foot courts and they bounce 50% slower than standard tennis balls. Their medium bounce allows more time to react and set up each shot for more consistency and control when learning. Finally, the Gamma Quick Kids 78 balls are designed to be used in regular (78 feet) courts and according to the manufacturer they are 25% slower than a standard tennis ball. Gamma Quick Kids 78 balls are ITF Stage 1 Type [150].

The specimens were probed first with the HNSW-based NDE method, and then subjected to the rebound and the compression tests. For each set of balls, the experiments lasted less than a week to minimize any effects associated with the loss of internal pressure due to the permeability of the rubber. At the end of this first round of experiments, the specimens were pierced with a hollow needle connected to a pressure gauge to measure the remaining internal pressure. Then, a second round of experiments were conducted to evaluate the differences between pristine and damaged conditions. To quantify the repeatability of the setup, fifty measurements were taken for each specimen.

During the rebound test, each ball was dropped vertically from a height of h_0=2.54 m (100 in.) on a polished concrete floor. Polished concrete can be considered equivalent to a smooth granite block because the surface is equally rigid, i.e. it will not deform when hit by the falling ball. A few cm from the impact, a microphone connected to an oscilloscope was placed on the floor to record the sound made by the first two collisions of the ball onto the concrete. The time $2\Delta t$ between these collisions was used to determine the rebound height h_1 of the ball using Eq. (4.13).

For the compression test, each specimen was placed between two plates and the load versus displacement was measured continuously. A WYKEHAM FARRANCE compression machine with the capacity of 50 kN was used to perform the test according to the ITS guidelines [150]. First, an 80.07 N (18 lb) load was applied and the "forward deformation" was recorded. Compression was applied further until the initial diameter decreased by 25.4 mm (1 in.), after which the compressive force was relieved, and deformation continued to be measured until the load on the ball is again 80.07 N (18 lb). At this point the "return deformation" was recorded. For each ball, the experiment was performed along three perpendicular axis as recommended by the ITF standard [150].

4.5.2 Experimental Results

Figure 4-26(a) shows the typical sound recorded by the microphone during the rebound experiments. From this graph and Eqs. (4.12) and (4.13) the CoR was computed and the results are presented in **Figure 4-26(b)**. The average value from the six drops of the CoR is shown for all 12 specimens at both conditions, new and damaged, along with the corresponding 2σ intervals. The coefficient of the new extra-duty and regular-duty balls decreased from ~0.76 to ~0.71 after piercing. As the balls were deflated, the rebound height and therefore the CoR decreased. While the coefficient decreases about 6%, the variation observed of the solitary wave feature was about 12%. This suggests that the proposed NDE approach is more sensitive than the CoR to the variation of the internal pressure, and therefore, stiffness.

As for the G-balls, their CoR slightly increased 2.8% to 7.2% after piercing. This behavior is somehow unexpected for the G78 as they are considered pressureless, and therefore no difference was expected prior and after the piercing. Part of this variation could be attributed to the variability of the measurements as the coefficient of variation of the rebound tests for the G-balls spanned from 1.17% to 8.32%. Another hypothesis is that the intrusive compression test may have permanently altered the microstructure of the rubber. It is worth noting that the CoR of specimen #2 of the G78 family diverges clearly from the other five G-balls. This is consistent with the outcomes of the solitary wave measurements and it may be attributed to differences of the final product.

Figure 4-27 presents the load versus displacement plot relative to the three PRD balls. The curves show the typical load-deformation response of tennis balls as for example discussed in [151]. The stiffness of the ball increases as the deformation increases, due to the combined effects

of the hyperelastic behavior of the rubber, geometry of the ball, and increase in the internal pressure according to the ideal gas law. The difference between the loading and the unloading curves (hysteresis behavior) denotes energy loss during strain recovery [148]. To align the analysis to the ITF standards, the deformation at 80 N (18 lbf) during the forward and return compression was recorded as shown in **Figure 4-27**. It is noted here that the final instant of the loading ramp does not coincide with a displacement equal to 2.54 cm (1 in.) due to some constraint in the loading machine, which however, did not affect the quality of the experimental findings and the validation of the research hypotheses.

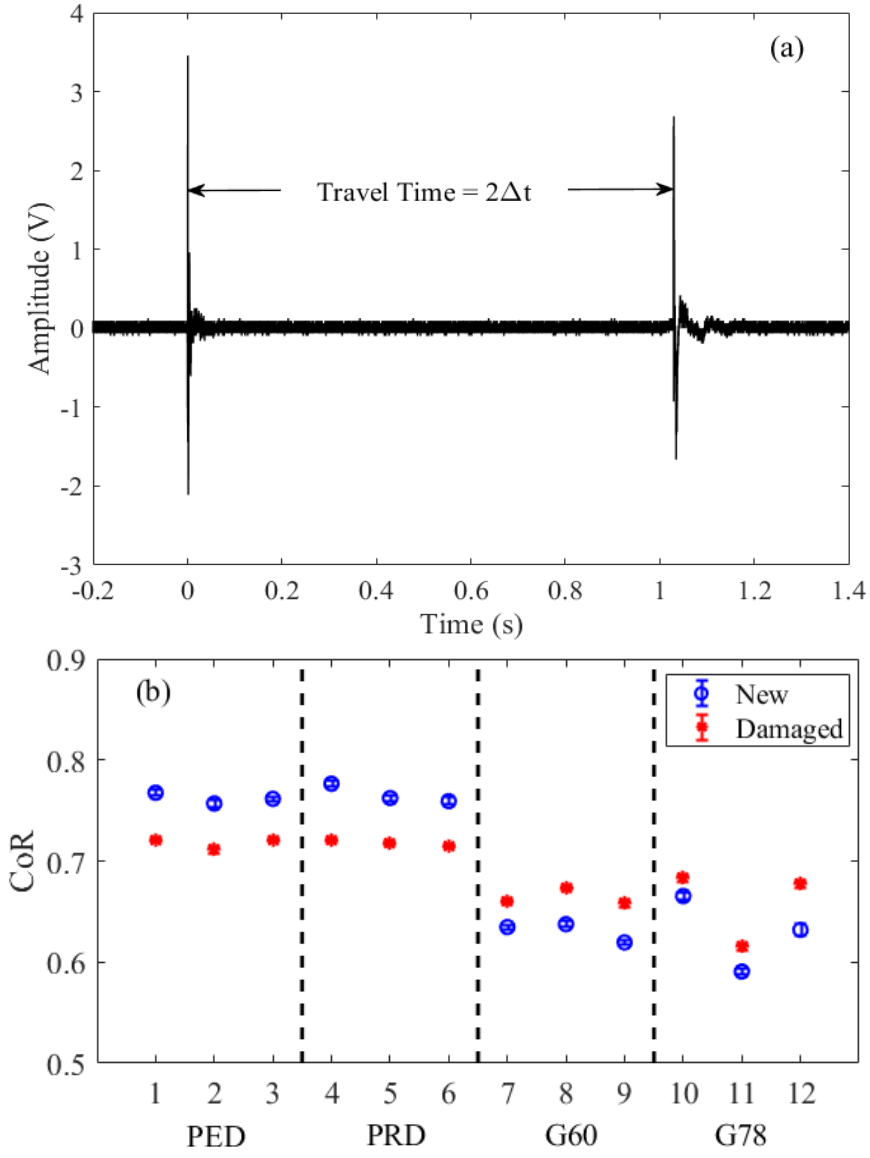

Figure 4-26 Rebound test. (a) Sound recorded when sample damaged PRD was tested. (b) Coefficient of restitution measured for all twelve specimens under new and damaged conditions

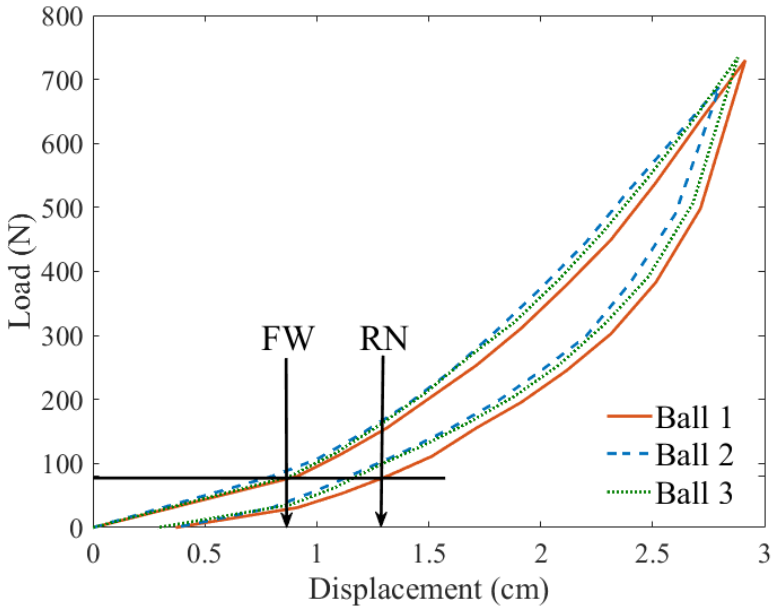

Figure 4-27 Compression test. Load vs deformation measured for PRD specimens. FW and RN identify the forward and the return deformation, respectively

The results are presented in **Figure 4-28(a)** for the forward deformation and **Figure 4-28(b)** for the return deformation. By looking at **Figure 4-28(a)**, the Penn specimens fell in the range 0.63-0.72 cm, well within the range accepted by the ITF for Type 2 (see **Table 4-5**). As expected, the return deformation was larger and comprised between 0.97 cm and 1.05 cm, also in agreement with the existing standard. After piercing, all the specimens increased the forward deformation by 15-30% and the return deformation by 36-100%. Overall, these results demonstrate that the internal pressure plays an important role in the deformation of the Type 2 balls. Owing to the role of the internal pressure, the results relative to the G-balls came as no surprise. In fact, the forward and the return displacements did not change with the damage, with the exception, again, of the G78 specimen #2. The difference in values across the same kind of ball is therefore attributable to the property of the rubber. As was said before, the G78 balls are about 20% thicker than the G60

and therefore stiffer. As such, their deformation was expected to be smaller. **Figure 4-28** confirms that the specimen #2 of the G78 family differs from the other two balls: its forward displacement changed by 2.91% while the other five balls varied between -2.50% and +1.00%; its return deformation increased by 9.44% while the other five varied between -0.09% and +3.56%. As such, the compression test confirms what predicted with the solitary wave measurements and observed with the rebound test.

4.5.3 Discussion and Conclusions

To ease the comparison between the CoR and the TOF and investigate a possible correlation, **Figure 4-29(a)** presents the feature of the PSW as a function of the CoR for all 24 cases considered in this study. For completeness, the horizontal and the vertical bars relative to the 2σ intervals are presented with the average values. Two clusters are clearly visible for the Type 2 balls. One cluster refers to the new condition whereas the other cluster identifies the damaged specimens. The new balls populate the bottom right portion of the diagram, where the CoR is closer to 1, i.e. good bouncing characteristics, and the TOF is small as the energy of the acoustic incident wave is immediately reflected at the chain-rubber interface. The main difference between the pressureless and the pressurized balls is that the latter display a significant variation between pristine and damaged conditions, whereas the G-balls do not form any cluster.

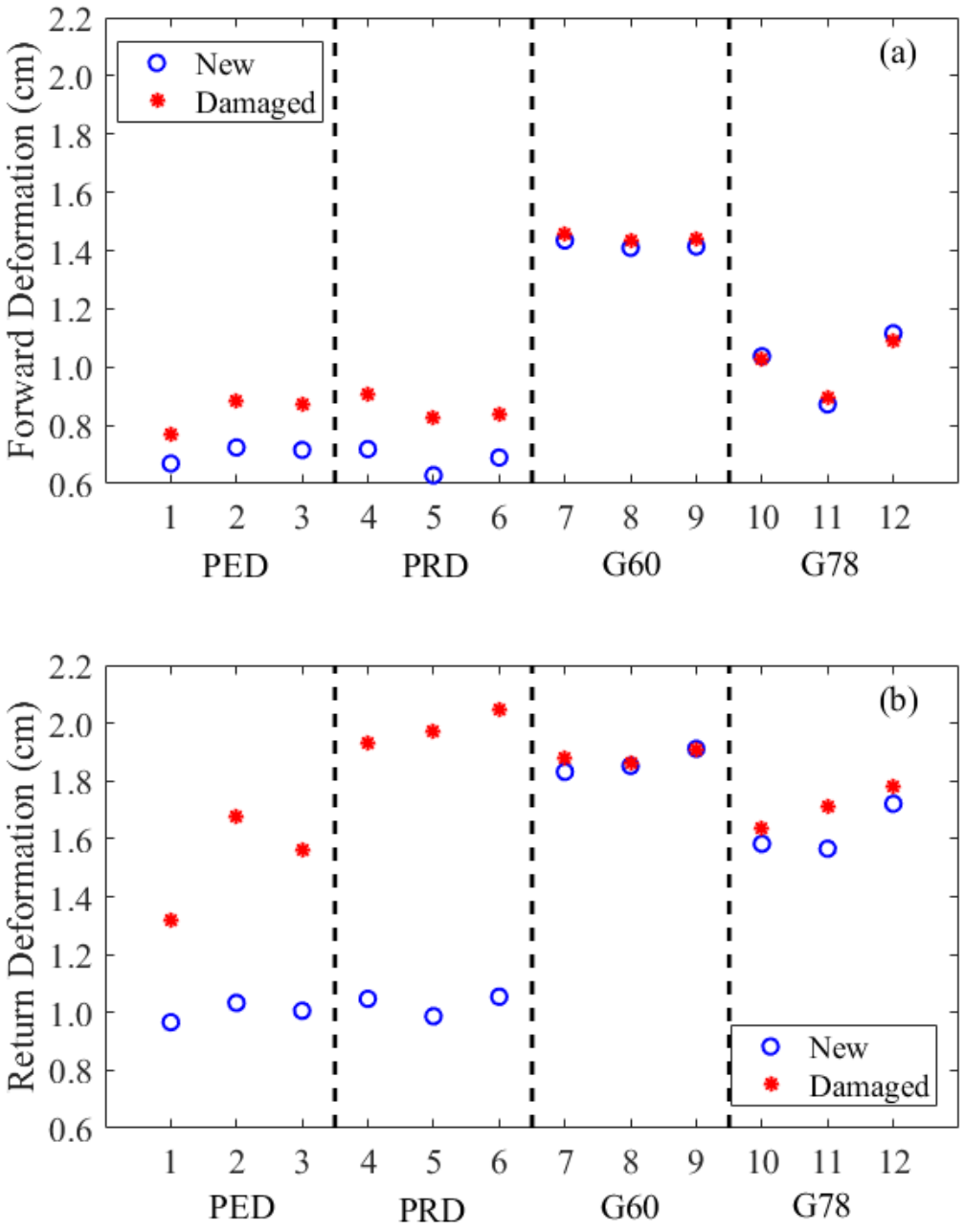

Figure 4-28 Compressive test. (a) Forward Deformation for all twelve specimens under new and damaged conditions. (b) Return Deformation for all twelve specimens under new and damaged conditions.

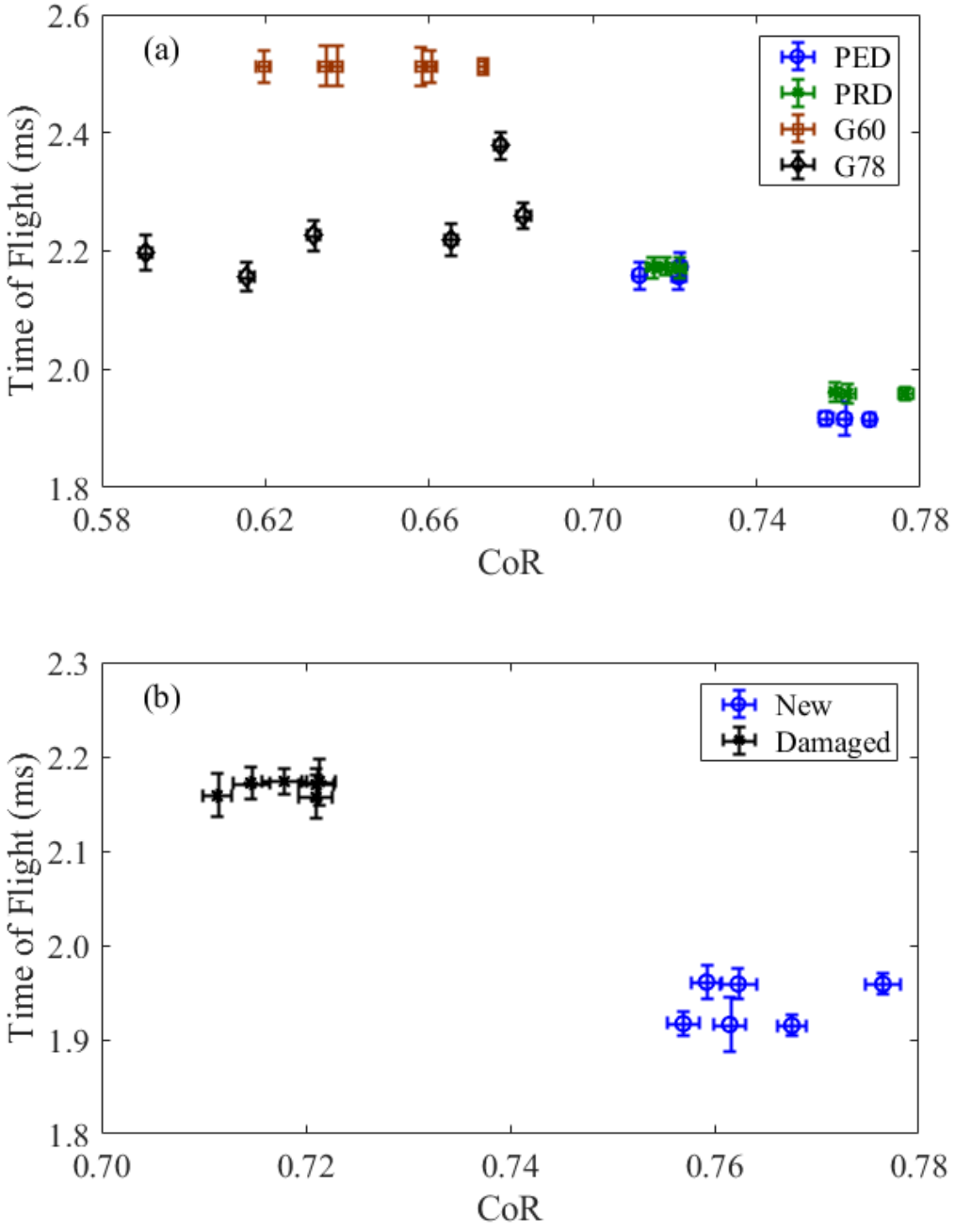

Figure 4-29 Empirical time of flight as a function of the coefficient of restitution. (a) Values of all twelve specimens under new and damaged conditions. (b) Linear relationship visible for Type 2 balls

To identify a possible relationship between pristine and damaged condition, **Figure 4-29(b)** displays the TOF as a function of the CoR for the Penn balls. A linear interpolation and the corresponding R^2 are overlapped to the experimental data, and the outcome is that the Penn specimens display a high correlation between the CoR and the TOF. Not shown here, the same procedure was applied to the G-balls; however, no significant correlation was found. This is consistent with the fact that the properties of the G-balls are expected to remain constant even with a small hole in the rubber. It is acknowledged here that such linear relationship is based on a small number of test samples. To corroborate this assumption, more samples with "intermediate" properties should be considered in the future, i.e. samples that are for instance aged but not pierced.

Similar to **Figure 4-29(a)**, **Figure 4-30** compares the TOF data to the static deformation by presenting the feature (TOF) of the solitary wave as a function of the forward deformation (**Figure 4-30(a)**) and the return deformation (**Figure 4-30(b)**). Overall, the empirical results seem to suggest that the two parameters are directly proportional to each other at least for the forward deformation. In fact, the stiffest balls populate the lower-left corner of the graph. No definite conclusions can be drawn yet for the return deformation.

It is emphasized here that the use of a chain of particles is necessary to support the propagation of the highly nonlinear solitary waves. The use of a solid rod of same diameter and length of the chain would support the propagation of liner guided waves instead. The physics associated with their propagation is such that only one pulse would be reflected at the rod-ball interface and the speed and amplitude of this reflected pulse would not be affected by the variation of the pressure inside the ball. As a matter of fact, the speed of the wave depends exclusively on the mechanical property of the rod, whereas the wave amplitude would depend on the acoustic mismatch between the rod and the rubber.

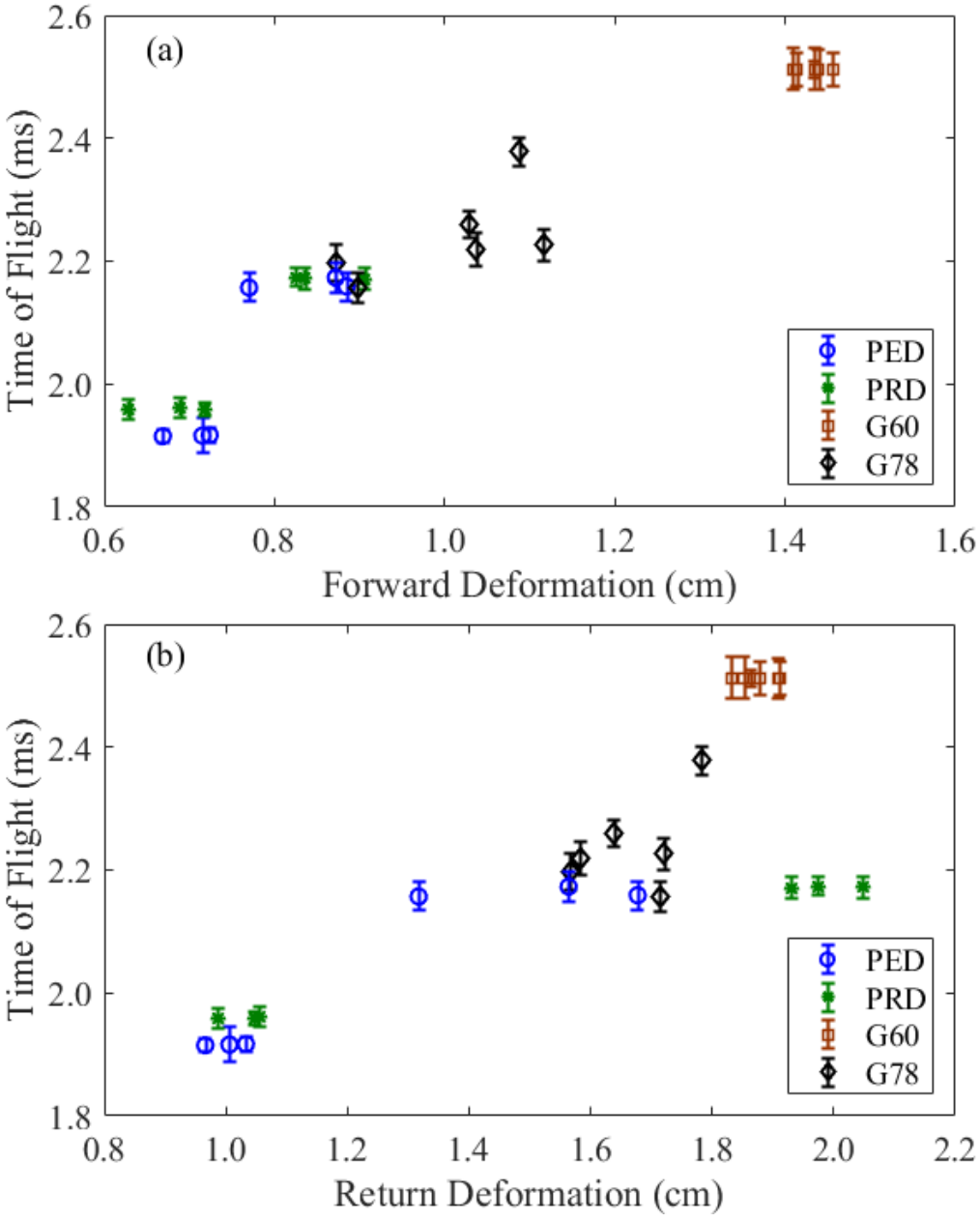

Figure 4-30 Empirical time of flight as a function of (a) the forward deformation and (b) the return deformation. To ease comparison, the vertical scale of both plots is identical

5.0 Determination of Axial Stress

This chapter is based on the study on the axial stress determination of thermally and mechanically stressed thick beams in press at the *Journal of Acoustical Society of America* [152] and numerical and experimental study of the interaction of HNSWs with rails under review at the *Journal of Sound and Vibration* [153].

5.1 Introduction

Columns, cables, and rails are common engineering structures subjected to axial load. Some of these structures, such as continuous welded rails (CWRs), experience tension-compression cyclic stress. When anchored, a CWR is pre-tensioned such that the rail neutral temperature (RNT) T_N, i.e. the temperature at which the net longitudinal force is zero, is between 32°C and 43°C. The pre-tension counteracts thermal expansion and cannot be too high because the rail may break in the cold season. However, over time the neutral temperature decreases due to many reasons and becomes unknown. With lower RNT, the risk of extreme compression in the warm season increases leading to rail buckling, a structural problem that occurs when the temperature T_R of the steel reaches the steel Euler temperature T_E, which is related to the Euler stress σ_{cr} with the formula:

$$\frac{\sigma_{cr}}{E\alpha} + T_N = T_{cr} \tag{5.1}$$

In Eq. (5.1), E and α indicate the elastic modulus and the coefficient of thermal expansion of the rail steel, respectively. As σ_{cr}, E, and α are typically known, buckling may be prevented by

estimating the temperature T_{cr} at which the rail will buckle. This would be possible by using a reliable nondestructive methodology able to measure T_N. Alternatively, T_N can be inferred by measuring non-invasively the rail stress at any temperature and then applying the equivalent of Eq. (5.1).

The current non-invasive methodologies have one or more limitations that prevent their widespread use. Perhaps the most important technology is the one commercialized under the name of VERSE® [154]. It is based on the beam-column bending theory that establishes that the axial load P affects the vertical force Q required to lift a rail by a certain amount Δ according to [154, 155]:

$$\Delta \approx \left(\frac{\lambda Q L^3}{EI}\right)\left(\frac{1}{1 - P/P_{cr}}\right) \tag{5.2}$$

In Eq. (5.2), λ is a constant that depends on the constraints, L is the length of an unfastened rail, EI is the flexural stiffness, and P_{cr} is the buckling load. From Eq. (5.2), the RNT is computed as:

$$T_N = T_R - \frac{P}{\alpha A} = T_R - \frac{P_{cr}}{\alpha A}\left(1 - \frac{1}{\delta}\frac{\lambda Q L^3}{EI}\right) \tag{5.3}$$

To the authors' knowledge, the method requires track closure and about 30 meters of rail must be unanchored from the fasteners, and a support spacer needs to be placed 10 meters away from the mid-span. Then, the vertical force Q necessary to lift the center of the detached rail by the fixed amount Δ is measured; alternatively, the displacement Δ induced by a lift force of 10 kN is measured. Another technology consists of a wayside installation system attached to the rail web to quantify the rate of decay of the RNT. The system is based on strain gages and is part of a rail safety monitoring solution, called IRIS (Intelligent Rail Integrity System), consisting of a network of remote sensors that monitor rail temperature and rail condition. Each sensor unit is attached to

the CWR to be monitored and continually tracks the changes of the rail temperature. Each unit contains welded strain gage to collect longitudinal strain data. Another method is based on the Magnetic Barkhausen Noise (MBN) that exploits the Barkhausen effect, i.e. the noise in the magnetic output of a ferromagnetic material when the magnetizing force applied to it is changed. When a rail is subjected to longitudinal stress, its magnetic permeability changes. Tension leads to an increase of the permeability and vice versa. MBN provides a quantitative evaluation of the permeability and therefore an indirect assessment of the stress [156].

Other methods show promise but have not been translated yet into commercial systems. For example, the electromechanical impedance technique exploits the relationship between the electrical impedance of a PZT and the mechanical impedance of the host structure to which the PZT is bonded. The method was tested in laboratory [157, 158] on a thick straight beam. The ultrasonic birefringence method uses, instead, linearly polarized shear waves propagating along two perpendicular directions. The difference in the time-of-flight of these two beams depends upon the stress and the residual stress on the material [159, 160]. The approach requires extremely accurate measurements. Another method is based on the nonlinear parameter associated with the higher harmonics of ultrasonic guided waves propagating along the rail web. Laboratory and field tests showed the feasibility of the method at determining the RNT [59, 60, 161].

This study consisted of three major steps. First, an accurate finite element formulation was implemented in MATLAB® and coupled to a discrete particle model to predict the dynamic interaction between the chain and a thick beam. A two-node beam element was used and the effect of the axial load due to temperature gradient was included in the geometric stiffness matrix of the beam elements. The chain-beam dynamic interaction was modeled and analyzed by coupling the differential equation of motion of the beam, and the Newton's second law applied to the beads. In

the second step, four identical transducers were assembled. In this study, the term transducer identifies a device able to trigger, sustain, and sense HNSWs. Each transducer was connected to a data acquisition system to control the repetition rate of the ISW and to digitize the sensed signals for post-processing analysis. The transducers were tested against a stress-free rail segment to quantify any variability of the wave features due to manufacturing and assemble. The last step consisted of two rounds of experiments to validate the numerical models. In the first round, a thick beam was mechanically loaded through three tension-compression cycles. In the second round, the same beam was pre-tensioned, held fixed in displacement control, and then heated with a thermal tape to mimic thermal stress in rails. The size of the beam was selected to have buckling temperature and buckling length commonly found in CWRs [160, 162-166]. Three different pre-tensions, namely 5%, 15%, and 25% of the steel yielding stress were chosen to mimic different neutral temperatures. In both rounds of experiments, one of the four transducers were used and placed in contact with the mid-span of the beam. The solitary waves were recorded at regular intervals and charted against the axial stress.

With respect to [13-15, 61], the novelty of the study presented in this dissertation is multi-fold: first, a more accurate and generalized formulation of the interplay between the acoustic phenomena associated with the propagation of the wave and the dynamic of the thermally-stressed beam is presented. In fact, the FEM provides a general framework that can be expanded to include curved beams and 3D simulations as well. Second, the discrete particle model used to describe the propagation of waves along a curved chain takes into account the effect of gravity. This was not done in [19] where the effect of curved chain on the propagation of waves was studied systematically and for the first time. Another novelty of this paper is the test of a thick beam which is a geometry closely related to real structural elements, including rails. Fourth, the test of four

transducers enabled the analysis of potential differences associated with manufacturing issues. This allows framing advantages and limitations of the proposed NDE method at inferring axial load in structures. To the best of the authors' knowledge, none of the existing studies considered the variability of the HNSW-based NDE method associated with the assembly of different transducers, regardless of the engineering application to be considered.

5.2 Modeling and Rail Equivalency

Several structural engineering models have been proposed to describe accurately the buckling of thermally stressed CWRs. The early studies replaced the railroad track with an "equivalent" single beam of finite length and analyzed the beam structure using analytic or finite element models [163, 167, 168]. Later studies proposed to replace the track structures with two parallel beams of finite length connected by linear springs located at the nodes of the finite element mesh. The springs account for the ballast and the cross-ties [166, 169-171]. For both single and double beam models, the ends of the "equivalent" beam(s) were considered as fixed supports. Another study replaced the real tracks with finite single or parallel beams at which an infinite support was considered [165].

Within these frameworks, the finite element analysis available in literature can be clustered in two groups: quasi-static and dynamic. For both analyses, the buckling was imposed by adding an initial imperfection at the beam midspan extending across a finite portion of the beam. Typically, the imperfection consists of a small lateral displacement as shown in **Figure 5-1**. One of the first quasi-static analyses was proposed by Kerr using a single equivalent beam and ignoring the influence of ballast [163]. The hypothesis was that the beam would buckle at temperature typically

observed in the field, and the analyses estimated the length and the mode of the rail at buckling. However, this approach seems to overestimate the length of the rail segments typically observed in the field. A dynamic analysis was carried instead by Kish and Samavaden who were among the first to include the lateral resistance provided by the crossties and the ballast, the dynamic load of vehicles, and imposed an initial imperfection on a 4.9 m-long single beam [172, 173]. These studies set the ground for the rail buckling safety criterion in used nowadays. Lim et al. [166] presented a 3-D finite element model FEM of CWRs replaced by a single beam with lateral springs to take into account the ballast and the ties. With respect to previous work, the cross-sectional area and the moment of inertia of the "equivalent" beam was as twice as the cross-sectional area and the moment of inertia of rail profile [166]. Two kinds of boundary conditions were analyzed for the end supports: hinged and linear springs. To improve the model, they later replaced the end boundary conditions with an infinite boundary condition using two bar elements with specific area, moment of inertia, and coefficient of thermal expansion. Furthermore, an imperfection with a half-sine shape was imposed to the beam [165].

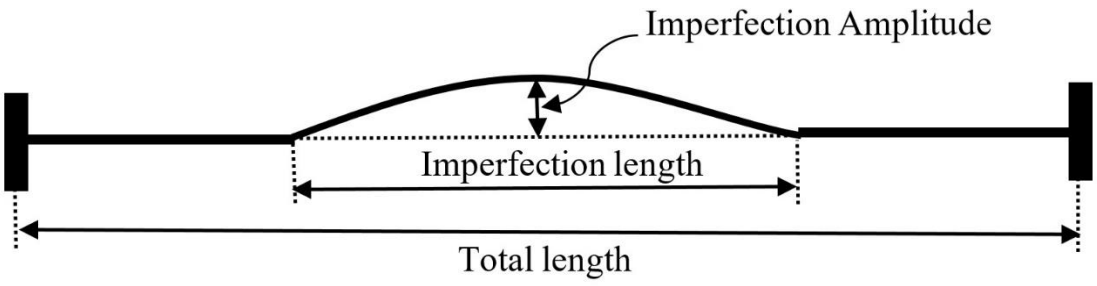

Figure 5-1 Schematic of a rail model where a CWR is replaced with a simple fixed-fixed beam with initial imperfection

A two-node beam element with two translational (r and s) and one rotational (t) degree of freedom at each node was considered (**Figure 5-2(a)**). This finite element model only requires the elastic modulus, geometric parameters including the length, area, and moment of inertia, and the axial stress of the beam structure (which can be the rail). The displacement vector of the element was therefore $\boldsymbol{u} = [r_1\ s_1\ t_1\ r_2\ s_2\ t_2]^T$, whereas the local elastic stiffness matrix was [174]:

$$\boldsymbol{K_E} = \begin{bmatrix} \frac{EA}{l_e} & 0 & 0 & -\frac{EA}{l_e} & 0 & 0 \\ 0 & \frac{12EI}{l_e^3} & \frac{6EI}{l^2} & 0 & -\frac{12EI}{l_e^3} & \frac{6EI}{l_e^2} \\ 0 & \frac{6EI}{l_e^2} & \frac{4EI}{l_e} & 0 & -\frac{6EI}{l_e^2} & \frac{2EI}{l_e} \\ -\frac{EA}{l_e} & 0 & 0 & \frac{EA}{l_e} & 0 & 0 \\ 0 & -\frac{12EI}{l_e^3} & -\frac{6EI}{l_e^2} & 0 & \frac{12EI}{l_e^3} & -\frac{6EI}{l_e^2} \\ 0 & \frac{6EI}{l_e^2} & \frac{2EI}{l_e} & 0 & -\frac{6EI}{l_e^2} & \frac{4EI}{l_e} \end{bmatrix} \tag{5.4}$$

where l_e represents the length of the element. In presence of axial stress σ, the geometric stiffness matrix $\boldsymbol{K_G}$ of the element became [174]:

$$\boldsymbol{K_G} = \frac{\sigma \cdot A}{l_e} \begin{bmatrix} 0 & 0 & 0 & 0 & 0 & 0 \\ 0 & \frac{6}{5} & \frac{l_e}{10} & 0 & -\frac{6}{5} & \frac{l_e}{10} \\ 0 & \frac{l_e}{10} & \frac{2l_e^2}{15} & 0 & -\frac{l_e}{10} & -\frac{l_e^2}{30} \\ 0 & 0 & 0 & 0 & 0 & 0 \\ 0 & -\frac{6}{5} & -\frac{l_e}{10} & 0 & \frac{6}{5} & -\frac{l_e}{10} \\ 0 & \frac{l_e}{10} & -\frac{l_e^2}{30} & 0 & -\frac{l_e}{10} & \frac{2l_e^2}{15} \end{bmatrix} \tag{5.5}$$

Here, σ is negative when the element is under compression. The stiffness matrix $\boldsymbol{K}$ of the element is the sum of the elastic and the geometric stiffness matrices, i.e [174]:

$$\boldsymbol{K} = \boldsymbol{K_E} + \boldsymbol{K_G} \tag{5.6}$$

The local compatibility mass matrix of the beam element is instead [174, 175]:

$$\boldsymbol{M} = \rho \cdot A \cdot l_e \begin{bmatrix} \frac{1}{3} & 0 & 0 & \frac{1}{6} & 0 & 0 \\ 0 & \frac{13}{35} & \frac{11l_e}{210} & 0 & \frac{9}{70} & -\frac{13l_e}{420} \\ 0 & \frac{11l_e}{210} & \frac{l_e^2}{105} & 0 & -\frac{13l_e}{420} & -\frac{11l_e^2}{210} \\ \frac{1}{6} & 0 & 0 & \frac{1}{3} & 0 & 0 \\ 0 & \frac{9}{70} & -\frac{13l_e}{420} & 0 & \frac{13}{35} & -\frac{11l_e^2}{210} \\ 0 & -\frac{13l_e}{420} & -\frac{11l_e^2}{210} & 0 & -\frac{11l_e^2}{210} & \frac{l_e^2}{105} \end{bmatrix} \tag{5.7}$$

where ρ is the density of the material.

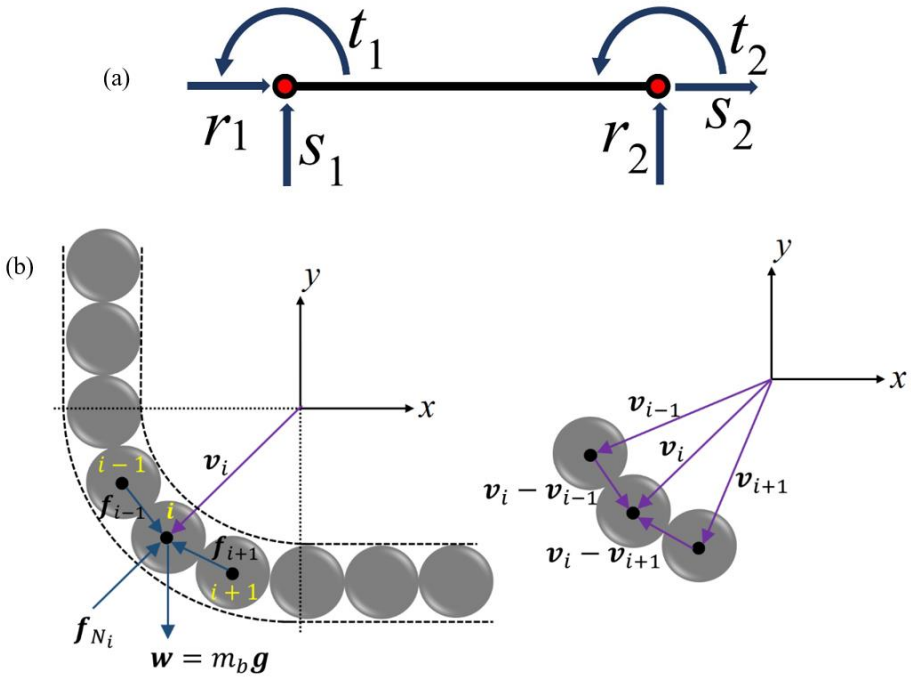

Figure 5-2 (a) Two-node beam element and displacement variables used in this study. (b) Free-body diagram of the ith particle in the L-shape chain

The beam was discretized, and the local stiffness and the local mass matrices of each element are obtained using Eqs. (5.4)-(5.7), transformed into the global coordinates, and then assembled to form the global stiffness and mass matrices of the beam.

The models with a single beam as the equivalent structure replacing CWRs, considered lengths comprised between 50 and 200 meters long, with an imperfection (**Figure 5-1**) extending along a shorter segment, typically comprised between 3.6 m to 20 m. The selection of long imperfections (10+ m) may result, however, too conservative, i.e. the temperature gradient at which the rail is expected to buckle would result much lower than the true T_{cr}, because the lateral stiffness provided by the cross-ties and the ballast is not taken into proper account. Overall, the model with one "equivalent" beam seems to be preferable to the two "equivalent" beams because real buckling begins from one track and then propagate to the second track through the crossties. The ties were modeled using spring (bar) elements with the following stiffness matrix [165]:

$$\boldsymbol{K_t} = \begin{bmatrix} k_t & -k_t \\ -k_t & k_t \end{bmatrix} \tag{5.8}$$

where k_t is the tie stiffness.

The global stiffness matrix $\boldsymbol{K}$ of the rail is then the sum of the global elastic and the global geometric stiffness matrices presented in Eq. (5.6) [173].

For the L-shaped granular medium, a 2-D discrete mass/spring model was formulated (**Figure 5-2(b)**). In the figure, $\boldsymbol{v}_i$ is the position vector of the i^{th} particle in the chain with respect to the center of the curve, $\boldsymbol{f}_n$, $\boldsymbol{f}_{Ni}$, and $\boldsymbol{w}$ are the force acting on the beam from the n^{th} particle, the surface reaction force of the inner wall applied to the i^{th} bead, and the weight vector of the bead, resepctively. The 2-D discrete mass/spring model was applied to each bead by considering two degrees of freedom for each particle. In this discrete model, the masses were assumed to be concentrated at the center of the sphere, and the Hertzian contact acted along the line of sight

between two adjacent particles [32, 38]. Therefore, two degrees of freedom were required to characterize the movement of the particles.

The differential equation of motion of the i^{th} bead in a general non-straight chain can be formulated as:

$$\boldsymbol{f}_{i-1}(t) = A_b\left[\left\|\left(\boldsymbol{v}_i + \boldsymbol{u}_i(t)\right) - \left(\boldsymbol{v}_{i-1} + \boldsymbol{u}_{i-1}(t)\right)\right\|\right]_+^{\frac{3}{2}} \cdot \frac{\boldsymbol{v}_i - \boldsymbol{v}_{i-1}}{\|\boldsymbol{v}_i - \boldsymbol{v}_{i-1}\|} \tag{5.9a}$$

$$\boldsymbol{f}_{i+1}(t) = A_b\left[\left\|\left(\boldsymbol{v}_{i+1} + \boldsymbol{u}_{i+1}(t)\right) - \left(\boldsymbol{v}_i + \boldsymbol{u}_i(t)\right)\right\|\right]_+^{\frac{3}{2}} \cdot \frac{\boldsymbol{v}_i - \boldsymbol{v}_{i+1}}{\|\boldsymbol{v}_i - \boldsymbol{v}_{i+1}\|} \tag{5.9b}$$

$$\boldsymbol{w} = m_b\boldsymbol{g} = -mg\hat{\boldsymbol{j}} \tag{5.9c}$$

$$\boldsymbol{f}_{\boldsymbol{N}_i}(t) = -(\boldsymbol{f}_{i-1} + \boldsymbol{f}_{i+1} + \boldsymbol{w}) \cdot \frac{\boldsymbol{v}_i}{\|\boldsymbol{v}_i\|} \tag{5.9d}$$

$$\begin{aligned} &\boldsymbol{f}_{i-1}(t) + \boldsymbol{f}_{i+1}(t) + \boldsymbol{w} + \boldsymbol{f}_{\boldsymbol{N}_i}(t) = \boldsymbol{M_b} \cdot \ddot{\boldsymbol{u}}(t) \\ &\rightarrow \ddot{\boldsymbol{u}}(t) = \boldsymbol{M_b}^{-1} \cdot \left[\boldsymbol{f}_{i-1}(t) + \boldsymbol{f}_{i+1}(t) + \boldsymbol{w} + \boldsymbol{f}_{\boldsymbol{N}_i}(t)\right] \end{aligned} \tag{5.9e}$$

Eqs. (5.8a) and (5.8b) examine the contact forces on the i^{th} particle exerted by the i^{th-1} and i^{th+1} particles, $\boldsymbol{u}_i(t)$ is the movement vector of the i^{th} particle, g is the gravitational acceleration and $\hat{\boldsymbol{j}}$ is the unit vector in y-direction. Eq. (5.8c) is the i^{th} particle weight vector, and Eq. (5.8d) is the surface reaction force. The second Newton's law for the i^{th} particle (differential equation of motion) is presented in Eq. (5.8e). In these equations, the operator $[x]_+$ means $\max(x,0)$, whereas A_b and $\boldsymbol{M_b}$ are the Hertizan contact coefficient and the lumped mass matrix of each bead, respectively, defined as:

$$A_b = \frac{E_b\sqrt{2R_b}}{3\left(1-\nu_b^2\right)} \tag{5.10}$$

$$\boldsymbol{M_b} = \begin{bmatrix} m_b & 0 \\ 0 & m_b \end{bmatrix} \tag{5.11}$$

where E_b, R_b, ν_b, and m_b are the elastic modulus, the radius, the Poisson ratio, and the mass of the bead, respectively. The pre-compression force vector acting on the i^{th} particle at t=0 is:

$$\boldsymbol{f}_i(0) = [\boldsymbol{f}_{i-1}(0) + \boldsymbol{w}] \cdot \frac{\boldsymbol{v}_i - \boldsymbol{v}_{i-1}}{\|\boldsymbol{v}_i - \boldsymbol{v}_{i-1}\|} \tag{5.12}$$

A finite element analysis of a beam under axial force in contact with an L-shape HNSW transducer was formulated according to **Figure 5-3**, by coupling the meshed beam along with the formulation of Eq. (5.9) of the chain particles. In this analysis the equation of motion of the beam is:

$$\ddot{\boldsymbol{u}}(t) = \boldsymbol{M}_{\boldsymbol{rg}}^{-1} \cdot \boldsymbol{f}_{\boldsymbol{rg}}(t) - \left(\boldsymbol{M}_{\boldsymbol{rg}}^{-1} \cdot \boldsymbol{K}_{\boldsymbol{rg}}\right) \cdot \boldsymbol{u}(t) \tag{5.13}$$

where $\boldsymbol{M}_{\boldsymbol{rg}}$ and $\boldsymbol{K}_{\boldsymbol{rg}}$ are the reduced global (rg) mass and the reduced global stiffness matrices, respectively, and $\boldsymbol{f}_{\boldsymbol{rg}}$(t) is the reduced global force vector, which are all obtained after applying the boundary conditions. The force vector includes the dynamic force associated with the ISW arriving at the particle-beam interface. By solving simultaneously Eqs. (5.8) and (5.12), the displacements of the particles and the transvers motion of the beam were found. From these displacements, the dynamic force at each bead was calculated using the Hertz's law, i.e.:

$$\boldsymbol{f}_1(t) = A_b \|[\boldsymbol{u}_2(t) - \boldsymbol{u}_1(t)]\|_{+}^{\frac{3}{2}}{}_{+} \cdot \frac{\boldsymbol{v}_2 - \boldsymbol{v}_1}{\|\boldsymbol{v}_2 - \boldsymbol{v}_1\|} \tag{5.14a}$$

$$\boldsymbol{f}_i(t) = \frac{1}{2}\left(A_b \|[\boldsymbol{u}_{i+1}(t) - \boldsymbol{u}_i(t)]\|_{+}^{\frac{3}{2}}{}_{+} \cdot \frac{\boldsymbol{v}_{i+1} - \boldsymbol{v}_i}{\|\boldsymbol{v}_{i+1} - \boldsymbol{v}_i\|} + A_b \|[\boldsymbol{u}_i(t) - \boldsymbol{u}_{i-1}(t)]\|_{+}^{\frac{3}{2}}{}_{+} \cdot \frac{\boldsymbol{v}_i - \boldsymbol{v}_{i-1}}{\|\boldsymbol{v}_i - \boldsymbol{v}_{i-1}\|}\right), \qquad i = 2,3,\dots,N-1 \tag{5.14b}$$

$$\boldsymbol{f}_N(t) = \frac{1}{2}\left(A_{beam} \|[\boldsymbol{u}_{beam}(t) - \boldsymbol{u}_N(t)]\|_{+} \cdot \frac{\boldsymbol{v}_{beam} - \boldsymbol{v}_N}{\|\boldsymbol{v}_{beam} - \boldsymbol{v}_N\|} + A_b \|[\boldsymbol{u}_N(t) - \boldsymbol{u}_{N-1}(t)]\|_{+}^{\frac{3}{2}}{}_{+} \cdot \frac{\boldsymbol{v}_N - \boldsymbol{v}_{N-1}}{\|\boldsymbol{v}_N - \boldsymbol{v}_{N-1}\|}\right) \tag{5.14c}$$

In Eq. (5.13c), u_{beam} is the transverse displacement of the beam, which is along the direction of motion of the last particle, and A_{beam} is the Hertzian stiffness of the bead/beam interaction equal to:

$$A_{beam} = \frac{4\sqrt{R_b}}{3}\left(\frac{1-\nu_b^2}{E_b} + \frac{1-\nu^2}{E}\right) \tag{5.15}$$

where the index *b* refers to the beam.

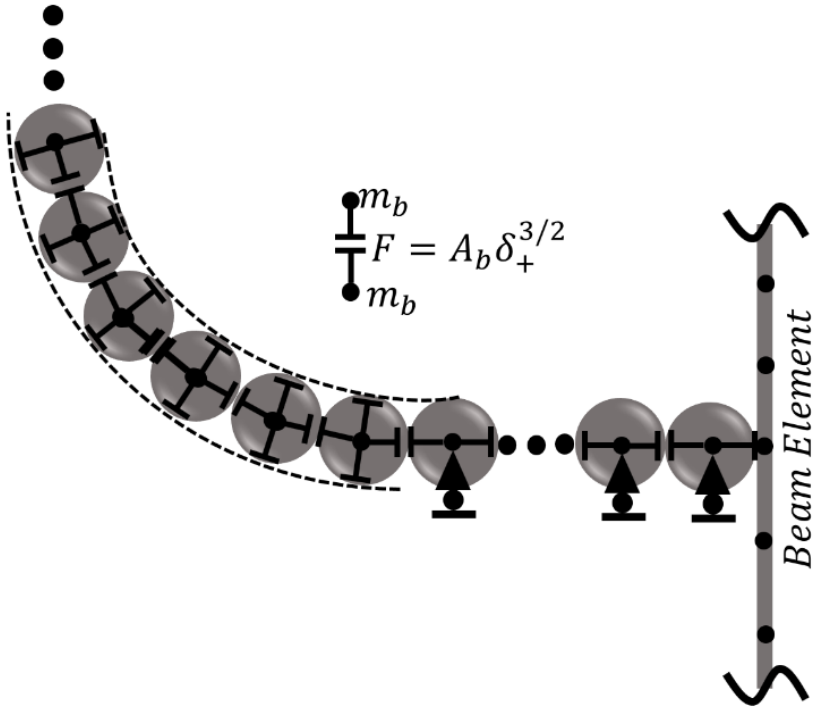

Figure 5-3 Finite element scheme of the overall problem studied in this paper

5.3 Transducer Validation

5.3.1 Experimental Setup

Four L-shaped transducers were assembled according to the scheme of **Figure 5-4**. They contained eighteen particles 19.05 mm in diameter. All beads but the second from the top, which was non-ferromagnetic, were made of ferromagnetic stainless steel. An electromagnet was connected to a commercial DC power supply to lift and release the first (ferromagnetic) particle of the chain to trigger an ISW. The falling height of the striker was about 3 mm. The sensing system was located five particles away from the chain/structure interface and consisted of a 19.05 mm diameter PZT (**Figure 5-5**) embedded between two 6.05 mm thick, 19.05 mm diameter disks. Kapton tape was used to insulate the PZT from the metal. The mass of the sensing system was equal to the single particle in order to avoid the formation of undesired spurious pulses and/or pulse attenuation at the disk-sphere interface.

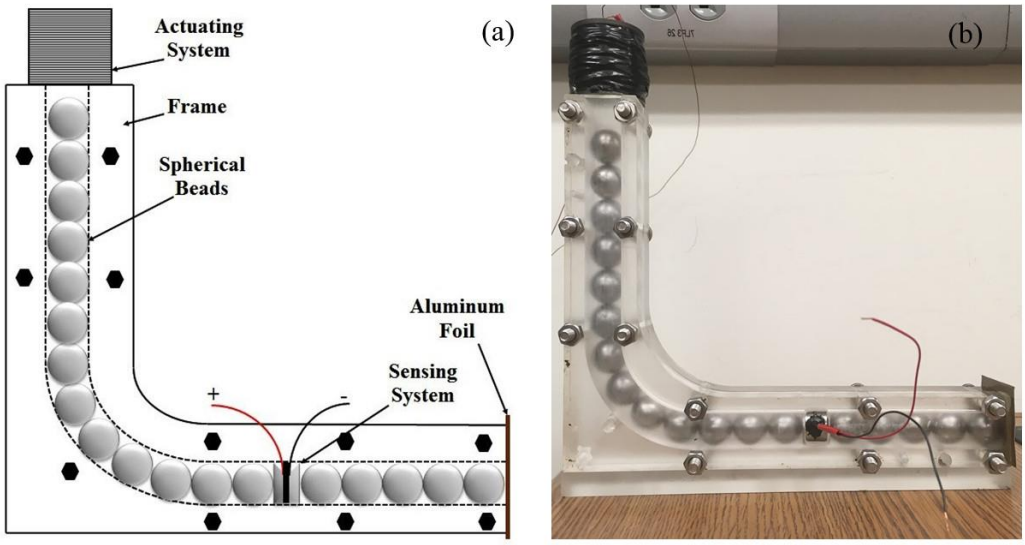

Figure 5-4 (a) Scheme of the assembled L-shaped transducers, (b) Photo of one transducer. The 0.25 mm-thick aluminum foil glued to the frame prevents the free fall of the beads

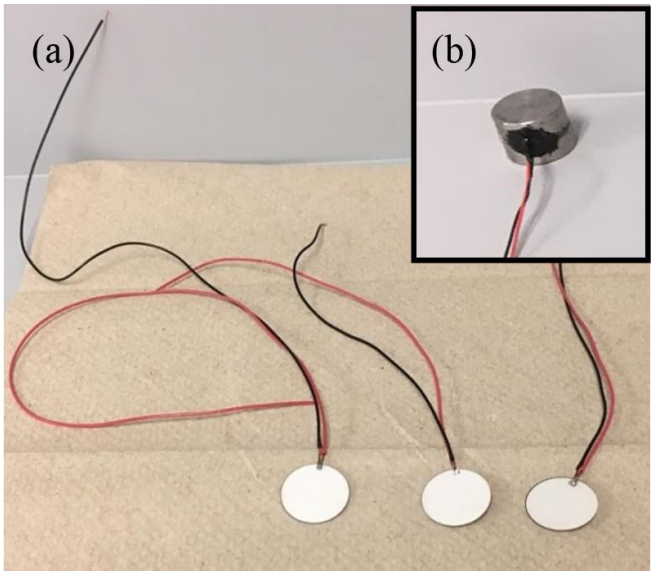

Figure 5-5 (a) Photo of the wafer transducers glued between two thick metallic disks, (b) Close-up view of one of the sensor disks embedded in the transducers.

The transducers were connected to and driven by a National Instrument-PXI 1042Q running in LabVIEW. One graphical user interface was created to drive the electromagnet and a matrix terminal block (NI TB-2643) was used to branch a TTL signal from the PXI's function generator into four switch circuits. A transistor was used to direct the electronic signals and operate the transducers sequentially.

To assess the repeatability of the ISW and determine any variability associated with differences in the assembly, the transducers were in contact with the web of a 900 mm long A.R.E.A. rail. To secure the contact between the chain and the web and avoid any undesired gap (**Figure 5-6(a)**) due to the tapered shape of the web, a small hole (**Figure 5-6(b)**) was made in the aluminum foil holding the grains. One hundred measurements were taken with each transducer and sampled at 4 MHz by setting the trigger of the digitizer to the incident pulse with a 10% pre-trigger to avoid any truncation of significant waveforms.

For post-processing, the following waveform features were considered: amplitude of the ISW, ratio of the amplitude of the wave reflected at the chain-rail interface to the amplitude of the ISW, and the TOF.

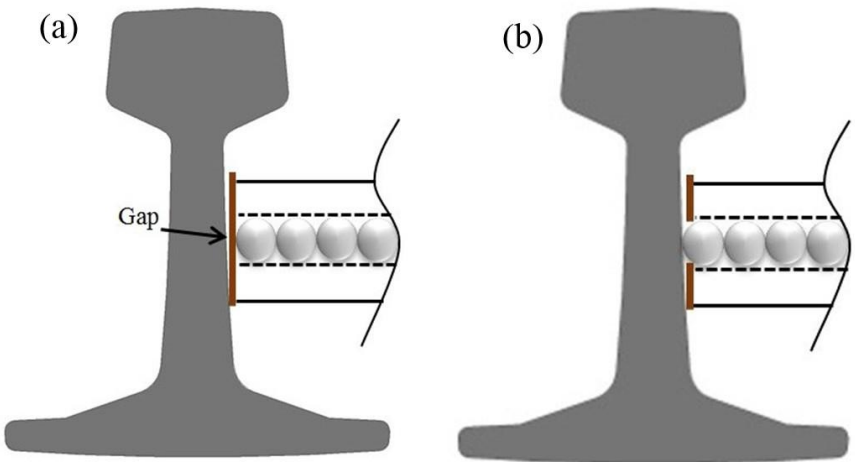

Figure 5-6 (a) A gap exists between the transducer and the web of rails because of the web geometry. (b) The gap was removed by devising a hole in the aluminum foil

5.3.2 Experimental Results

Figure 5-7 shows the average value and the corresponding 2×SD (standard deviation) interval associated with the 100 measurements. For convenience, the results are also presented in **Table 5-1**. **Figure 5-7(a)** shows the amplitude of the incident wave. This feature is expected to be immune to the properties of the chain/structure interface. The results show that, regardless of the transducers, the solitary pulse being generated is very repeatable as the coefficient of variation (CoV), i.e. the ratio of the standard deviation to the average, is between 0.81% and 2.24%. The small CoV implies that the use of an electromagnet to trigger a solitary pulse is a cost-effective solution to produce highly repeatable pulses. The average amplitude of the incident signal across the four transducers was 2.89 V with a CoV relative to the four averages equal to 0.91%. This is also an excellent result as it demonstrates the possibility to assemble many transducers with nearly identical responses. Such repeatability of the amplitude of the generated pulse can be secured by having the same gap between the electromagnet and the striker, and by minimizing the dynamic

friction between the striker and the inner wall of the frame. It must be noted though that the amplitude voltage depends also on dielectric properties of the PZT. These are properties that cannot be controlled by the user.

Table 5-1 Experimental results of the L-shape transducers tests

Transducer	ISW (V)			PSW/ ISW (%)			TOF (ms)		
	Mean	SD	CoV (%)	Mean	SD	CoV (%)	Mean	SD	CoV (%)
#1	2.86	0.02	0.81	100.80	3.54	3.51	0.4311	0.0036	0.83
#2	2.91	0.07	2.24	97.18	4.16	4.28	0.4398	0.0080	1.81
#3	2.87	0.04	1.29	95.33	3.32	3.48	0.4401	0.0041	0.93
#4	2.93	0.05	1.75	96.42	4.93	5.12	0.4428	0.0054	1.22

The feature of the PSW to the ISW ratio is presented in **Figure 5-7(b)** and **Table 5-1**. By looking at the results of Transducer #1, the amplitude of the reflected wave was slightly higher than the amplitude of the incident pulse. Although this result may seem counterintuitive, it will be thoroughly justified in the next section. In terms of the standard deviation, the feature is not as repeatable as the amplitude of the incident wave, given that the CoV spans from 3.5% to 5%. The results confirm instead the excellent repeatability of the assemble. In fact, the average of the four average ratios was 97.43% with CoV equal to 2.1%.

Finally, the results relative to the TOF are presented in **Figure 5-7(c)** and show that this feature has the highest repeatability as the CoV within the same transducer did not exceed 1.8% whereas the average of the mean values was 0.4385 ms and CoV equal to 1%. These outcomes suggest that the TOF shall be considered the main feature to infer the axial stress along thermally loaded rails as operation variability due to factors external to thermal and physical loading have little to none effects on the feature.

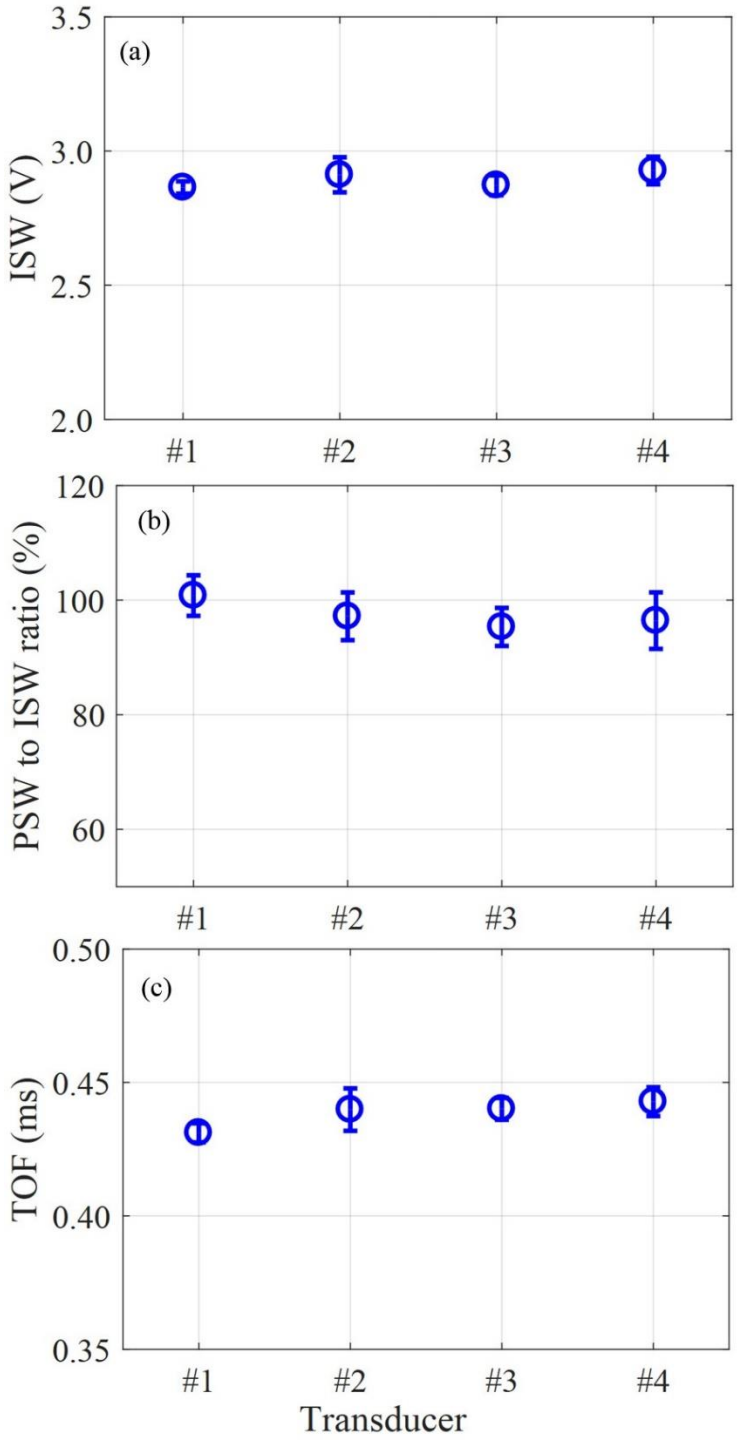

Figure 5-7 Average value of the 100 measurements of: (a) ISW, (b) PSW to ISW ratio, and (c) TOF measured from each L-shaped transducer. The vertical bars denote twice the standard deviation

5.4 Model Validation

Two analyses were performed with the models described in section 5.2. The first analysis considered the free vibration of a beam and compared its natural frequency to that obtained from the close-form solution known in structural dynamics. This was done to evaluate the accuracy of the finite element model. The geometric and mechanical properties of the beam are listed in **Table 5-2**. The second analysis delved with the interaction of an L-shaped transducer, identical to the ones which were assembled in the experiments and will be discussed later in this chapter, and a rigid beam that mimicked the rigid rail segment described in the previous section. For this second analysis, the moment of inertia was set close to infinite, and the mechanical properties of the particles were E=205 GPa, ν=0.3, ρ=7850 kg/m^3. The falling height of the striker was 3 mm. The dynamic force of the 14th bead was estimated to compare the experimental wave features with the numerical ones.

Table 5-2 Geometric and mechanical properties of the beam tested in this study

w (mm)	h (mm)	L (mm)	E (GPa)	σ_y (MPa)	α (1/^{o}C)	k	ρ (kg/m^3)
127	15.875	1200	205	250	1.0E-05	0.5	7850
I (mm^4)	A (mm^2)	r (mm)	λ	P_{cr} (kN)	σ_{cr} (MPa)	ΔT (^{o}C)	m (kg)
42341	2016	5	131	238	118	48	19

w: width, h: depth, L: free length, α: coefficient of thermal expansion, k: buckling length ratio, ρ: density, r: radius of gyration, λ: slenderness

In any FEM, it is known that smaller number of elements in the discretization reduces the accuracy of the results; on the other hand, a large number of elements significantly increases the computational cost. Therefore, a tradeoff must be reached between accuracy and computational

cost. In this study, one hundred elements were considered and the results were compared to the analytical solution obtained from applying the general equation [176]:

$$f_n = \frac{(\beta_n L)^2}{2\pi}\sqrt{\frac{EI}{\rho A L^4} + \frac{\sigma}{4\pi^2 \rho L}} \tag{5.16}$$

where f_n is the natural frequency of the n^{th} mode, and $\beta_n L$ is the root of the differential equation of the vibration of a single-span beam according to specific boundary conditions for each mode. The natural frequency changes because the axial stress changes the stiffness of the beam. **Figure 5-8** presents the frequency of vibration of the first mode, i.e. n=1 for which $\beta_1 L$=4.73 [176], as a function of the axial stress. The two curves are in excellent agreement with each other proving that the same number of beam elements in the model can be reliably used to capture the stiffness change of the beam, which is hypothesized to affect some features of the solitary waves reflected at the beam-transducer interface.

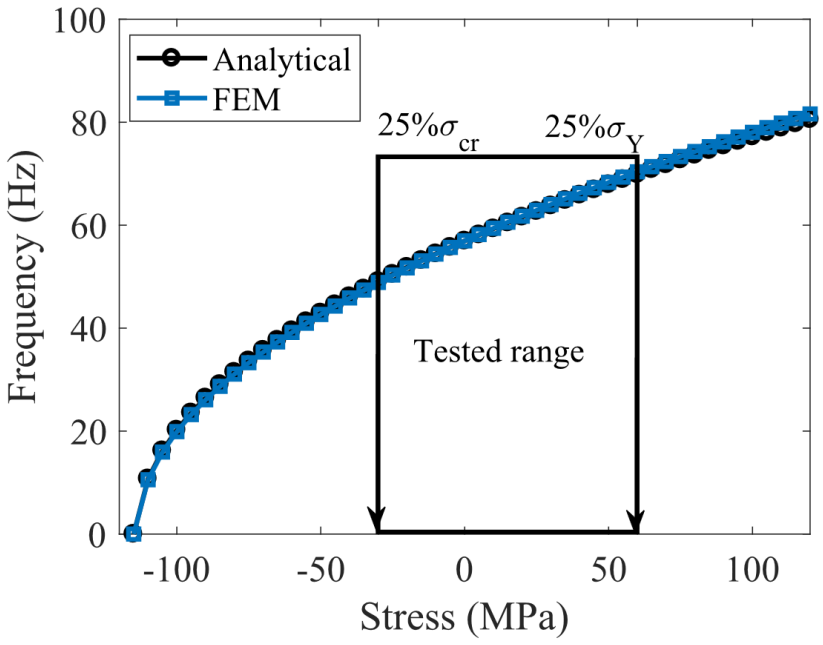

Figure 5-8 Frequency of the first mode of vibration of the beam as a function of the axial stress

The results of the second analysis are presented in **Figure 5-9** where the numerical time-waveform is displayed. As for the experimental results, only one reflected wave is generated because the material in contact with the chain is too stiff to give rise to a secondary pulse. Interestingly, the amplitude of the PSW is larger than the amplitude of the incident wave. This is due to the peculiar characteristics of the wave propagation along the granular medium. Owing to the power-law dependence of the phase velocity on the force amplitude, the incident pulse gains speed as it travels along the vertical leg of the chain due to the increasing pre-compression generated by the gravity. In the elbow, part of the dynamic force is balanced by the reaction ($\boldsymbol{f}_{Ni}$) perpendicular to the inner wall of the guide (see **Figure 5-2**); the effect is that the solitary pulse slows down because the total (dynamic plus static) compressive force along the propagation direction of the ISW is smaller than at entrance of the elbow. Along the horizontal leg, the static pre-compression across the particles is constant because the gravity is perpendicular to the leg. The effect is that once it passes the elbow, the ISW gradually regains speed over a certain distance. At the chain-beam interface, the speed and therefore the amplitude of the incident wave is higher than at the sensing particle. The outcome is that the numerical amplitude of the reflected pulse at the sensing particle is larger than the amplitude of the incident wave and the ratio PSW/ISW is 1.12 or 112%. This phenomenon was not evident in the experiments presented in Section 3 (except for Transducer #1) because the dynamic friction between the beads and the inner wall of the guide dissipates the acoustic energy. In **Figure 5-9**, the numerical TOF is to 0.4266 ms, about 2.78% smaller than the average of the four transducers and 3.1% smaller than Transducer #1. This result is consistent with the fact that the numerical reflected pulse was faster than the experimental pulse described in the previous section. A note about the small bumps trailing the reflected pulse and visible at about 1.25 ms and 1.5 ms; they represent the arrival of small spurious pulses generated

by the bouncing of the striker and do not have any detrimental effects on the physical phenomena being exploited in this study.

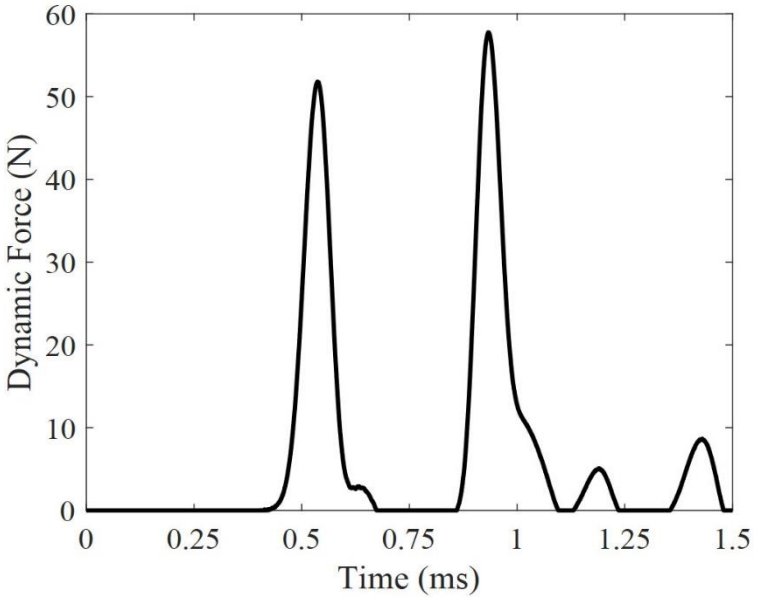

Figure 5-9 Numerical results. Waveform relative to the transducer in contact with a rigid beam

5.5 Testing a Thick Beam

5.5.1 Experimental Setup

A 127×15.88×1400 mm^3 A36 steel beam was tested. Its mechanical and geometric properties are listed in **Table 5-2**. The beam was connected to a MTS machine using two angles wedges at each end. The L-shaped Transducer #1 was placed in contact with the mid-span of the beam. This transducer was chosen for its high repeatability; the internal friction was reduced further by increasing the guide width by 0.5 mm, and the falling height of the striker was raised to 4 mm to

generate stronger pulses. The setup is shown in **Figure 5-10**. Two rounds of experiments were conducted. In the first round, the beam was mechanically loaded to its 25% of the yielding stress (σ_Y=60 MPa), and the load was changed with -11 MPa steps to reach the beam's 25% Euler stress (σ_{cr}=-30 MPa). These two extremes are identified in **Figure 5-8** and within them the natural frequency decreases about 30% from 69.87 Hz to 49.08 Hz. At each step, ten measurements were taken with the transducer. Three tension-compression cycles were completed.

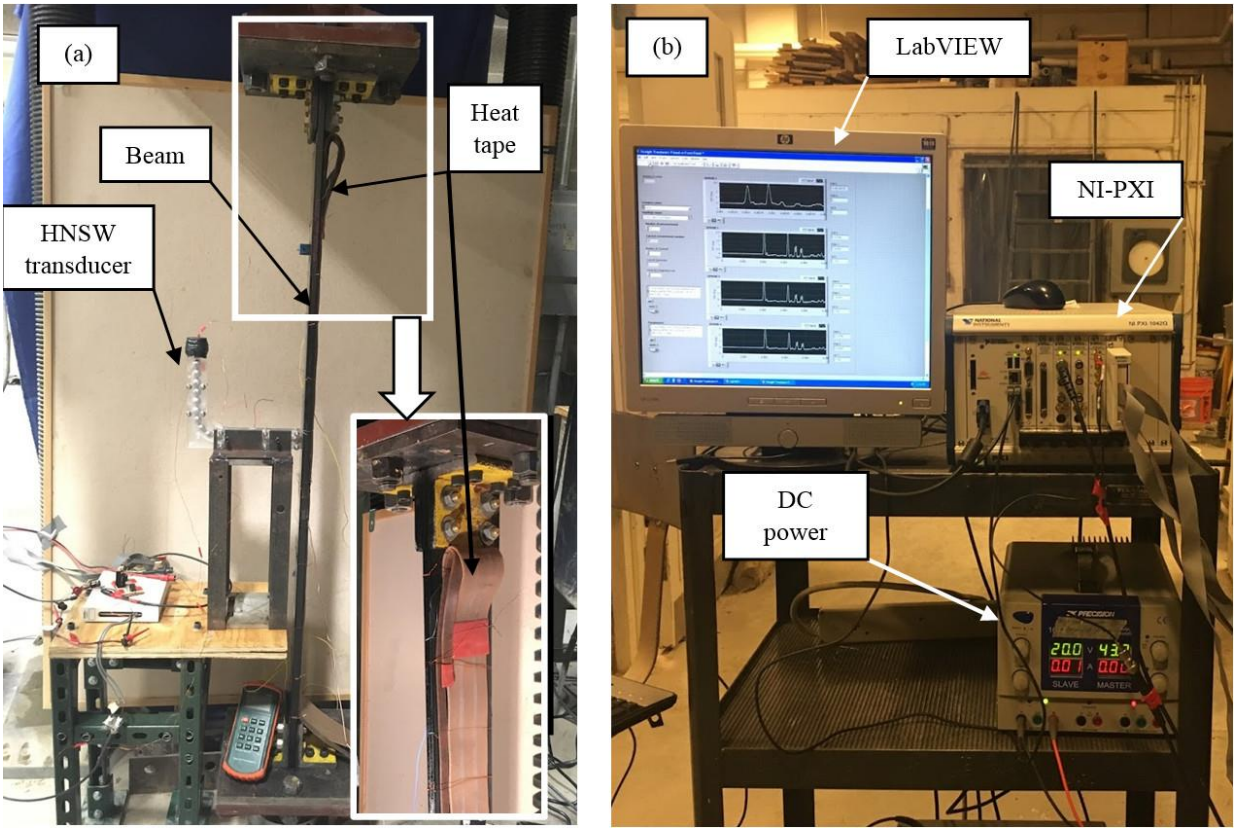

Figure 5-10 Photo of the: (a) test setup and (b) hardware used to run the transducer

In the second round of experiments, the specimen was pre-tensioned, held in displacement control, and then heated with a thermal tape to induce thermal stress. Three experiments were conducted corresponding

to three levels of pre-tension, namely 25%, 15%, and 5% of the steel yielding stress. This mimicked different neutral temperatures. Heat was imparted until the surface temperature of the steel was about 82.5ºC, 71.6 ºC, and 63.3 ºC, respectively. Then, the beam was cooled naturally until the initial temperature was reached. Two heating-cooling cycles were completed. Owing to the fixed-fixed boundary conditions, the Euler load P_{cr} was:

$$P_{cr} = \frac{4\pi^2 EI}{L^2} \tag{5.17}$$

and the corresponding values for the test specimens are presented in **Table 5-3**.

Table 5-3 The loading protocol and details of different tests

Test No.	1	2	3	4
Load Type	Mechanical	Thermal	Thermal	Thermal
Pre-tension stress (MPa)	62.5	62.5	37.5	12.5
Yielding percentage	25	25	15	5
Compressive stress (MPa)	-30	-6	-18	-30
Buckling percentage	25	5	15	25
$\Delta\sigma$ (MPa)	92.5	68.5	55.5	42.5
Neutral temperature (ºC)	25	25	15	5
Measurements per step	10	5	5	5
Completed cycles	3	2	2	2

Using known formulation, the thermal load P_T and the stress σ_T imparted to the beam can be calculated as:

$$P_T = EA\alpha\Delta T = EA\alpha\left(T_0 - T_f\right) \tag{5.18a}$$

$$\sigma_T = E\alpha\Delta T = E\alpha\left(T_0 - T_f\right) \tag{5.18b}$$

where T_0 and T_f are the initial and the final temperature of the beam, respectively. The critical temperature occurs when $P_{cr} = P_T$, i.e. the temperature raise ΔT_{cr} necessary to induce buckling was equal to:

$$\Delta T_{cr} = \frac{4\pi^2 I}{A\alpha L^2} \tag{5.19}$$

equivalent to:

$$\Delta T_{cr} = \frac{\pi^2 h^2}{3\alpha L^2} \tag{5.20}$$

For the test specimen probed in this study, ΔT_{cr} was equal to 48 ºC.

A digital thermocouple was used to measure the temperature at the center of the beam, and five measurements were taken with the HNSW transducer at 5ºC temperature step. Five measurements were taken instead of ten, to make sure that the beam temperature could be assumed constant during the measurements. At each step, the axial load shown in the MTS control box was recorded as well. Two cycles were completed for each test in one day. **Table 5-3** summarizes the tests protocol.

5.5.2 Experimental Results: Mechanical Loading

Figure 5-11 shows the stress-strain relationship retrieved from the control unit of the MTS machine and overlapped to the theoretical values predicted by the Hooke's law. The discrepancy between the empirical and the theoretical value is attributed to local elastic deformation of the reaction plates placed at the end of the beam and to small, yet relevant, adjustments in the MTS machine during the transition from tension to compression and viceversa. These uncontrollable phenomena affected also the amount of heat imparted to the beam to achieve the desired stress range. Nonetheless, it is demonstrated in this and next sub-section that these constraints of the loading setup did not affect in any manner the objective of the study and the validation of the research hypothesis.

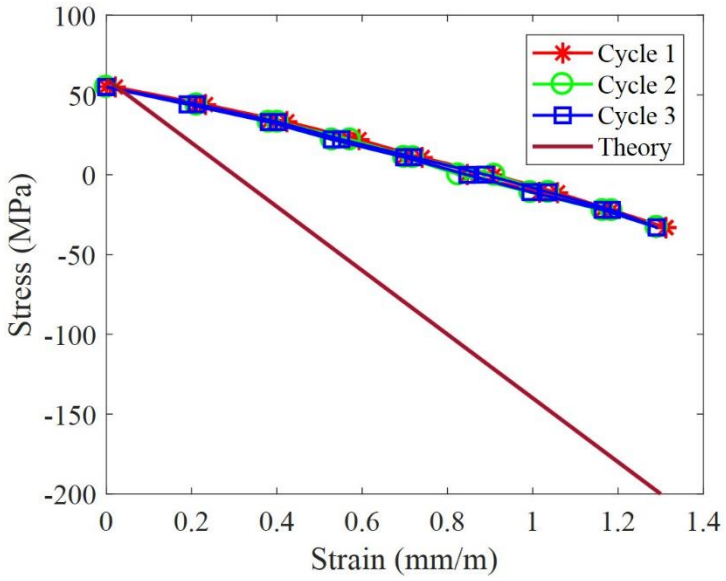

Figure 5-11 The experimental and theoretical stress-strain relationship

Figure 5-12 shows two waveforms, one associated with 25% yielding and one associated with 25% buckling stress. The arrival time of the ISW is identical whereas the amplitude and the TOF are different. To quantify the effect of axial stress on the features of the solitary waves, **Figure 5-13** shows the amplitude ratio and the TOF as a function of the axial stress: the three loading and unloading ramps are overlapped to the numerical predictions. The vertical bars represent the 2×SD confidence interval associated with the ten measurements. Overall, the experimental data show the same trend predicted numerically, i.e. a monotonic variation of the features with respect to the axial stress. This variation is the effect of the change in the beam stiffness due to the axial stress: for example, compression reduces the lateral stiffness of the beam [174]. As discussed in several manuscripts [48, 132, 138, 140], the reduction of the stiffness of the contact material increases the TOF and decreases the amplitude ratio. **Figure 5-13** also shows that the experimental data are smaller than the numerical values. This is likely due to the absence of friction and dissipating terms in the simulation. Nonetheless, both numerical and experimental values vary about 15% across the

stress range considered in this study. Finally, not shown here, the amplitude of the incident wave did not follow any trend associated with the axial stress. This result was expected, as the ISW is not influenced by the condition of the material in contact with one end of the chain.

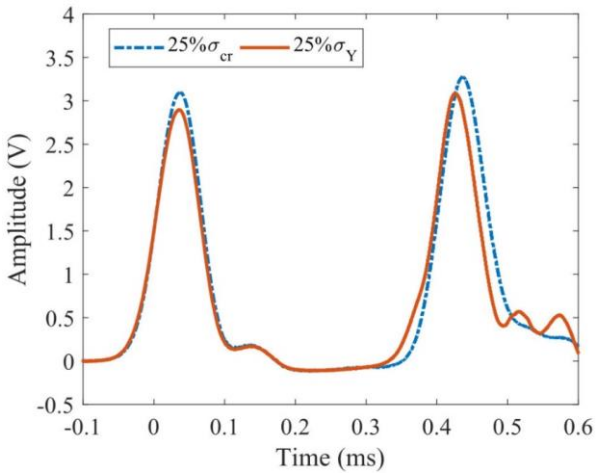

Figure 5-12 Experimental results. Example of time waveforms recorded when the beam was subjected to 25% of its yielding tension and 25% of its buckling compression

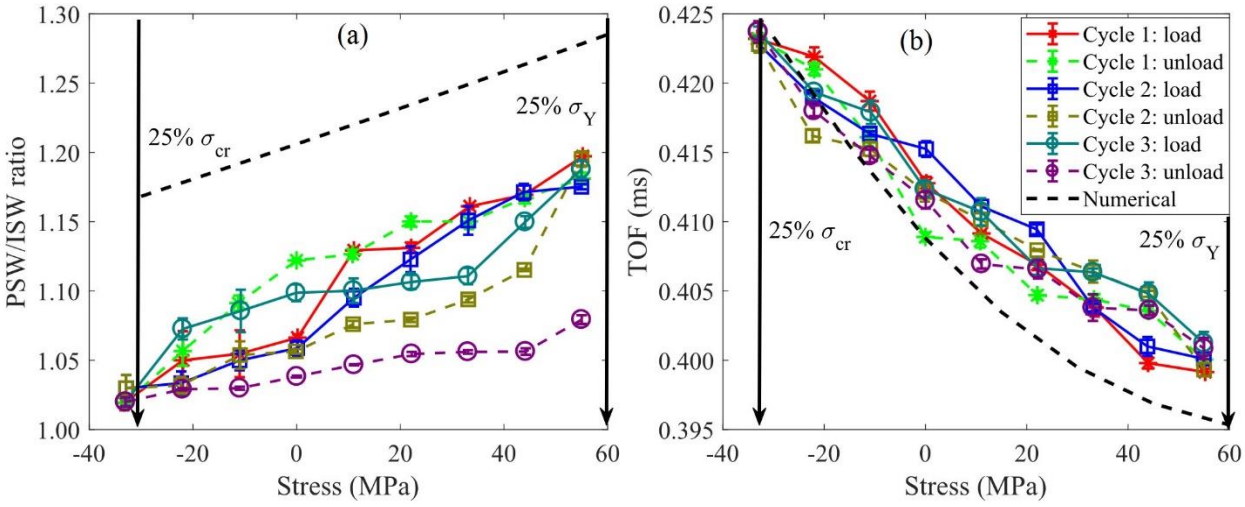

Figure 5-13 Mechanical testing, experimental results: (a) PSW/ISW ratio, (b) TOF as a function of the applied stress. The numerical prediction is overlapped

5.5.3 Experimental Results: Thermal Loading

Figure 5-14 shows the ratio and the TOF associated with Tests #2 to #4. The experimental data are overlapped to the numerical predictions. The vertical bars represent the 2×SD confidence interval associated with the five measurements. The same trends seen in the mechanical loading are observed. The change in the TOFs was 4.9%, 3.3%, and 2.4% for Test #2, Test #3, and Test #4, respectively. The results are consistent with the moderate change in natural frequency (consequently, a moderate change in the stiffness) predicted with **Figure 5-8**. It is expected that for stresses close to buckling, the variation of the TOF would be much larger as the stiffness drop of the beam would be much larger than the tested range.

To quantify the feature gradient with respect to the axial stress, the data points relative to the two heating and cooling ramps at any given stress were averaged and the results are presented in **Figure 4-15**, overlapped to the numerical results. By looking at the equations of the line interpolation several conclusions can be drawn. Except **Figure 4-15(f)**, the slopes of the numerical and the experimental data are very similar. This means that the experimental slopes agree with the numerical prediction in terms of the sensitivity of the wave feature to the change in axial stress. The equations also reveal that the neutral temperature does not affect the sensitivity of the wave-based NDE method as the *y*-intercept does not change with the level of pre-tension: at zero stress, irrespective of the neutral temperature, the amplitude ratio is about 1.08 (108%) and the TOF is 0.414 ms. This implies that the method can be applied anytime regardless of the neutral temperature. In the field, the transducer would probe any thick beam with identical geometric properties. The empirical TOF or amplitude ratio would be plugged into the *y* variable of the above equations to solve for the *x* variable, which represents the actual stress (σ_T). By measuring with a thermocouple, the actual temperature T_f of the steel, Eq. 5.17(b) would be used to infer the beam's

neutral temperature. The possibility to use two wave features increases the redundancy of the proposed NDE system.

5.5.4 Conclusions

This section presented a numerical and an experimental study about the use of highly ninlinear solitary waves to estimate the axial stress of thermally loaded thick beams. The numerical work consisted of a finite element model coupled to a discrete particle model to predict the dynamic interplay between the propagation of solitary waves within a chain of particles and beams undergoing axial stress and in contact with the chain. The models were validated experimentally by assembling four HNSW transducers, able to trigger, sustain, and sense the solitary pulses. First the chains were tested to quantify repeatibility and reliability. Then, one transducer was used to monitor a thick beam subjected to mechanical loading and to thermal loading. The results demonstrated that the proposed nondestructive evaluation system is robust in terms of repeatibility and sensisitvity to the variation of axial stress, as the wave features are monotonically dependent on the axial stress and do not depend on the initial neutral temperature of the beam. This implies that the system can be applied anytime without the need for a day long obervation that would eventually require the neutral temperature crossing. It is noted here that the findings presented in this manuscript are valid to any beam possessing the same geometric and mechanical properties of the beam tested in this study. For different beam, the generalized model presented in this article can be used to predict the variation of the features of the reflected solitary waves due to the presence of thermal or mechanical stress.

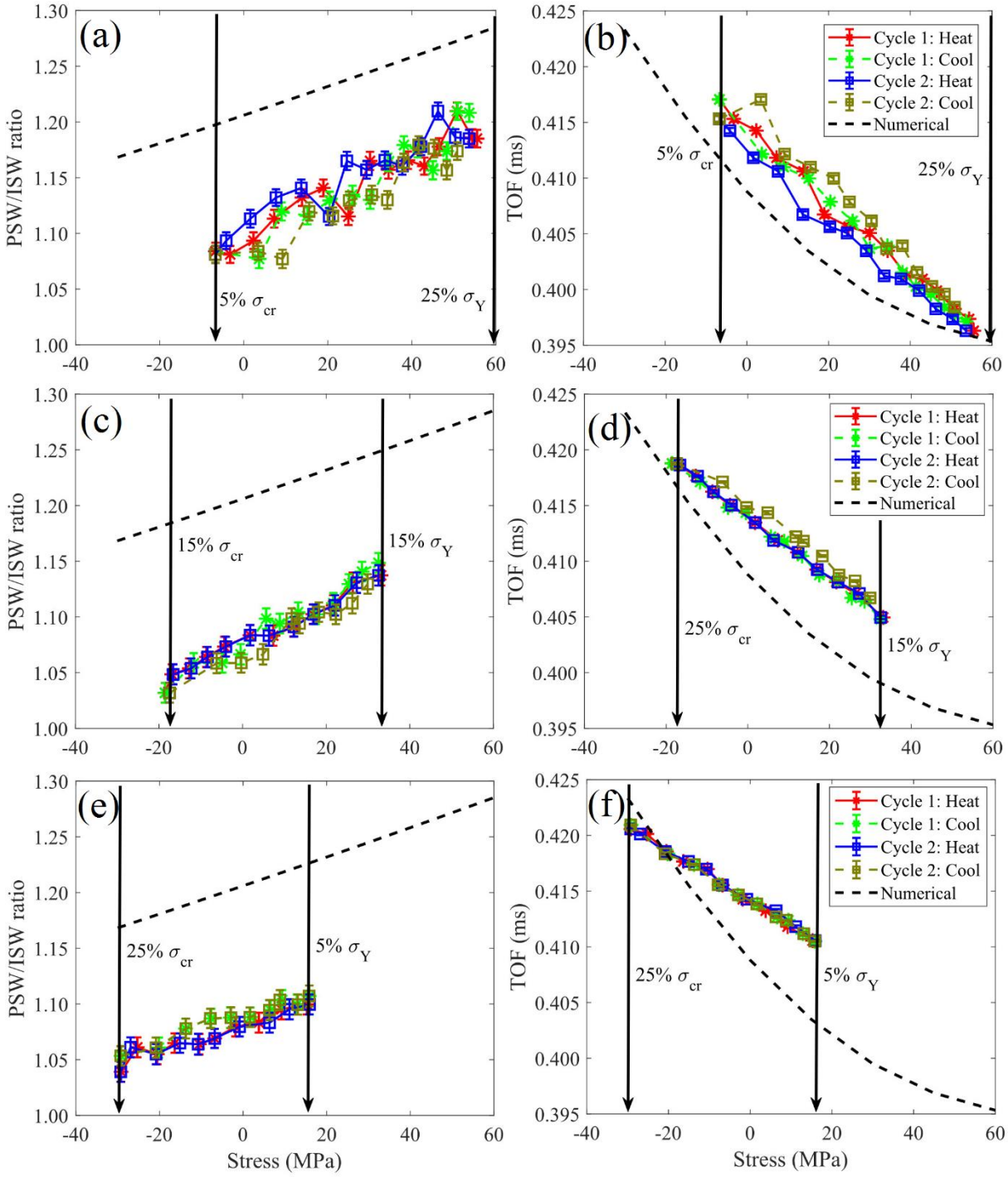

Figure 5-14 Thermal loading tests, experimental results: (a) PSW/ISW ratio and (b) TOF across [0.05σ_{cr}, 0.25σ_Y]; (c) PSW/ISW ratio and (d) TOF across [0.15σ_{cr}, 0.15σ_Y]; (e) PSW/ISW ratio and (f) TOF across [0.25σ_{cr}, 0.05σ_Y].

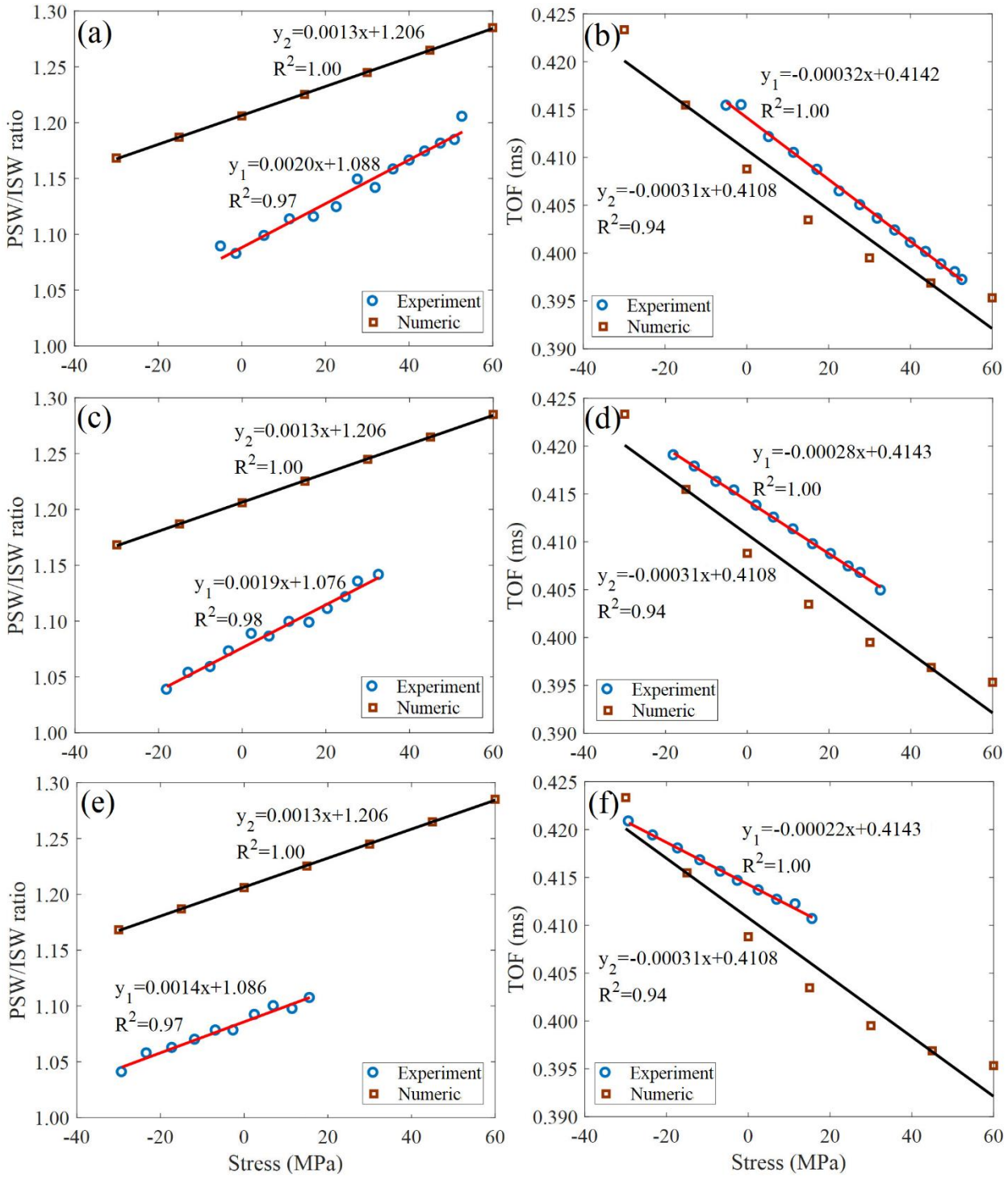

Figure 5-15 Thermal loading tests, experimental results. Analysis of the features' trend: (a) PSW/ISW ratio and (b) TOF across [$0.05\sigma_{cr}$, $0.25\sigma_Y$]; (c) PSW/ISW ratio and (d) TOF across [$0.15\sigma_{cr}$, $0.15\sigma_Y$]; (e) PSW/ISW ratio and (f) TOF across [$0.25\sigma_{cr}$, $0.05\sigma_Y$].

5.6 Testing Rails

5.6.1 Numerical Setups and Results

Three analyses were performed. In the first analysis, a single unconstrained 3.6 m-long rail was modeled (**Figure 5-16(a)**) whereas the second analysis was about the same rail but constrained with lateral springs (**Figure 5-16(b)**) spaced 0.45 m apart and k_t equal to 2.6×10^7 N/m, in accordance to [173]. The third analysis was about a 0.9 m-long unconstrained rail in order to validate the model with the experiment conducted in this study. The length of 3.6 m is consistent with the appropriate "equivalent" beam discussed in section III whereas the shorter rail corresponds to the length of the sample tested experimentally. The 3.6 m-long rail was discretized with 80 elements whereas the 0.9 m-long rail was meshed with 20 elements. After discretization, the local stiffness and the local mass matrices of each element were obtained using Eqs. (5.4)-(5.8), transformed into the global coordinates, and then assembled to form the global stiffness and mass matrices.

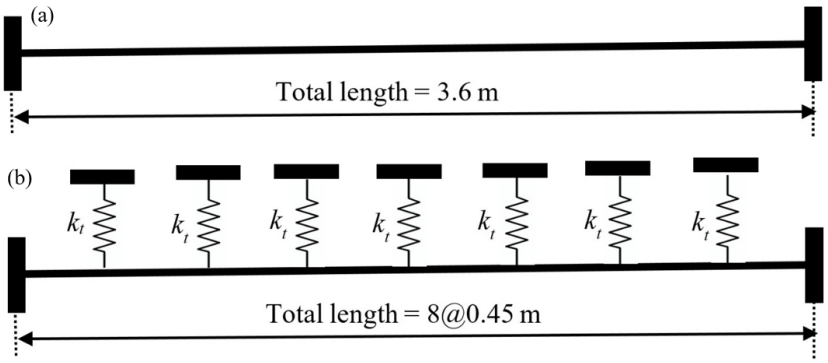

Figure 5-16 Schematic of the rail models implemented in this study. (a) 3.6 m-long unconstraint rail; (b) 3.6 m-long tied rail at 0.45 m (18 in.) spacing

To adhere our analysis to the experimental sample an AREMA $6^{13/16}$ rail profile was modeled. The elastic modulus of the steel was assumed 200 GPa, while the cross-sectional area and the moment of inertia were 8736 mm^2 and 7.04×10^6 mm^4, respectively. For the granular medium, an L-shaped array of eighteen particles 19.05 mm in diameter was modeled. All beads but the second from the top, which was non-ferromagnetic, were made of ferromagnetic stainless steel with the elastic modulus and the Poisson's ratio equal to 200 GPa and 0.3, respectively. To trigger the incident wave, the initial velocity of the particle was set to 0.28 m/s equivalent to the speed at the moment of the impact of a striker freely falling striker from 4 mm. The dynamic force of the solitary waves was measured at the center of the bead located five particles away from the chain/rail interface. This numerical design of the array was consistent with the *transducer* assembled for the experiment and visible in **Figure 5-4**.

Figure 5-17 shows the waveforms associated with the three analyses: the 3.6 m long uncontrained rail (**Figure 5-17(a)**), the 3.6 m long rail with lateral springs (**Figure 5-17(b)**), and the 0.9 m long unconstrained rail (**Figure 5-17(c)**). The plots relative to the longer rail (**Figure 5-17(a)** and **Figure 5-17(b)**) show the existence of the SSW. This implies that the acoustic energy carried by the incident wave was sufficient to trigger a local oscillation of the structure and induced the separation of the bead from the rail.

With respect to **Figure 5-17(a)** and **Figure 5-17(b)**, **Figure 5-17(c)** reveals that the amplitude of the reflected pulse is higher than the amplitude of the incident wave. This apparent counterintuitive result is justified by the geometry of granular medium. Owing to the power-law dependence of the phase velocity on the force amplitude, the incident pulse gains speed as it travels along the vertical leg of the chain due to the increasing pre-compression generated by the gravity. Along the elbow, part of the dynamic force is balanced by the reaction exerted by the inner wall

of the guide holding the spheres. The effect is that the solitary pulse slows down because the total (dynamic plus static) compressive force along the propagation direction is smaller than at the entrance of the elbow. Along the horizontal leg, the static pre-compression remains constant with the consequence that the ISW gradually regains speed over a certain distance with the consequence that the speed and therefore the amplitude of the incident wave is higher at the chain-rail interface than at the sensing particle.

The comparison of the three incident waves reveals also an unexpected outcome. The three pulses are not identical despite the fact that the ISW is expected to be immune by the conditions at the chain-rail interface. Both the amplitude and the arrival time are not identical with the largest difference noted in the short rail. In addition, an offset is visible during the first 0.3 ms of the signal in **Figure 5-17(a)** and **Figure 5-17(a)**.

The origin of such apparent incongruence is in part due to the flexural stiffness of the rail and in part due to the design of the transducer. The flexural stiffness of the rail is proportional to EI/l^3. As such, the short rail is $4^3=64$ times stiffer than the 3.6 meter long rail. In the model, the virtual impact of the striker causes the rebound of the striker itself. This event temporarily changes the overall weight of the chain causing a small deformation of the rail which in turn causes the generation of a small pulse traveling apposite to the ISW direction. This is visible in **Figure 5-18** where the time waveforms recorded at the center of the fifth particle from the top, i.e. right before the elbow, are presented for the two unconstrained beams. However, as demonstrated in what follows, this small pulse does not affect the overall NDE method proposed here. As the ISW and the spurious pulse travels they interfere with each other giving rise to the differences oberved in **Figure 5-17**.

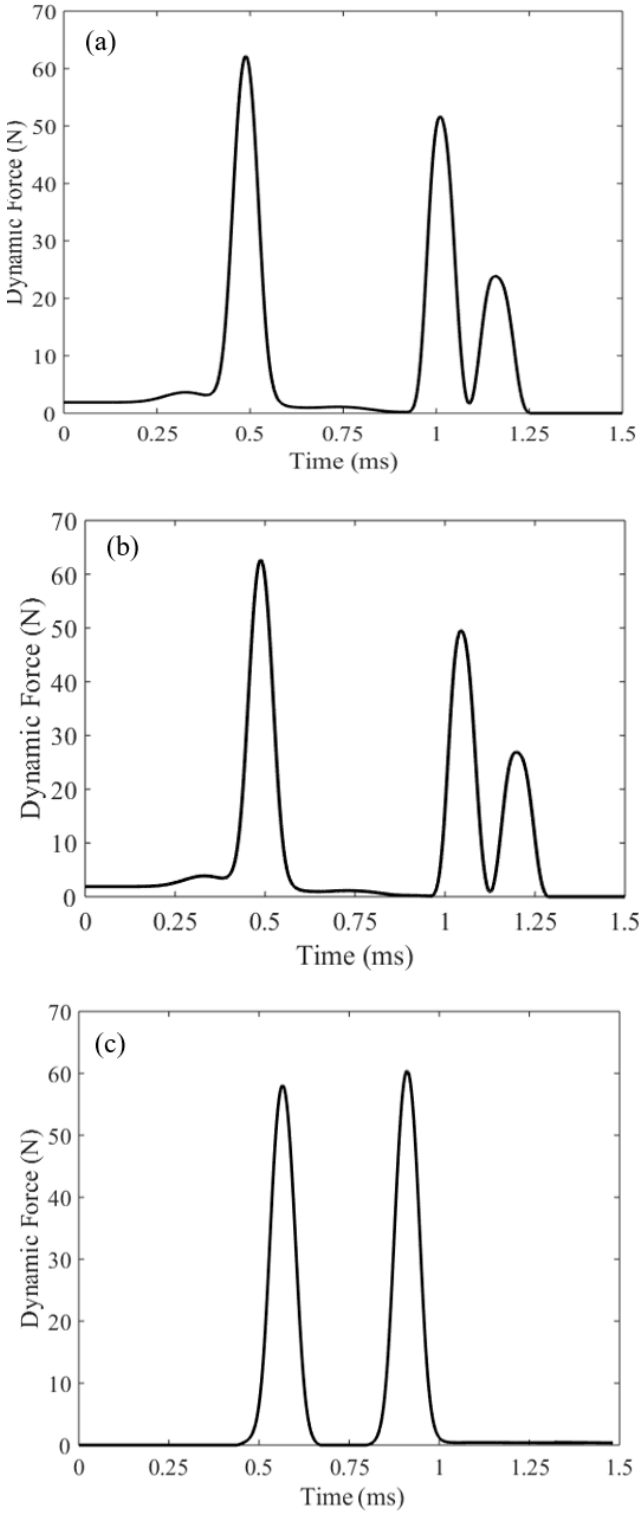

Figure 5-17 Results of the numerical analysis. Time waveforms associated with an AREA 613/16 rail (a) 3600 mm-long unconstraint rail; (b) 3600 mm-long tied rail; and (c) 900 mm long

To investigate the influence of the axial stress on the characteristics of the waves reflected at the interface, some features were computed for different values of the longitudinal stress of the rail. The results relative to the 3.6 m unconstrained rail are presented in **Figure 5-19** and they refer to the stress range comprised between 95% of buckling stress, namely ~120 MPa in compression, and 25% yielding, namely ~60 MPa in tension. **Figure 5-19 (a)** shows the PSW/ISW ratio, **Figure 5-19(b)** presents the SSW/ISW ratio, **Figure 5-19(c)** displays the time-of-flight relative to the primary wave, and **Figure 5-19(d)** shows the time-of-flight of the secondary wave. The PSW/ISW ratio was obtained by dividing the peak amplitude of the primary reflected wave to the peak amplitude of the incident wave.

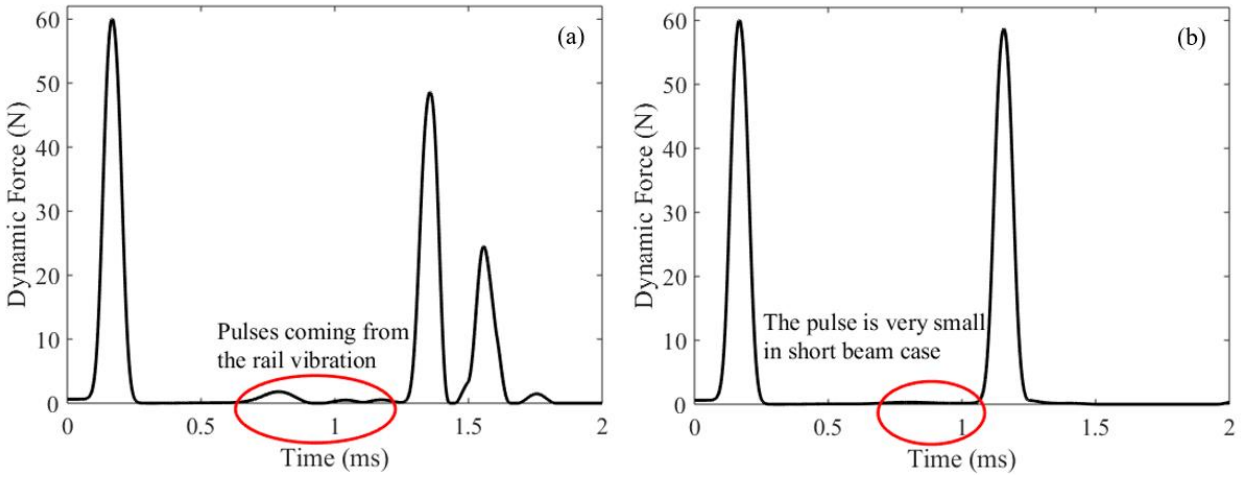

Figure 5-18 Numerical analysis. Solitary waveforms measured at the center of the particle on the vertical leg of the chain, i.e. at the entrance of the elbow. (a) 3.6 uncontrained beam; (b) 0.9 unconstrained beam

Similar procedure was adopted to compute the SSW/ISW ratio. The time of flight represents instead the difference in the arrival time at the same sensing particle of the reflected pulses with respect to the incident pulse. In **Figure 5-19**, the first two features are express in percent to indicate

the fraction of the reflected amplitude with respect to the incident pulse amplitude. All four plots denote a clear monotonic trend with significant variation of the wave features across the stress range considered. In numbers the PSW/ISW ratio, SSW/ISW ratio, TOF of PSW, and TOF of SSW vary by 6%, 13%, 9%, and 7%, respectively. These numbers are significantly higher than what would be expected by using, for example, acoustoselasticity as a non-invasive method to infer the applied stress on the structure [122, 177, 178].

Another interesting outcome of **Figure 5-19** is that the features do not show any abrupt variation as the rail approaches to buckling; as a matter of fact, the polynomial interpolating the numerical results have residual R^2 equal to 1. In practice, by plugging the known mechanical and geometric properties of the rail, and by assuming an "equivalent" beam length of, let say 3.6 meters, the inspectors can infer the current stress of the rail by measuring the features of the solitary waves propagating along a transducer assembled according to the specifications described here. The fact that all plots present a monotonic trend across a wide range of stresses, guarantees that the solitary wave readings provide a unique value of the axial stress by applying the equations presented in **Figure 5-19**. With the inferred stress σ (the x variable on the aforementioned equations) the neutral temperature would be estimated using Eq. (5.1) once a thermocouple or a rail thermometer has provided the current temperature T_R of the rail. This estimate would be done having four potential features (four potential equations) instead of one, i.e. having redundancy in the NDE system. The method also would not require daylong monitoring along which the neutral temperature needs to be crossed. It is noteworthy that the results presented here apply to a transducer with the characteristics presented in **Figure 5-4**. Nonetheless the model implemented in this study is generalizable: any transducer with any number of spheres of any size and material can be modeled effortlessly.

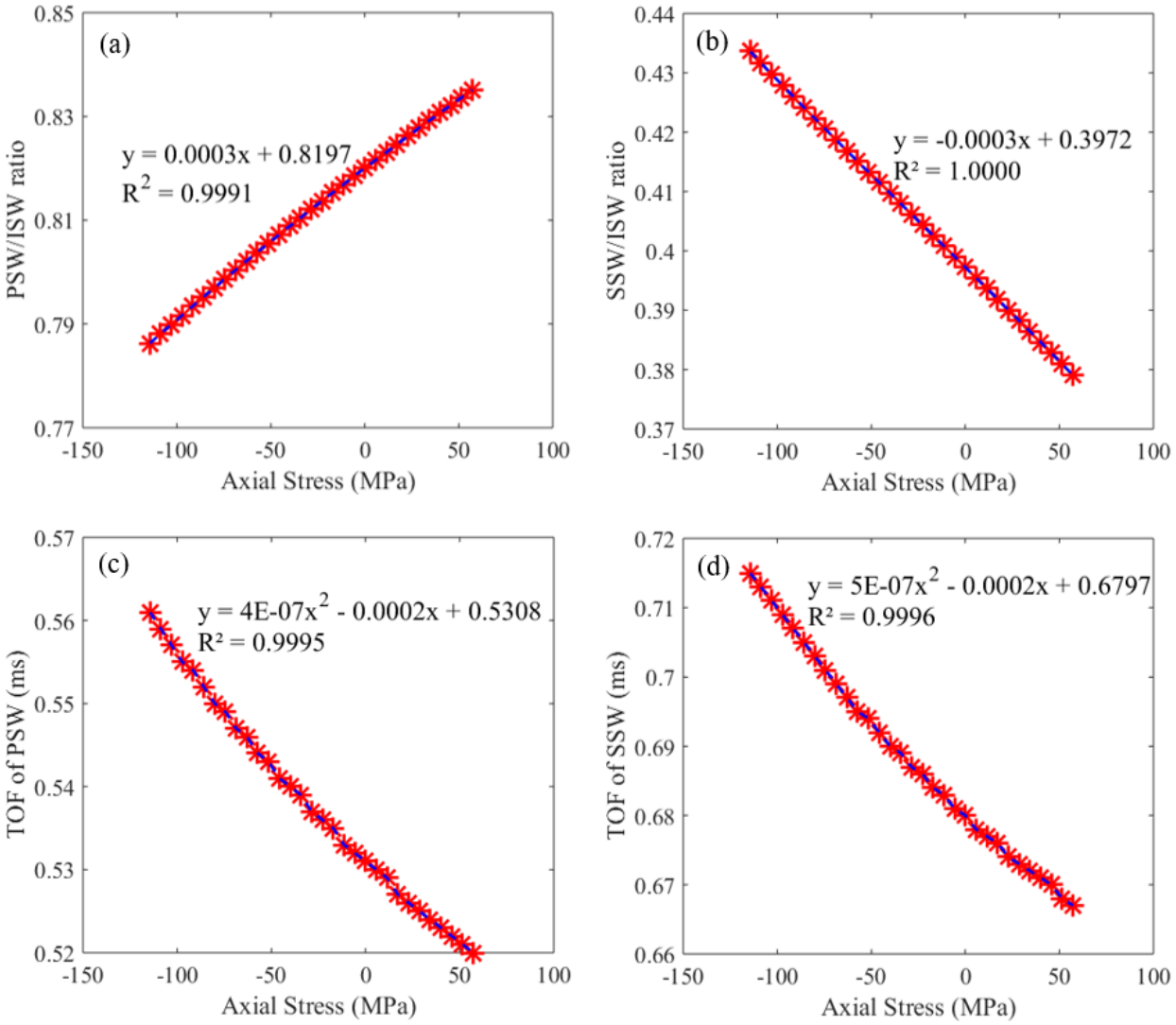

Figure 5-19 Numerical analysis. Solitary waves features as a function of the axial stress acting on an AREA 613/16 3600 mm-long unconstrained rail. (a) PSW/ISW raio; (b) SSW/ISW ratio; (c) TOF of PSW; (d) TOF of SSW

The same analysis carried for the 3.6 m long unconstrained rail was carried for the other two cases examined in this study. **Figure 4-20** shows the numerical results relative to the laterally confined rail. The same waveform features were considered, and very similar trends and equations were found, with only some slight difference in quantitative values. The PSW/ISW ratio, SSW/ISW ratio, TOF of PSW, and TOF of SSW vary by 6%, 13%, 9%, and 7%, respectively. This reveals that the stiffness provided by the ties is negligible compared to the stiffness of the rail. In addition, any practical consideration discussed above applies here.

Finally, the results relative to the 0.9 long rail are presented in **Figure 5-21**. In this case only the features associated with the PSW can be extracted because the rail is too stiff to induce any secondary reflection. Although the stress range that was considered was the same as **Figure 4-19** and 5-20, the compressive stress of ~120 MPa is equivalent to about 20% of the rail yield stress and only 2.5% of buckling. In other words, the rail yields well before it buckles. The graphs of **Figure 5-21** show the absence of any significant variation across the stress range considered. The variation of the geometric stiffness of the rail due to the axial stress is negligible in comparison with the material stiffness. **Figure 5-21(a)** reveals that the amplitude of the reflected wave is about 4% higher than the incident wave. As discussed earlier this is due to the L-shaped geometry of the transducer. This phenomenon was not observed in the longer rail because part of the incident acoustic energy is converted into the SSW.

5.6.2 Experimental Setup and Results

The L-shaped transducer shown in **Figure 5-4(b)** was used to probe the 0.9 m-long rail. It contained eighteen particles 19.05 mm in diameter. The sample stood vertically in an MTS machine and the transducer was in contact with the rail web at the midspan. **Figure 5-22** shows

the overall experimental setup. Mechanical compression at 44.5 kN (10 kips) step was applied up to 445 kN (100 kips). The load was recorded with the MTS control box and the highest load corresponded to approximately 20% of the rail's yield stress and 2.5% only of the Euler buckling load. As said earlier, the profile and the length of the sample were such that the sample would yield before buckle. At each step, ten measurements were taken with the L-shaped transducer in order to investigate the repeatability of the setup; the solitary waveforms were sampled at 4 MHz and stored for post-processing analysis. The trigger was set to the incident pulse with a 10% pre-trigger to avoid any truncation of significant waveforms. Two load-unload cycles were completed. In the post-processing the amplitude of the incident wave, the PSW/ISW ratio, and the time of flight of the reflected wave were analyzed.

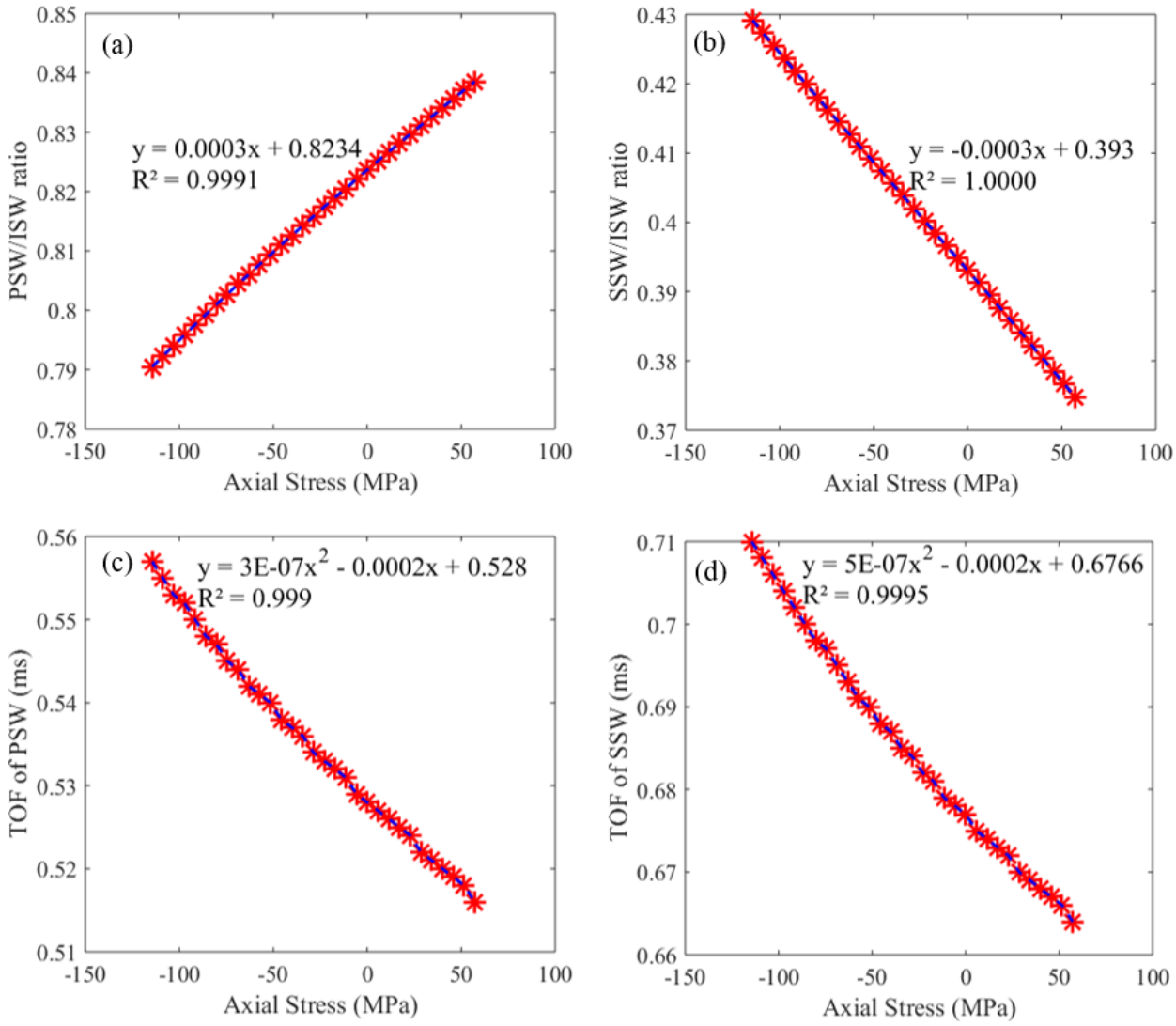

Figure 5-20 Numerical analysis. Solitary waves features as a function of the axial stress acting on an AREMA 613/16 3600 mm long tied rail. (a) PSW/ISW raio; (b) SSW/ISW ratio; (c) TOF of PSW; (d) TOF of SSW

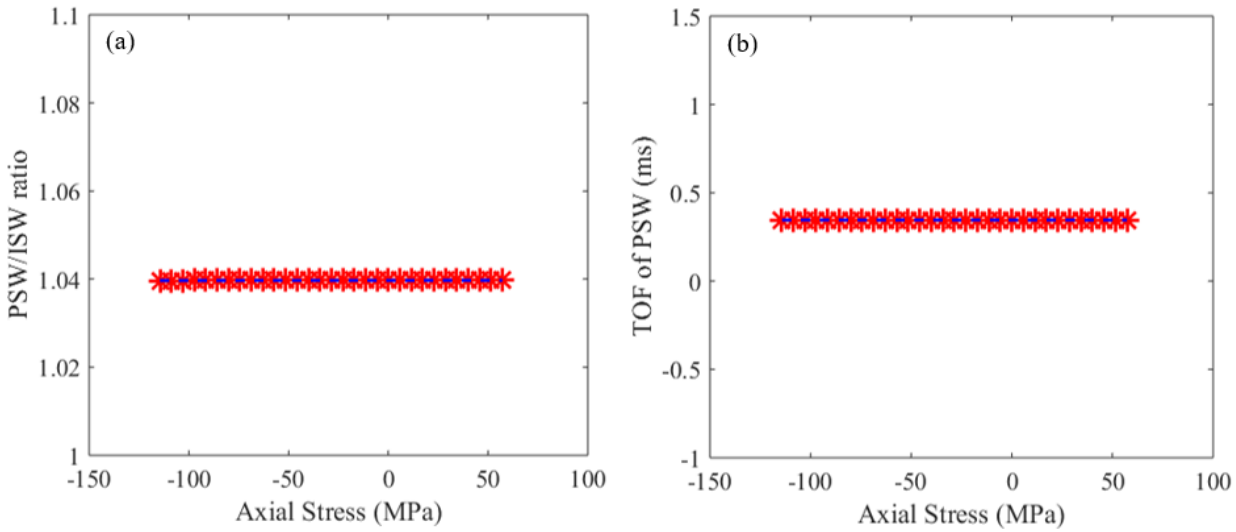

Figure 5-21 Numerical analysis. Solitary waves features as a function of the axial stress acting on an AREA 613/16 900 mm long unconstrained rail. (a) PSW/ISW ratio; (b) TOF of PSW

The results of the experiment are presented in **Figure 5-23**. **Figure 5-23(a)** shows one of the waveforms recorded at zero stress. As predicted numerically, the amplitude of the reflected wave is larger than the amplitude of the incident pulse. Not seen in the numerical model, a few bumps tailing both incident and reflected waves are visible. These bumps may likely due to the rebound of the striker at the moment of the impact and to reaction forces generated by the frame at the elbow. Future studies may consider using of a high-speed camera to capture the movement of the striker at the impact to verify such hypothesis.

Figure 5-23(b) displays the amplitude ratio as a function of the axial stress for both loading and unloading cycles. Each experimental point represents the average of the ten measurements and the vertical bars are twice the standard deviation associated with the measurements. The plot proves that the measurements were highly repeatable and that the solitary waves are basically unaffected by the stress. Across the stress range considered in this study the mean value of the PSW/ISW ratio was equal to 1.09, comparable to the numerical value of 1.04 (**Figure 5-21**(a)).

Therefore, the difference between the numerical and the experimental results is less than 5%. Similar considerations can be drawn for the time of flight (**Figure 5-23(c)**): the measurements were highly repeatable and in excellent agreement with the numerical prediction, namely 0.341 ms vs 0.346 ms, i.e. only 1.4% difference. The excellent match between the model and the experiment highlights the quality of the model and proves that the new NDE method can be applied in the field to any rail profile provided an accurate account of the "equivalent" length is attainable.

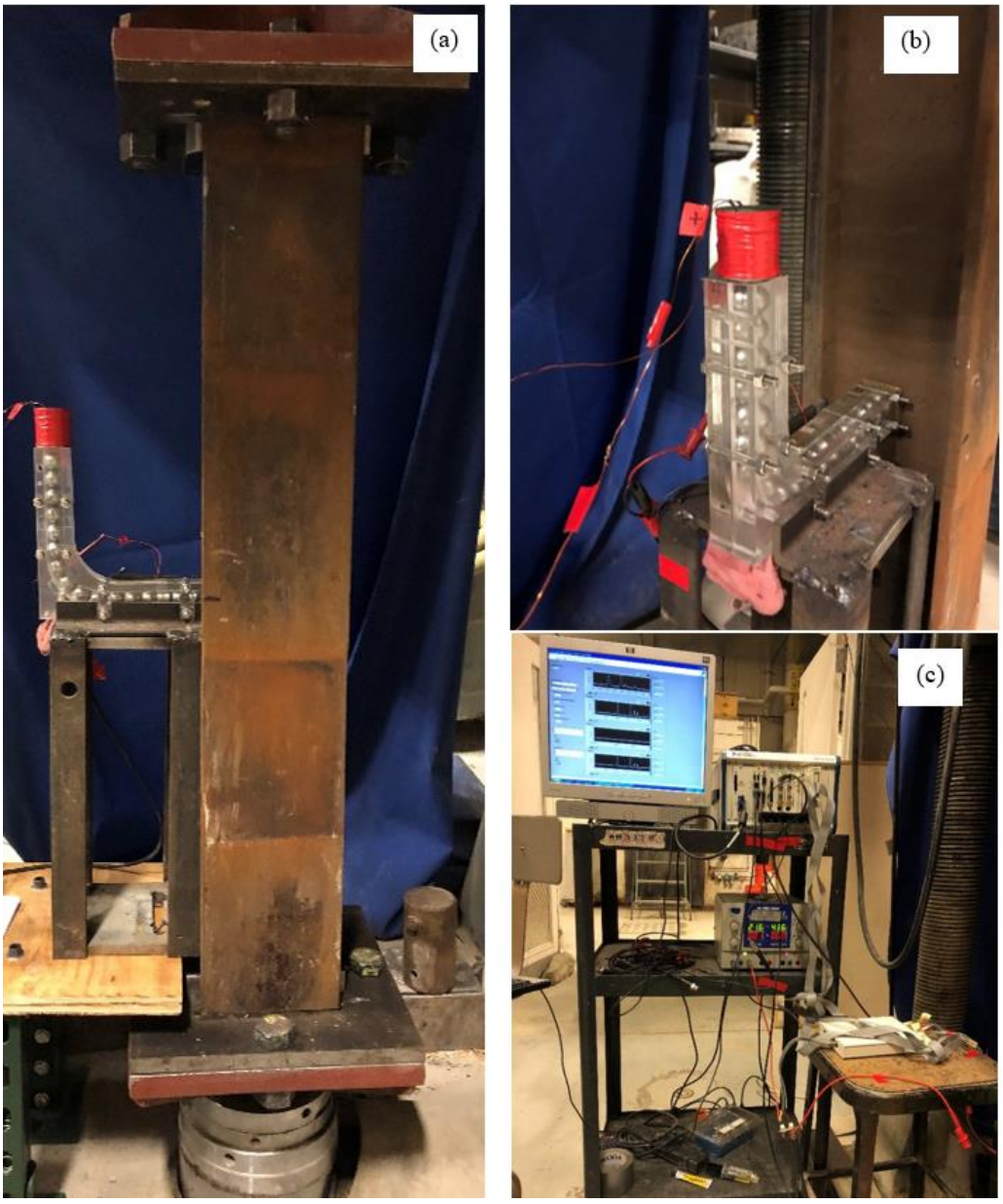

Figure 5-22 Test setup: (a) a photo of the position of the transducer; (b) the transducer in contact with the web of the rail; (c) the hardware system running the transducer

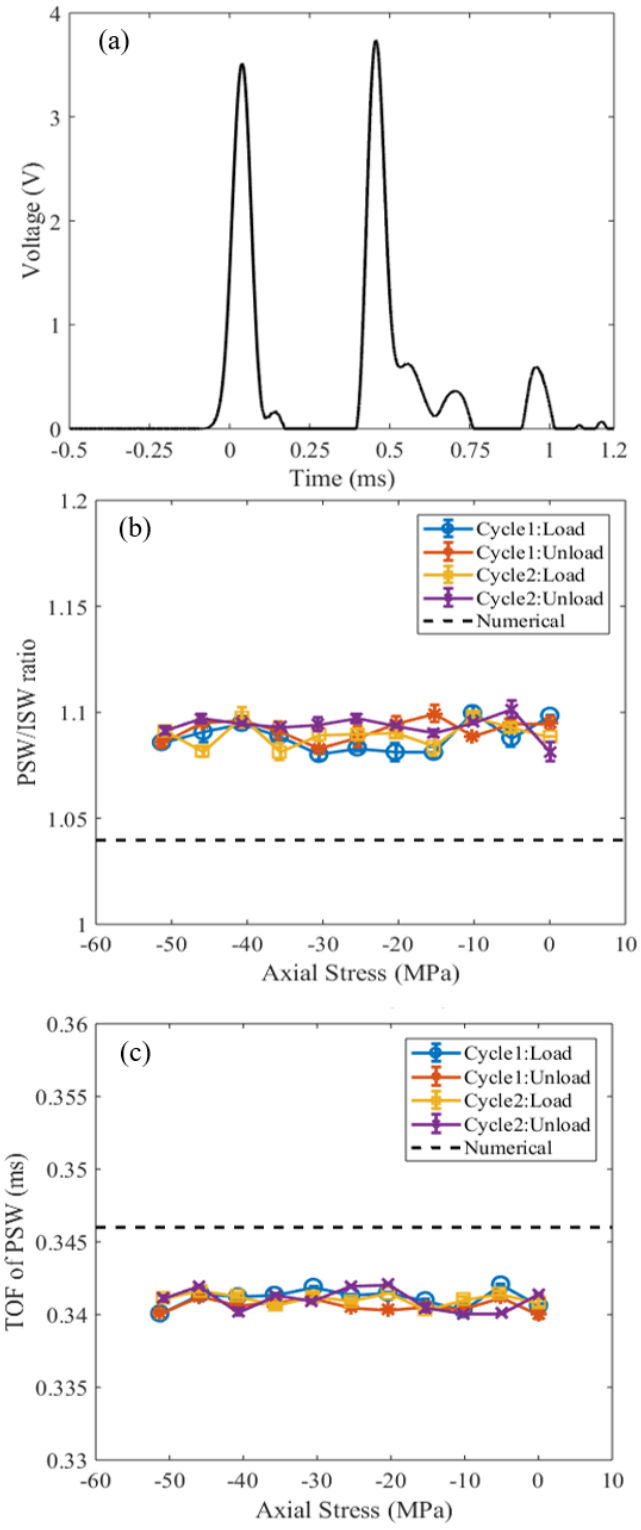

Figure 5-23 Experimental results. (a) Time waveform measured at zero axial stress; (b) the PSW/ISW ratio for different axial stresses; (c) the time of flight of the waveforms for different axial stresses

5.6.3 Conclusions

In this section, we presented a numerical and an experimental study about the use of highly ninlinear solitary waves to infer the longitudinal stress in continuous welded rails. The numerical analysis consisted of a finite element model coupled to a discrete particle model to predict the dynamic interplay between the propagation of solitary waves within a chain of particles and rails undergoing axial stress and in contact with the chain. A few features of the solitary waves were observed and charted against the axial stress to identify any variation of the features with respect to the stress. For the rail two lenghts were considered. The first length was equal to 3600 mm and consistent with some models found in the scientific literature in which the structural behavior of rialroad tracks subjected to high compressive thermal stress was considered equivalent to a straight unconstrained beam 3.6 m-long. The second rail segment was much shorter and equal to 900 mm in order to compare the numerical prediction with the experiment presented in the second part of this article. In the experiment a rail segment was subjected to mechanical compression. The numerical results proved that the characteristics of the solitary waves were significantly affected by the axial stress when the rail to be considered was 3600 mm long. When the track under investigation is too short, the rail is too stiff and the waves are largely unaffected by the stress. The latter numerically results agreed very well with the experimental results, both in terms of qualitative trend and quantitative values of the features. Overall, the results demonstrated that the proposed nondestructive evaluation system is robust in terms of repeatibility and sensisitvity to the variation of axial stress if the structural response of railroad tracks can be assumed equivalent to straight beams of identical cross-sectional area and moment of inertia and at least three meters long. The numerical results also implied that the nondestructive method can be applied anytime of the year without the need for a day long obervations that would eventually require the neutral

temperature crossing. In addition, the model presented in this article can be genralized and extended to any rail profile.

Future studies shall look at more experiments in a laboratory setting with longer rails and test the transducer in the field to collect important information to refine and validate the model.

6.0 Summary and Conclusions

6.1 Summary

This Ph.D. dissertation aimed at utilizing highly nonlinear solitary waves (HNSWs) for nondestructive evaluation applications. In particular, the following applications were considered: (1) characterization of concrete; (2) measurement of internal pressure of tennis balls; (3) measurement of axial stress of beams and rails. To reach this goal, several HNSW transducers were designed and assembled, and tested to quantify their repeatability and reliability. After that, numerical and experimental studies were conducted to investigate the dynamic interaction between solitary waves and structure under consideration. A graphical outline of the dissertation is shown in **Figure 6-1**.

For nondestructive evaluation of concrete, we accomplished the two studies: 1. estimation of the elastic modulus of concrete cylindrical samples with various *w/c* ratios, and 2. the effect of excessive surface water during concreting. In the study on the repeatability of the HNSW transducers, the main findings were: 1. the results show a small variation within and across the transducers. The repeatability was checked based on the TOF of the solitary pulses, the ratio of the PSW to the ISW, and the SSW to the ISW. These features are a function of the stiffness of the material in contact with the chain. 2. Using the features of HNSWs, we estimated the elastic modulus of several concrete small slabs. The same methodology was applied on cylindrical samples with different *w/c* ratios. The results show that this HNSW method is sensitive enough to capture the changes in the elastic modulus due to the change in *w/c* ratio. Compared to the standard tests, HNSW method was more accurate than conventional widely-used UPV method. Finally, this

methodology was applied to concrete short beams made with excessive water on the top or bottom surfaces during concreting. Because HNSW method can estimate the surface method, the changes can be estimated more accurately than UPV method which provides an average value over the thickness of the samples.

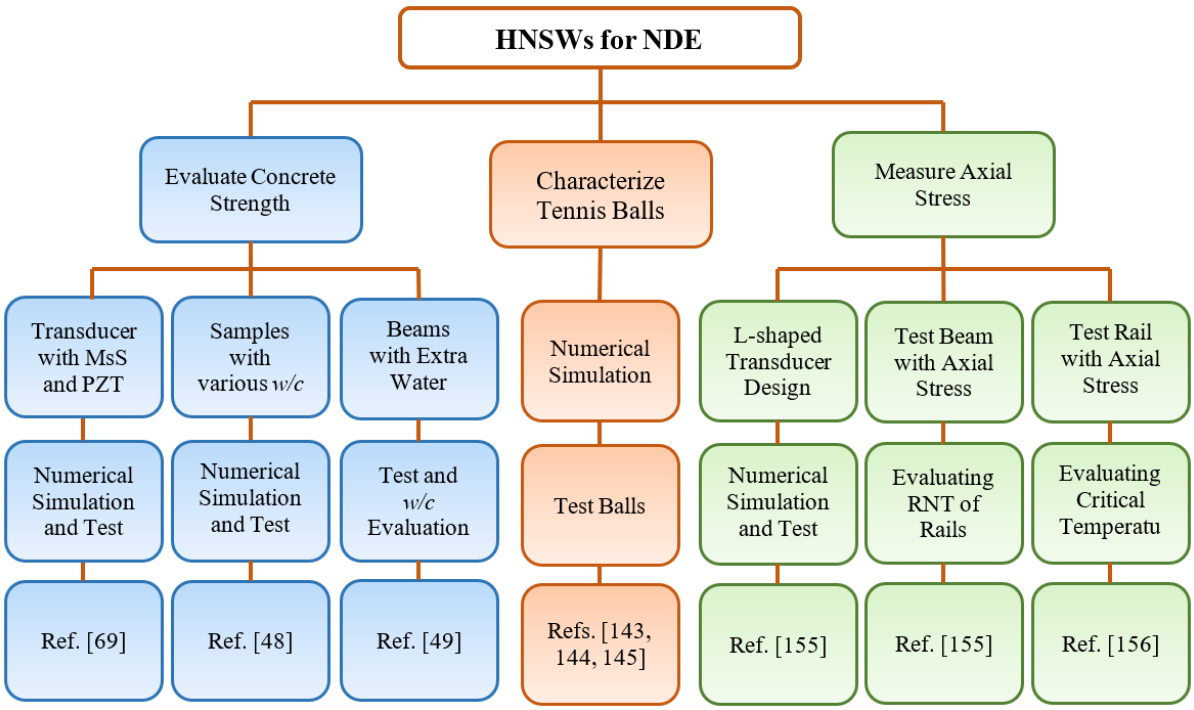

Figure 6-1 The studies accomplished in the Ph.D. program and presented in this dissertation

The application delved with the dynamic interaction between HNSWs and tennis balls The study enabled to understand whether HNSWs can be used to: estimating the internal pressure and performance of balls, to identify rubber degradation, and to establish new standards to be adopted by the ITF. For the estimation of the internal pressure and the material degradation of balls, a finite element model of the ball/chain interaction was coded in MATLAB. Several experiments were performed to prove the robustness of the proposed method. The results show that both internal

pressure change and the material degradation can be captured by HNSW method. However, the internal pressure changes the HNSW features more than the material stiffness. Finally, the coefficient of restitution and the forward and the return deformations of tennis balls, which are the standard ITF tests for balls, were correlated to the HNSW travel time in a transducer in contact with the balls. The results show that HNSW can be applied in characterizing the dynamic properties of tennis balls

The last part of the dissertation is about the determination of axial stress of thick beams and CWRs. The study was performed by making four L-shape transducers. The repeatability of the transducers were tested by running them several hundred times in contact with a short rail segment. To prove the effect of the methodology, a thermally and mechanically stressed thick beam was tested at different temperatures ranging from 25% of it yield stress to 25% of the buckling. The results proved the applicability of the method for determining the online axial stress in the beams. A finite element model was implemented in MATLAB using beam elements to correlate the axial stress changes to the HNSW features. Finally, the model was expanded to account for rail sections with ties. A short rail segment was tested to validate the numerical results.

6.2 Suggestions for Future Studies

The study presented in this dissertation shows the robustness of the HNSW method in determining the elastic modulus of concrete, characteristics of tennis balls, and axial stress of CWRs. All the studies were performed in the laboratory, and none of the applications have been tested in the field. In future studies, the hardware/software system should be transformed to

portable devises. Depending on the application, the portable device may be different. It is also recommended that the hardware/data processing systems to be included in the one device.

The field tests of each application is another open study area. The field test may require calibration and optimization of the device. For example, in the concrete application, the surface moisture or surface roughness may affect the results. In the case of rail application, the effect of ballast, ties, and curves on the sensitivity and the feasibility of the method should be studied further. In the case of tennis ball applications, the study performed in this dissertation was limited to a few commercial ball types and brands. The recommendation for this application can be a comprehensive study on various ball types and brands and draft new standards based on the HNSW features. The device should be built in a portable box which can be easily used at home or in sport facilities.

Bibliography

1. Hussein, M.I., M.J. Leamy, and M. Ruzzene, *Dynamics of phononic materials and structures: Historical origins, recent progress, and future outlook.* Applied Mechanics Reviews, 2014. **66**(4): p. 040802.

2. Cummer, S.A., J. Christensen, and A. Alù, *Controlling sound with acoustic metamaterials.* Nature Reviews Materials, 2016. **1**: p. 16001.

3. Brûlé, S., et al., *Experiments on seismic metamaterials: Molding surface waves.* Physical review letters, 2014. **112**(13): p. 133901.

4. Bell, J.S., et al., *Low acoustic transmittance through a holey structure.* Physical Review B, 2012. **85**(21): p. 214305.

5. Zigoneanu, L., B.-I. Popa, and S.A. Cummer, *Three-dimensional broadband omnidirectional acoustic ground cloak.* Nat Mater, 2014.

6. Guenneau, S.R., S. Enoch, and S. Brule, *Seismic metamaterials: Shielding and focusing surface elastic waves in structured soils.* The Journal of the Acoustical Society of America, 2014. **136**(4): p. 2077-2077.

7. Deymier, P.A., *Acoustic metamaterials and phononic crystals*. Vol. 173. 2013: Springer Science & Business Media.

8. Aravantinos-Zafiris, N. and M. Sigalas, *Large scale phononic metamaterials for seismic isolation.* Journal of Applied Physics, 2015. **118**(6): p. 064901.

9. Fraternali, F., et al., *Multiscale tunability of solitary wave dynamics in tensegrity metamaterials.* Applied Physics Letters, 2014. **105**(20): p. 201903.

10. Casadei, F., et al., *Piezoelectric resonator arrays for tunable acoustic waveguides and metamaterials.* Journal of Applied Physics, 2012. **112**(6): p. 064902.

11. Hussein, M.I. and M.J. Frazier, *Metadamping: An emergent phenomenon in dissipative metamaterials.* Journal of Sound and Vibration, 2013. **332**(20): p. 4767-4774.

12. Daraio, C. and P. Rizzo, *Method and apparatus for nondestructive evaluation and monitoring of materials and structures*. 2012, Google Patents.

13. Bagheri, A., P. Rizzo, and L. Al-Nazer, *A numerical study on the optimization of a granular medium to infer the axial stress in slender structures.* Mechanics of Advanced Materials and Structures, 2016. **23**(10): p. 1131-1143.

14. Bagheri, A., et al., *On the use of l-shaped granular chains for the assessment of thermal stress in slender structures.* Experimental Mechanics, 2015. **55**(3): p. 543-558.

15. Bagheri, A., P. Rizzo, and L. Al-Nazer, *Determination of the neutral temperature of slender beams by using nonlinear solitary waves.* Journal of Engineering Mechanics, 2014. **141**(6): p. 04014163.

16. Rizzo, P., et al., *A solitary wave-based sensor to monitor the setting of fresh concrete.* Sensors, 2014. **14**(7): p. 12568-12584.

17. Li, K., P. Rizzo, and X. Ni, *Alternative designs of acoustic lenses based on nonlinear solitary waves.* Journal of Applied Mechanics, 2014. **81**(7): p. 071011.

18. Cai, L., P. Rizzo, and L. Al-Nazer, *On the coupling mechanism between nonlinear solitary waves and slender beams.* International Journal of Solids and Structures, 2013. **50**(25): p. 4173-4183.

19. Cai, L., et al., *Propagation of highly nonlinear solitary waves in a curved granular chain.* Granular Matter, 2013. **15**(3): p. 357-366.

20. Rozina, S., et al. *Nondestructive testing of advanced materials using sensors with metamaterials*. in *IOP Conference Series: Materials Science and Engineering*. 2016. IOP Publishing.

21. Madeo, A., L. Placidi, and G. Rosi, *Towards the design of metamaterials with enhanced damage sensitivity: second gradient porous materials.* Research in Nondestructive Evaluation, 2014. **25**(2): p. 99-124.

22. Savin, A., et al., *Enhancement of spatial resolution using a metamaterial sensor in nondestructive evaluation.* Applied Sciences, 2015. **5**(4): p. 1412-1430.

23. Li, K. and P. Rizzo, *Energy harvesting using arrays of granular chains and solid rods.* Journal of Applied Physics, 2015. **117**(21): p. 215101.

24. Li, K. and P. Rizzo, *Energy harvesting using an array of granules.* Journal of Vibration and Acoustics, 2015. **137**(4): p. 041002.

25. Chen, Z., et al., *Metamaterials-based enhanced energy harvesting: A review.* Physica B: Condensed Matter, 2014. **438**: p. 1-8.

26. Carrara, M., et al., *Metamaterial-inspired structures and concepts for elastoacoustic wave energy harvesting.* Smart Materials and Structures, 2013. **22**(6): p. 065004.

27. Hu, G., et al., *Metastructure With Piezoelectric Element for Simultaneous Vibration Suppression and Energy Harvesting.* Journal of Vibration and Acoustics, 2017. **139**(1): p. 011012.

28. Bigoni, D., et al., *Elastic metamaterials with inertial locally resonant structures: Application to lensing and localization.* Physical Review B, 2013. **87**(17): p. 174303.

29. Rosenblatt, G. and M. Orenstein, *Perfect lensing by a single interface: defying loss and bandwidth limitations of metamaterials.* Physical review letters, 2015. **115**(19): p. 195504.

30. Bénédicto, J., et al., *Ultimate resolution of indefinite metamaterial flat lenses.* Physical Review B, 2013. **88**(24): p. 245138.

31. Kaina, N., et al., *Negative refractive index and acoustic superlens from multiple scattering in single negative metamaterials.* Nature, 2015. **525**(7567): p. 77.

32. Nesterenko, V., *Propagation of nonlinear compression pulses in granular media.* Journal of Applied Mechanics and Technical Physics, 1983. **24**(5): p. 733-743.

33. Coste, C., E. Falcon, and S. Fauve, *Solitary waves in a chain of beads under Hertz contact.* Physical review E, 1997. **56**(5): p. 6104.

34. Daraio, C., et al., *Tunability of solitary wave properties in one-dimensional strongly nonlinear phononic crystals.* Physical Review E, 2006. **73**(2): p. 026610.

35. Khatri, D., D. Ngo, and C. Daraio, *Highly nonlinear solitary waves in chains of cylindrical particles.* Granular Matter, 2012: p. 1-7.

36. Ngo, D., et al., *Highly nonlinear solitary waves in chains of hollow spherical particles.* Granular Matter, 2013. **15**(2): p. 149-155.

37. Ngo, D., D. Khatri, and C. Daraio, *Highly nonlinear solitary waves in chains of ellipsoidal particles.* Physical Review E, 2011. **84**(2): p. 026610.

38. Nesterenko, V., *Dynamics of heterogeneous materials*. 2013: Springer Science & Business Media.

39. Yang, J., et al., *Interaction of highly nonlinear solitary waves with linear elastic media.* Phys Rev E, 2011. **83**(4): p. 046606.

40. Schiffer, A., et al., *Interaction of highly nonlinear solitary waves with elastic solids containing a spherical void.* International Journal of Solids and Structures, 2017.

41. Yang, J., et al., *Interaction of highly nonlinear solitary waves with linear elastic media.* Physical Review E, 2011. **83**(4): p. 046606.

42. Job, S., et al., *How Hertzian solitary waves interact with boundaries in a 1D granular medium.* Physical review letters, 2005. **94**(17): p. 178002.

43. Job, S., et al., *Solitary wave trains in granular chains: experiments, theory and simulations.* Granular Matter, 2007. **10**(1): p. 13-20.

44. Manciu, F.S. and S. Sen, *Secondary solitary wave formation in systems with generalized Hertz interactions.* Physical Review E, 2002. **66**(1): p. 016616.

45. Falcon, E., et al., *Collision of a 1-D column of beads with a wall.* The European Physical Journal B-Condensed Matter and Complex Systems, 1998. **5**(1): p. 111-131.

46. Ni, X., et al., *Monitoring the hydration of cement using highly nonlinear solitary waves.* NDT & E International, 2012. **52**: p. 76-85.

47. Ni, X. and P. Rizzo, *Use of highly nonlinear solitary waves in nondestructive testing.* Materials evaluation, 2012. **70**(5).

48. Nasrollahi, A., et al., *Nondestructive testing of concrete using highly nonlinear solitary waves.* Nondestructive Testing and Evaluation, 2017. **32**(4): p. 381-399.

49. Rizzo, P., et al., *Detecting the presence of high water-to-cement ratio in concrete surfaces using highly nonlinear solitary waves.* Applied Sciences, 2016. **6**(4): p. 104.

50. Deng, W., et al., *On the Reliability of a Solitary Wave Based Transducer to Determine the Characteristics of Some Materials.* Sensors, 2016. **16**(1): p. 5.

51. Vergara, L., *Scattering of solitary waves from interfaces in granular media.* Physical review letters, 2005. **95**(10): p. 108002.

52. Ni, X., et al., *Monitoring the hydration of cement using highly nonlinear solitary waves.* NDT&E Int, 2012. **52**: p. 76-85.

53. Cai, L., P. Rizzo, and L. Al-Nazer, *On the coupling mechanism between nonlinear solitary waves and slender beams.* Int J Solids Struct, 2013. **50**(25): p. 4173-83.

54. Bagheri, A., et al., *On the coupling dynamics between thermally stressed beams and granular chains.* Archive of Applied Mechanics, 2015: p. 1-16.

55. Bagheri, A., et al., *On the use of L-shaped granular chains for the assessment of thermal stress in slender structures.* Experimental Mechanics, 2014. **55**(3): p. 543-558.

56. Aydin, A. and A. Basu, *The Schmidt hammer in rock material characterization.* Eng Geol, 2005. **81**(1): p. 1-14.

57. Phillips, R.R., *Ultrasonic methods for rail inspection*. 2012, Inuversity of California San Diego.

58. Bartoli, I., et al., *Stress dependence of ultrasonic guided waves in rails.* Transportation Research Record: Journal of the Transportation Research Board, 2010(2159): p. 91-97.

59. Nucera, C. and F.L. di Scalea, *Nonlinear wave propagation in constrained solids subjected to thermal loads.* Journal of Sound and Vibration, 2014. **333**(2): p. 541-554.

60. Nucera, C. and F. Lanza di Scalea, *Nondestructive measurement of neutral temperature in continuous welded rails by nonlinear ultrasonic guided waves.* The Journal of the Acoustical Society of America, 2014. **136**(5): p. 2561-2574.

61. Bagheri, A., et al., *On the coupling dynamics between thermally stressed beams and granular chains.* Archive of Applied Mechanics, 2016. **86**(3): p. 541-556.

62. Ni, X., P. Rizzo, and C. Daraio, *Laser-based excitation of nonlinear solitary waves in a chain of particles.* Phys Rev E, 2011. **84**(2): p. 026601.

63. Hertz, H., *On the contact of elastic solids.* J Reine Angew Math, 1881. **92**(156-171): p. 110.

64. Nesterenko, V.F., *Dynamics of heterogeneous materials*. 2013: Springer Science & Business Media.

65. Daraio, C., et al., *Tunability of solitary wave properties in one-dimensional strongly nonlinear phononic crystals.* Phys Rev E, 2006. **73**(2): p. 026610.

66. Nesterenko, V.J.J.o.A.M. and T. Physics, *Propagation of nonlinear compression pulses in granular media.* 1983. **24**(5): p. 733-743.

67. Herbold, E.B., *Optimization of the dynamic behavior of strongly nonlinear heterogeneous materials*. 2008: University of California, San Diego.

68. Deng, W., et al., *On the Reliability of a Solitary Wave Based Transducer to Determine the Characteristics of Some Materials.* Sensors, 2016. **16**(5).

69. Malhotra, V.M. and N.J. Carino, *Handbook on Nondestructive Testing of Concrete Second Edition*. 2003: CRC press, Boca Raton, FL, USA.

70. Karaiskos, G., et al., *Monitoring of concrete structures using the ultrasonic pulse velocity method.* Smart Materials and Structures, 2015. **24**(11): p. 113001.

71. Shah, A., Y. Ribakov, and C. Zhang, *Efficiency and sensitivity of linear and non-linear ultrasonics to identifying micro and macro-scale defects in concrete.* Materials & Design, 2013. **50**: p. 905-916.

72. Ye, G., et al., *Study on the development of the microstructure in cement-based materials by means of numerical simulation and ultrasonic pulse velocity measurement.* Cement and Concrete Composites, 2004. **26**(5): p. 491-497.

73. Lin, Y., C.-P. Lai, and T. Yen, *Prediction of ultrasonic pulse velocity (UPV) in concrete.* ACI Materials Journal, 2003. **100**(1): p. 21-28.

74. Shariq, M., J. Prasad, and A. Masood, *Studies in ultrasonic pulse velocity of concrete containing GGBFS.* Construction and Building Materials, 2013. **40**: p. 944-950.

75. Komlos, K., et al., *Ultrasonic pulse velocity test of concrete properties as specified in various standards.* Cement and Concrete Composites, 1996. **18**(5): p. 357-364.

76. Popovics, S., *Analysis of the concrete strength versus ultrasonic pulse velocity relationship.* Materials Evaluation, 2001. **59**(2): p. 123-130.

77. Hong, S., et al., *Estimation of compressive strength of concrete structures using the ultrasonic pulse velocity method and spectral analysis of surface wave method.* Materials Research Innovations, 2015. **19**(S5): p. S5-1289-S5-1294.

78. Huang, Q., P. Gardoni, and S. Hurlebaus, *Predicting concrete compressive strength using ultrasonic pulse velocity and rebound number.* ACI Materials Journal, 2011. **108**(4): p. 403-412.

79. Choi, H. and J.S. Popovics, *NDE application of ultrasonic tomography to a full-scale concrete structure.* Ultrasonics, Ferroelectrics, and Frequency Control, IEEE Transactions on, 2015. **62**(6): p. 1076-1085.

80. Völker, C. and P. Shokouhi, *Multi sensor data fusion approach for automatic honeycomb detection in concrete.* NDT & E International, 2015. **71**: p. 54-60.

81. Kim, G., et al., *Air-coupled detection of nonlinear Rayleigh surface waves in concrete—Application to microcracking detection.* NDT & E International, 2014. **67**: p. 64-70.

82. Saravanan, T.J., et al., *Comparative performance of various smart aggregates during strength gain and damage states of concrete.* Smart Materials and Structures, 2015. **24**(8): p. 085016.

83. Clayton, D.A., et al., *Nondestructive Evaluation of Thick Concrete Using Advanced Signal Processing Techniques*. 2015, DOI: 10.2172/1221739, Oak Ridge National Laboratory (ORNL).

84. Shih, Y.-F., et al., *Improving Non-Destructive Concrete Strength Tests Using Support Vector Machines.* Materials, 2015. **8**(10): p. 7169-7178.

85. Cano-Barrita, P.d.J., et al., *Monitoring Compressive Strength of Concrete by Nuclear Magnetic Resonance, Ultrasound, and Rebound Hammer.* ACI Materials Journal, 2015. **112**(1): p. 147-154.

86. Amini, K., M. Jalalpour, and N. Delatte, *Advancing concrete strength prediction using non-destructive testing: Development and verification of a generalizable model.* Construction and Building Materials, 2016. **102**: p. 762-768.

87. Saleem, M., et al., *Nondestructive Testing Procedure to Evaluate the Load-Carrying Capacity of Concrete Anchors.* Journal of Construction Engineering and Management, 2015: p. 04015104.

88. Pucinotti, R., *Reinforced concrete structure: Non destructive in situ strength assessment of concrete.* Construction and Building Materials, 2015. **75**: p. 331-341.

89. Azari, H. and S. Nazarian, *Optimization of Acoustic Methods for Condition Assessment of Concrete Structures.* ACI Materials Journal, 2015. **112**(4).

90. Ham, S. and J.S. Popovics, *Application of Micro-Electro-Mechanical Sensors Contactless NDT of Concrete Structures.* Sensors, 2015. **15**(4): p. 9078-9096.

91. Hoegh, K., et al., *Evaluating asphalt concrete air void variation via GPR antenna array data.* Case Studies in Nondestructive Testing and Evaluation, 2015. **3**: p. 27-33.

92. Iliopoulos, S.N., D.G. Aggelis, and D. Polyzos, *Wave dispersion in fresh and hardened concrete through the prism of gradient elasticity.* International Journal of Solids and Structures, 2016. **78**: p. 149-159.

93. Dimter, S., T. Rukavina, and K. Minažek, *Estimation of elastic properties of fly ash–stabilized mixes using nondestructive evaluation methods.* Construction and Building Materials, 2016. **102**: p. 505-514.

94. Pessiki, S. and N. Carino, *Setting time and strength of concrete using the impact-echo method.* ACI Mater J, 1988. **85**(5): p. 389-99.

95. Jenq, Y. and S. Kim. *Control of Random Crack Formation in Portland Cement Concrete Pavements*. in *Structures Congress XII*. 1994. ASCE.

96. Pessiki, S. and M. Johnson, *Nondestructive evaluation of early-age concrete strength in plate structures by the impact-echo method.* ACI Mater J, 1996. **93**(3): p. 1-12.

97. Ye, G., K. Van Breugel, and A. Fraaij, *Experimental study and numerical simulation on the formation of microstructure in cementitious materials at early age.* Cem Concr Res, 2003. **33**(2): p. 233-39.

98. Lee, H., et al., *Ultrasonic in-situ monitoring of setting process of high-performance concrete.* Cem Concr Res, 2004. **34**(4): p. 631-40.

99. Reinhardt, H. and C. Grosse, *Continuous monitoring of setting and hardening of mortar and concrete.* Constr Build Mater., 2004. **18**(3): p. 145-54.

100. Ye, G., et al., *Study on the development of the microstructure in cement-based materials by means of numerical simulation and ultrasonic pulse velocity measurement.* Cem Concr Compos, 2004. **26**(5): p. 491-97.

101. De Belie, N., et al., *Ultrasound monitoring of the influence of different accelerating admixtures and cement types for shotcrete on setting and hardening behaviour.* Cem Concr Res, 2005. **35**(11): p. 2087-94.

102.Robeyst, N., et al., *Monitoring the setting of concrete containing blast-furnace slag by measuring the ultrasonic p-wave velocity.* Cem Concr Res, 2008. **38**(10): p. 1169-76.

103.Voigt, T., et al., *Comparison of ultrasonic wave transmission and reflection measurements with P-and S-waves on early age mortar and concrete.* Mater Struct, 2005. **38**(8): p. 729-38.

104.Rapoport, J.R., et al., *Using ultrasound to monitor stiffening process of concrete with admixtures.* ACI Mater J, 2000. **97**(6): p. 675–83.

105.Subramaniam, K., et al., *Ultrasonic technique for monitoring concrete strength gain at early age.* ACI Mater J, 2002. **99**(5).

106.Akkaya, Y., et al., *Nondestructive measurement of concrete strength gain by an ultrasonic wave reflection method.* Mater Struct, 2003. **36**(8): p. 507-14.

107.Voigt, T., Y. Akkaya, and S.P. Shah, *Determination of early age mortar and concrete strength by ultrasonic wave reflections.* J Mater Civ Eng, 2003. **15**(3): p. 247-54.

108.Voigt, T. and S.P. Shah, *Properties of early-age Portland cement mortar monitored with shear wave reflection method.* ACI Mater J, 2004. **101**(6): p. 473-82.

109.Subramaniam, K.V., J. Lee, and B.J. Christensen, *Monitoring the setting behavior of cementitious materials using one-sided ultrasonic measurements.* Cem Concr Res, 2005. **35**(5): p. 850-57.

110.Voigt, T., et al., *Early age microstructure of Portland cement mortar investigated by ultrasonic shear waves and numerical simulation.* Cem Concr Res, 2005. **35**(5): p. 858-66.

111.Garnier, V., et al., *Setting time study of roller compacted concrete by spectral analysis of transmitted ultrasonic signals.* NDT&E Int, 1995. **28**(1): p. 15-22.

112.Öztürk, T., et al., *Improved ultrasonic wave reflection technique to monitor the setting of cement-based materials.* NDT&E Int, 2006. **39**(4): p. 258-63.

113.Öztürk, T., et al., *Monitoring the setting and hardening of cement-based materials with ultrasound.* Concr Sci Eng., 1999. **1**(2): p. 83-91.

114.Al-Jumaili, S.K., et al., *Acoustic emission source location in complex structures using full automatic delta T mapping technique.* Mechanical Systems and Signal Processing, 2016. **72**: p. 513-524.

115. *ASTM C39. Standard test method for compressive strength of cylindrical concrete specimens*. 1997.

116. Barile, C., et al., *Analysis of crack propagation in stainless steel by comparing acoustic emissions and infrared thermography data.* Engineering Failure Analysis, 2016.

117. Deng, W., Nasrollahi, A, Rizzo, P, Li, K, *On the Reliability of a Solitary Wave Based Transducer to Determine the Characteristics of some Materials.* Sensors, 2015. **In Press**.

118. http://www.azom.com/article.aspx?ArticleID=6114#4.

119. Rizzo, P., *Health monitoring of tendons and stay cables for civil structures*. 2004: University of California, San Diego.

120. Rizzo, P. and F. Lanza di Scalea, *Wavelet-based unsupervised and supervised learning algorithms for ultrasonic structural monitoring of waveguides.* Progress in smart materials and structures research, 2007: p. 227-90.

121. Ni, X., L. Cai, and P. Rizzo, *A Comparative Study on Three Different Transducers for the Measurement of Nonlinear Solitary Waves.* Sensors, 2013. **13**(1): p. 1231-1246.

122. Lanza di Scalea, F., P. Rizzo, and F. Seible, *Stress measurement and defect detection in steel strands by guided stress waves.* J Mater Civ Eng, 2003. **15**(3): p. 219-27.

123. Rizzo, P. and F. Lanza di Scalea, *Feature extraction for defect detection in strands by guided ultrasonic waves.* Struct Health Monit, 2006. **5**(3): p. 297-308.

124. Rizzo, P. and F. Lanza di Scalea, *Wavelet-based feature extraction for automatic defect classification in strands by ultrasonic structural monitoring.* Smart Struct Syst, 2006. **2**(3): p. 253-74.

125. http://asm.matweb.com/search/SpecificMaterial.asp?bassnum=MQ304A.

126. http://www.sawbones.com/UserFiles/Docs/biomechanical_catalog.pdf.

127. Timoshenko, S., S. Woinowsky-Krieger, and S. Woinowsky-Krieger, *Theory of plates and shells*. Vol. 2. 1959: McGraw-hill New York.

128. Eaton, W.P., et al. *A new analytical solution for diaphragm deflection and its application to a surface micromachined Pressure sensor*. in *International Conference on Modeling and Simulation, MSM*. 1999.

129.Lydon, F. and R. Balendran, *Some observations on elastic properties of plain concrete.* Cement Concrete Res, 1986. **16**(3): p. 314-24.

130.Popovics, J., J. Zemajtis, and I. Shkolnik, *A study of static and dynamic modulus of elasticity of concrete*. 2008, ACI-CRC Final Report, Civil and Environmental Engineering, University of Illinois, Urbana IL.

131.Malhotra, V.M. and N.J. Carino, *CRC handbook on nondestructive testing of concrete*. 1991: CRC press.

132.Piervincenzo Rizzo, A.N., Wen Deng, Julie M. Vandenbossche, *Detecting the Presence of High Water-to-Cement Ratio in Concrete Surfaces Using Highly Nonlinear Solitary Waves.* applied sciences, 2016. **6**(4).

133.Standard, A., *Standard Test Method for Static Modulus of Elasticity and Poisson's Ratio of Concrete in Compression.* 2010.

134.Kim, H.J., et al., *Numerical simulation of guided waves using equivalent source model of magnetostrictive patch transducers.* 2014. **24**(1): p. 015006.

135.Kim, C.-Y., K.-J.J.N. Park, and E. International, *Mode separation and characterization of torsional guided wave signals reflected from defects using chirplet transform.* 2015. **74**: p. 15-23.

136.Kannan, E., et al., *SHM of pipes using torsional waves generated by in situ magnetostrictive tapes.* 2007. **16**(6): p. 2505.

137.Popovics, J., J. Zemajtis, and I.J.U.o.I. Shkolnik, Urbana, IL, *A study of static and dynamic modulus of elasticity of concrete: ACICRC Final Report.* 2008.

138.Nasrollahi, A., et al., *Highly nonlinear solitary waves to estimate the modulus of concrete with different water-to-cement ratios.* NDT & E International: p. (under review).

139.Farrar, C.R. and K. Worden, *Structural health monitoring: a machine learning perspective*. 2012: John Wiley & Sons.

140.Nasrollahi, A., P. Rizzo, and M.S. Orak, *Numerical and Experimental Study on the Dynamic Interaction Between Highly Nonlinear Solitary Waves and Pressurized Balls.* Journal of Applied Mechanics, 2018. **85**(3): p. 031007-031007-11.

141.Nasrollahi, A., R. Lucht, and P. Rizzo, *Solitary Waves to Assess Internal Pressure and Rubber Degradation in Tennis Balls.* Experimental Mechanics. **In Press**.

142.Nasrollahi, A., et al., *An alternative noninvasive approach to characterize tennis balls.* Under Review.

143.Bagheri, A. and P. Rizzo, *Assessing the pressure of tennis balls using nonlinear solitary waves: a numerical study.* Sports Engineering, 2017. **20**(1): p. 53-62.

144.Belytschko, T., et al., *Nonlinear finite elements for continua and structures*. 2013: John wiley & sons.

145.Frey, P.J. and P.L. George, *Mesh generation: application to finite elements*. 2000: Wiley Online Library.

146.Goodwill, S., R. Kirk, and S. Haake, *Experimental and finite element analysis of a tennis ball impact on a rigid surface.* Sports engineering, 2005. **8**(3): p. 145-158.

147.Lédeczi, Á., et al., *Wireless acoustic emission sensor network for structural monitoring.* IEEE Sensors Journal, 2009. **9**(11): p. 1370-1377.

148.Sissler, L., *Advanced modelling and design of a tennis ball*. 2012, © Lise Sissler.

149.Sissler, L., et al. *Viscoelastic modelling of tennis ball properties*. in *IOP Conference Series: Materials Science and Engineering*. 2010. IOP Publishing.

150.Na, S., R. Tawie, and H.-K. Lee, *Electromechanical impedance method of fiber-reinforced plastic adhesive joints in corrosive environment using a reusable piezoelectric device.* Journal of Intelligent Material Systems and Structures, 2012: p. 1045389X12440754.

151.Cross, R.J.A.J.o.P., *The bounce of a ball.* 1999. **67**(3): p. 222-227.

152.Nasrollahi, A. and P. Rizzo, *Axial stress determination using highly nonlinear solitary waves.* Journal of Acoustical Society of America, In Press.

153.Nasrollahi, A. and P. Rizzo, *Dynamic interaction between highly nonlinear solitary waves and rails: Numerical Analysis and Experimental Validation* Journal of Sound and Vibration, Under Review.

154.Tunna, J.J.L.R.f.V.I.T.T.C., Inc., Pueblo, CO, *Vertical rail stiffness equipment (VERSE) trials.* 2000.

155.Kish, A. and G.J.A.r.e.a. Samavedam, *Longitudinal force measurement in continuous welded rail from beam column deflection response.* 1987. **88**.

156.Wegner, A. *Prevention of track buckling and rail fracture by non-destructive testing of the neutral temperature in cw-rails*. in *Proceedings International Heavy Haul Conference*. 2007.

157.Phillips, R. and X.Z.J.M.e. di Scalea, *The influence of stress on Electro-mechanical impedance measurements in rail steel.* 2012. **70**(10): p. 1213-1218.

158.Zhu, X. and F.L. di Scalea, *Sensitivity to axial stress of electro-mechanical impedance measurements.* Experimental Mechanics, 2016. **56**(9): p. 1599-1610.

159.Szelazek, J.J.E.N.T., *Monitoring of thermal stresses in continuously welded rails with ultrasonic technique.* 1998. **98**.

160.Hurlebaus, S., *Determination of longitudinal stress in rails*. 2011.

161.Nucera, C., et al., *RAIL-NT System for the in-situ measurement of neutral temperature in CWR: results from laboratory and field test.* Journal of the Transportation Research Board, 2013. **3511**.

162.Kerr, A.J.R.I., *The effect of lateral resistance on track buckling analysis.* 1976. **7**(1).

163.Kerr, A.D., *Analysis of thermal track buckling in the lateral planeAnalyse des thermischen Geleisebeulens in die Querebene.* Acta Mechanica, 1978. **30**(1-2): p. 17-50.

164.Bao, Y. and E.J.T.R.R.J.o.t.T.R.B. Barenberg, *Three-dimensional nonlinear stability analysis of tangent continuous welded rail track under temperature and mechanical loads.* 1997(1584): p. 31-40.

165.Lim, N.-H., et al., *Parametric study on stability of continuous welded rail track-ballast resistance and track irregularity.* Steel Structures, 2008. **8**: p. 171-181.

166.Lim, N.-H., N.-H. Park, and Y.-J. Kang, *Stability of continuous welded rail track.* Computers & Structures, 2003. **81**(22-23): p. 2219-2236.

167.Donley, M.G. and A.D. Kerr, *Thermal buckling of curved railroad tracks.* International Journal of Non-Linear Mechanics, 1987. **22**(3): p. 175-192.

168.Kerr, A.D., *Lateral buckling of railroad tracks due to constrained thermal expansions—a critical survey*, in *Railroad track mechanics and technology*. 1978, Elsevier. p. 141-169.

169.Kerr, A.D., *An improved analysis for thermal track buckling.* International Journal of Non-Linear Mechanics, 1980. **15**(2): p. 99-114.

170.Kish, A., *On the fundamentals of track lateral resistance.* American Railway Engineering and Maintenance of Way Association, 2011.

171.Martínez, I.N., et al., *Analytical model for predicting the buckling load of continuous welded rail tracks.* Proceedings of the Institution of Mechanical Engineers, Part F: Journal of Rail and Rapid Transit, 2015. **229**(5): p. 542-552.

172.Kish, A., G. Samavedam, and D. Jeong, *Analysis of thermal buckling tests on US railroads*. 1982, Federal Railroad Administration, Office of Research and Development.

173.Kish, A. and G. Samavedam, *Dynamic buckling of continuous welded rail track: Theory, tests, and safety concepts.* Transportation Research Record, 1991. **1289**: p. 23-38.

174.Zienkiewicz, O.C. and R.L. Taylor, *The finite element method for solid and structural mechanics*. 2005: Elsevier.

175.Chopra, A.K., *Dynamics of Structures. Theory and Applications to.* Earthquake Engineering, 2017.

176.Tedesco, J.W., W.G. McDougal, and C.A. Ross, *Structural dynamics: theory and applications*. 1999: Addison-Wesley Menlo Park, CA.

177.Rizzo, P. and F. Lanza di Scalea, *Effect of frequency on the acoustoelastic response of steel bars.* Experimental Techniques, 2003. **27**(6): p. 40-43.

178.Rizzo, P. and F.L.J.M.e. DI SCALEA, *Load measurement and health monitoring in cable stays via guided wave magnetostrictive ultrasonics.* 2004. **62**(10): p. 1057-1065.